From 2d-van der Waals magnets to superconductor hybrid devices

Von der Fakultät für Mathematik, Informatik und Naturwissenschaften der RWTH Aachen University zur Erlangung des akademischen Grades eines Doktors der Naturwissenschaften genehmigte Dissertation

vorgelegt von

Lara Celine Ortmanns, M. Sc.

aus Duisburg

Berichter: apl.-Prof. Dr. rer. nat. Maarten Rolf Wegewijs
Prof. Dr. rer. nat. Janine Splettstößer
Univ.-Prof. Dr. rer. nat. Volker Meden

Tag der mündlichen Prüfung: 21. Juni 2023

Diese Dissertation ist auf den Internetseiten der Universitätsbibliothek online verfügbar.

Thesis for the degree of Doctor of Philosophy

From 2d-van der Waals magnets to superconductor hybrid devices

Lara Celine Ortmanns

Department of Microtechnology and Nanoscience MC2
Chalmers University of Technology

Göteborg, Sweden 2023

From 2d-van der Waals magnets to superconductor hybrid devices
Lara Celine Ortmanns
ISBN 978-91-7905-882-1

Doktorsavhandlingar vid Chalmers tekniska högskola
Ny serie nr 5348
ISSN 0346-718X

Department of Microtechnology and Nanoscience
Chalmers University of Technology
SE-412 96 Gothenburg
Sweden
Telephone + 46 (0)31-772 1000

Institute for Theory of Statistical Physics
RWTH Aachen
D-52056 Aachen
Germany

Printed by Chalmers Reproservice
Gothenburg, Sweden 2023

Eidesstattliche Erklärung

Ich, Lara Celine Ortmanns, erkläre hiermit, dass diese Dissertation und die darin dargelegten Inhalte die eigenen sind und selbstständig, als Ergebnis der eigenen originären Forschung, generiert wurden.

Hiermit erkläre ich an Eides statt:

1. Diese Arbeit wurde vollständig oder größtenteils in der Phase als Doktorand dieser Fakultät und Universität angefertigt;
2. Sofern irgendein Bestandteil dieser Dissertation zuvor für einen akademischen Abschluss oder eine andere Qualifikation an dieser oder einer anderen Institution verwendet wurde, wurde dies klar angezeigt;
3. Wenn immer andere eigene- oder Veröffentlichungen Dritter herangezogen wurden, wurden diese klar benannt;
4. Wenn aus anderen eigenen- oder Veröffentlichungen Dritter zitiert wurde, wurde stets die Quelle hierfür angegeben. Diese Dissertation ist vollständig meine eigene Arbeit, mit der Ausnahme solcher Zitate;
5. Alle wesentlichen Quellen von Unterstützung wurden benannt;
6. Wenn immer ein Teil dieser Dissertation auf der Zusammenarbeit mit anderen basiert, wurde von mir klar gekennzeichnet, was von anderen und was von mir selbst erarbeitet wurde;
7. Teile dieser Arbeit wurden zuvor veröffentlicht und zwar in den Referenzen [1–3].

Ort, Datum	Lara Celine Ortmanns

List of publications

- Lara C. Ortmanns, Gerrit E. W. Bauer and Yaroslav M. Blanter
  "Magnon dispersion in bilayers of two-dimensional ferromagnets"
  Phys. Rev. B **103**, 155430 (2021)

- Lara C. Ortmanns, Maarten R. Wegewijs and Janine Splettstoesser
  "Solution of master equations by fermionic-duality: Time-dependent charge and heat currents through an interacting quantum dot proximized by a superconductor"
  SciPost Phys. **14**, 095 (2023)

- Lara C. Ortmanns, Janine Splettstoesser and Maarten R. Wegewijs
  "Transient transport spectroscopy of an interacting quantum dot proximized by a superconductor: Charge- and heat-currents after a switch"
  arXiv:2304.14893 (2023)

Parts of the text of this thesis closely follow the publications listed above.

Acknowledgments

First of all, I would like to thank my supervisors Prof. Maarten R. Wegewijs (RWTH Aachen University) and Prof. Janine Splettstößer (Chalmers University of Technology in Göteborg, Sweden) for letting me join their respective groups. Thanks to you, Janine, for zoom meetings from Sweden, while I was still in Aachen during Corona times and the institute in Aachen was closed, for your warm welcome when I came to Chalmers University, for encouraging me to participate in conferences, and for valuable discussions. Thanks to you also for suggesting to include the additions to my master thesis as part of the PhD thesis when I was working for the first paper of the master thesis in the beginning of my time at Chalmers. Thanks to you, Maarten, for valuable discussions and suggestions about the PhD project, recommending conferences and being available whenever you could make it possible in spite of difficult circumstances. Thanks to you, Matteo Acciai and Christian Spånslätt Rugarn at Chalmers for our interesting discussions on physics outside the topic of my thesis. I enjoyed very much the interesting lectures at Chalmers University on Quantum Optics and Quantum Information and on Quantum Computing, which I appreciated a lot. I would like to thank my former supervisor of the master thesis Prof. Yaroslav M. Blanter (Technical University of Delft) and the coauthor Prof. Gerrit E. W. Bauer (Technical University of Delft, AIMR Tohoku University & KITS UCAS) for valuable discussions during the review process of the first paper. I would like to thank the DFG (RTG 1995) for financial support and the speaker of this research training group, Prof. Volker Meden, for his constructive advice.

Foremost I would like to thank my family and friends for their moral support during a rather tough time, since the work had to be done under extreme conditions due to atmospheric disturbances, whereas I enjoyed the scientific aspects of the work very much.

Short Summary

In this thesis, we focus on two distinct topics in different lines of research within mesoscopic physics, the first is related to spin-waves in 2d-van der Waals magnets, the second to the transient dynamics of a quantum dot device attached to a normal metal and proximized with a superconducting material. Based on our earlier work on the magnon dispersion in bilayers of 2d-ferromagnets, in this thesis we complement the earlier work by further analyzing the competing interactions in the Hamiltonian. Moreover, we explain the magnon dispersion degeneracy and the topology of the magnon spectrum in terms of an underlying PT-symmetry. As a result, we can exclude a magnon (thermal) Hall effect for our type of exchange anisotropy spin model, but indicate extensions of our model that would allow for non-trivial topological effects. The analysis of this first topic amounts to a study of equilibrium properties of 2d bulk materials, which exhibit magnetic order. The relevant excitations of interest are magnons, which are bosons. Differently, for the second topic we deal with the transient dynamics of a quantum dot device after a switch in gate voltage, where instead of magnetic order we have superconducting order in the lead attached, which induces a pronounced proximity effect on the sensitive quantum dot. The main degrees of freedom here are fermions. In our limit of interest, we do not resolve coherences in the description of the dynamics and determine the kernel of the time-evolution operator based on Fermi's Golden rule and the electrostatics of the device. In spite of this simplification, we show that it is still advantageous to formulate the traditional approach in Liouville space to study the transient dynamics instead of the stationary state. In the large gap limit, we make use of a dissipative symmetry, termed fermionic duality, that refers to a generalized hermiticity relation of the time-evolution kernel. The duality leads to non-trivial relations between the quantities that determine the state and transport evolution. It is then the duality that further facilitates the analysis, as the transient behavior of the quantum dot can be understood in great detail in terms of stationary quantities of the real and dual system. In particular the heat current is an interesting transport observable, as it probes the interplay of Coulomb interaction and superconducting pairing. Based on a microscopic understanding of the underlying processes, we describe how to control the charge and heat currents in these NDS-devices by a suitable choice of the parameters. We give outlooks to further extensions of our approach to quantum dots attached to two superconductors, which promise interesting physics both from a theoretical and experimental perspective.

Kurzzusammenfassung

In dieser Arbeit betrachten wir zwei Themen aus verschiedenen Forschungsrichtungen innerhalb der mesoskopischen Physik. Das erste betrifft Spinwellen in zwei-dimensionalen van der Waals Materialien, das zweite die transiente Dynamik eines Quantenpunkts verbunden mit einem normalleitenden Metall und einem Supraleiter. Basierend auf unserer früheren Arbeit über Magnon-Dispersionsrelationen in Zweischichten-2d Ferromagneten, ergänzen wir die frühere Arbeit durch Analysen der konkurrierenden Wechselwirkungen. Ferner erklären wir die Magnon-Dispersionsentartung und die Topologie des Magnonspektrums in Termen einer zu Grunde liegenden PT-Symmetrie. Als Ergebnis können wir einen Magnon-(thermischen) Hall Effekt für unser Austausch-Anisotropie Spin Modell ausschließen, deuten aber Erweiterungen unseres Modells an, die auf nicht triviale topologische Effekte führen könnten. Die Analyse des ersten Themas beläuft sich auf Gleichgewichtseigenschaften eines zwei-dimensionalen Materials, das magnetische Ordnung zeigt, die relevanten Anregungen sind Magnonen, das sind Bosonen. Beim zweiten Thema haben wir es dagegen mit der transienten Dynamik eines Quantenpunkts nach einem Switch in der Gate-Spannung zu tun, dessen angrenzendes Material, anders als das im ersten Teil der Arbeit betrachtete, keine magnetische, sondern supraleitende Ordnung aufweist, und einen ausgeprägten Proximity-Effekt auf dem sensiblen Quantenpunkt verursacht. Die wesentlichen Freiheitsgrade hier sind Fermionen. In unserem betrachteten Limes lösen wir keine Kohärenzen in der Beschreibung der Dynamik auf und bestimmen den Kern des Zeit-Evolutionsoperators basierend auf Fermis Goldener Regel und der Elektrostatik der Anordnung. Trotz dieser Vereinfachung zeigen wir, dass es im betrachteten Grenzfall von Vorteil ist, den traditionellen Zugang im Liouville-Raum zu formulieren, um die transiente Dynamik nach einem Switch anstelle des stationären Zustands zu betrachten. Im Grenzfall großen supraleitenden Ordnungsparameters machen wir Gebrauch von einer dissipativen Symmetrie, genannt fermionische Dualität, die eine verallgemeinerte Hermitizitätsrelation des Zeitentwicklungskerns betrifft und auf nicht-triviale Relationen zwischen Größen führt, die Zustand und Transportentwicklung beschreiben. Es ist dann die Dualität, die die Analyse weiter vereinfacht, weil das transiente Verhalten des Quantenpunktes in vollem Detail in Termen von stationären Größen des realen und dualen Systems verstanden werden kann. Insbesondere ist der Wärmestrom eine interessante Transport-Observable, als er das Wechselspiel von Coulomb-Wechselwirkung und supraleitender Paarung testet. Basierend auf einem mikroskopischen Verständnis der zu Grunde liegenden Prozesse

beschreiben wir, wie man Wärme- und Ladungsstrom in diesen NDS-Bauelementen durch geeignete Wahl der Parameter kontrollieren kann. Wir geben Ausblicke auf Erweiterungen unseres Zugangs zu Quantenpunkten, verbunden mit zwei Supraleitern, die sowohl vom theoretischen als auch vom experimentellen Standpunkt interessante Physik versprechen.

Contents

1

Introduction

During the last decades, considerable progress was made in mesoscopic physics. The reduction of the dimension of the devices to the nanometer scale offers the possibility of realizing a range of new technologies, which exploit quantum mechanical transport phenomena. The quantum mechanical aspects can no longer be ignored as soon as the size of the system is in the range of quantum mechanical scales such as the Fermi wavelength or the phase relaxation length.

In this thesis, we focus on two distinct, intensely studied topics in different lines of research within mesoscopic physics: Chapter 2 studies spin-waves in 2d-van der Waals magnets (2d-vdWM), a specific class of 2d layered magnetic material, whereas Chapters 3-5 deal with the transient dynamics of a quantum dot device with superconducting material. In the following, we will give an overview of the diverse topics studied in this thesis and will point out some connections between them.

In Chapter 2, we consider 2d-vdWM., which provide a platform that recently has been discovered for the study of magnetism in two dimensions. These materials are composed of 2d-layers bonded to each other through weak van der Waals interactions. They can be cleaved into monolayer crystals. Such structures are often formed by binary compounds with compositions of metal cations, such as Cr or Ti and halogen anions, such as I_3, Br_3 and Cl_3.

Their 2d-magnetism is associated with strong intrinsic spin fluctuations and possibly new quantum phases that can be studied in these materials [4]. They offer the possibility to examine well-established theories of magnetism. As these materials are now confined to two dimensions, it is possible to analyze the competition between Kitaev[1], Heisenberg, and anisotropic exchange terms of the Hamiltonians. Such spin Hamiltonians can be

[1]Kitaev interaction is a specific type of exchange coupling, significant in many vdWM with strong spin-orbit coupling and where neighboring magnetic ions share an edge bond [4].

studied in a broad range of parameter regimes, as there is a rich variety of magnetic 2d-materials that can be isolated. Furthermore, by external manipulations of the material such as gating or strain, a modification in an effective spin Hamiltonian is achievable that is associated with a change in the electronic structure. Especially anisotropy can be tuned which is crucial for strengthening or reducing spin fluctuations and hence tuning various forms of order [4]. The sensitivity of 2d-vdWM to external manipulations is an important feature of the low dimensionality of the material.

Moreover, it is possible to examine magnetism in various heterostructures, as the 2d-structures do not require lattice matching [4]. The technological possibility of designing heterostructures on the nanoscale in a well-defined way and the sensitivity of the material to external manipulations are in general important aspects when studying quantum transport phenomena. These will also be relevant aspects in Chapters 3-5, where transport through a quantum dot device will be studied.

In work prior to this thesis [5], we studied spin waves, termed magnons, and determined the magnon dispersion in bilayers of 2d-ferromagnets. This is essential for understanding the spin dynamics and spin transport. In this thesis, we complement this work by a further analysis of the dispersion relation, including the topology of the magnon spectrum. This is of interest in view of detecting topology via transport measurements. As a result, we can exclude a magnon (thermal) Hall effect for our type of exchange anisotropy spin model, which does not account for spin-orbit interaction and any type of complex spin texture. The analysis amounts to study equilibrium properties of 2d bulk materials, which exhibit magnetic order. The relevant excitations of interest are magnons, which are bosons.

There is a loose but interesting connection between the 2d-vdWM and quantum dots coupled to ordered solids: Magnon excitations can in principle be detected and used in quantum dot devices. For example, magnonic excitations were used to let a quantum dot system with two ferromagnetic leads acting as a converter of heat to spin-polarized charge or to a pure spin current. In this way, it was possible to construct a heat engine [6]. Here, magnonic excitations were particularly useful compared to other multiterminal thermoelectric devices, as magnons can be electrically excited via the spin Hall effect. Therefore, no thermal gradients between the metals and the insulator providing the magnons are needed. The system can thus be operated at low temperatures, without parasitic phonons. Furthermore, magnons facilitate to operate the quantum dot device in a regime, where the maximum Carnot efficiency can be reached, by admitting energy-independent transmissions between the dot and the reservoirs [6].

Restricting the previously described magnon heat engine to an even simpler building block, one ends up with a quantum dot attached to two spin-polarized leads. This

quantum dot system shows already non-trivial behavior: When such a system with competing magnetic order in the leads is out of equilibrium due to an applied bias, non-trivial behavior of the quantum dot spin (precession) is caused. Here it is the combination of spin polarized leads and strong Coulomb interaction on the dot, which induces an exchange field that acts on the quantum dot spin [7]. Furthermore, if we replace the spin-polarized leads by a superconducting one, we end up with the device, which we study in much detail in Chapters 4-5.

In Chapters 4-5, we deal with a quantum dot device, where instead of magnetic order we have superconducting order in the leads, which induces a pronounced proximity effect on the sensitive quantum dot. In contrast to Chapter 2, the main degrees of freedom are fermions. Differently from quantum dots attached to differently polarized ferromagnetic reservoirs, we can neglect coherences in spin-space of the quantum dot, as there is no spin-coupling term in the Hamiltonian of our problem of interest. Instead, coherences are induced in the even parity charge sector when coupling the dot to a superconducting material and tuning all parameters smaller than the gap of the superconductor, as we shall see. Such a normal conductor-quantum dot-superconductor (NDS) system that is studied in this thesis is an important building block of more complex superconducting hybrid devices. They are relevant in the context of thermal nano-machines, where they can act as thermolelectric devices also in the infinite gap limit [8]. However, when they are used for cooling and energy filtering, one needs to go beyond the large gap description [9, 10].

So far, in Chapter 5, we discuss the standard effective repulsive Coulomb interaction on the quantum dot. We devote a separate Chapter 6 to the case of an effective attractive Coulomb interaction. Such quantum dot systems are also of experimental relevance [11–14].

Superconductor-quantum dot hybrid devices have been extensively studied so far: in important prior work, which this thesis is based upon [15], an NDS building block was studied even including ferromagnetic leads. Furthermore, the full dynamics of a quantum dot weakly coupled to two superconducting reservoirs was studied after a quench and under periodic driving of the system in [16]. In these works, the time evolution kernel of the problem was carefully derived based on a real-time diagrammatic approach. By this kind of treatment, it was possible to fully account for coherences in the problem, more specifically in [16], the coherent dynamics of a Cooper pair on the dot. In our studies, however, we restrict our attention to an NDS building block without ferromagnetic leads. We further restrict to a time-averaged description of coherences in the energy basis, such that their explicit dependence can be neglected. In our problem, it therefore turns out to be sufficient to determine the kernel of the time-evolution operator

based on the electrostatics of the device, which corresponds to applying Fermi's golden rule. Inspite of this simplification, we show that in the limit we consider it is considerably advantageous to formulate this traditional approach in Liouville space to completely analyze the dynamics.

We profit from the formulation in Liouville space, when, differently from [15], we study the transient dynamics after a switch instead of the stationary state. To make progress in understanding the complex transient behavior, we use a dissipative symmetry, termed fermionic duality, which was recently developed but applied so far only to purely normal conducting quantum-dot systems [17, 18]. Fermionic duality refers to a generalized hermiticity relation of the time-evolution kernel, which relates the kernel of the real system to the one of a dual system at inverted energy scales. By the generalized hermiticity, non-trivial relations can be established between the quantities that determine the state and transport evolution (the left-and right eigenvectors of the real and dual kernel). This does not only simplify the solution of the problem, but also yields physical insights as we shall discuss in detail.

Fermionic duality in general applies to a class of fermionic models, where the coupling to the reservoirs can be described in the wide-band limit and the reservoirs can be treated as non-interacting. Particular to our approach is that it allows to treat the strong Coulomb interaction exactly. In our system of interest, we use an effective description of induced superconducting pairing incorporated into the quantum-dot Hamiltonian, such that the complete model obeys the above mentioned constraints imposed by duality. It is then the duality that further facilitates the analysis, as the transient behavior of the quantum dot can be understood in great detail in terms of stationary quantities of the real and dual system. This is a very unusual but powerful view of the time-dependent problem, and we managed to find the "right" observables for a superconducting quantum dot. Also, in earlier work, the simplifications by duality had not been extended to deal with the transport observables themselves, referring to the degrees of freedom outside the system, that is, the reservoirs the quantum dot is coupled to. This is done here for the first time. Especially the heat current is an interesting transport observable, as it probes the interplay of Coulomb interaction and superconducting pairing. This is confirmed by our detailed analysis of the time-dependent transport.

In each chapter we provide a more in-depth introduction to the problem studied and together with the conclusions give an outlook to possible extensions of each specific project.

2

Magnon dispersion in bilayers of 2d-ferromagnets

2.1 | Theoretical Background

In the master thesis, we have dealt with the class of 2d-van der Waals magnets and more specifically, with the strictly 2d spectrum of the elementary excitations of their magnetic structure, which are called magnons. To this end, we briefly give an introduction to the material compositions considered there, how the magnetic structure is incorporated there and how it can be described by spin-models. After that, we will introduce to the concept of spin waves.

2.1.1 | Spin-models for 2d- van der Waals magnets

The material compositions considered in this work are insulating and of type MX_3, such as CrI_3 or $CrBr_3$, where M is a metal cation and X is a halogen anion. These compounds exhibit magnetism, as M is chosen to be a transition metal with a partially filled d-shell. Hence it has a large total angular momentum (e.g. $s = \frac{3}{2}$ for the Cr-ions of CrI_3). Direct M-M-exchange interactions between the transition metal ions are not dominant in compounds of type MX_3 [19], which are arranged on honeycomb nets, as the M-M distance is too large in these compounds. The in-plane M-M magnetic interactions are instead mediated by their shared halogen ions, due to a mechanism called superexchange [19]. Among many other factors, the sign of the superexchange interaction depends on the M-X-M-angle. For example, an angle of 90° as realized in layered MX_3 compounds can result in both ferromagnetic (FM) or antiferromagnetic (AFM) behaviour. So the microscopic structure of the material determines the parameters of the corresponding effective spin-model such as the exchange coupling constant J. Estimates of the parameters have

been given by density functional theory calculations [20], which were not considered in this project. Alternatively, the parameters can be extracted from the dispersion measured in neutron scattering experiments such as in [21] . In order to get a realistic order of magnitude for the ratio of the different parameters, we will later refer to the work of [20].

The choice of the effective Hamiltonian is based on the assumption that magnetism is effectively driven by interactions between neighboring spins, i.e. short-range interactions. Under this assumption, the most general spin Hamiltonian has the form [22]

$$H = -\frac{1}{2} \sum_{i,j} \left(J \, \vec{S}_i \vec{S}_j \; + \; \Lambda \, S_i^{\alpha} S_j^{\alpha} \right) \; - \; \sum_i A \, (S_i^z)^2 \quad . \tag{2.1}$$

Here, J denotes the exchange coupling between neighbouring spins, which can favor ferromagnetic $(J > 0)$ or antiferromagnetic $(J < 0)$ order with parallel and antiparallel oriented spins in the classical ground state, respectively. A is the strength of single-ion anisotropy and Λ denotes an anisotropy in the exchange interaction for spin direction α. It is these parameters of the effective spin Hamiltonian that depend on the choice of the material with its specific microscopic interaction mechanisms. They can be additionally tuned by external parameters such as an applied magnetic field or a gate voltage which changes the electronic structure of the material and hence the anisotropy.
In the previous project of the master thesis, we first considered an isotropic Heisenberg model $(\Lambda = 0, A = 0)$ with spin-dimensionality three for FM and AFM type of magnetic order and then included different types of anisotropy $(\Lambda \neq 0)$ with the spin favoring a specific direction parallel or perpendicular to the plane of the material. This reduces the spin-dimensionality of the isotropic Heisenberg model to one. Such cases of perpendicular and in-plane anisotropy are realized e.g. in layers of CrI_3 and $CrCl_3$, respectively, which supports our choice.

Throughout the project, we considered magnetism that can be described by a Hamiltonian of the form (2.1). In principle, in CrI_3, for example, Dzyaloshinski-Moriya interaction (DMI) should have been added to (2.1) to obtain a more complete description of the material. DMI breaks the inversion symmetry of the lattice and introduces a non-trivial topology to the energy bands. Furthermore, when we restrict the discussion to Hamiltonians of the form (2.1), along with that we will restrict to short-range interactions of atomic spins that are relevant for magnons in the limit of large wavevectors $\vec{k}$. In the other extreme case, that is, the opposite limit of long wavelengths $(\vec{k} \approx 0)$, the dispersion would be dominated by dipolar interactions. However, for neighbouring spins, dipolar

interactions are less significant than the exchange interaction, have a longer range and are therefore relevant in the limit of long wavelengths.

2.1.2 | The concept of spin waves

Having introduced a general spin Hamiltonian for the description of magnetism in 2D vdW materials, we next introduce the concept of a spin wave at the example of a linear chain of spins with ferromagnetic exchange coupling between pairs of nearest neighbours. The Hamiltonian reads:

$$H = -\frac{2J}{\hbar^2} \sum_n \vec{S}_n \vec{S}_{n+1} \quad .$$

The ground state configuration of lowest energy is the one with parallel oriented spins. We assume this direction to be the z-direction, which is the direction of quantization. The Hamiltonian can be expressed in terms of raising and lowering operators S_i^+,S_i^-, which increase and decrease the quantized spin-component by one, respectively, as well as S_i^z that gives the z-component of the spin at site i which equals s for the ground state. Thus, the spins are assumed to be oriented along the positive z-direction. For simplicity, we consider a single spin excitation in the system throughout the project that corresponds to a flip of $\Delta S_z = 1$ in the z-component of the spin. The ansatz for the eigenfunction that solves the Schrödinger equation is then a superposition of states $|i\rangle$, for which the spin-flip of one is located at site i. Inserting the ansatz into the Schrödinger equation, the coefficients are determined to be $\frac{1}{\sqrt{N}} e^{i\vec{k}\vec{R}_i}$, such that

$$\Psi_{\vec{k}} = \frac{1}{\sqrt{N}} \sum_i e^{i\vec{k}\vec{R}_i} |i\rangle. \tag{2.2}$$

The eigenstate $\Psi_{\vec{k}}$ is hence the bosonic analogue ($\Delta S^z = 1$) of an electronic Bloch wave function with lattice periodic part $u_{n,\vec{k}}$ normalized to the unit cell and phase factor $e^{i\vec{k}\vec{r}}$. For the spin wave on the linear chain, the probability for a spin flip of $\Delta S^z = 1$ is equally distributed over all N lattice sites, with probability density $\frac{1}{\sqrt{N}}$ for a spin flip to be localized at a specific site i and phase factor $e^{i\vec{k}\vec{R}_i}$. Accordingly, the expectation value of the z-component at each site,

$$\langle S_i^z \rangle = \hbar(s - \frac{1}{N}), \tag{2.3}$$

corresponds to a change by an amount of $\frac{\hbar}{N}$ on average with respect to its value s in the ground state.

In the semi-classical limit of a large number of lattice sites compared to the inverse total spin per site, $Ns \gg 1$, the Heisenberg equations of motion result in the following

time dependence of the spin operators for an excitation $\Psi_{\vec{k}}$ with energy $\hbar\omega_{\vec{k}}$,

$$\begin{aligned} S_i^x(t) &\propto \cos\Big((\omega_k t - \vec{k}\vec{R}_i\Big) \\ S_i^y(t) &\propto \sin\Big((\omega_k t - \vec{k}\vec{R}_i\Big) \\ S_i^z &\approx \hbar s. \end{aligned} \tag{2.4}$$

The phase $\Delta\Phi = \vec{k}\vec{R}_i$ can hence be visualized in spin space as the angle of precession of the spin vector around the quantization axis at site i, see Fig. 2.1. Also beyond this limit, the picture of Fig. 2.1 illustrates interference of two phase shifted wave functions (2.2) when adding corresponding vector components in the xy-plane. Summing two visualized spin vectors that are shifted by an amount of π, for instance, would result in a vector aligned parallel to the quantization axis, i.e. with no excitation, corresponding to destructive interference of two states that are shifted by π.

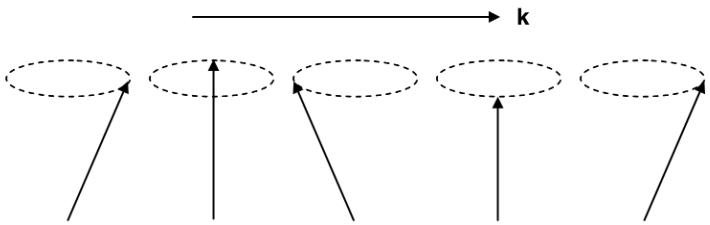

Figure 2.1. Propagation of a spin wave through a linear chain of spins, with spins on sites i, i' precessing at phase difference $\Delta\phi = i\vec{k}(\vec{R}_i - \vec{R}_{i'})$, taken from [23].

If we are finally interested in a confined region of high probability for a spin flip $\Delta S^z = 1$ that propagates through the chain as a wave packet, it can be constructed from a superposition of eigenfunctions according to

$$\int dk\; g(k)\; \Psi_{\vec{k}}(t) \;=\; \sum_i |i\rangle \int dk\; g(k)\; e^{i(\vec{k}\vec{R}_i - \omega_{\vec{k}} t)}, \tag{2.5}$$

where $g(k)$ selects wave vectors $\vec{k}$ out of a small interval around some value $\vec{k}_0$ such that the integral then describes the wave packet through the chain.

In the master thesis, we studied the band structure of a bilayer system with honeycomb layers and both FM and AFM exchange coupling for different choices of anisotropy. We will summarize the results in the following section and introduce the notation required in view of the further analysis given in the PhD thesis.

2.2 | Summary of results for the magnon dispersion of different choices of anisotropy

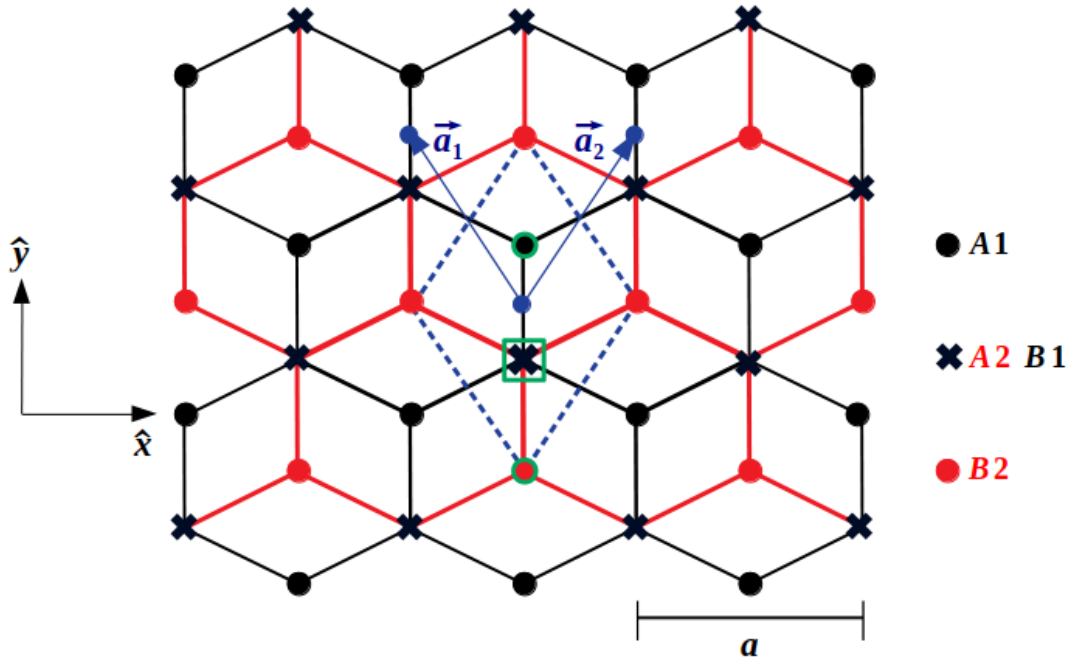

Figure 2.2. A bilayer with AB-stacking as, for example, in bulk BiI_3 crystals. The bottom layer (label 1) is indicated in black color and the top layer (label 2) in red. The two sublattices A and B of atoms within a layer are represented by crosses and dots, see the legend. The crosses refer to dimers. A dimer contains one atom of each layer coupled to each other providing the only type of coupling between the two layers. The primitive unit cell (dashed blue lines) with basis vectors $\vec{a}_1$, $\vec{a}_2$ spans the lattice. It contains four atoms marked in green: $A1$ (green-rimmed black dot), $B2$ (red-green) and the dimer pair $B1$-$A2$ (black-green cross).

In the master thesis, we determined bilayer dispersions for vdW-magnets, where the metal cations within a layer are arranged on a hexagonal lattice, see Fig. 2.2. Typical candidates for such a lattice are CrI_3 and BrI_3. Our main result referred to the analytical derivation of the band dispersion for a bilayer with FM intralayer and AFM interlayer exchange coupling (short: AFM bilayer), where we allowed for a general type of perpendicular plane anisotropy.

AFM bilayer dispersion: Our starting point was a Heisenberg Hamiltonian with anisotropic exchange terms:

$$H = - \sum_{\substack{\alpha\in\{x,y,z\} \\ \langle i,j\rangle\in\{\text{intra}\}}} 2J_{\parallel}^{\alpha\alpha}\, S_i^{\alpha}\cdot S_j^{\alpha} \; + \sum_{\substack{\alpha\in\{x,y,z\} \\ \langle i,j\rangle\in\{\text{inter}\}}} 2J_{\perp}^{\alpha\alpha}\, S_i^{\alpha}\cdot S_j^{\alpha}. \tag{2.6}$$

Here we considered nearest neighbor exchange interactions of FM type within the layer (intralayer coupling $J_{\parallel} > 0$) and AFM type between the layers (interlayer coupling $J_{\perp} > 0$). Perpendicular plane anisotropy is incorporated by choosing $J_{\kappa}^{zz} > J_{\kappa} := J_{\kappa}^{xx} = J_{\kappa}^{yy}$ for $\kappa = \parallel, \perp$, and z is the direction perpendicular to the plane of the material. Furthermore, an AB type of stacking of 2D hexagonal lattices is here assumed with a lateral shift by $[2/3, 1/3]$ unit vectors (see Fig. 2.2) [20]. We chose a unit cell for a bilayer with four atoms, A-atoms $A1$ in the bottom-layer (1) and $A2$ in the top-layer (2) as well as B-atoms $B1$ and $B2$ (see Fig. 2.2). Each A-(B)-atom has three nearest neighbors in the same layer belonging to the B-(A)-sublattice. The atoms $A2$ on top of $B1$ form another pair of nearest-neighbours per unit cell, a so-called dimer pair between the layers.

The Hamiltonian of type 2.6 can be diagonalized in two steps. First, we applied the Holstein-Primakoff (HP) transformation [24],

$$S_j^{+} = \sqrt{2s}\left(1 - \frac{a_j^{\dagger}a_j}{2s}\right)^{1/2} a_j\,,\; S_j^{-} = \sqrt{2s}\,a_j^{\dagger}\left(1 - \frac{a_j^{\dagger}a_j}{2s}\right)^{1/2},\; S_j^{(z)} = s - a_j^{\dagger}a_j\,, \tag{2.7}$$

with total spin s of the metal cation and a the bosonic annihilation operators, which still had to be adapted to our lattice. The HP transformation is a common method to determine the low-frequency magnon spectrum at low temperatures with weak excitation (few flipped spins as compared to the total number of spins), as we can then restrict to the zeroth order in $a/\sqrt{2s}$ in the series expansion of the square root. A single boson excitation $\langle a^{\dagger}a\rangle = 1$ here changes the spin projection by $\Delta S^z = \hbar$ parallel to the quantization axis z and perpendicular to the plane. After the HP-transformation, H is casted into the following form

$$\hat{H} \;=\; E_0 + E_c \;+\; \sum_{\vec{k}} (\vec{a}_{\vec{k}}^{\dagger}, \vec{a}_{-\vec{k}})\; \mathfrak{D}\; (\vec{a}_{\vec{k}}, \vec{a}_{-\vec{k}}^{\dagger})^T \quad , \tag{2.8}$$

with $\vec{a}_{\vec{k}} = \left[a_{\vec{k},A1}, a_{\vec{k},B1}, a_{\vec{k},A2}, a_{\vec{k},B2}\right]$ and E_0, E_c some constants to be specified below. $\mathfrak{D}$ is an 8x8 matrix which takes the form

$$\mathfrak{D} = \begin{pmatrix} A & B \\ B & A \end{pmatrix}$$

with

$$A = \left(\begin{array}{cc|cc} 3J_{\parallel}^{zz}s & -J_{\parallel}s\,c_{\vec{k}}^{*} & \multicolumn{2}{c}{0} \\ -J_{\parallel}s\,c_{\vec{k}} & 3J_{\parallel}^{zz}s + J_{\perp}^{zz}s & \multicolumn{2}{c}{} \\ \hline \multicolumn{2}{c|}{0} & 3J_{\parallel}^{zz}s + J_{\perp}^{zz}s & -J_{\parallel}s\,c_{\vec{k}}^{*} \\ \multicolumn{2}{c|}{} & -J_{\parallel}s\,c_{\vec{k}} & 3J_{\parallel}^{zz}s \end{array}\right), \quad B = \left(\begin{array}{ccc} \multicolumn{3}{c}{0} \\ \hline 0 & \begin{array}{cc} 0 & J_{\perp}s \\ J_{\perp}s & 0 \end{array} & 0 \\ \hline \multicolumn{3}{c}{0} \end{array}\right). \tag{2.9}$$

The upper diagonal 4x4 block of $\mathfrak{D}$ refers to the particle space and the lower one to the hole space. The term $c_{\vec{k}} = 1 + e^{-i\vec{k}\vec{a}_1} + e^{-i\vec{k}\vec{a}_2}$ is the structure factor of the lattice with unit cell vectors $\vec{a}_1, \vec{a}_2$, as depicted in Fig. 2.2. The explicit form of $\mathfrak{D}$ will be relevant for later symmetry considerations.

In a second step, we diagonalized the Hamiltonian by a paraunitary transformation of operators

$$(\vec{\gamma}_{\vec{k}}, \vec{\gamma}_{-\vec{k}}^{\dagger})^T = \mathfrak{T}\,(\vec{a}_{\vec{k}}, \vec{a}_{-\vec{k}}^{\dagger})^T \ , \tag{2.10}$$

$$\mathfrak{T}\,\eta\,\mathfrak{T}^{\dagger} = \eta \equiv \sigma_z \otimes \mathbb{1}_4 \ , \tag{2.11}$$

with σ_z the Pauli matrix. The paraunitarity (2.11) of the matrix $\mathfrak{T}$ assures that the new set of operators fulfills bosonic commutation relations. In its diagonal form, the Hamiltonian reads

$$H = E_0 + E_c + \sum_{\vec{k}} \sum_{r=1}^{4} \left[\hbar\omega_{r,\vec{k}}\gamma_{r,\vec{k}}^{\dagger}\gamma_{r,\vec{k}} + \hbar\omega_{r,-\vec{k}}\gamma_{r,-\vec{k}}\gamma_{r,-\vec{k}}^{\dagger}\right]. \tag{2.12}$$

Some notes are in order with respect to the structure of H: As the classical Neel state is no eigenstate of the Hamiltonian, its ground state energy $E_0 = -12NJ_{\parallel}^{zz}s^2 - 2J_{\perp}^{zz}Ns^2$ is shifted due to quantum corrections, in total by an amount of $\Delta E = E_c + \sum_{\vec{k}}\sum_{r=1}^{4}\hbar\omega_{r,\vec{k}}$, $E_c = E_0/s$. We did not further consider these corrections in our project. There are two twofold degenerate particle like bands with dispersion $\hbar\omega_{r,\vec{k}}$ and two hole like bands with dispersion $-\hbar\omega_{r,-\vec{k}}$ as described by the third and fourth terms of H, respectively. The multi-index $r = (n, \sigma)$ here comprises the band index $n = \pm$ and spin-index $\sigma = (\uparrow, \downarrow)$ of the degenerate modes which we further discuss below. Particle and hole like bands are trivially related to each other by particle-hole symmetry, $Ph^{-1}\mathfrak{D}^{*}(\vec{k})Ph = \mathfrak{D}(-\vec{k})$, with $[Ph]_{jm} \equiv \delta_{|j-m|,4}$ the particle-hole operator, which exchanges particles and holes. In the following, we therefore restrict the further analysis to the set of two twofold degenerate particle like bands.

The transformation $\mathfrak{T}$ was obtained from a standard diagonalization procedure applied to the matrix $\eta\mathfrak{D}$, which results in the two twofold-degenerate (particle) like energy

bands,

$$\hbar\omega_{n=\pm}(\vec{k}) = \frac{s}{\sqrt{2}}\sqrt{18J_{\parallel}^{zz\,2} + 6J_{\parallel}^{zz}J_{\perp}^{zz} + J_{\perp}^{zz\,2} - J_{\perp}^{2} + 2J_{\parallel}^{2}|c_k|^2 \pm \sqrt{(6J_{\parallel}^{zz}J_{\perp}^{zz} + J_{\perp}^{zz\,2} - J_{\perp}^{2})^2 + [(12J_{\parallel}^{zz} + 2J_{\perp}^{zz})^2 - 4J_{\perp}^{2}]J_{\parallel}^{2}|c_k|^2}}, \tag{2.13}$$

shown in Fig. 2.3. The eigenvectors are encoded in the columns of $\mathfrak{V} \equiv \mathfrak{T}^{-1}$. They describe the periodic prefactors of Bloch wave functions contained in the decomposition of eigenmodes, $(\vec{\gamma}_{\vec{k}}^{\dagger}, \vec{\gamma}_{-\vec{k}}) = (\vec{a}_{\vec{k}}^{\dagger}, \vec{a}_{-\vec{k}})\eta\mathfrak{V}\eta$, which are analytically accessible as well.

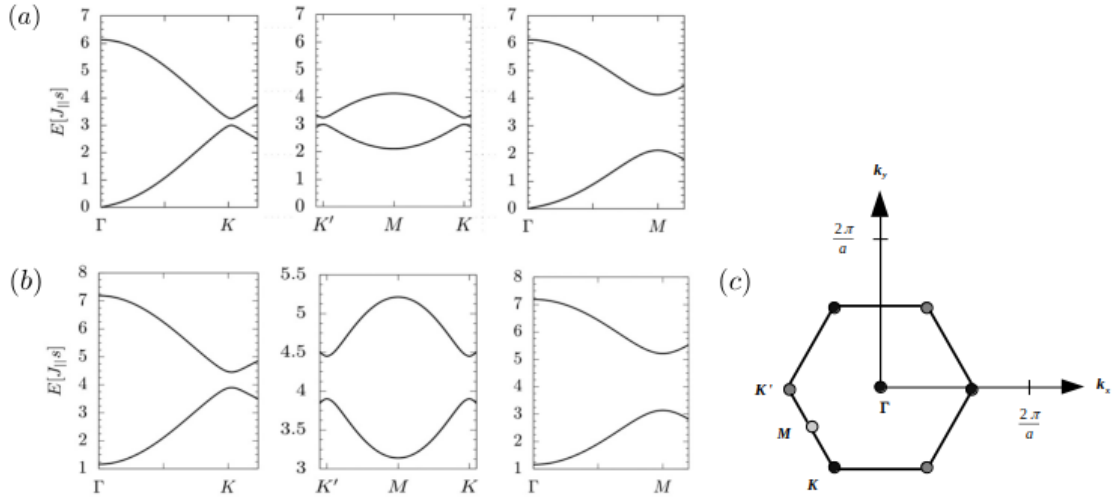

Figure 2.3. Dispersion of a bilayer with AFM inter-layer and FM intra-layer coupling. (a) For isotropic exchange coupling constants and a ratio of inter- vs. intralayer coupling $J_{\perp} = 0.26\, J_{\parallel}$, (b) for anisotropic exchange coupling $J^{zz} \neq J^{xx} = J^{yy} = J$. Here the inter-layer couplings $J_{\perp} = 0.26\, J_{\parallel}$, $J_{\perp}^{zz} = 0.56\, J_{\parallel}$ and intra-layer coupling $J_{\parallel}^{zz} = 1.3\, J_{\parallel}$.
(c) Wigner-Seitz cell of the reciprocal lattice with two types of equivalent Dirac-points K and K' and lattice points M, Γ.

We now point out a few properties of the derived AFM-bilayer dispersion for the case of isotropic ($J_{\kappa}^{zz} = J_{\kappa}, \kappa = \parallel, \perp$) and anisotropic coupling ($J_{\kappa}^{zz} > J_{\kappa}$, as above) and in comparison with the dispersion of mono- and bilayers with exclusively FM exchange coupling, as well as the dispersion of π-electrons in graphene.

Anisotropy. In the presence of anisotropy, the AFM dispersion exhibits a gap $\sim J_{\parallel}s$ at the Γ-point ($\vec{k} = 0$) w.r.t. the zero-point energy of the magnon system. In the following, we refer to this gap as the fundamental gap, compare Figs. 2.3 (a) for the isotropic and (b) for the anisotropic case. Anisotropy causes in general a gap at the Γ-point, also for mono-and bilayers with pure FM coupling. However, the origin and functional behavior of the gap in dependence of the exchange coupling strengths differs for FM and AFM

couplings [Sec. 2.3.1]. In the master thesis, we analyzed the interplay between the FM and AFM coupling as manifest in the bilayer gap. We complement our arguments in the PhD thesis based on the finite-wave vector magnon dispersion. We will provide both arguments in Sec. 2.3.1.

Behavior at the Dirac points. In the master thesis we analyzed the behavior of the dispersion at the Dirac points for different types of couplings (FM/AFM) and layers (mono- and bilayer). For a monolayer with isotropic FM coupling, the full spectrum is isomorphic to that of π-electrons in monolayer graphene: It consists of two bands exhibiting a degeneracy and linear behavior at the Dirac points. For a bilayer with isotropic FM intra- and interlayer coupling (short: FM bilayer), there are four bands which are non-degenerate except at the Dirac-points, where they exhibit a threefold degeneracy. Thus, the dispersion differs from the parabolic and twofold degenerate one of π-electrons in bilayer graphene [25]. By evaluation in terms of the Landau-Lifshitz equation, we saw that the spin precession in the FM bilayer reflects the structure of the hexagonal lattice at these points. Finally, for the AFM bilayer our results were two twofold degenerate bands. The AFM coupling opens a gap of the order $\sim sJ_{\perp}^{zz}$ for (an)-isotropic exchange couplings, leading to a quadratic rather than a linear dispersion found for an FM monolayer at K, K'. This gap motivated a closer examination of the topology in the first phase of this PhD thesis in terms of the Berry curvature [Sec. 2.3.3].

2.3 | Extensions of the master thesis

In extension of the master thesis and partially also of [1], we first complement the discussion of the interplay of different exchange couplings [2.3.1] and then trace back the degeneracy of the magnon band dispersion as well as its vanishing Berry curvature to an underlying $\mathcal{PT}$-symmetry of our system in Sec. 2.3.2 and 2.3.3.

2.3.1 | On the interplay of different exchange couplings

We analyze the interplay between different types of magnetic coupling, inter-and intralayer, by two arguments referring to different properties of the magnon band dispersion, the fundamental gap and the finite wave-vector magnon dispersion.

Argument based on the fundamental gap. We start with analyzing the fundamental gap $\hbar\omega_{-}(\vec{k}=0)$ (see Eq. (2.13)) plotted in Fig. 2.4(a) as a function of the FM coupling

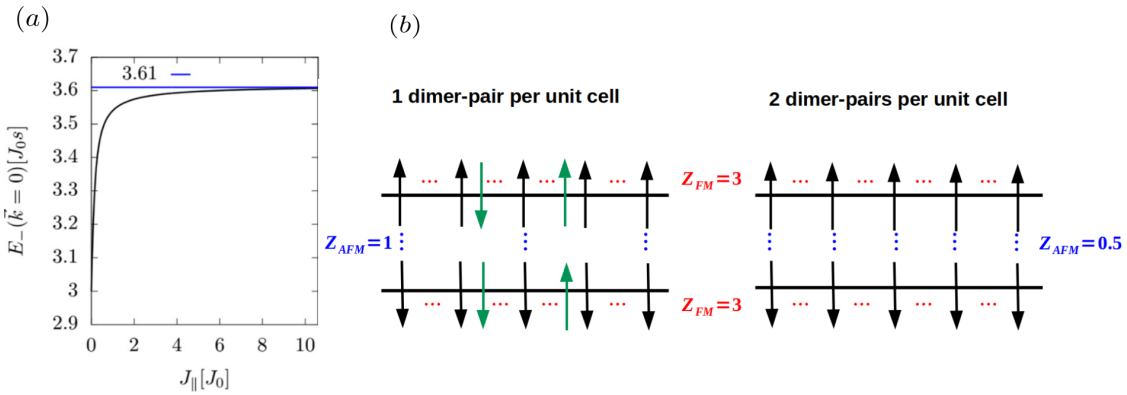

FIGURE 2.4. (a) Magnon gaps for a realistic (black line) and a hypothetical bilayer (blue line) as a function of the FM coupling strength $J_\parallel$. The anisotropy is constant with $J_\parallel^{zz} - J_\parallel = 1.0\,J_0$, $J_\perp^{zz} - J_\perp = 0.3\,J_0$ and $J_\perp = 1.0\,J_0$. (b) Left: Realistic bilayer schematic with coordination numbers $Z_{AFM} = 1$ and $Z_{FM} = 3$. Green arrows indicate deviations from the classical Néel state order. (b) Right: Hypothetical bilayer schematic with $Z_{AFM} = 0.5$ and $Z_{FM} = 3$. For further explanation see the text.

strength $J_\parallel$ for $J_\perp = 1.0\,J_0$, $J_\parallel^{zz} - J_\parallel = 1.0\,J_0$ and $J_\perp^{zz} - J_\perp = 0.3\,J_0$. In a pure FM, the gap

$$\Delta_{FM} \propto s(J_\parallel^{zz} - J_\parallel) \tag{2.14}$$

depends on $J_\parallel$ only via anisotropy. The anisotropy gap in a pure AFM, on the other hand,

$$\Delta_{AFM} \propto s\sqrt{(J_\perp^{zz} - J_\perp)(J_\perp^{zz} - J_\perp + 2J_\perp)} \tag{2.15}$$

depends not only on the anisotropy $J_\perp^{zz} - J_\perp$, but also explicitly on the AFM coupling strength $J_\perp$ [26]. The increase of the intra-layer FM coupling increases the gap $E_-(\vec{k}=0)$ according to Eq. (2.13), which by the reduced number of thermal magnons is equivalent to an enhanced AFM coupling.

Next we want to understand the stabilizing effect of FM intralayer on the AFM interlayer order based on the fundamental gap. To this end, we choose as reference a hypothetical bilayer system, different from our model system (2.6), which we term a "realistic bilayer" (bilayer I) with AB-stacking and only one dimer pair per unit cell. In contrast, the hypothetical bilayer (bilayer II) has two dimer pairs per unit cell and a stronger AFM order, assumed to be enforced by the very stacking as a plausible mechanism for supporting the AFM order.

As a side remark, in the hypothetical structure II the contributions from Eq. (2.14) of the FM and Eq. (2.15) of the AFM coupling at $\vec{k} = 0$ are clearly separated. The stacking of two ferromagnetic monolayers in this bilayer (II) is slightly shifted such that there are

two AFM-coupled dimer pairs $A2-B1$ and $A1-B2$ per unit cell. Hence, we can assume a more stable AFM order to be enforced merely by the stacking. However, to adjust the system as a suitable reference point for the stability of AFM order in the realistic bilayer I, we compensate the doubling of the number of dimers by reducing the coordination number from $Z_{AFM}=1$ [Fig. 2.4 (b (left))] to $Z_{AFM}=0.5$ [Fig. 2.4 (b (right))]. This way we have isolated the stabilizing effect due to pure stacking.

The gap of this modified hypothetical system

$$\hbar\omega_-(k=0) = s\sqrt{((J_\parallel^{zz}-J_\parallel)Z_{FM} + (J_\perp^{zz}-J_\perp)Z_{AFM})\,((J_\parallel^{zz}-J_\parallel)Z_{FM} + (J_\perp^{zz}-J_\perp)Z_{AFM} + 2J_\perp Z_{AFM})} \tag{2.16}$$

does not depend explicitly on $J_\parallel$, but on $J_\parallel^{zz}-J_\parallel$, see Fig. 2.4 (a) (blue line) corresponding to Eq. (2.16).

Let us now consider the behavior of the realistic bilayer (I) w.r.t. the hypothetical one as a reference. For $J_\parallel=0$, the gap $3J_0 s = s(J_\parallel^{zz}-J_\parallel)Z_{FM}$ of bilayer (I) is governed by the anisotropy of the FM intralayer exchange only, while the AFM coupling does not contribute to the gap. The gaps converge to $\sim 3.61\,J_0 s$ only when the FM coupling in bilayer (I) $J_\parallel \gtrapprox 5J_\perp$. Indeed, in the limit of strong FM intralayer coupling, the gap of the realistic bilayer approaches the reference value of the hypothetical bilayer, compare black and blue lines of Fig. 2.4 (a), confirming the stabilizing effect of the FM intralayer coupling on the AFM interlayer coupling and the fact that the reference point was suitably chosen. In the limit of weak FM coupling, on the other hand, the AFM order of the classical ground state is less stable than in bilayer (II) (see green arrows in Fig. 2.4 (b)).

Argument based on the finite wave-vector magnon dispersion. As the fundamental gap is not a direct measure of AFM order though, we provide a second argument by the finite k-dispersion, which corresponds to the total energy to excite the magnon. We consider the finite-wave vector magnon dispersion $\Delta E_{k,0} = E_-(\vec{k}) - E_-(0)$ as a function of the FM coupling. The zero-k-magnon is that of an interlayer AFM in its classical ground state. As $\Delta E_{k,0}$ measures the energy cost of exciting a finite-k-magnon, it thereby measures the AFM coupling strength. Fig. 2.5 (b) shows a $\Delta E_{k,0}$, which indeed increases with $J_\parallel$ for both bilayers (I) and (II). Fig. 2.5 (a) shows the difference $\Delta E^h_{k,0} - \Delta E^r_{k,0}$ of the hypothetical and the real bilayer as a function of $J_\parallel$ for different points along the $\Gamma - K$ direction in the first BZ with values as encoded by the colors according to the legend. The difference decreases with increasing $J_\parallel$, confirming that the real bilayer approaches the effective AFM coupling strength of the hypothetical bilayer for large $J_\parallel$.

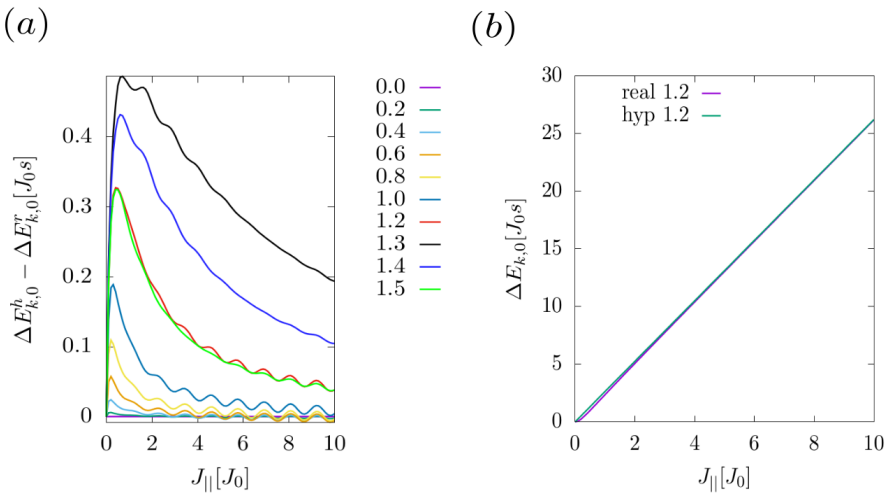

FIGURE 2.5. (a) Difference $\Delta E^h_{k,0} - \Delta E^r_{k,0}$ between the hypothetical and the realistic bilayer structure as a function of the FM coupling for different values of $(k_x, 0)$ in units of $[\frac{\pi}{a}]$ along the $\Gamma - K$ direction in the first BZ. (b) Energy difference $\Delta E_{k,0}$ between a magnon with wavevector $(1.2, 0)[\frac{\pi}{a}]$ and zero wavevector in the lower band as a function of the FM coupling strength $J_{||}$ for bilayers I (green) and II (violet). For further explanation see the main text.

Both properties of the magnon dispersion, the fundamental gap and the finite wavevector magnon dispersion, hence confirm that the impact of increasing the intralayer coupling on the interlayer order of the real bilayer structure can be equivalently modeled by choosing a different type of stacking with an effective coordination number instead.

2.3.2 | Degeneracy and $\mathcal{PT}$-symmetry

As already mentioned above, each band n of the AFM bilayer is twofold degenerate. The degeneracy results from the fact that in the AFM bilayer, the total spin S^z is a conserved quantity and therefore excitations with $\Delta S^z = \pm\hbar$ have to come in degenerate pairs. The underlying symmetry is the $\mathcal{PT}$ symmetry of the momentum space Hamiltonian [27],

$$\left[\eta\mathfrak{D}(\vec{k}),\, \mathcal{PT}\right]_- = 0. \tag{2.17}$$

Note that the symmetry relation (2.17) includes η as given by Eq. (2.11) instead of the more familiar version in which η would be replaced by the identity. The reason is that the states which lead to a degeneracy of the energy are eigenstates of the non-hermitian matrix $\eta\mathfrak{D}$ rather than $\mathfrak{D}$. Recall that the occurrence of η was to assure bosonic

commutation relations of the new set of operators γ, in which the Hamiltonian becomes diagonal, see Sec. 2.2.

Next, we have to specify the $\mathcal{PT}$-operator for our specific bilayer system (2.6). It is given by

$$\mathcal{PT} = \sigma_0 \otimes \sigma_x^{\otimes 2} \mathcal{K}. \tag{2.18}$$

Here, σ_0 is the identity, σ_x the Pauli matrix and $\mathcal{K}$ the complex conjugation. Let us now explain the operations associated with $\mathcal{PT}$: The parity operation $P : \vec{r} \to -\vec{r}, \vec{k} \to -\vec{k}$ here corresponds to an exchange of sublattices $A2 \leftrightarrow B1, B2 \leftrightarrow A1$ between the top and bottom layers, hence a mere spatial inversion in the z-direction,

$$[a^\dagger_{\vec{k},A1}, a^\dagger_{\vec{k},B1}, ...] \to [a^\dagger_{\vec{k},B2}, a^\dagger_{\vec{k},A2}, ...].$$

Additionally, the spin direction is inverted when changing the layer as required by the time reversal operation $\mathcal{T}$ as well as the wavevector $\vec{k}$ by complex conjugation $\mathcal{K}$.

One can visualize the transformation as follows: A cone with spin $-s$ and left-handed precession from the bottom layer is transferred by parity to the top layer, while time reversal $t \to -t$ transforms it into spin s keeping the left handed precession in the top layer. The transformation remains within one of the 4x4 blocks of (2.9). Excitations in the bottom layer (spin $-s$) corresponding to $\Delta S^z = \hbar$ (short: $\uparrow$) are hence mapped onto excitations in the top layer with $\Delta S^z = -\hbar$ (short: $\downarrow$).

Therefore, an eigenstate $\Psi_\uparrow$ of $\eta\mathfrak{D}$ as encoded in the inverse transformation matrix $\mathfrak{V}$ is related to another eigenstate $\Psi_\downarrow$ at the same energy by $\Psi_\uparrow = \mathcal{PT}\Psi_\downarrow$, as can also be seen from equation (2.17):

$$\eta\mathfrak{D}(\mathcal{PT})\Psi_\uparrow = (\mathcal{PT})\eta\mathfrak{D}\Psi_\uparrow = (\mathcal{PT})E_\uparrow\Psi_\uparrow = E_\uparrow(\mathcal{PT})\Psi_\uparrow. \tag{2.19}$$

The degeneracy can, for example, be removed by breaking the interlayer symmetry due to application of perpendicular electric or magnetic fields [28].

2.3.3 | Topology of the magnon spectrum in terms of the Berry curvature

In this section, we will characterize the topology of the magnon band structure in terms of its Berry curvature. Differently from [1], we will here derive its vanishing from the underlying $\mathcal{PT}$-symmetry. The Berry curvature and the related Berry phase go back to Berry's work on the geometrical phase in quantum mechanics [30]. Since then, they played a central role in classifying the topology of condensed matter systems and understanding related topological phenomena.

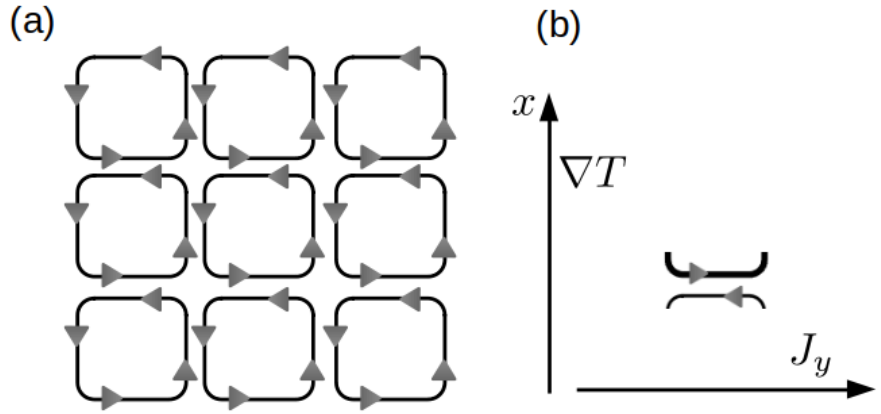

FIGURE 2.6. Magnon Hall effect schematically, drawn after [29]. A transverse magnon Hall current J_y develops in response to a longitudinal temperature gradient $\nabla T \parallel \hat{x}$, the x-direction as indicated in (b). (a) The 2D sample is constructed from small neighboring confined regions, shown are the edge currents. (b) In the presence of a temperature gradient, edge currents of neighboring regions $J_y(x) \neq -J_y(x + \Delta x)$ no longer cancel out and therefore result in a net transversal current (magnon Hall current).

Here we start with introducing the Berry curvature $\vec{\Omega}_n(\vec{k})$ as it appears in the semiclassical equations of motion for magnons and briefly describe the related measurable phenomenon of a transverse magnon Hall current in the presence of a longitudinal temperature gradient. For simplicity, let us first consider a single layer as it occurs as part of our bilayer model (2.6) with purely FM exchange coupling. In the layer, we consider a wave packet (2.5) with central position $\vec{r}$ and $\vec{k}$ in real and reciprocal space, which can be constructed from a superposition of Bloch waves. It obeys the semiclassical equations of motion [29, 31, 32]

$$\dot{\vec{r}} = \frac{\partial \omega_n}{\partial \vec{k}} - \dot{\vec{k}} \times \vec{\Omega}_n(\vec{k}), \tag{2.20}$$

$$\hbar \dot{\vec{k}} = -\nabla U(\vec{r}), \tag{2.21}$$

with $\hbar\omega_n$ the dispersion of the n-th band, $U(\vec{r})$ the magnon confinement potential at the edges of the 2D structure and $\vec{\Omega}_n(\vec{k})$ the Berry curvature of the n-th band. The Berry curvature is introduced via a gauge potential $\mathcal{A}_{n,\nu}(\vec{k})$ and constructed from the periodic part of the Bloch wave function $u_{n\vec{k}}$, which is encoded in the n-th column vector of the unitary matrix U:

$$\vec{\Omega}_n(\vec{k}) = \partial k_x \mathcal{A}_{n,y}(\vec{k}) - \partial k_y \mathcal{A}_{n,x}(\vec{k}), \tag{2.22}$$

$$\mathcal{A}_{n,\nu}(\vec{k}) = i[U^\dagger(\partial k_\nu U)]_{nn} = i\langle u_{n,\vec{k}} | \partial k_\nu | u_{n,\vec{k}} \rangle, \quad \nu = x, y\,, \tag{2.23}$$

leading to the following form of the Berry curvature, as used in [29]:

$$\vec{\Omega}_n(\vec{k}) = \nabla_{\vec{k}} \times \langle u_{n\vec{k}} | i\nabla_{\vec{k}} | u_{n\vec{k}} \rangle. \tag{2.24}$$

The confinement potential causes a gradient directed perpendicular to the edges of the sample. In 2D, $\vec{\Omega}_n(\vec{k}) = \Omega_n^z(\vec{k})$ is a vector field pointing along the perpendicular plane ($\hat{z}$)-direction, which hence results in an anomalous velocity of the magnon wave packet directed parallel to the edges due to the potential gradient. If we think of the whole sample as a collection of small confined neighboring regions, the oppositely directed edge currents at their interface cancel *within* the sample [Fig. 2.6], leaving the non-vanishing currents at the *edges* of the whole sample. In an FM, the magnon current is defined as the number of magnons per unit time.

Let us now incorporate a temperature gradient along the x-direction of the sample, which results in an x-dependent magnon distribution function $\rho(T(x))$ and hence in oppositely directed edge currents of different strengths, $J_y(x) \neq -J_y(x + \Delta x)$, at the interfaces of neighboring regions *within* the sample. The longitudinal magnon current J_x caused by the temperature gradient in x-direction is thus deflected in the perpendicular y-direction. Hence the result is in general both, a total perpendicular magnon current and a magnon heat current, provided that there is a non-vanishing Berry curvature. These phenomena are termed the magnon Hall effect and the magnon thermal Hall effect [29, 33], respectively. The Berry curvature is non-vanishing if there is, for example, an inversion-breaking Dyaloshinskii–Moriya (DM) interaction in the material (see below). So far to our knowledge, the magnon thermal Hall effect has actually been measured in an insulating ferromagnet $Lu_2V_2O_7$ with exchange and DM interactions [34].

In view of a possible magnon Hall effect in our AFM bilayer system of interest, we now evaluate the expressions for a transversal magnon current as recently derived in [27, 32], where we apply a temperature gradient in x-direction as $T(x) = T_0 - x\nabla T$. Up to second order in the temperature gradient, the transverse magnon current reads [27]

$$J_y = \frac{\nabla T}{\hbar V} \sum_n \int_{BZ} d^2k \; c_1(\rho_0(E_n(\vec{k}), T_0)) \; \Omega_n^z(\vec{k}) \tag{2.25}$$

$$+ \frac{\tau(\Delta T)^2}{\hbar^2 V T_0} \sum_n \int_{BZ} d^2k \; c_1(\rho_0(E_n(\vec{k}), T_0)) \frac{\partial}{\partial k_x} \left(E_n(\vec{k}) \Omega_n^z(\vec{k}) \right) + O((\nabla T)^3). \tag{2.26}$$

Here, $\rho_0(E_n(\vec{k}), T_0)$ is the equilibrium distribution function $\rho_0(E, T_0) = [e^{T/T_0} - 1]^{-1}$ of magnons at average temperature T_0, τ the magnon relaxation time, c_1 a weight function and V the area of the sample.

Let us now specify the Berry curvature. Note that we cannot use Eq. (2.23) nor (2.24) for the gauge potential and the Berry curvature, respectively. In our AFM bilayer with FM

intralayer and AFM interlayer exchange interaction, we have to deal with the BdG type Hamiltonian (2.8), which does not conserve the particle number due to terms quadratic in the field operators ($\sim aa, a^\dagger a^\dagger$). As the periodic part of Bloch wave functions $\Psi_{\uparrow,\downarrow}(\vec{k})$ are eigenvectors of the *non-hermitian* matrix $\eta\mathfrak{D}$ and bosonic, their inner product has to be adapted [35]:

$$\langle \Psi_\uparrow, \Psi_\downarrow \rangle = \Psi_\uparrow^\dagger \eta \Psi_\downarrow.$$

Due to the non-hermiticity, the Berry curvature $\Omega_r^z(\vec{k})$ of mode $r = (n, \sigma)$, not to be mixed up with the Berry curvature $\Omega_n^z(\vec{k}) = \sum_\sigma \Omega_{n,\sigma}^z(\vec{k})$ of band n, is defined via a modified gauge connection $\mathcal{A}_{r,\nu}$ as

$$\Omega_r^z(\vec{k}) = \partial k_x \mathcal{A}_{r,y}(\vec{k}) - \partial k_y \mathcal{A}_{r,x}(\vec{k}) = -2\mathfrak{Im}[\eta(\partial k_x \mathfrak{V}^\dagger)\eta(\partial k_y \mathfrak{V})]_{rr} \tag{2.27}$$

$$\mathcal{A}_{r,\nu}(\vec{k}) = i[\eta \mathfrak{V}^\dagger \eta(\partial k_\nu \mathfrak{V})]_{rr}, \tag{2.28}$$

with the paraunitary transformation matrix $\mathfrak{V} \equiv \mathfrak{T}^{-1}$ fulfilling $\eta\mathfrak{V}^\dagger\eta\mathfrak{V} = \mathbb{1}$ as introduced in Eq. (2.11) of Sec. 2.2. In the hermitian case, $\eta\mathfrak{V}^\dagger\eta$ would be replaced by a unitary matrix $U^\dagger$. In particle space $r = 1, .., 4$, expression (2.27) corresponds to

$$\Omega_r^z(\vec{k}) = -2\mathfrak{Im}[(\partial k_x \Psi_r(\vec{k})^\dagger)\eta(\partial k_y \Psi_r(\vec{k}))] \tag{2.29}$$

for mode r.

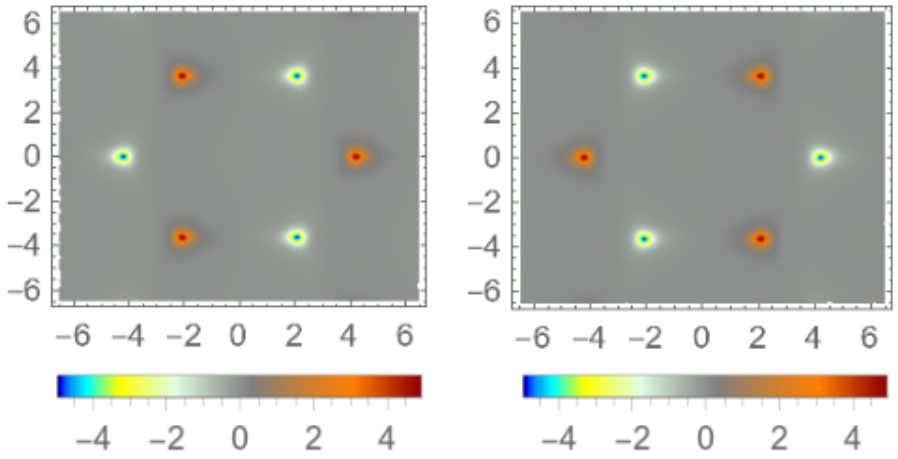

Figure 2.7. Berry curvatures $\Omega_{n\sigma}^z$ for the twofold degenerate bands $E_\pm$ with modes $\sigma = \uparrow, \downarrow$ in the first BZ. Left: $\Omega_{\pm,\downarrow}^z$, right: $\Omega_{\pm,\uparrow}^z$. Summing over σ results in the vanishing Berry curvature $\Omega_n^z(\vec{k}) = 0$ of band n.

Fig. 2.7 shows $\Omega_{n,\sigma}^z$ for $n = \pm$ and $\sigma = \uparrow, \downarrow$. Let us now discuss its implications for a magnon Hall current based on symmetry considerations. As discussed in Sec. 2.3.2, the

eigenmodes $\sigma = \uparrow, \downarrow$ are related by $\mathcal{PT}$-symmetry. Consequently, the Berry curvature $\Omega_n^z(\vec{k}) = \sum_\sigma \Omega_{n,\sigma}^z(\vec{k})$ of band n vanishes, as $\Omega_{n,\uparrow}^z(\vec{k}) = -\Omega_{n,\downarrow}^z(\vec{k})$ in the whole BZ:

$$\begin{aligned}\Omega_{n,\uparrow}^z(\vec{k}) &= -2\mathfrak{Im}[(\partial k_x \Psi_\uparrow(\vec{k}))^\dagger \eta (\partial k_y \Psi_\uparrow(\vec{k}))] = -2\mathfrak{Im}[(\partial k_x (P\,\Psi_\downarrow^*(\vec{k})))^\dagger \eta (\partial k_y (P\,\Psi_\downarrow^*(\vec{k})))] \\ &= -2\mathfrak{Im}[(\partial k_x (\Psi_\downarrow^*(\vec{k})))^\dagger P^\dagger \eta P (\partial k_y (\Psi_\downarrow^*(\vec{k})))] = 2\mathfrak{Im}[(\partial k_x (\Psi_\downarrow(\vec{k})))^\dagger \eta (\partial k_y (\Psi_\downarrow(\vec{k})))] \\ &= -\Omega_{n,\downarrow}^z(\vec{k}). \end{aligned} \tag{2.30}$$

Thus, we cannot expect any transversal magnon current according to Eq. (2.26). Also the spin-resolved Nernst current, which is defined by replacing $\Omega_n(\vec{k}) \to [\Omega_{n,\uparrow}(\vec{k}) - \Omega_{n,\downarrow}(\vec{k})]$ in Eq. (2.26), vanishes to first order in the temperature gradient due to the point symmetry of $\Omega_{n,\sigma}(\vec{k}) = -\Omega_{n,\sigma}(-\vec{k})$, see Fig. 2.7. In Ref. [27], it has been shown that a non-vanishing second order can still be expected from the so-called extended Berry curvature dipole $\partial_{kx}[E_n(\vec{k})\Omega_{n\sigma}(\vec{k})]$ for a honeycomb layer with AFM coupling, if rotational and inversion symmetry are broken on the level of exchange coupling strengths. In our AFM bilayer, further investigations w.r.t a second order contribution would therefore be of interest, while we can clearly exclude a magnon Hall effect and, up to linear order also a spin Nernst effect[1], as long as the bilayer fulfills $\mathcal{PT}$-symmetry. On the other hand, a direct manifestation of the Berry curvature in the linear response regime has so far been shown in the presence of the DMI [36, 37], which can result from spin-orbit coupling in the material [38].

2.4 | Summary and outlook

We reported analytical expressions for the magnon band structure of bilayers of two-dimensional ferromagnets with (anti-) ferromagnetic interlayer exchange coupling and perpendicular anisotropy, complementing previous numerical analysis [24].

We analyzed the interplay between FM intra- and AFM interlayer coupling by two arguments referring to different properties of the magnon band dispersion, the fundamental gap and the finite wave-vector magnon dispersion. To summarize the first argument, we considered the fundamental gap of a hypothetical bilayer system for comparison, in which AFM order is per se more stable due to the different choice of stacking, two dimers per unit cell, but the AFM coupling enters with half of the coordination number 0.5. Hence, the constant gap of this system served as a reference value for the realistic bilayer system, which it approaches in the limit of strong FM coupling. This suggests that an increased $J_\parallel$ stabilizes AFM order in a similar manner as the stacking

[1] The spin Nernst effect refers to the occurrence of the related spin Nernst current.

does. This result was also confirmed by the second argument based on the energy cost associated with adding an additional magnon to the system.

Moreover, we identified an underlying $\mathcal{PT}$-symmetry in our bilayer system. Based on that, we explained the degeneracy of the magnon band dispersion and explored possible topological phenomena. For our system we can exclude a magnon Hall effect due to a vanishing Berry curvature Ω_n^z of band n. Furthermore, a spin-Nernst effect was excluded to linear order in the temperature gradient as a result of the point symmetry of the spin-resolved Berry curvature $\Omega_{n,\sigma}^z$. Therefore, a natural extension would be to examine under which circumstances topological phenomena like the spin-Nernst effect would be visible in second order response caused by a non-vanishing extended Berry curvature dipole [27].

As further extensions of this work, I see the following four directions: In view of a more realistic model, our model 2.6 should be complemented with next-nearest-neighbour exchange interactions, which have been shown to have an impact on magnetic interlayer coupling [20] for the AB-type stacking considered in this work.

The second one deals with analyzing fundamental aspects of competing interactions in the Hamiltonian which here are experimentally accessible. One could study spin dynamics as a function of anisotropies and ratios of exchange coupling parameters for 2D-van der Waals materials with hexagonal lattice structures. The main observable there is a spin-spin correlation function, which allows to examine spin fluctuations in the ground state with predictions that can be experimentally checked in neutron scattering. I would be interested in how the results depend on the competition between the strength of different interaction terms.

The third direction would try to exploit the formal analogy between the description of electrons as Bloch waves and magnons as spin waves. One could explore the option of weak localization of magnons on hexagonal lattices such as in CrI_3 . Weak localization usually refers to a coherence phenomenon related to coherent backscattering of electrons in disordered materials. Weak localization in CrI_3 is expected in analogy to graphene based on the analogy mentioned before.

The fourth direction amounts to a quantum transport phenonmenon, dealing with the propagation of magnons in van-der Waals heterostructures. The goal would be to predict transmission coefficients associated with possible tunneling processes through barriers. Primarily I would use analytical methods such as the Green's function method or a description of magnons in terms of quasiparticles.

3

Superconductor quantum dot hybrid device

The main purpose of this chapter is to give the theoretical background required for the study of our normal metal-quantum dot superconductor hybrid device (NDS-device) in Chapters IV-VI.

Section 3.1 introduces to the theoretical approaches used in this thesis to study the (transient) dynamics of an open quantum system in general. In Section 3.1.1, we will start with the description of their time evolution in terms of a general quantum master equation and specify the description of Markovian quantum systems in the limit of weak coupling to normal conducting reservoirs. In Section 3.1.2, we will introduce to the Liouville space formulation of the open system dynamics, including the time-evolution kernel and the time-evolving state. This formulation will be beneficial for finding a suitable basis for the solution of the dynamics (Chapter IV) and will facilitate its analysis. Next, we will introduce the dissipative symmetry relation of the time-evolution kernel- the so-called fermionic duality- as it was previously found in Ref. [17] in Section 3.1.3. Thereby, we specify the class of systems, which obey a duality and explain how duality generically facilitates the solution of the transport problem.

Having introduced some concepts for the description of open systems, which will be relevant for this thesis, we will give some background on superconductor hybrid devices in Section 3.2 with an emphasis on quantum dot systems attached to superconducting material. After discussing Andreev reflection as a central concept in mesoscopic superconductivity in Section 3.2.1, we will give some background on superconductor-quantum dot -superconductor (SDS) devices, specifying relevant regimes considered so far, the main phenomena associated with them and referring to their treatment by theoretical approaches. Also we will point out relevant applications of these mesoscopic devices with two superconductors in Section 3.2.2. We introduce to SDS-devices in

some detail, because from a physical point of view we find them the most interesting extensions of NDS-devices which we treat in detail in this thesis by a duality-adapted approach.

Afterwards, we will discuss our system of interest, a superconductor quantum dot system in the infinite gap limit and weakly coupled to a normal metal (NDS device). The model will be introduced in Section 3.3 and the time evolution kernel will be derived in the energy basis by applying Fermi's golden rule in Section 3.4. These steps are the starting point for the detailed analysis of our transport problem by fermionic duality, which is the subject of the next Chapter 4.

3.1 | Theoretical Background

3.1.1 | Open Quantum Systems

In this thesis, we study the transient dynamics of a dissipative open quantum system, a nanostructure (quantum dot), which interacts with a macroscopic reservoir in the presence of strong effective Coulomb interaction on the quantum dot. To this end, we introduce in this section the basic theoretical framework for the study of open quantum systems in terms of a generalized master equation, starting from the closed system dynamics. We will then specify the approximations that can be made in our limits of interest leading to the Born-Markov equation for the reduced density operator of the quantum dot (QD).

The pure or mixed state $\rho^{\text{tot}}(t)$ of a closed system with time-independent Hamiltonian obeys the Liouville-von Neumann equation

$$\partial_t \rho^{\text{tot}}(t) = -i[H^{\text{tot}}, \rho^{\text{tot}}(t)] = -iL^{\text{tot}}\rho^{\text{tot}}\,. \tag{3.1}$$

The total Hamiltonian

$$H^{\text{tot}} = H_Q + H_R + H_T \tag{3.2}$$

we want to consider here consists of three parts describing the nanostructure (Q), the macroscopic fermionic reservoir (R) and the tunnel coupling (T) between them. The total Liouvillian $L^{\text{tot}}\bullet = [H^{\text{tot}}, \bullet]$ here denotes the commutator of the total Hamiltonian with some operator in Liouville space to be introduced below. As the many-particle Hilbert space of the total macroscopic system is too large for a direct treatment of Eq. (3.1), we are interested in the time evolution of the reduced density operator $\rho(t) = Tr_R[\rho^{\text{tot}}(t)]$ of the open subsystem (QD), which is obtained by tracing out the reservoir degrees of freedom of the total density operator. As a first step in solving Eq. (3.1) for the reduced

system, one assumes that the QD and the reservoirs are initially uncoupled at time $t_0 = 0$ and the total system is hence initially in a product state of the reduced open-system state and the state of the reservoirs, $\rho^{\text{tot}} = \rho_0 \otimes \rho_0^R$. The solution of Eq. (3.1) for the reduced system then reads

$$\rho(t) = Tr_R[\rho^{\text{tot}}(t)] = Tr_R[e^{-iL^{\text{tot}}(t-t_0)}\rho_0^{\text{tot}}] = Tr_R[e^{-iL^{\text{tot}}(t-t_0)}\rho_0^R]\rho_0 = \Pi(t,t_0)\rho_0\,, \tag{3.3}$$

with the time propagator $\Pi(t,t_0)$. Here, each reservoir is assumed to be in thermal equilibrium at chemical potential μ_α and temperature T_α, such that the total reservoir state can be characterized by a product of grand canonical ensembles, $\rho_0^R = e^{-\sum_\alpha (H_\alpha - \mu_\alpha N_\alpha)/T_\alpha} / Tr[e^{-\sum_\alpha (H_\alpha - \mu_\alpha N_\alpha)/T_\alpha}]$.

The goal is now to explicitly evaluate the reservoir trace in Eq. (3.3). Under the above assumptions and for the case of effectively non-interacting reservoirs, a real-time diagrammatic approach can be applied in the form of [39, 40] or [41, 42] to perturbatively expand the time propagator Π in the tunnel coupling H_T or $L_T = [H_T, \bullet]$ between the reservoir and the dot. Note that the fermionic duality [17] to be later considered in this thesis was derived based on the Liouville space adapted approach developed in [41, 42]. The result of the real-time diagrammatic approach is a generalized time non-local master equation for the time-evolution of the reduced state,

$$\partial_t \rho = -iL\rho + \int_{t_0}^{t} dt' \mathcal{W}(t-t')\rho(t')\,. \tag{3.4}$$

Here, the first term $L\bullet = [H_D, \bullet]$ captures the coherent dynamics of the reduced system, while the dissipative coupling to the reservoirs is accounted for by the time evolution kernel $\mathcal{W}$.

At this stage, no approximation has yet been made. The real-time diagrammatic approach is well suited when the tunnel coupling Γ is weak as compared to the reservoir temperature T. In the limit $\Gamma \ll T$, subsequent tunneling events between the dot and the reservoir become decoupled from each other (sequential tunneling picture) and the dynamics is represented by the leading, linear order in Γ of the expansion of $\mathcal{W}$, $\mathcal{W}(t-t') \to \mathcal{W}_1(t-t')$, corresponding to the second order in the tunneling Hamiltonian H_T. Corrections to sequential tunneling (co-tunneling), which become more important for larger Γ, can be included by evaluating higher orders of $\mathcal{W}$.

In this thesis, we will consider the limit of weak coupling $\Gamma \ll T$ and restrict the kernel to the leading order in Γ (Born-approximation). Furthermore, we can neglect the memory time of the reservoir as set by its inverse temperature $1/T$ in this limit (Markov-approximation): As at finite temperature, the kernel $\mathcal{W}_1(t-t')$ decays when the time difference $t-t'$ exceeds the memory time of the reservoir, and particles tunnel

on the time scale $1/\Gamma$, which is much larger in this limit, the kernel can be replaced by $\mathcal{W}_1(t-t') \propto \delta(t-t')$ and t_0 can be set to $-\infty$ in Eq. (3.4):

$$\partial_t \rho(t) \approx [-iL + \int_{-\infty}^{t} dt' \mathcal{W}_1(t-t')]\rho(t).$$

As a final result, one obtains the time-local Born-Markov master equation for the reduced density matrix

$$\partial_t \rho(t) = [-iL + W]\rho(t)\,,\; W = \lim_{\omega \to i0} \int_0^\infty dt \mathcal{W}_1(t) e^{i\omega t}\,. \tag{3.5}$$

Here, W can be considered as the Laplace transform of $\mathcal{W}_1$ in the limit of zero imaginary frequency.

3.1.2 | Liouville-space formulation

In view of our later evaluation of the dynamics by a duality-adapted approach, we now introduce to the Liouville space-notation, in which the different constituents to the dynamics can be clearly distinguished: The time-evolution kernel W in Eq. (3.5) is formally a linear superoperator acting on so called supervectors $|x)$ in Liouville space, which are operators x in Hilbert space. Furthermore, the density matrix $|\rho)$ of the state is represented by a (right) supervector in Liouville space, whereas transport observables such as the charge- or energy currents can be identified with (left) so called supercovectors $(x|\bullet$ out of the adjoint Liouville-space, as we shall later see by our application of duality. Hence, the state evolution is formally distinguished from the transport evolution.

The Liouville space is the space of all linear operators $|x)$ that act on the Hilbert space of the reduced system. The dual Liouville space is the space of adjoint supercovectors $(x|\bullet$, which are defined through the Fock-space trace over the open system, $(x|\bullet = Tr[x^\dagger \bullet]$. The scalar product of any two vectors $(A|\bullet$ and $|\rho)\bullet$ is then defined as

$$(A|\rho) = Tr[A^\dagger \rho]\;(= \langle A \rangle_\rho)\,. \tag{3.6}$$

The last term introduces already the notation for the expectation value of some transport observable A in some state ρ of the system. The Hermitian adjoint $\dagger$ for superoperators S is analogously to $\dagger$ for operators in Hilbert space, defined as $(x|\mathcal{S}^\dagger|y) = [(y|\mathcal{S}|x)]^*$.

Having introduced the scalar product, we can finally give the expansion of any super(co)vector x with respect to some Liouville space basis. Later in the thesis, we will expand the dynamics in bi-orthogonal bases $\{|v_n)\}, \{(v_n'|\}$ only, i.e. they fulfill

$$(v_n'|v_m) = Tr[(v_n')^\dagger v_m] \propto \delta_{nm}\,,\; \mathcal{I}\bullet = \sum_n \frac{1}{(v_n'|v_n)} |v_n)(v_n'|\bullet\,. \tag{3.7}$$

Here, $\mathcal{I}\bullet$ indicates the superidentity. Any supervector ρ can then be expanded according to

$$|\rho) = \sum_n \rho_n |v_n) \, , \; \rho_n \equiv \frac{(v_n'|\rho)}{(v_n'|v_n)} \, , \tag{3.8}$$

and any supercovector analogously, by applying $\mathcal{I}\bullet$ from the right.

The transport observables are in Liouville-space notation expressed by supercovectors, such that their corresponding average values are given by the scalar product of the supercovector with the state $|\rho)$. As an example, the average current I_A is represented by a corresponding covector $(I_A|\bullet$, such that

$$I_A = (I_A|\rho) \, . \tag{3.9}$$

3.1.3 | Fermionic duality- a dissipative symmetry

Recently, a useful relation has been found that simplifies the solution procedure of the dynamics of fermionic open quantum systems and the analysis of the results of interest in a systematic way, even in the presence of many-particle interactions and dissipation. This so-called fermionic duality relation is truly dissipative in nature due to the explicit involvement of the special fermion-parity decay rate Γ, which depends only on the interface properties between the open system of interest and the reservoirs [17, 43].

Assuming that the reduced state of interest obeys a generalized master equation of type (3.4) with a total Hamiltoninan of type (3.2) and further assumptions to be specified below, fermionic duality in its most general form reads [17, 43]

$$W(\omega; H, H^T, \{\mu\})^\dagger = -\Gamma + \mathcal{P} W(\bar{\omega}; \bar{H}, \bar{H}^T, \{\bar{\mu}\}) \mathcal{P} \tag{3.10}$$

with $W(\omega) = \int_0^\infty dt e^{i\omega t} \mathcal{W}(t)$ the Laplace transform of the time evolution kernel of Eq. (3.4). By Eq. 3.10, fermionic duality can be considered a "generalized hermiticity" of the time evolution kernel, as it relates the kernel matrix W to its adjoint, conjugated with fermion parity $\mathcal{P}$ and shifted by a scalar Γ. The scalar Γ is the lumped sum over the system and reservoir-indices of the energy-independent tunnel couplings characterizing the tunnel Hamiltonian H_T, which we will further specify in Sec. 3.3 for our system of interest. The parity superoperator $\mathcal{P}\bullet := (-\mathbb{1})^N \bullet$ multiplies an operator by the fermion-parity operator p, which contains the fermion-number operator N of the local charge on the nanostructure (QD). Furthermore, the duality relation comprises a parameter substitution in the original model as indicated by the overbar, which constructs a dual model with inverted local energies $\bar{H} := -H$, a dual coupling $\bar{H}_T := iH_T$ to reservoirs with dual chemical potentials $\bar{\mu} := -\mu$ at dual frequency $\bar{\omega} := i\Gamma - \omega^*$, but with the same reservoir Hamiltonian H_R and temperature T [17].

The relation 3.10 applies to any fermionic system of type 3.2 fulfilling the following criteria: (i) The open system contains a discrete, finite number of fermionic modes. Otherwise, the open system Hamiltonian H can be of arbitrary (fermionic) type with arbitrary types of many-particle interactions. Furthermore, it conserves parity $[H, p] = 0$, and hence obeys the fermion-parity superselection principle[1] [44, 45]. (ii) The fermionic reservoirs (H_R) are effectively non-interacting with structureless, infinitely wide bands. (iii) The coupling between the modes of the open system and the reservoir is bilinear in the fermionic fields and independent of the energy of the reservoir modes, but allowed to be arbitrarily strong.

So far, fermionic duality has been applied to open systems with weak bilinear energy-independent coupling to a metal [17, 18, 46–48], but has been extended to energy-dependent coupling in the presence of coherences [49] and combined with detailed balance [49] in the weak-coupling limit. As signalled by $\mathcal{P}$ and †, fermionic duality turns out to include the so-called PT-symmetry specific to Markovian Lindblad dynamics [50] which it generalizes to strongly coupled non-Markovian systems. Indeed, duality as formulated above was shown to remain valid [17, 43] and exploited [41, 42] for strong bilinear but energy-independent coupling.

Let us now anticipate the main benefit resulting from the fermionic duality (3.10), by comparing the open with the closed system dynamics: In a closed system, the time evolution of a quantum state is governed by its Hamiltonian which is hermitian. Expanding the time-dependent quantum state in the eigen basis of the Hamiltonian, only the right eigenvectors have to be determined as the left eigenvectors are simply related by the adjoint. The time-evolution kernel W of the open system, however, is non-hermitian, $W \neq W^\dagger$. Therefore, a corresponding relation between the right eigenvectors (modes) and left eigenvectors (amplitudes) of the kernel's spectral decomposition in terms of an adjoint does not hold. The main simplification of the solution procedure that results from the fermionic duality relation (3.10) is the implication of cross-relations between right and left vectors of the kernel's decomposition, which reduces the number that has to be determined by half. Also the eigenvalues are cross related: As written in the form of (3.10), duality then implies that Γ is always the largest (parity) decay rate γ_p of the dynamics in the limit of weak coupling, $\Gamma \equiv \gamma_p$. We will further introduce the specific relations in Sec.4.1, when applying the duality to our system and limit of interest.

[1] The fermion-parity superselection principle prohibits any physical quantum state to be in a coherent superposition of a many-body state with an even and another state with an odd fermion number.

3.2 | Superconductor-quantum dot hybrid devices

In the following, we introduce to the concept of Andreev reflection (AR), which is widely used to describe the subgap physics in mesoscopic heterostructures with superconductors. It will be relevant as well for our later NDS-device. Afterwards, we discuss superconductor-QD hybrid devices as interesting platforms in mesoscopic superconductivity, before we turn to our specific NDS-device.

3.2.1 | The concept of Andreev reflection (AR)

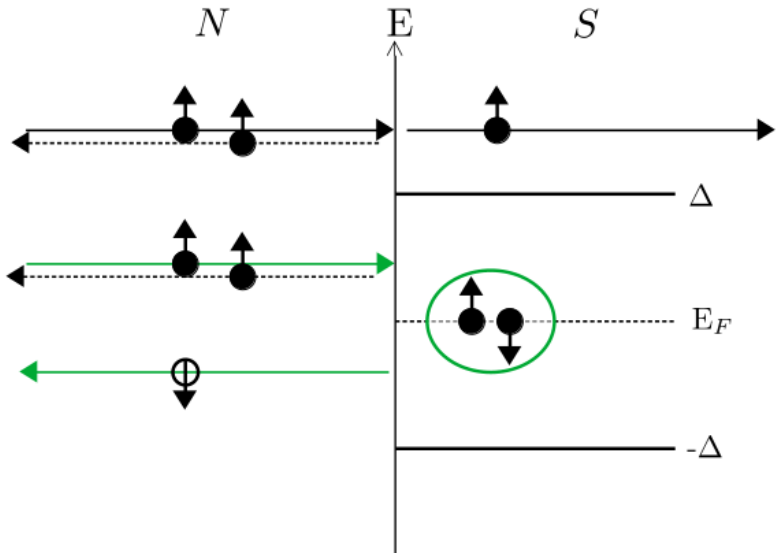

Figure 3.1. Possible transport processes at a normal metal-superconductor (NS) interface in dependence of energy E (vertical axis): An electron incident on the interface (black arrow) can be transmitted into the superconductor as a quasi particle (black arrow) only above the superconducting gap Δ or it is back reflected as an electron into the normal metal (black dashed arrow). If incident below the gap (green arrow), it is either normally reflected (black dashed arrow) or Andreev reflected as a hole (green arrow), leaving in the latter case a Cooper pair in the superconductor.

Fig. 3.1 shows schematically charge transport at a normal metal-superconductor (NS) interface. Above the superconducting gap Δ, quasi particles from the normal metal can be either transmitted into the superconductor as quasi particles or reflected back into the normal metal. Below the gap, quasi particles do not exist in the superconductor and the corresponding transmission process as a single quasi particle has zero amplitude accordingly. Instead, an electron with wave vector k and spin σ at energy E above the Fermi level can be Andreev reflected from the interface as a hole with approximately the

same wave vector and opposite spin at energy E below the Fermi level, picking up an Andreev phase χ . The hole is reflected back into the normal metal and a Cooper pair (CP) of zero spin is transmitted into the s-wave superconductor. Energy and spin are hence conserved. Alternatively, an electron from the normal metal can be reflected back as a normal electron, transferring no charge to the superconductor at the Fermi level E_F.

These processes and their amplitudes follow directly from the solution of the Bogoliubov de-Gennes equation for the quasi particle amplitudes of an NS interface [51, 52]. For the case of a superconductor-normal metal-superconductor (SNS) junction, Andreev bound states (ABS) form in the normal metal when Andreev reflecting at the interfaces with the superconductors. Their energies depend on the transmission through the junction and the phase difference ϕ between the superconductors. The ABS give rise to the ϕ-dependent persistent supercurrent (Josephson current) through the coherent transfer of CPs across the junction.

In our later normal metal dot superconductor (NDS) device with one superconductor, the superconducting phase ϕ does not play a role and AR takes place at a single NS interface. As we allow for strong Coulomb interaction on the QD, the dot-superconductor (DS)-system can assume a doublet ground state when Coulomb repulsion dominates the local pairing, which is induced on the QD by the proximity effect of the SC, as we shall see. In the opposite limit of strong pairing, the GS is the lower-energetic of the two singlet states that result from an effective modeling of the DS-system in the large-gap limit [53, 54] in addition to the doublet state. These even-parity singlet eigenstates of the DS-system are coherent superpositions of zero and two charges and hence contribute to the transfer of CPs through the QD. This transfer can be understood in the AR-picture, as we shall see [Sec. 4.2.3].

3.2.2 | Superconductor-quantum dot hybrids in mesoscopic superconductivity

After all, in this thesis, we will consider a very special case of a superconductor quantum dot hybrid device (NDS). From the theoretical approach (we will use fermionic duality) it amounts to a generalization of an ND-device [17]. In view of interesting physics and applications, the next step would be to consider SDS-devices. SDS-devices are interesting both from the perspective of applications and of fundamental physics. They combine the physics of the microscopic single level QD with the macroscopic phase of the superconductor.

Superconductivity. Originally, superconductivity is known as a macroscopic quantum phenomenon which was justified by the microscopic BCS theory [55, 56]. Below the superconducting transition temperature, electrons near the Fermi-energy form Cooper pairs, pairs of two electrons with opposite spin and momentum, due to a phonon mediated attractive electron-electron interaction. They condense into a collective quantum state containing a macroscopic number of electrons in even small samples ($\sim \mu m^3$), which is characterized by a macroscopic wave function with the macroscopic quantum phase ϕ. (The collective motion of the electrons in the condensate leads to a dissipationless flow of charge.) Gradients in ϕ can drive the dissipationless supercurrents. The pairing of electrons into a boson-like state results in a gap Δ in the energy spectrum, which is needed to excite a quasi particle from the ground state. Below the gap, only Cooper pairs are responsible for transport.

Mesoscopic superconductivity. In mesoscopic superconductivity, one can even add / remove single Cooper pairs to a superconducting electrode by choosing a sufficiently small interface between the SC electrode and the gate, i.e. a high enough capacitance (large charging energy) such that the electrode can be charged in discrete steps. The superconducting electrode (island) still contains a macroscopic number of Cooper pairs (in contrast to our QD later) and can be further tunnel coupled to a superconducting reservoir, thus forming an SNS-junction. In the limit of small Josephson energy $E_J \ll E_C$ of the junction, single energy levels can be isolated by the charging energy and a qubit can be designed[2]. Differently from the conventional macroscopic Josephson effect, the number of Cooper pairs rather than the phase difference across the junction is the good quantum number in this limit. A most basic element for the design of such a qubit in this limit is called Cooper pair box [58], and the corresponding electric circuits it can be easily embedded to are cavity QED geometries [59].

Andreev spin qubit. These geometries are well suited for quantum computation tasks because qubit interactions can be well designed. However, the involved electric variables charge and flux in general are still sensitive to noise, thereby decreasing the decoherence times in these devices [57, 60, 61]. In contrast, qubit designs which are based on microscopic, well protected systems, easily allow for long decoherence times. An example of such a system is a spin of a single electron confined in a semiconductor quantum dot [62, 63]. In the recently developed platform of Andreev spin qubits (ASQ) [64, 65] , one aims in the end at combining the long decoherence time of spin-qubits in quantum

[2]Note that it is also possible to design qubits in the opposite limit $E_J \gg E_C$ leading to the more sophisticated type of transmon qubit [57]

dots with the possibility to design qubit interactions and the potential scalability of solid state devices [65], by embedding the ASQ into cavity quantum electrodynamics (cQED) geometries. The corresponding building block, the ASQ, is a superconductor quantum dot[3] hybrid device (S-QD-S) consisting of a semiconductor nanowire acting as a weak link between two superconductors [64]. In the S-QD-S device, the supercurrent across the junction depends on the single spin in the QD as a result of spin-orbit interaction in the nanowire (QD). In the presence of spin-orbit interaction, the phase across the junction polarizes the QD-spin, as it lifts the degeneracy of the two spin-doublet states. Hence, mediated by the (macroscopic) supercurrent, the single spin of the QD can then be coherently manipulated and read out by the surrounding cQED geometry, in a way unavailable to electrostatically confined spin qubits [64].

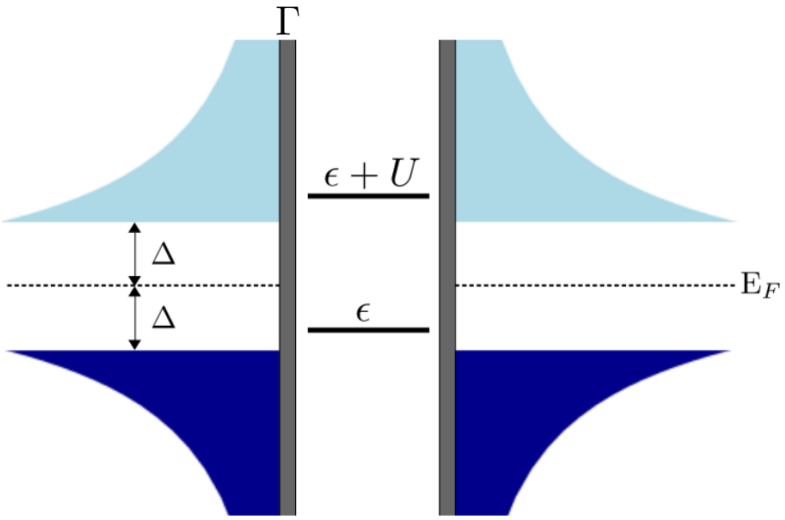

Figure 3.2. A quantum dot attached to superconducting reservoirs (SDS-device) schematically: Indicated are the single level QD with energy level ϵ, charging energy $E_C = U/2$ and tunnel coupling strength Γ to the two superconductors. Their BCS-density of states is indicated in blue with the superconducting gap Δ. The states are here filled (dark blue) up to the Fermi energy E_F.

Superconductor quantum dot hybrid devices have also been of interest for studies of fundamental physics, when quantum dot like properties (Coulomb blockade (CB) and Kondo) are combined with macroscopic phenomena like the Josephson current. The physics of S-QD-S devices in general depends strongly on their regimes of operation.

[3] We refer to the weak link as a QD in the sense that in the semiconducting nanowire, discrete levels can be controlled and a single spin can be isolated.

Regimes. We now give a basic overview on three regimes and the main phenomena associated with them, also in view of understanding our later NDS device [66].These are strong, weak and intermediate regimes, which are specified by the relation of three energy scales: (i) the coupling strength Γ between the single level QD and the superconductors, (ii) the superconducting gap Δ and (iii) the charging energy U needed to overcome the Coulomb repulsion between the electrons when charging the dot (see Fig. 3.2). In the Anderson model of the single level QD to be presented in [Sec. 3.3], U will be introduced as the strength of effective Coulomb repulsion U between the electrons on the dot. By comparison of the Anderson model with the capacitance model [67], $U = 2E_C$ can be identified with the charging energy $E_C = \frac{e^2}{2C}$ needed to charge the dot with a single electron, where C is the total capacitance between the dot and the leads/gates attached. As the capacitance is small for nanoscale objects such as the QD, the charging energy is accordingly large enough to play a role in these mesoscopic devices compared to macroscopic objects.

Strong coupling. In the regime of strong coupling ($\Gamma >> \Delta, U$), the charging energy $E_C = U/2$ is negligible and the Coulomb blockade absent. Consequently, the quantum dot can be equally likely charged with $0, 1$ or 2 electrons or holes as in the case of non-interacting particles (see the concept of addition energies of Sec. 3.4). Given that the extension of the QD is small compared to the coherence length ξ_0 of the superconductors at phase difference ϕ, a supercurrent can hence flow between the leads from resonant tunneling of Cooper pairs ($2\epsilon = 0$) through the QD, when the single level ϵ is on resonance with the Cooper pair condensate at chemical potential zero of the superconductors. These subgap processes are the main transport mechanism in the strong coupling regime and can be understood in the Andreev reflection picture 3.2.1, which will also be relevant for our NDS system.

Weak coupling. In the regime of weak coupling ($\Gamma << \Delta, U$), Cooper pair tunneling is suppressed as a pair of $2e$ cannot overcome the charging energy. Transport is dominated by quasi particle tunneling instead: Single electrons can tunnel from occupied quasi particle states below the gap of the source to empty states above the gap in the drain, when a voltage is applied. The corresponding $I - V$-characteristics of the device reflects the divergence of the density of states (DOS) at the superconducting gap edges and hence differs from the $I - V$ of single particle tunneling between two normal metal contacts, showing a step-like behavior. In our later NDS-device, with the QD weakly coupled to the normal metal, quasi particle tunneling will only be possible between the QD and a

normal metal, whereas particle exchange between the QD and the SC will be restricted to the subgap regime and hence due to AR.

Intermediate coupling. In the regime of intermediate coupling ($\Gamma \sim \Delta \sim U$), one can study the competition between QD-like phenomena such as the CB and the quantum coupling between the superconductors via their macroscopic phase difference: U is large enough for the QD to assume well defined charge/spin-states via the CB and Γ large enough to transfer CPs coherently in this regime: When the single level is off-resonance with the Fermi-energy of the SCs, the CPs can be transferred between them via 4th order cotunneling [60, 66]. Depending on the spin-state of the QD level (singlet or doublet), the phase of the Josephson relation can then be shifted by 0 of π, and hence the direction of the macroscopic current through the device can be reversed by removing (adding) a single electron from (to) the QD [68, 69]. Note, that differently in the above mentioned example of the ASQ [64], the dependence of the Josephson current on the QD doublet-spin relies on spin-orbit interaction, which allows for a sophisticated control of the QD spin, when the SDS device is embedded in a cQED geometry.

Theoretical approaches. SQDS-systems have been treated theoretically by various approaches. It is in general not possible to exactly account for all energy scales simultaneously. For example, the functional renormalization group (FRG) as a non-perturbative method can account for finite superconducting gap delta, thus allowing for quasiparticle transport, but only for small values of the Coulomb interaction [70]. A complementary approach is the real-time diagrammatic transport theory first developed for the normal conducting Anderson model [40] and then extended to quantum dots attached to both NC and SC leads by [71]. In this approach, a systematic perturbation expansion in the tunnel couplings is performed, and it allows to take into account the Coulomb interaction on the quantum dot exactly. Here, non-equilibrium situations can be caused by arbitrary bias voltages. In the real-time diagrammatic approach, the non-interacting fermionic degrees of freedom of the leads are integrated out to obtain an effective description of the reduced system in terms of the state of the quantum dot and the number of Cooper pairs in the superconducting leads. The time-evolution of the reduced density matrix is then described by a generalized master equation of type (3.4).

In follow-up works to [71], a QD attached to two superconducting electrodes has been considered in the limits of weak [72] and strong [73] coupling (infinite gap limit): Here, the dynamics of the reduced dot state was studied after a quench and under periodic driving of the system. In the recent work [74], a particle conserving approach to AC-DC driven interacting quantum dots with superconducting leads was developed to study

the combined action of a DC bias and a microwave drive on the transport characteristic of an SDS junction.

Our transport problem of interest is a special case of the ones that have been previously treated based on the approach of [71]: We study a quantum dot with strong Coulomb interaction, weakly tunnel coupled to a normal metal and proximized by a superconductor in the large gap limit. We are interested in the transient dynamics after a switch in the gate voltage. In the next subsection, we first introduce our model of interest, and discuss the transport theory afterwards.

3.3 | Model for the NDS-system

A quantum dot (D') attached to normal (M) and superconducting (S) leads can be modeled by a total Hamiltonian of the general form

$$H = H_{\mathrm{M}} + H_{\mathrm{S}} + H'_{\mathrm{D}} + H_{\mathrm{T}} \tag{3.11}$$

$$H_r = \sum_{k\sigma} \omega_{rk}\, c^\dagger_{rk\sigma} c_{rk\sigma} - \sum_k \left(\Delta_r\, c^\dagger_{rk\uparrow} c^\dagger_{r-k\downarrow} + h.c. \right), \quad r = \mathrm{M,S} \tag{3.12}$$

$$H_{\mathrm{T}} = \sum_{k\sigma} t_r \left(d^\dagger_\sigma c_{rk\sigma} + \mathrm{h.c.} \right), \tag{3.13}$$

$$H'_{\mathrm{D}} = \epsilon N_{\mathrm{D}} + U N_\uparrow N_\downarrow, \quad N_{\mathrm{D}} = N_\uparrow + N_\downarrow,\ N_\sigma = d^\dagger_\sigma d_\sigma. \tag{3.14}$$

Here, H_{M} with $\Delta_{\mathrm{M}} = 0$ denotes the Hamiltonian of the non-interacting metallic reservoir kept at temperature T and electrochemical potential μ with $c_{rk\sigma}$, the fermionic annihilation operators for electrons with momentum $\boldsymbol{k}$, spin σ and energy ω_k in the reservoir. The superconducting reservoir Hamiltonian H_{S} here includes the standard mean-field BCS terms with a non-vanishing superconducting order parameter Δ_{S} in addition to the non-interacting terms.

The single level quantum dot is described by the Anderson model with level ϵ, which can be controlled by a gate voltage, and effective repulsive Coulomb interaction U between the dot electrons with number operators N_{D} and N_σ. As already indicated in Sec. 3.2.2, $U = 2E_C$ can then be identified with the charging energy E_C required to charge the QD with a single electron. The tunnel Hamiltonian H_{T} describes the tunneling of single electrons between the reservoir and the dot with tunnel-amplitude t_r and tunnel-strength $\Gamma_r = 2\pi|t_r|^2\rho_{\mathrm{N}}$, with ρ_{N} the density of states (DOS) of the reservoir in its normal state.

Let us now further specify the NDS-system to be studied in Chapters 3-5 of this thesis. It consists of a QD attached to a normal metal and proximized by a superconductor in

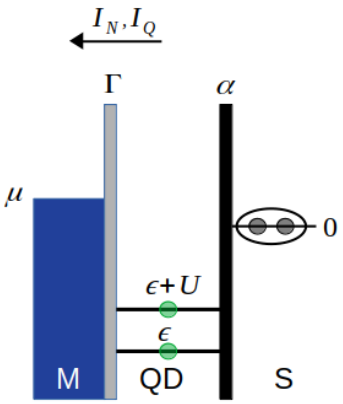

FIGURE 3.3. The system to be studied consists of a quantum dot (QD) with level ϵ and Coulomb interaction U, weakly coupled to a normal metal (M) with coupling Γ and proximized by a superconductor (S) in the large gap limit with superconducting pairing strength α. The black dots indicate a Cooper pair in the condensate. By convention the particle- and heat currents I_N and I_Q are directed into the normal metal.

the so-called large gap limit,[4] in which the superconducting gap Δ exceeds all other energy scales of the problem. In this limit, a valid description of the combined QD-superconductor system (D), later referred to as proximized QD, is given by [53, 54]

$$H_{\mathrm{D}} = H'_{\mathrm{D}} + H_{\mathrm{S}}\,, \tag{3.15}$$

$$H_{\mathrm{S}} = -\tfrac{1}{2}\alpha d^\dagger_\uparrow d^\dagger_\downarrow + \mathrm{h.c}\,. \tag{3.16}$$

Here, H'_{D} is the Anderson model (3.14) for the single level QD and H_{S} replaces the BCS-Hamiltonian given in Eq. 3.12. In the large gap limit, $\Delta >> \epsilon, \alpha, U, T, \mu$, the effect of the superconductor on the QD can therefore be simply included by two pairing terms of (real) pairing strength α.

In the large gap limit, single particle tunneling as described by (3.13) can only occur between the QD and the normal metal. In this thesis, the coupling between the system and the normal metal is considered to be weak, $\Gamma_{\mathrm{M}} \ll T$ and furthermore energy-independent. Thereby we neglect the details of the density of states of the metal ρ_N (wide-band limit). Note that the dissipative tunnel coupling strength Γ appearing in the duality relation (3.10) is the lump sum of tunnel strengths that arises when eliminating spin in the tunnel amplitudes t_r of Eq. (3.13), i.e. $\Gamma = 2\Gamma_{\mathrm{M}}$. From now on, we will already use the duality-adapted notation in terms of the parity decay rate, $\Gamma \equiv \gamma_p$ [3.1.3]. We further note that the superconductor is kept at reference potential $\mu_{\mathrm{S}} = 0$ throughout the thesis.

[4] By *proximized* we mean superconducting correlations that are induced between electrons and holes on the QD due to the presence of the superconductor.

Diagonalization of the Hamiltonian The Hamiltonian of the reduced SQD system in its diagonal form is given by

$$H_{\mathrm{D}} = H'_{\mathrm{D}} + H_{\mathrm{S}} = \sum_{\tau} E_{\tau} \left|\tau\right\rangle \left\langle\tau\right| + E_1 \sum_{\sigma} \left|\sigma\right\rangle \left\langle\sigma\right|, \tag{3.17}$$

with the Andreev Bound States (ABS) $|\tau = \pm\rangle$ of the even parity charge sector with eigen energies E_τ, as well as the single occupied spin states $\sigma = \uparrow, \downarrow$ of the odd parity-charge sector with eigen energy E_1. As introduced in Sec. 3.1.3, the term parity refers to the parity of the QD-charge. Note that the description of the latter two spin states can be restricted to a single corresponding equally weighted mixture $|1) = \frac{1}{2}\sum_\sigma |\sigma\rangle\langle\sigma|$ in Liouville space, as the Hamiltonian (3.17) does not couple to the spin degree of freedom. In Eq. (3.17), the superconducting pairing introduces an Andreev-splitting $\delta_{\mathrm{A}} \geq |\alpha|$ of the discrete 0- and 2- electron levels [75], which differs from the detuning energy δ as follows:

$$E_\tau = \tfrac{1}{2}\left(\delta + \tau\delta_{\mathrm{A}}\right) \quad , \begin{cases} \delta & = 2\epsilon + U \\ \delta_{\mathrm{A}} & = \sqrt{\delta^2 + \alpha^2} \end{cases}. \tag{3.18}$$

The corresponding ABS, which are hybridizations of 0-and 2-charge states, read [5,6]

$$|\tau\rangle = \sqrt{\tfrac{1}{2}\left[1 - \tau\frac{\delta}{\delta_{\mathrm{A}}}\right]}\,|0\rangle - \tau\,\frac{\alpha}{|\alpha|}\sqrt{\tfrac{1}{2}\left[1 + \tau\frac{\delta}{\delta_{\mathrm{A}}}\right]}\,|2\rangle\,. \tag{3.19}$$

The single occupied states $|\sigma\rangle$ are unaffected by the pairing and have energy

$$E_1 = \epsilon = \tfrac{1}{2}\left(\delta - U\right). \tag{3.20}$$

Note that although the bias μ can be arbitrary relative to the induced pairing gap $|\alpha|$ on the dot, the considered model only describes non-equilibrium physics for values of μ within the superconductor gap which is taken to be infinite here. In this description, quasi particles of the superconductor are energetically inaccessible. This implies that coherent Cooper pair transfer ($N = 0, 2$ superpositions) within the SQD-system is not internally damped and the only source of dissipation is the weak coupling to the metal probe M. We furthermore focus on the regime considered in Ref. [15],

$$|\alpha| \gg \Gamma, \tag{3.21}$$

[5] Differently from Ref. [15],the ABS have to be modified by a sign $\alpha/|\alpha| = sign(\alpha)$ to be valid eigenstates of the dual Hamiltonian with inverted energy scales (Sec. 4.1), and therefore of the whole real and extended dual parameter space.

[6] For the case $\alpha = 0$, the labeling of even parity charge eigenstates is not unique for $\delta = 0$ and is therefore replaced by $\delta \to 0^+$ at this point.

where only the occupation probabilities ρ_τ of the Andreev states $\tau = \pm$ together with the odd-parity occupation ρ_1 need to be considered, i.e. at all times the proximized dot is in a *mixture* of energy states (see also Chap. 5).

3.4 | Kernel in the energy basis

Having introduced the eigen-states and energies of the reduced SQD-system in the previous section, we will derive its time-evolution kernel in the eigen-energy basis in this subsection. In the limit of weak coupling studied in this thesis, we will restrict the expansion to leading order in the tunnel coupling Γ. Differently from Ref. [15], where coherences in spin-space had to be considered, we will derive the kernel based on Fermi's Golden Rule without relying on perturbation theory. In view of expressing the kernel and more generally the transient solution to our problem (including the transport observables) in a compact and basis-independent form later on, we start with defining the Liouville space for the SQD-system, which we introduced already in Sec.3.1.2 for the normal conducting NQD-system.

The full 16-dimensional Liouville-space of the SQD-system is spanned by the basis $|\alpha, \alpha') \equiv |\alpha\rangle\langle\alpha'|$, with $\alpha, \alpha' \in \{+, -, \uparrow, \downarrow\}$, the energy eigenstates. By the fermion-parity superselection principle [Sec. 3.1.3] the physical solution ρ of the time-evolution is restricted to the subspace, which is spanned by off-diagonal elements with states α, α' from the same parity sector, thereby reducing its dimension to 8. Throughout this thesis, we furthermore assume that elements off-diagonal in the energy basis can be neglected in the description of the time-dependent SQD-state. The assumption is based on the limit $\alpha >> \Gamma$ specified in Sec.(3.3) and the initialization procedure to be introduced in Chapter 5, as we will argue then in more detail. Therefore, at all times, the solution ρ can be restricted to the 4-dimensional *diagonal* subspace of the 16-dimensional Liouville space, which after the elimination of the spin degree of freedom has dimension 3. This reduction of space leads to the following choice of basis in the three-dimensional subspace,

$$|\tau) \equiv |\tau\rangle\langle\tau|, \quad \tau = \pm, \qquad |1) \equiv \tfrac{1}{2}\sum_\sigma |\sigma\rangle\langle\sigma|, \tag{3.22}$$

corresponding to the identity superoperator

$$\mathcal{I} = \sum_\tau |\tau)(\tau| + 2|1)(1|. \tag{3.23}$$

Note that $(\tau|\tau) = 1$ and $(1|1) = \frac{1}{2}$ due to the elimination of spin. As a result, the state ρ of the SQD-system reads

$$|\rho) = \sum_{\tau=\pm} \rho_\tau |\tau) + \rho_1 |1) \tag{3.24}$$

in terms of its occupation probabilities $\rho_\lambda \equiv (\lambda|\rho)/(\lambda|\lambda)$, as we find via applying the identity (3.23) to ρ.

To leading order in the tunnel coupling and restricting the dynamics to the diagonal subspace, the time-evolution of $|\rho)$ is now in its basis-independent form given by

$$\frac{d}{dt}|\rho(t)) = W|\rho(t)), \qquad |\rho(0)) = |\rho_0), \tag{3.25}$$

with the rate superoperator defined as

$$W = -\sum_\tau W_{1,\tau}|\tau)(\tau| + \sum_\tau W_{1,\tau}|1)(\tau| + \sum_\tau 2W_{\tau,1}|\tau)(1| - \sum_\tau 2W_{\tau,1}|1)(1|. \tag{3.26}$$

As a result, the time-evolution of the occupation probabilities ρ_i in the energy basis is analogously to Eq. (3.25) given by

$$\frac{d\rho_\tau}{dt} = W_{\tau,1}\rho_1 - W_{1,\tau}\rho_\tau, \qquad \frac{d\rho_1}{dt} = \sum_\tau W_{1,\tau}\rho_\tau - \sum_\tau W_{\tau,1}\rho_1, \tag{3.27}$$

without additional normalization factors in the matrix representation of W. In the following, we will justify why the rate superoperator has the form of (3.26). In deriving the matrix elements $W_{i,j}$ of Eq. (3.27), we will now apply Fermi's Golden Rule by properly accounting for the electrostatic balance of the device.

To leading order in Γ, the time-evolution kernel W is determined by single particle transfers between the metal and the SQD-system, thereby transitioning the SQD-state from the odd- to the even-parity charge sector or vice versa, i.e. $|\sigma\rangle \leftrightarrow |\pm\rangle, \sigma = \uparrow, \downarrow$. The difference in the corresponding eigen-energies (3.18, 3.20) of the SQD,

$$E_{\gamma,\tau} = \gamma\Big(E_\tau - E_1\Big) = \tfrac{1}{2}\Big(\gamma\tau\delta_\mathrm{A} + \gamma U\Big), \tag{3.28}$$

equals the addition energy for the related state transition, $\gamma = \pm$ indicating that the transition is directed from $|\sigma\rangle \rightleftarrows |\tau\rangle$, respectively. According to Eq.(3.28), the eigen-energies of the SQD are related to the addition energies for realizing a specific transition in the same manner as for a QD attached to only a normal conducting reservoir by comparison with the capacitance model [67].

For a quantum dot without a superconductor, however, the charge of the quantum dot directly determines its energy eigen state, and therefore the associated charge transfers

are trivially connected to the addition energies, required to induce the state transitions. In contrast, for a hybridized quantum dot, the charge transfer cannot be easily concluded from the state transfer, as in general the same state transition can be realized by both types of charges (electrons or holes). Taking into account that all charge transfers have to obey the electrostatic energy balances of the device, each state transition can be realized by an electron ($\eta = -$) or a hole ($\eta = +$) transfer from the metal to the dot, once the corresponding transition energy can be paid by the normal metal kept at chemical potential μ. At zero temperature, the related energy threshold reads [52]:

$$\begin{aligned} -\eta\mu &\geq E_f - E_i \\ \Leftrightarrow -\eta\mu - E_{\gamma,\tau} &\geq 0\,, \end{aligned} \tag{3.29}$$

with $E_{i,f}$ the energies of the initial and final states of the transition. Table 3.1 gives

$\kappa\kappa'$	threshold	coupling rate	real transition $\overset{e}{\underset{h}{\rightleftarrows}}$	dual transition $\overset{h}{\underset{e}{\rightleftarrows}}$
$-+$	$\mu - E_{-+} \gtrless 0$	Γ_-	$+ \rightleftarrows 1$	$1 \rightleftarrows +$
$+-$	$\mu - E_{+-} \gtrless 0$	Γ_-	$1 \rightleftarrows -$	$- \rightleftarrows 1$
$--$	$\mu - E_{--} \gtrless 0$	Γ_+	$- \rightleftarrows 1$	$1 \rightleftarrows -$
$++$	$\mu - E_{++} \gtrless 0$	Γ_+	$1 \rightleftarrows +$	$+ \rightleftarrows 1$

Table 3.1. Overview of all possible real and dual transitions between $+, -, 1$-states of the hybridized quantum dot. They are constrained by corresponding energy thresholds at zero temperature and have coupling rates $\Gamma_\pm$ (see Fig. 3.4). $\rightleftarrows$ corresponds to $\gtrless$ in column 2 and refers to an $\overset{e}{h}$ ($\overset{h}{e}$)-transfer from the metal to the dot in the real (dual) system, respectively.

an overview of all state transitions and associated particle transfers of the real system in column 4, their corresponding energy thresholds listed in column 2. In Fig. 3.4, the latter are indicated as black curves as functions of the gate parameter ϵ, together with the other three parameters (α, U, μ) of the four-dimensional parameter space.

Having derived the energetic condition for any possible state transition γ at zero

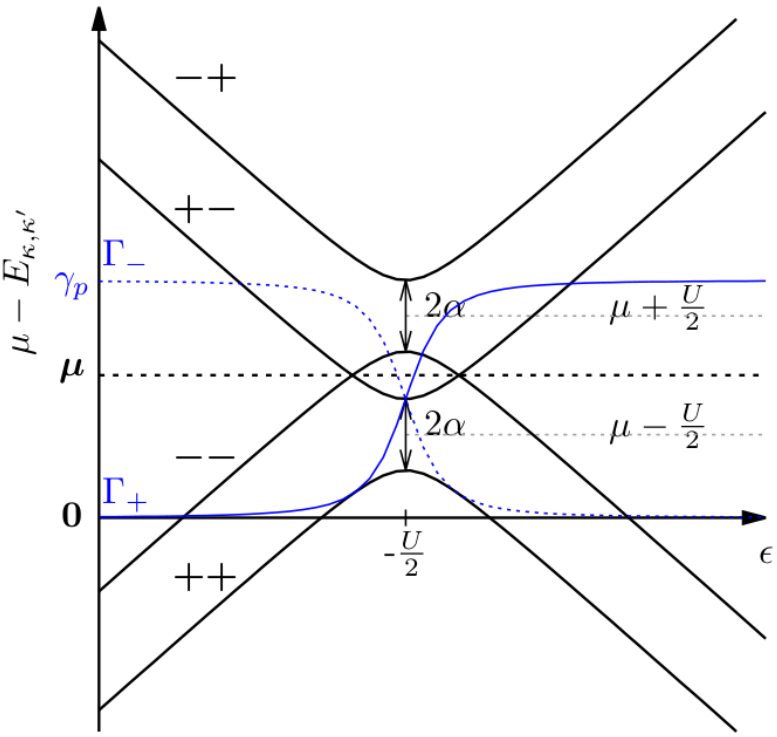

Figure 3.4. Addition energies $E_{\kappa,\kappa'}$ for adding a particle (e) or a hole (h) from the metal to the quantum dot and coupling rates $\Gamma_\pm$ with $\eta\tau = \pm$ (blue lines) between the metal and the quantum dot in dependence of gate voltage ϵ. The $E_{\kappa,\kappa'}$ are given relative to the chemical potential. U denotes the Coulomb interaction and α the superconducting coupling strength.

temperature, the corresponding Fermi function

$$f^{-\eta}(E_{\bar{\eta}\gamma,\tau} - \mu)\,, \tag{3.30}$$

with $f^{-\eta}(\omega) = (e^{-\eta\omega/T} + 1)^{-1}$, gives the probability at temperature T that the state transition γ is enabled by transfer of the corresponding particle η from the metal to the SQD, under the condition that the SQD is initially in state i.

Given the conditional probability, what remains to be determined is the effective tunneling rate for the transition between all initial and final energy eigenstates $i, f \in \{\uparrow, \downarrow, +, -\}$ from different parity sectors. According to Fermi's Golden Rule, it is given by the overlap of the final state f with the initial state i after annihilation or

creation of a dot electron,

$$\begin{aligned}\Gamma_{\eta\gamma,\tau} &= \tfrac{\gamma_p}{2}\left|\langle f|\,\hat{d}^{(\dagger)}\,|i\rangle\right|^2 \\ &= \tfrac{\gamma_p}{2}\left[1+\eta\bar{\gamma}\tau\frac{\delta}{\delta_{\mathrm{A}}}\right]\left[\tfrac{1}{4}(3+\bar{\gamma})\right] \overset{\gamma=-1}{=} \tfrac{\gamma_p}{2}\left[1+\eta\tau\frac{\delta}{\delta_{\mathrm{A}}}\right] \equiv \Gamma_{\eta\tau}\,. \end{aligned} \tag{3.31}$$

Here, $\hat{d}^{(\dagger)} = \sum_\sigma \hat{d_\sigma}^{(\dagger)}$ denotes the annihilation or creation operator of a dot electron. In the last term we fixed the direction of the state transition from initially even to finally odd parity for clarity.

Finally, the time-evolution kernel of our problem is determined by the total probabilities for the state transitions from the even parity sector τ to the odd parity sector 1 and vice versa, i.e. by the product of Eqs (3.31) and (3.30)[7].

$$W^{\eta}_{1,\tau} = \Gamma_{\eta\tau} f^{-\eta}(E_{\eta,\tau}-\mu), \qquad W^{\eta}_{\tau,1} = \tfrac{1}{2}\Gamma_{\bar{\eta}\tau} f^{+\bar{\eta}}(E_{\bar{\eta},\tau}-\mu). \tag{3.32}$$

The factor $1/2$ distinguishing the rates (3.32) is due to the elimination of the spin degree of freedom in the odd-parity sector 1, accounting for the two spin options of tunneling into the odd sector, but only one option vice versa, when starting from a specific spin state. Note that we explicitly account for the direction of the state transition in Eq. (3.32) and therefore skip the index γ. Furthermore, we here explicitly keep the η-index, facilitating the later analysis of the transport currents. However, the time evolution of the SQD-state $\rho(t)$ is insensitive to the type of particle transferred during a state transition. In the diagonal subspace, it is given by the master equation (3.27), with the kernel rates

$$W_{1,\tau} = \sum_\eta W^{\eta}_{1,\tau}, \qquad W_{\tau,1} = \sum_\eta W^{\eta}_{\tau,1}, \tag{3.33}$$

where the kernel rates are now specified. Note that the diagonal matrix elements $W_{\tau,\tau} = -W_{1,\tau}$ and $W_{1,1} = -\sum_\tau W_{\tau,1}$ in the master equation (3.27) follow from probability conservation.

We finally point out that a corresponding master equation can be derived for the dual system as well (App. A). We will define the dual system in the subsequent Sec. 4.1 when introducing the fermionic duality for our real system of interest. From the real and dual master equations, the stationary states of the real and dual systems can be determined, which will be beneficial for analyzing transport observables, as we will show in Chapter 5. Table 3.1 together Fig. 3.4 give an overview of all possible state

[7] Note that this derivation correctly contains the case $\alpha = 0$ of an ND-system, for which the dynamics is induced by single particle transfers to lowest order in γ_p and restricted to the diagonal subspace $0, 1, 2$. The criterion $\alpha \gg \gamma_p$, referring to coherences, is hence lifted. However, the case $\alpha = 0$ is discontinuously connected to this regime of valid α. For further discussion, see Sec. 4.4.3

transitions and associated particle transfers in the real and dual system for the whole four-dimensional parameter space of the problem. Therefore, they provide a more efficient and alternative way of estimating the real and dual stationary states as compared to scanning the four-dimensional parameter space and directly determining the states from the corresponding master equations, as we will explain in more detail in Chapter 5.

4

Fermionic duality applied to an NDS-device

In the previous Chap. 3, fermionic duality was introduced as a "generalized hermiticity" so far known for purely normal conducting systems. In the above cited prior works, the duality facilitated the solution of the master-equation eigenvalue problem, as half of its eigenvectors could be expressed in relation to the other half, which is assumed to be known by some standard calculation. However, it was not systematically exploited to find suitable variables and a suitable basis that would simplify finding the first half of the solution, and, more importantly, to automatically bring it into a form that facilitates its analysis. In this chapter, we push this idea of fermionic duality as "generalized hermicity" further: Sec. 4.2 serves to show that duality can be systematically exploited from the starting point of expressing the time evolution kernel: One considers quantities that are invariant under the duality transformation, the so-called duality invariants and finds a corresponding duality-adapted basis, the so-called polarization basis. We will start with the standard procedure of applying fermionic duality to diagonalize the rate-superoperator in the energy basis in Sec. 4.2.1. This is possible, since the derivation of fermionic duality reported in Refs. [17, 49] comprises systems with Hamiltonians describing large-gap superconductors. Fermionic duality in this case is a property of the part of the dynamics induced by the normal reservoirs and can thus be immediately applied. In the standard diagonalization procedure, we find already the Andreev polarization vector to be further introduced in Sec. 4.2.2, a quantity of central importance for our quantum dot device proximized with superconductivity.

Afterwards, we proceed with the evaluation of the transient charge current from the metal to the SD-system in analogy to the prior work [17] on the purely normal conducting ND-system, where the transient current could be expressed in terms of differences of stationary charge expectation values between the initial and the final state. This way

of determining the transient charge current leads to different contributions, which will motivate the previously mentioned duality invariant rates to be established in Sec. 4.2.4. Once the corresponding duality adapted, so-called polarization basis has been found in Sec. 4.2.5, the kernel can then be easily expressed in terms of these rates. Here, we emphasize that without diagonalizing the transition-rate matrix W , duality allows the exact time scales of the dynamics of the problem to simply be read off. Moreover, the eigenvectors can be expressed compactly in terms of the decay rates and just a single additional duality-invariant parameter.

Sec. 4.3 is devoted to physical constraints imposed by duality. We establish relations between the relevant stationary observables, parity and polarization, and their duals in Sec. 4.3.1. A "universal" stationary duality relation will be given in Sec. 4.3.2, which connects stationary values of observables in the actual model with the ones in the corresponding dual model. "Universal" here refers to the fact that this relation is independent of the values of all physical parameters: temperature T, coupling Γ, voltage μ, but also the –attractive or repulsive– interaction U.

Having established the relevant physical constraints, the state supervector and transport current supercovectors will be derived in Sec. 4.4 in a most compact duality adapted form, i.e. in terms of a minimum number of duality invariant rates and two stationary observables of the real and dual system. Here, we emphasize that we do not only apply the duality-based analysis to the transition rates that govern the evolution of the state via the master equation, but also the transport rates that occur in the expression for the currents.

In Sec. 4.4 we further discuss our SD-system in the limit of self-duality, either fulfilled exactly as by a proximized dot without interaction or in the limit of high bias. Sec. 4.5 contains the conclusions and an outlook.

4.1 | Fermionic duality for the NDS-system

After the derivation of the time evolution kernel W, the time evolution of the state can be obtained from the formal solution

$$|\rho(t)) = e^{Wt}|\rho_0), \tag{4.1}$$

after diagonalizing W and explicitly expressing $|\rho(t))$ in the left and right eigenvectors of W. The diagonalization procedure can be considerably facilitated by applying the fermionic duality previously introduced in Sec. 3.1.3, and derived by [17], here to the SD system, which will be the subject of this section.

Generic duality relation. First, we note that the present system belongs to the large class of models, which was shown to obey a fermionic duality [Sec. 3.1.3], as it fulfills the following criteria: The SD is bilinearly and energy-independently coupled to a metal, which is treated as non-interacting. Furthermore, the superconductor-QD system, as described by the effective Hamiltonian H_{D} (3.17) in the large-gap limit, does not commute with the local dot charge N_{D}, but with the fermion parity operator, $[H_{\mathrm{D}}, p] = 0$. Given these criteria, the rate superoperator W of the master equation (3.27) obeys a fermionic duality relation [17, 43, 76]:

$$W + \tfrac{1}{2}\gamma_p \mathcal{I} = -\big[\mathcal{P}\overline{\big(W + \tfrac{1}{2}\gamma_p \mathcal{I}\big)}\mathcal{P}\big]^\dagger. \tag{4.2}$$

Relation (4.2) follows from relation (3.10) when taking the limit $\omega, i\Gamma \to i0$ in the frequency arguments (Markov approximation) and expanding the full time evolution kernel W up to second order in H_T (Born approximation)[1]. As written in Eq. (4.2), the duality relation states that the *shifted* rate-superoperator is *invariant* under a duality mapping up to a sign. Here, similarly to Sec. 3.1.3, the duality mapping is defined as a "generalized hermitian adjoint" consisting of three parts: the ordinary hermitian adjoint $\dagger$, the superoperator $\mathcal{P} = p\,\bullet$, containing the fermion-parity operator $p = (-\mathbb{1})^N$ for the QD-charge N, and the over-bar, which denotes an inversion of parameters to be specified in the following for our system.

Parameter inversion. For the SD-model, the latter parameter transformation corresponds to the inversion

$$\overline{X(\epsilon, U, \alpha, \mu)} = X(\bar{\epsilon}, \bar{U}, \bar{\alpha}, \bar{\mu}) \tag{4.3}$$

of energy scales for any function X with $\bar{x} = -x$ for $x = \epsilon, U, \alpha, \mu$, such that the duality relation (4.2) is fulfilled. For the dual kernel $\bar{W}$ introduced in Eq. (4.2), we define $\mathcal{W} \equiv \bar{W}$ to avoid confusion with the parameter transformed real kernel matrix elements $\bar{W}_{ij}$. By Eq. (4.3), the real SD-system with Hamiltonian H_{D} is related to a fictitious dual one at inverted energies with the Hamiltonian $\bar{H}_{\mathrm{D}} = -H_{\mathrm{D}}$. The dual system obeys a corresponding dual master equation $\dot{\bar{\rho}} = \mathcal{W}\bar{\rho}$ with the dual kernel $\mathcal{W}$, which we derive in App. A in analogy to Sec. 3.4, to efficiently extract the dual stationary states for the whole parameter space. As introduced in Sec. 3.1.3, temperature T and coupling Γ are here left unaffected by the inversion (4.3) for the SD model as well, as the treatment of these parameters is generic to the class of QD-Hamiltonians obeying a fermionic duality relation.

[1] Taking the Born approximation yields the additional minus sign in Eq. 4.2 as compared to Eq. 3.10, as $W(\bar{H}_T) \propto \bar{H}_T^2$ and $\bar{H}_T = iH_T$. Γ is therefore left untouched by the parameter inversion (4.3).

Parameter dependent bases. Differently from the normal-conducting case introduced in Sec. 3.1.3, we have here to deal with bases that are parameter-dependent due to the superconducting pairing α. These are the energy basis, the kernel eigen basis and the so-called polarization basis used in this thesis to study the dynamics. Let us therefore briefly introduce the parameter transformations for the energy basis and eigen energies as building blocks for the related quantities used in the later sections. The Andreev states transform according to $|\tau) \to |-\tau)$ under parameter inversion, as can be seen from Eq. (3.19). This labeling has the advantage that $\tau = -$ labels the ground state for all real α, i.e. for the real and dual system.[2] The transformed eigen energies, addition energies and the off- diagonal matrix elements of the dual kernel in the energy basis read

$$\bar{E}_\tau = -E_{\bar{\tau}}\,, \tag{4.4}$$

$$\bar{E}_{\gamma,\tau} = -E_{\gamma,\bar{\tau}}\,, \tag{4.5}$$

$$\mathcal{W}^\eta_{1,\tau} = \bar{W}^\eta_{1,\bar{\tau}}\,,\ \mathcal{W}^\eta_{\tau,1} = 2\bar{W}^\eta_{\bar{\tau},1}\,, \tag{4.6}$$

respectively. Based on the behavior of the Fermi Dirac function under inversion of the energy (4.3), useful relations are implied between the real and dual kernel rates, $W_{i,j}, \bar{W}_{i,j}$, which allow to eliminate kernel rates for one direction of the state transition in favor of the opposite direction, see App. D.

Cross relations. From Eq. (4.2) we see that the rate superoperator W shifted by $\gamma_p/2$ is antisymmetric with respect to the three-fold duality mapping even though W itself is not (anti-)hermitian $W \neq \pm W^\dagger$. This relation implies that left and right eigenvectors of $W + \frac{1}{2}\gamma_p \mathcal{I}$ – and thus of W– for in general *different* eigenvalues labeled by their operators x, y are *cross*-related in pairs

$$\left[\mathcal{P}\overline{|x)}\right]^\dagger \propto (y|, \qquad \left[\overline{(x|}\mathcal{P}\right]^\dagger \propto |y). \tag{4.7}$$

The corresponding eigenvalues λ obey

$$\lambda_x = -\bar{\lambda}_y\,, \tag{4.8}$$

while the eigenvalues λ' of the original unshifted kernel W obey

$$\lambda'_x = -[\gamma_p + \bar{\lambda}'_y]\,. \tag{4.9}$$

[2] Note that an alternative labeling $|\tau'\rangle \equiv |\tau\alpha/|\alpha|\rangle$ would be also possible, which leaves the states invariant.

Therefore, only one half of the eigenvectors of the (un)shifted kernel has to be determined, while the remaining half follows from cross-relations. We will profit from this fact in the next Sec. 4.2, when diagonalizing the kernel and finding a suitable basis for its representation.

4.2 | Optimal exploitation of fermionic duality

In this section, we will diagonalize the kernel to find the time-dependent solution (4.1) of the SD-system by applying fermionic duality. In the first part of this section, Subsecs. 4.2.1- 4.2.3, the solution ρ including its representation in terms of the eigenvectors of the kernel, as well as the charge current as a first transport observable, will be determined in the energy basis. We will discuss the so-called Andreev polarization, a central observable we find in the diagonalization procedure, in comparison with its analogue for the normal conducting ND-system in Sec. 4.2.2. In Secs. 4.2.4- 4.2.5, we will diagonalize the kernel starting from another duality adapted, so-called polarization basis, instead of the energy basis used in the first part of this section. We will motivate the polarization basis by a duality-adapted splitting of the total charge current found in Sec. 4.2.3. It will considerably facilitate the later analysis of the transport observables.

4.2.1 | Diagonalization of the rate superoperator in the energy basis

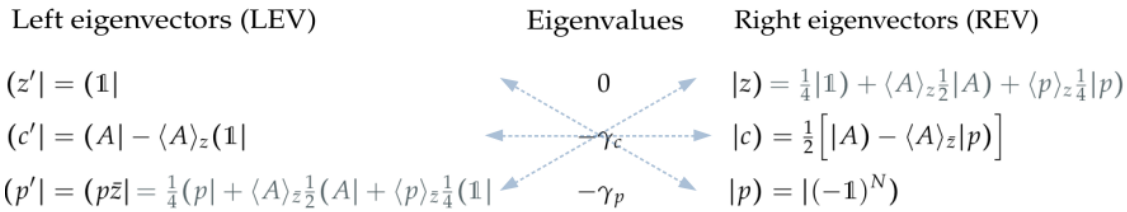

Figure 4.1. Left and right eigenvectors and eigenvalues of the kernel W. Their cross-relations are indicated by dashed arrows.

Fermionic duality allows to determine half of the eigenvectors of W by the other half from the cross-relations given in Eq. (4.7). First, we note that the state $|\rho)$ at any time has to conserve probability, its trace being one, $(\mathbb{1}|\rho) = 1$, corresponding to $(\mathbb{1}|W\bullet = 0$. Therefore, the supercovector $(\mathbb{1}| \equiv (z'|$ is a left eigenvector (LEV) of W with eigenvalue zero. The corresponding right eigenvector (REV) with eigenvalue zero is given by the stationary state $|z)$ of the SD-system. By the cross-relations (4.9) for the eigenvalues of

W, the fastest decay rate (smallest eigenvalue) of the kernel is given by γ_p, as zero is the slowest decay rate. The corresponding L- and REVS cross-related with $(z'|$ and $|z)$ are, according to Eq. (4.7), given by $|p)$ and $(p\bar{z}| \equiv (p'|$, respectively. For an explicit representation of these four vectors in the energy basis, see App. B.1

By the dimensionality three of the problem, as discussed in Sec. 3.4, there are two remaining self-dual EVs, $(c'|, |c)$[3], which can be found by the orthonormality (3.7) of the kernel eigen basis introduced in Sec. 3.1.2: As the LEV has to fulfill $(c'|p) = 0$, it belongs to the two-dimensional subspace of supercovectors orthogonal to $|p)$. A most general ansatz is therefore given by

$$(c'| = c_1(A| + c_2(\mathbb{1}|\,, \tag{4.10}$$

$$(A| \equiv (+| - (-|\,, \tag{4.11}$$

as A and $\mathbb{1}$ are mutually orthogonal, $(A|\mathbb{1}) = (\mathbb{1}|A) = 0$. The REV $|c)$ follows from the cross-relation (4.7) and the remaining constants c_1, c_2 are fixed by normalization, see the App. B.1 for a more detailed derivation. As a result, we obtain,

$$(c'| = (A| - \langle A\rangle_z(\mathbb{1}|, \qquad\qquad |c) = \tfrac{1}{2}\Big[|A) - \langle A\rangle_{\bar{z}}|p)\Big]. \tag{4.12}$$

We evaluate the remaining eigenvalue $-\gamma_c$ explicitly in the energy basis, using the kernel representation (3.26) and the energy basis representations of A, p and z given in App. B.1. An overview of the L-and REVs, the corresponding eigenvalues and their cross-relations is given in Fig. 4.1. In the overview of Fig. 4.1, we give already the representation of the stationary state and its cross-related left eigenvector in the so-called polarization $(\mathbb{1}, A, p)$- basis, which we will carefully introduce in Sec. 4.2.5.

Finally, given the EVs of the kernel, the state evolution $\rho(t)$ follows from Eq. (4.1),

$$|\rho(t)) = |z) + e^{-\gamma_p t}(p\bar{z}|\rho_0)|p) + e^{-\gamma_c t}\Big[\langle A\rangle_{\rho_0} - \langle A\rangle_z\Big]|c)\,, \tag{4.13}$$

its transient decay being dictated by the parity decay rate $\gamma_p \equiv \gamma$, which is a mere interface property also in the presence of the superconductor, and the charge decay rate γ_c. The decay amplitudes specific to the choice of the initial state will be extensively discussed in Chap. 5, when considering different preparation scenarios for the initial state. Note that the components of the state evolution $\rho_\kappa(t), \kappa = \pm, 1$ in the energy basis can be extracted from Eq. (4.13), by replacing the REVs v with their corresponding components v_κ (3.8) given in the App. B.1. In general, it is useful to know these components, as the energy basis is a natural choice to start with the derivation of the time-dependent charge-and energy currents, which will be subject of Secs. 4.2.3 and 4.4.3.

[3]Similarly to Ref. [17], c refers to charge and refers to the fact that the corresponding amplitude describes single particle decay in contrast to interaction energy decay as described by the p-amplitude, as we will be discussed in Chap. 5.

4.2.2 | Andreev-polarization supervector

As can be seen from Eq. (4.13), the form of the state evolution, as dictated by fermionic duality and by the dimensionality of the problem, is very similar to the one of the normal conducting ND system studied in Ref. [17]. The parity decay rate γ_p is unaltered due to the presence of the superconductor. Its amplitude is still given by the parity times the stationary state of the dual system. The main difference with respect to the ND system that is caused by the superconductor is the hybridization of 0-and $2-$ charge states in the Andreev states. The hybridization explicitly enters the charge amplitude of (4.13) through the so-called Andreev polarization A introduced in Eq. (4.11) by orthogonality of the eigenbasis. Let us therefore explicitly compare the charge modes and amplitudes of the SD as given in Fig. 4.1 with the corresponding ones of the ND [17], which are given by

$$(c'| = (N_{\mathrm{D}}| - \langle N_{\mathrm{D}}\rangle_z(\mathbb{1}|, \qquad |c) = \tfrac{1}{2}(-\mathbb{1})^{N_{\mathrm{D}}}\Big[|N_{\mathrm{D}}) - \langle N_{\mathrm{D}}\rangle_{\bar{z}}|\mathbb{1})\Big]. \tag{4.14}$$

Here, we see that the relevant analogue of A in the ND-system is the quantum dot charge N_{D}. The observables are related in the following way:

$$|A) = |+) - |-) = \frac{\delta_{\mathrm{A}}}{\delta}|N_{\mathrm{D}}^{\mathrm{diag}} - \mathbb{1}) \tag{4.15}$$

$$\overset{\alpha\to 0}{=} \frac{\delta}{|\delta|}|N_{\mathrm{D}} - \mathbb{1}) \,. \tag{4.16}$$

In the limit of zero superconducting pairing α, the polarization A reduces to a difference in even parity charges, its sign being determined by the detuning δ. This corresponds to the fact that the ground state labeled by the $|-)$-state changes from 2 to 0 charges when swapping the sign of the detuning from minus to plus. Eq. (4.16) gives the corresponding expression in terms of the QD-charge N_{D}. In the limit of nonzero pairing α, the hybridization is visible in the prefactor $\frac{\delta_{\mathrm{A}}}{\delta}$ of Eq. (4.15). Furthermore, A is not directly represented by the full dot charge N_{D} anymore, but only by its projection onto the subspace diagonal in the Andreev states, i.e. neglecting coherences of type $|+,-), |-,+)$. However, by left-action of $(A|\bullet$ onto a state ρ diagonal in the subspace of ABS, A is again correctly represented by the full dot-charge operator N_{D} in Eq. (4.15). The connection (4.15-4.16) between the central observables of the SD and the ND system will be used in the 2d spectroscopy of Chap. 5, when gate switching procedures will be compared with the one analyzed for the ND-system in Ref. [17].

Given the time evolution of ρ, the transient transport observables such as the charge and heat currents into the metal, can be determined. The goal of the next Sec. 4.2.3 is

to express the charge current, which can be directly derived from the kernel (3.32) in the energy basis, in a duality-adapted compact way, i.e. via local observables evaluated in the stationary state of the real (dual) system and a minimum number of transient quantities. This will facilitate the analysis of the transient transport to be presented in Chap. 5.

In deriving the charge current, we first proceed in analogy to Ref. [17], where the mentioned local stationary observable was given by the dot charge N_{D} of the ND system. For the SD system, this charge operator has to be extended by an additional term N_{cp} if one wants to find a corresponding total charge operator N. The two contributions N_{D} and N_{cp} to the total charge lead to an artificial splitting of the total charge current with corresponding current kernel rates, which are not only sensitive to the particle index η, as one would expect, but also to the index τ of the state transition. Motivated by these current kernel rates [Sec. 4.4.3], we will express the general kernel rates (3.32) in duality-invariant rate variables [Sec. 4.2.4] and hence perform the first task in exploiting fermionic duality from the very beginning, at the stage of setting up the state evolution (3.27)- and transport equations[4].

Afterwards, we will introduce the $\mathbb{1}, A, p$-basis as an intermediate step to be taken after having set up the transport equations in the energy basis and before obtaining the kernel in its diagonalized form [Fig. 4.1]. In view of finding duality-adapted expressions of the transport observables, these two steps are important: Starting instead from the kernel eigenvectors in the energy basis representation [App. B.1] is not optimal, as it is then not obvious how the expectation values of local observables should be extracted in the expressions of the transient non-local observables [Table C.1].

By diagonalization of the kernel in the polarization basis [Sec. 4.2.5] and by further inspection of the duality-invariant rate variables, we will find useful constraints imposed on the transport problem in the remaining part of this chapter, further facilitating the analysis.

4.2.3 | Charge currents in energy basis

In the energy basis, the total average charge current[5] I_{N} directed into the metal can be determined from Eq. (3.32) by accounting for the type of particle η transferred during a

[4] Note that these invariant rate variables are motivated by the general charge current expressions (4.31)-(4.32) and hence prior to having solved the transient evolution of the state (4.13).

[5] Throughout the thesis, the charge current is given in units of $-e$.

state transition from $1 \leftrightarrows \tau$,

$$I_N = \sum_{\eta\tau} \eta \left[W^{\eta}_{1,\tau} \rho_+ + W^{\eta}_{\tau,1} \rho_1 \right]. \tag{4.17}$$

The corresponding left supercovector (3.9)is given by

$$(I_{\rm N}| = \sum_{\eta\tau} \eta \left[W^{\eta}_{1,\tau} (\tau| + 2 W^{\eta}_{\tau,1} (1| \right], \qquad C^{\rm N}_{\kappa} \equiv (I_{\rm N}|\kappa)\,, \kappa = \pm, 1\,, \tag{4.18}$$

with $C^{\rm N}_{\kappa}$ its components in the energy representation. Inserting the components ρ_κ of the state evolution (4.13) into Eq. (4.17), we obtain the following duality-adapted form,

$$I_N = e^{-\gamma_c t} \left[\langle A \rangle_{\rho_0} - \langle A \rangle_z \right] \sum_{\kappa=\pm,1} C^{\rm N}_{\kappa} c_\kappa + \sum_{\kappa=\pm,1} C^{\rm N}_{\kappa} z_\tau\,, \tag{4.19}$$

the first term describing the transient part. In the following, we want to understand how this expression compares to the corresponding duality-adapted expression found in Ref. [17] for the ND-system. There, the charge current into the metal M could be easily expressed in terms of the dot-charge operator $N_{\rm D}$ via $I_{\rm N} = \frac{dN_{\rm M}}{dt} = -(N_{\rm D}|W\rho)$, with ρ the reduced density matrix of the QD. Using the representation (4.14) of $|c)$ in terms of $N_{\rm D}$, the ansatz directly led to the duality-adapted expression of $I_{\rm N}$,

$$I_{\rm N} = -\gamma_c (N_{\rm D}|c)(c'|\rho_0) \tag{4.20}$$

$$= -\gamma_c \left[\langle N_{\rm D} \rangle_{\rho_0} - \langle N_{\rm D} \rangle_z \right] e^{-\gamma_c t}\,. \tag{4.21}$$

As suggested by comparison of the transient part of the SD-charge current (4.19) with the (transient) charge current of the normal conducting ND-system (4.21), using Eq. (4.15) for the polarization, it is natural to ask, whether the transient charge current of the SD-system is exclusively due to the change in the dot-charge $(N_{\rm D}|W\rho)$. Let us anticipate the result: As we will verify, this is *not* the case and the total transient charge current has an additional contribution coming from the cooper pair condensate in the BCS ground state of the superconductor. To this end, we extend the dot-charge operator $N_{\rm D}$ by an additional contribution $2N_{\rm cp}$ to represent the total charge of the SD-system

$$N = N_{\rm D} + 2N_{\rm cp}\,. \tag{4.22}$$

The total charge current is then correctly reproduced by the extended charge operator according to

$$I_{\rm N} = \frac{d}{dt} \langle N_{\rm M} \rangle = -(N|W^{+{\rm S}} \rho^{+{\rm S}})\,, \tag{4.23}$$

where the kernel and the state are extended by an additional labeling to account for the condensate, as we will specify below. This derivation provides an alternative way of determining the total transient charge current contribution from a corresponding operator, instead of evaluating just the dot charge contribution and identifying the remaining cooper pair contribution by subtraction of the former from the total charge current given in (4.17). This way, we will get a better understanding of the connection between the transient behavior of the dot charge and the total charge of the SD-system. In the following, we will give the derivation.

As $(N|$ in Eq. (4.23) counts the total number of charges in the SD, it is no longer sufficient to keep track of the QD-charges in the reduced density matrix of the SD-system and its time derivative. Instead, we extend the labeling from $W\rho$ to $W^{+S}\rho^{+S}$, by explicitly accounting for the changes in the number of Cooper pairs in the SD associated with a specific process. We start with extending the eigenstates of the effective DS-Hamiltonian[6],

$$|\pm, n\rangle = \frac{1}{\sqrt{\gamma_p}}(\sqrt{\Gamma_\mp}\,|0, n+1\rangle \mp \sqrt{\Gamma_\pm}\,|2, n\rangle) \tag{4.24}$$

$$|\sigma, n\rangle\,, \tag{4.25}$$

where n denotes the number of Cooper pairs in the superconductor. Here, we assume that the total number of charges N is conserved in the SD, when it is in one of the states (4.24,4.25) and decoupled from the metal. We further allow a general reduced state of the SD to be in a mixture of $|\tau)$, $\tau = \pm, 1$-states, where the probability $p_\tau(t)$ of being in state $|\tau)$ is no longer associated with a conserved number of Cooper pairs, but distributed over an arbitrary number n in time instead:

$$\rho^{+S}(t) = \sum_{n,\tau\in\pm,1} p_{\tau,n}(t)|\tau, n) \tag{4.26}$$

$$p_\tau(t) = \sum_n p_{\tau,n}(t). \tag{4.27}$$

The ansatz (4.24-4.25) corresponds to an extension of the effective SD-Hamiltonian (3.17) by an additional projector, and therefore to reintroducing an explicit labeling of the Cooper pairs (App. C). Note that for a fully quantum mechanical treatment, the compatibility of the ansatz 4.26 with a correct treatment of the BCS-ground state of the superconductor in the should be checked. In this thesis, however, we directly continue with a labeling of the Cooper pair number in the master equation (3.27), using the ansatz (4.24-4.25), as the main purpose of this section is to newly derive and additionally

[6]Here, we use the short notation $\Gamma_\tau \equiv \Gamma_{++,\tau}$ for the effective tunnel coupling rates introduced in Eq. (3.31).

reproduce known contributions to the (transient) charge current in the semiclassical approximation of Eq. (3.27). By the extended labeling, however, the involved processes in the charge transfer between the metal and the SD and their interpolation to the normal conducting case studied in Ref.[17] become more obvious, as we will see.

In a next step, we therefore explicitly account for the Cooper pair number in Eq. (3.27), which describes the time evolution of the state (4.26). By the n-labeling (4.24) of the eigenstates, it is obvious that Cooper pairs are exchanged between the metal and the SD by a "ladder" of two subsequent electron or hole transfers, though the processes described in the modified master equation are only due to single particle transfers. Keeping explicitly track of n, the equation reads

$$\begin{aligned}\frac{d\rho^{+\mathrm{S}}}{dt} &= W^{+\mathrm{S}}\rho^{+\mathrm{S}} \\ &= \sum_{n,\tau\in\pm}[W^e_{\tau 1}p_{1,n} + W^h_{\tau 1}p_{1,n+1} - (W^h_{1\tau} + W^e_{1\tau})p_{\tau,n}]|\tau,n) \\ &+ \sum_{n,\tau\in\pm}[W^h_{1\tau}p_{\tau,n} + W^{e,+1}_{1\tau}p_{\tau,n-1} - (W^e_{\tau 1} + W^h_{\tau 1})p_{1,n}]|1,n).\end{aligned} \tag{4.28}$$

In view of expressing the total charge current via (4.23), we express $N = \sum_\sigma d^\dagger_\sigma d_\sigma + 2N_{\mathrm{cp}}$ in the $|\tau,n)$-basis according to

$$|N) = \sum_{n,\tau\in\pm}[(2n+2)|n,\tau) + \frac{(2n+1)}{(n,1|n,1)}|n,1)], \tag{4.29}$$

with a factor $(n,1|n,1) = \frac{1}{2}$ due to normalization. From Eq. (4.29), the total charge current (4.17) can indeed be reproduced (see App. C). Furthermore, we can identify two contributions to I_N. One is due to the change in the charges of the QD and the other one due to the corresponding change in the Cooper pair condensate:

$$I_N = I_{N_{\mathrm{D}}} + I_{N_{\mathrm{cp}}} = -(N_{\mathrm{D}}\otimes \mathbb{1}_{\mathrm{S}}|W^{+\mathrm{S}}\rho^{+\mathrm{S}}) - (2N_{\mathrm{cp}}\otimes \mathbb{1}_{\mathrm{D}}|W^{+\mathrm{S}}\rho^{+\mathrm{S}})\,. \tag{4.30}$$

The first term is equivalent to $-(N_D|W\rho)$ and can be directly derived without keeping track of the cooper pairs, but is correctly reproduced from tracing out the Cooper pairs, (see App. C). It is given by

$$I_{N_{\mathrm{D}}} = -\sum_{n,\tau\in\pm}(-\tau\frac{\delta}{\delta_{\mathrm{A}}})\Big[p_\tau[W^h_{1\tau} + W^e_{1\tau}] - p_1[W^e_{\tau 1} + W^h_{\tau 1}]\Big]. \tag{4.31}$$

The second term $I_{N_{\mathrm{cp}}}$ reads

$$I_{N_{\mathrm{cp}}} = -\sum_{\tau\in\pm}\frac{2}{\gamma_p}(p_\tau[\Gamma_\tau W^e_{1\tau} - \Gamma_{\bar\tau}W^h_{1\tau}] + p_1[\Gamma_{\bar\tau}W^e_{\tau,1} - \Gamma_\tau W^h_{\tau 1}]). \tag{4.32}$$

The rate-prefactors $\propto \frac{\delta}{\delta_A}, \frac{\Gamma_\kappa}{\gamma_p}$ in Eqs. (4.31) and (4.32) are due to the differences in the average dot charge and cooper pair-number, respectively, between the initial and final state of the transition (see App. C).

We point out that we determine the current at both interfaces of the QD. In the stationary limit with nonzero pairing α, I_N at the normal metal and $I_{N_{\mathrm{cp}}}$ have to be identical because of charge conservation. The transient behavior, however, is different: charge can accumulate on the QD and $\frac{d}{dt}\langle N_{\mathrm{D}}\rangle = -I_{N_{\mathrm{D}}} = -I_{N_D} = -(I_N - I_{N_{\mathrm{cp}}}) = 0$. In the limit of $\alpha = 0$, we recover the situation of Ref. [17], where the transient current into the metal equals the current out of the dot at every time. The fast switch initialization to be introduced in Chap. 5 interpolates between these two cases as α is varied. In other words, the current into the metal equals the superconductor current plus a displacement current $I_N = I_{N_{\mathrm{cp}}} - \frac{d}{dt}\langle N_{\mathrm{D}}\rangle$. Extracting the components $C_\kappa^{N_{\mathrm{cp}}}$ of the $I_{N_{\mathrm{cp}}}$-current contribution (4.32) in the energy basis, the transient and stationary CP-charge contributions can be determined from Eq. (4.19), inserting the components c_κ of the charge-supervector and z_κ of the stationary state in the energy basis.
As a result, we verify indeed that there is a non-vanishing transient contribution of $I_{N_{\mathrm{cp}}}$ despite the proportionality of the polarization difference in Eq. (4.19) to the corresponding difference of the dot charge. The stationary contribution of $I_{N_{\mathrm{D}}}$ is indeed zero due to charge conservation.

Furthermore we note that differently from the current kernel rates of the total charge current, which are anti-symmetric in the particle index η, some rates appearing in the expressions (4.31) and (4.32) of $I_{N_{\mathrm{D}}}$ and $I_{N_{\mathrm{cp}}}$ are anti-symmetric in the sign of the Andreev state τ involved in the transition. Motivated by this fact, we will find duality-invariant kernel rate combinations in the next subsection, which are (anti-)symmetric in τ, η, or both. Starting from these current kernel expressions and further choosing the duality-adapted polarization basis in Subsec. 4.2.5, the (shifted) kernel $W(+\frac{\gamma_p}{2}\mathcal{I})$ can be diagonalized in a most efficient way and the expressions for the (transient) currents in terms of stationary observables (table C.1) will be easily accessible.

4.2.4 | Duality-invariant rate variables

Motivated by the different sign combinations, which appear in the different constituents of the total charge decay introduced in the previous section (see Eqs.(4.31-4.32)), we consider η-and τ-resolved kernel rates as the elementary building blocks of the transient transport problem. Hence, we decompose all kernel rates into contributions, which are (anti-) symmetric with respect to inversion of the energy state (τ) or electron-transfer direction (η) or both. We start with decomposing the effective tunnel coupling rate

(3.31),

$$\Gamma_{\eta\tau} = \tfrac{1}{2}(\gamma_p + \eta\tau\gamma'_p), \qquad \gamma_p \equiv \Gamma, \qquad \gamma'_p \equiv \gamma_p \frac{\delta}{\delta_A}. \tag{4.33}$$

Here γ_p is the simple lump sum rate of Eq. (3.31) featuring in the duality relation (4.2) and γ'_p adds a dependence on the detuning relative to the pairing. Explicitly accounting for $\Gamma_{\eta\tau}$, the kernel rates $W^{\eta}_{1,\tau}$ can be similarly decomposed by the following ansatz

$$W^{\eta}_{1,\tau} = \tfrac{1}{2}\Gamma_{\eta\tau} + \tfrac{1}{2}\big[\gamma_C + \eta\gamma'_c + \tau\gamma_s + \eta\tau\gamma'_S\big], \tag{4.34a}$$

$$2W^{\eta}_{\tau,1} = \tfrac{1}{2}\Gamma_{\bar{\eta}\tau} - \tfrac{1}{2}\big[\gamma_C - \eta\gamma'_c + \tau\gamma_s - \eta\tau\gamma'_S\big], \tag{4.34b}$$

with the corresponding relation (4.34b) for the opposite direction of the state transition following from Eq. (D.2) in the App. D. By the relations (D.1) between the real and dual kernel rates, it is obvious that indeed these new variables are $(\pm)$ invariant under the scalar duality mapping of physical parameters: Inserting the ansatz into the first of Eqs. (D.1) and summing over $\eta, \tau = \pm$ as either $\sum_{\eta\tau}$ or $\sum_{\eta\tau}\eta$ or $\sum_{\eta\tau}\tau$ or $\sum_{\eta\tau}\eta\tau$, we obtain

$$\gamma_p = +\bar{\gamma}_p, \qquad \gamma_C = -\bar{\gamma}_C, \qquad \gamma_s = +\bar{\gamma}_s, \tag{4.35a}$$

$$\gamma'_p = -\bar{\gamma}'_p, \qquad \gamma'_c = -\bar{\gamma}'_c, \qquad \gamma'_S = +\bar{\gamma}'_S. \tag{4.35b}$$

Therefore, these are the appropriate variables in which we should express the shifted rate superoperator $W + (\gamma_p/2)\mathcal{I}$ from the very beginning to optimally exploit the duality relation (4.2). In terms of the kernel rates, their explicit form is given by

$$\gamma_p \equiv \tfrac{1}{2}\sum_{\eta\tau}\Big(W^{\eta}_{1,\tau} + 2W^{\bar{\eta}}_{\tau,1}\Big), \qquad \gamma_C \equiv \tfrac{1}{2}\sum_{\eta\tau} W^{\eta}_{1,\tau} - \frac{\gamma_p}{2}, \qquad \gamma_s \equiv \tfrac{1}{2}\sum_{\eta\tau}\tau W^{\eta}_{1,\tau}, \tag{4.36a}$$

$$\gamma'_p \equiv \tfrac{1}{2}\sum_{\eta\tau}\eta\tau\Big(W^{\eta}_{1,\tau} + 2W^{\bar{\eta}}_{\tau,1}\Big), \qquad \gamma'_c \equiv \tfrac{1}{2}\sum_{\eta\tau}\eta W^{\eta}_{1,\tau}, \qquad \gamma'_S \equiv \tfrac{1}{2}\sum_{\eta\tau}\eta\tau W^{\eta}_{1,\tau} - \frac{\gamma'_p}{2}. \tag{4.36b}$$

The prime notation is physically motivated: Unprimed (= η-symmetric) invariants determine the state evolution (insensitive to electron transfer direction), whereas the primed (= η-antisymmetric) invariants enter only into *transport* quantities (sensitive to electron-transfer direction. The motivation of subscripts p (parity), C (charge) and S (isospin polarization) will become clear later in the expressions for the transport observables.

In summary, we decomposed the kernel rates $W^{\eta}_{1,\tau}$ into its η, τ-(anti)-symmetric parts γ (Eq. 4.34a) as motivated by the different current contributions introduced in the previous subsection. As indicated by the relations (D.1) and (D.2) between the real and

dual kernel rates, it was then clear that the whole parameter dependence of the real system, as described by $W^{\eta}_{1,\tau}$ and $W^{\eta}_{\tau,1}$ (see Eqs. (4.34a),(4.34b)) and that of the dual system ($\bar{W}^{\eta}_{1,\tau} = 2W^{\bar{\eta}}_{\bar{\tau},1}$) as well (see Eq. (D.1)), is determined by these γ-rates (4.35). Therefore, the most non-trivial parameter dependence of the total time-dependent problem is contained in the four duality invariants γ_C, γ'_c, γ_s, γ'_S. We emphasize that in the standard brute force linear algebra approach of diagonalizing the kernel in the energy basis, simplifications are merely based on the mutual linear dependence of the kernel rates, such as the probability conservation of the kernel. Here, in the duality based approach, we additionally exploited the functional parameter dependence of the kernel rates to find that minimal set of non-trivially parameter-dependent rates.

4.2.5 | Duality-adapted polarization basis

Given the invariants, we now aim at finding a corresponding cross-related basis from the beginning, before actually having solved the diagonalization problem [Fig. 4.1]. In this basis, the (shifted-) kernel is fully represented by these invariants [Eq. (4.36)]. Self-duality of the invariants then ensures that the corresponding cross-related terms of the kernel (as required by the duality relation (4.2)) are represented by one and the same rate, which enables a most compact representation. For the same reason, it is then advantageous that the corresponding cross-related basis has self-dual pairs of basis-elements as well, as we will explain in the following.

Starting from the duality relation (4.2) for the shifted kernel $V := W + \frac{\gamma_p}{2}\mathcal{I}$, we consider its implications on the matrix elements of any complete spectral decomposition i, j of V:

$$\begin{aligned} V &= -[\mathcal{P}\overline{V}\mathcal{P}]^{\dagger} \\ &= -\sum_{i,j}[\mathcal{P}|\bar{i})\bar{V}_{i,j}(\bar{j}|\mathcal{P}]^{\dagger} \\ &= -\sum_{i,j}\bar{V}^{*}_{i,j}|p\bar{j})(p\bar{i}| = \sum_{i,j}V_{i,j}|i)(j|\,. \end{aligned} \tag{4.37}$$

Eq. (4.37) implies that the matrix elements $V_{i,j}$ of (i,j) and $V_{p\bar{j},p\bar{i}}$ of $(p\bar{j},p\bar{i})$ are related as $V_{p\bar{j},p\bar{i}} = -\bar{V}^{*}_{i,j}$, given that the corresponding elements of the chosen spectral composition $\mathcal{B}$ are duality cross-related, i.e. $\overline{\mathcal{P}|i)}^{\dagger}, \overline{(j|\mathcal{P}}^{\dagger} \in \mathcal{B}$ for any $|i), (j| \in \mathcal{B}$. For self-dual elements of the decomposition $|i)(j| \overset{*}{=} |p\bar{j})(p\bar{i}|$, the corresponding matrix elements are even duality-invariant up to a sign, i.e $V_{i,j} = -\bar{V}^{*}_{i,j}$.

Now, it becomes evident that differently from the energy basis, the $(\mathbb{1}, A, p)$-basis is a suitable choice in terms of obtaining invariant rates. First, let us note that the $(\mathbb{1}|$-vector is a natural choice because any physical density matrix has to obey probability

normalization, the second basis vector $|p)$ following as its cross-related vector. Finally the third basis vector $|A)$ is orthogonal to p and $\mathbb{1}$ and self-dual, $\overline{\mathcal{P}|A)}^{\dagger} = -(A|$. We note that the $(\mathbb{1}, A, p)$-basis has in total three self-dual $(*)$ elements,

$$|\mathbb{1})(p|,\ |p)(\mathbb{1}|,\ |A)(A|\,. \tag{4.38}$$

The corresponding duality-invariant matrix elements read

$$0,\ -\frac{\gamma_C}{2},\ -\frac{\gamma_C}{2}\,, \tag{4.39}$$

as we find by inserting

$$|\tau) = \tfrac{1}{4}\Big[|\mathbb{1}) + |p)\Big] + \tau\tfrac{1}{2}|A), \quad \tau = \pm, \qquad |1) = \tfrac{1}{4}\Big[|\mathbb{1}) - |p)\Big] \tag{4.40}$$

into the energy representation (3.26) of W. The complete decomposition of the shifted kernel is now given by the lower triangular form

$$\begin{aligned} &W + \tfrac{1}{2}\gamma_p\mathcal{I} = \\ &\tfrac{1}{2}\gamma_p\tfrac{1}{4}\Big[|\mathbb{1})(\mathbb{1}| - |p)(p|\Big] - \gamma_C\tfrac{1}{2}\Big[|p)(\mathbb{1}| + |A)(A|\Big] - \gamma_s\tfrac{1}{2}\Big[|p)(A| + |A)(\mathbb{1}|\Big]. \end{aligned} \tag{4.41}$$

We conclude that the matrix elements are indeed determined by the τ-(anti)symmetric rates $\gamma_s, \gamma_C, \gamma_p$ previously introduced in (4.36a), (4.36b) and motivated by the splitting of I_N into partial currents (4.30). Thus, we have reduced the four independent off-diagonal elements of the shifted kernel in the energy basis representation to just three independent rates in the polarization basis with the non-trivial parameter dependence being contained in γ_s, γ_C.

The lower triangular form (4.41) of the shifted kernel facilitates its diagonalization

$$W + \tfrac{1}{2}\gamma_p\mathcal{I} = \tfrac{1}{2}\gamma_p|z)(z'| - \gamma_C|c)(c'| - \tfrac{1}{2}\gamma_p|p)(p'| \tag{4.42}$$

as compared to Sec. 4.2.1, where we started from the energy basis, in the following ways: All eigenvalues, especially γ_C, can be read off from the diagonal of Eq. (4.41). Furthermore, the shifted kernel in its diagonal form is easily obtained from the triangular form by forward (backward) recursion. Like this, the kernel modes and amplitudes are represented in the $(\mathbb{1}, A, p)$-basis and in the duality-invariant rates γ, which will be of central importance in view of further determining the transport observables. Their explicit forms in γ are given in App. B.2, while their representation by local observables, A and p, evaluated in the stationary states in the real and dual systems is already given in Fig. 4.1. Here, we emphasize that the expressions

$$|z) = \tfrac{1}{4}|\mathbb{1}) + \langle A\rangle_z\tfrac{1}{2}|A) + \langle p\rangle_z\tfrac{1}{4}|p)\,, \tag{4.43a}$$

$$(p'| = \tfrac{1}{4}(p| + \langle A\rangle_{\bar{z}}\tfrac{1}{2}(A| + \langle p\rangle_{\bar{z}}\tfrac{1}{4}(\mathbb{1}| \tag{4.43b}$$

follow immediately from the completeness relation (B.13) for the $(\mathbb{1}, A, p)$-basis.

Thus, we managed to express all left and right eigenvectors of the (shifted) kernel in terms of expectation values of two physical observables, parity and polarization. The explicit representation of these stationary observables in terms of the rate variables γ is given in App. B.2 as well.

So far, we have exploited the duality invariance relation (4.2) for the shifted kernel to solve the eigenvector problem. We now shift back to the original kernel of interest,

$$W = \gamma_p \tfrac{1}{4}\Big[|p)(\mathbb{1}| - |p)(p|\Big] - \gamma_c \tfrac{1}{2}\Big[|p)(\mathbb{1}| + |A)(A|\Big] - \gamma_s \tfrac{1}{2}\Big[|p)(A| + |A)(\mathbb{1}|\Big] \tag{4.44}$$

$$= -\gamma_c |c)(c'| - \gamma_p |p)(p'|. \tag{4.45}$$

Here, we furthermore introduce the variables

$$\gamma_c \equiv \gamma_C + \tfrac{1}{2}\gamma_p = \tfrac{1}{2}\sum_{\eta\tau} W^{\eta}_{1,\tau}, \qquad \gamma'_s \equiv \gamma'_S + \tfrac{1}{2}\gamma'_p = \tfrac{1}{2}\sum_{\eta\tau} \eta\tau W^{\eta}_{1,\tau}, \tag{4.46}$$

which obey a shifted duality invariance

$$\gamma_c = \gamma_p - \bar{\gamma}_c, \qquad \gamma'_s = \bar{\gamma}'_s - \bar{\gamma}'_p, \tag{4.47}$$

though they are not strictly invariant under duality. Like this, we obtain the set of variables γ_c, γ'_c, γ_s, γ'_s, which have the nice feature that they are linear combinations of transport rates (anti)symmetrized with respect to η and/or τ, compare (4.46) with (4.36).

4.3 | Physical constraints imposed by fermionic duality

As we have now expressed the time evolution kernel in the polarization basis, both explicitly in terms of the duality-invariant rates (B.15) and in terms of real and dual stationary observables (Fig. 4.1,Eq. 4.43), we will now discuss physical constraints as imposed by the fermionic duality in these representations. They will turn out to further simplify the state and transport evolution to be discussed in Sec. 4.4. In the next Subsec. 4.3.1, we will start with physical constraints imposed on the duality invariants and the stationary state. Afterwards, further constraints imposed on the real and dual stationary observables will be pointed out in terms of a "universal" stationary duality relation.

4.3.1 | Physical constraints on duality invariants and stationary state

Duality invariants. First, we note that the decay rates of the time-dependent state (4.13), the (shifted) duality invariants γ_c and γ_p, are clearly non-negative, as they are proportional to the sums (4.36a) of non-negative transition rates of the master equation. However, their individual non-negativity imposes stronger physical constraints involving the invariant γ_s, which can be negative like γ_c' and γ_s'. These variables are not rates but "rate asymmetries" Eq. (4.36b) which account for various *differences* of the transport rates [electron/hole (η) and state asymmetry (τ)]. The non-negativity of $W_{1,\tau}$ and $W_{\tau,1}$ [Eq. (3.32)] imposes a bound on the negativity of γ_s:

$$\gamma_p \geq 0, \quad \gamma_c, \gamma_p - \gamma_c \geq |\gamma_s|. \tag{4.48}$$

Thus the decay rate γ_c should not only be non-negative but even larger than the magnitude of the rate-asymmetry γ_s. Likewise, the decay rate γ_p should not only exceed the decay rate γ_c, but it must do so by more than the magnitude of γ_s. The latter two conditions are equivalent to one, duality-invariant condition on $\gamma_C = \gamma_c - \gamma_p/2$:

$$|\gamma_C| \;=\; |\gamma_c - \tfrac{1}{2}\gamma_p| \;\leq\; \big|\,|\gamma_s| - \tfrac{1}{2}\gamma_p\,\big|, \tag{4.49}$$

expressing that the sum of transition rates $2\gamma_c = \sum_\tau W_{1,\tau}$ is always closer to γ_p than their difference $2\gamma_s = \sum_\tau \tau W_{1,\tau}$. Interestingly, whether γ_c dominates $\gamma_p/2$ or vice versa is determined by the sign of γ_C which can be either $+$ or $-$ [see Eq. (4.59) below].

Stationary state. By these constraints, we can explicitly verify in the polarization basis that the stationary supervector (4.43a) is a valid physical state for all parameter values of the model: Splitted into two operators with parity $+1$ and -1, the stationary state reads

$$|z) = \Big\{\tfrac{1}{2}\big[1 + \langle p\rangle_z\big]\tfrac{1}{4}\big[|\mathbb{1}) + |p)\big] + \tfrac{1}{2}\langle A\rangle_z|A)\Big\} + \tfrac{1}{2}\big[1 - \langle p\rangle_z\big]\tfrac{1}{4}\big[|\mathbb{1}) - |p)\big]. \tag{4.50}$$

The expectation values (B.19) and the conditions (4.48) then imply

$$0 \leq \tfrac{1}{2}[1 - \langle p\rangle_z] \leq 1, \quad 0 \leq \tfrac{1}{2}[1 + \langle p\rangle_z] \leq 1, \quad |\langle A\rangle_z| \leq \tfrac{1}{2}[1 + \langle p\rangle_z]. \tag{4.51}$$

Hence, the first two conditions ensure that the probabilities $\frac{1}{2}[1 \pm \langle p\rangle_z]$ of being in the parity ± 1 sector lie in the range [0,1]. The third condition ensures that conditional on being in the parity $+1$ sector, the difference of the individual occupations of its states $|\tau)$ cannot become too large: For a valid physical state in the parity $+1$ sector, the length of the (1-dimensional) Bloch vector $\langle A\rangle_z$ should not exceed the radius of the (1-dimensional) Bloch sphere, which equals the total probability $\frac{1}{2}[1 + \langle p\rangle_z]$ of being in

that sector. Applying the duality mapping, we find that the dual quantities of the dual state also obey the corresponding constraints:

$$0 \leq \tfrac{1}{2}[1 - \langle p\rangle_{\bar{z}}] \leq 1, \quad 0 \leq \tfrac{1}{2}[1 + \langle p\rangle_{\bar{z}}] \leq 1, \quad |\langle A\rangle_{\bar{z}}| \leq \tfrac{1}{2}[1 + \langle p\rangle_{\bar{z}}]. \tag{4.52}$$

Thus, the dual and actual stationary vector are simultaneously legitimate states.

4.3.2 | "Universal" stationary duality relation between expectation values

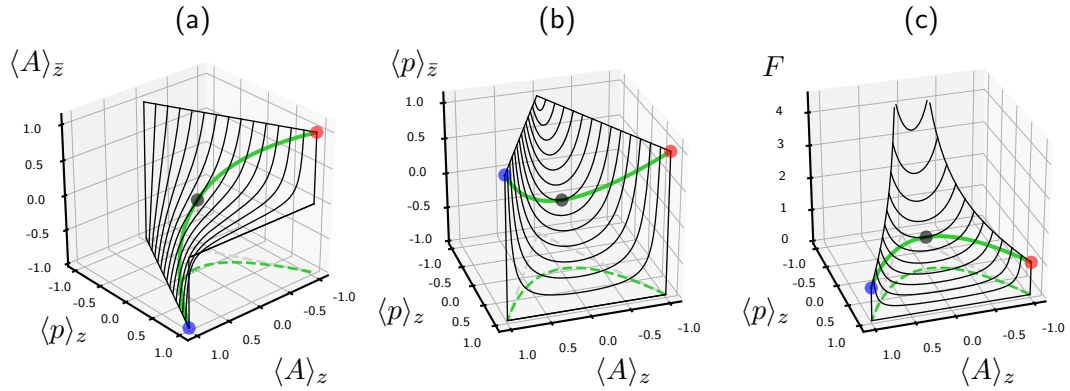

Figure 4.2. (a) Stationary polarization $\langle A\rangle_{\bar{z}}$ and (b) parity $\langle p\rangle_{\bar{z}}$ of the dual system as function of the stationary parity $\langle p\rangle_z$ for various polarizations $\langle A\rangle_z$ of the actual system [Eq. (4.54a)]. (c) Non-linear rescaling factor F as function of $\langle A\rangle_z$ and $\langle p\rangle_z$ [Eq. (4.54b)]. The self-duality condition $F(\langle A\rangle_z, \langle p\rangle_z) = 1$ (green 3D curve) holds along the curve $\langle p\rangle_z = \langle A\rangle_z^2$ (dashed green 2D curve) in the base plane, which includes the pure states $|\pm)$ (blue/red points) and the maximally mixed state (black point). The latter is the only state for which $|\bar{z}) = |z)$. Corresponding values are shown in (a) and (b).

So far, Eqs. (4.51)- (4.52) point out constraints, which separately apply to stationary observables of the real and the dual system. In this subsection, we go one step further and point out relations connecting the stationary observables of these two systems.

We start from the bi-orthogonality of the kernel-eigenvectors, which is already guaranteed by the mere form of their representation in the polarization basis (Fig. 4.1,Eq. 4.43). Only the bi-orthogonality of $(p'|$ and $|z)$ implies a non-trivial relation between pairs of stationary expectation values of the physical system and of the dual system,

$$(p'|z) = \tfrac{1}{4}\big[\langle p\rangle_{\bar{z}} + \langle p\rangle_z\big] + \tfrac{1}{2}\langle A\rangle_z\langle A\rangle_{\bar{z}} = 0. \tag{4.53}$$

This is verified to hold by inserting Eqs. (B.19), but in earlier related work [17], it was overlooked that such an additional constraint can be expected, as the four quantities depend on only three invariants γ_p, γ_C and γ_s.

"Universal" stationary duality. In App. B.2 we derive the result (B.19) that expresses the stationary observables for the system and the dual system in the same set of (shifted-)duality invariants. Going further than (4.53), the dual polarization and parity can therefore be entirely expressed in terms of the corresponding real observables:

$$\langle \bar{A} \rangle_{\bar{z}} = -\langle A \rangle_{\bar{z}} = F\big(\langle A \rangle_z, \langle p \rangle_z\big) \cdot \langle A \rangle_z, \qquad \tfrac{1}{2}\big[1 + \langle p \rangle_{\bar{z}}\big] = F\big(\langle A \rangle_z, \langle p \rangle_z\big) \cdot \tfrac{1}{2}\big[1 + \langle p \rangle_z\big] \tag{4.54a}$$

This stationary duality relation thereby explicitly expresses $|\bar{z})$ in terms of $|z)$ [Eq. 4.43a] by a rational function

$$F\big(\langle A \rangle_z, \langle p \rangle_z\big) \equiv \frac{\frac{1}{2}\big[1 - \langle p \rangle_z\big]}{\frac{1}{2}\big[1 + \langle p \rangle_z\big] - \langle A \rangle_z^2}, \tag{4.54b}$$

which is universal in the following sense: Given only polarization and parity expectation values of the actual system with physical parameters $(\epsilon, U, \alpha, \mu, T, \Gamma)$, it allows to compute these values for the system with dual physical parameters $(-\epsilon, -U, -\alpha, -\mu, T, \Gamma)$, without requiring any reference to these parameters. We plot in Fig. 4.2(a-b) the (components of the) dual stationary state as a *non-linear* function of the (components of the) stationary state of the actual system. In Fig. 4.2(c) we plot the scaling factor (4.54b) which takes non-negative values on the domain (4.51) of physically allowed values, since there $\frac{1}{2}[1 + \langle p \rangle_z] \geq |\langle A \rangle_z| \geq \langle A \rangle_z^2$. F can be arbitrarily large (even diverging at $\langle p \rangle_z = -1$ and $\langle A \rangle_z = 0$), while always producing legitimate values $\langle p \rangle_{\bar{z}}, \langle A \rangle_{\bar{z}} \in [-1, 1]$. This is possible due to the non-linearity of the duality relation (4.54), i.e., the dependence of F on $\langle A \rangle_z$ and $\langle p \rangle_z$.

Detailed balance. We point out that the stationary duality (4.54) can be alternatively derived based on detailed balance and fermionic duality for our master equation [49], rather than starting from the representation of parity and polarization in the same set of (shifted-) duality invariant rate variables (B.19).

Detailed balance presupposes that the system assumes a unique stationary state with strictly positive probabilities $P_i > 0$ and furthermore that Kolmogorov's criterion is fulfilled. The first criterion corresponds to a positively recurrent system, i.e. all pairs of states i, j are connected by a sequence of transitions $i_1 \to i_2$ with strictly positive couplings $W_{i_2,i_1} > 0$. This criterion holds as the temperature is nonzero in our limit and

the tunneling rates $\Gamma_\pm > 0$. The second criterion states that for any sequence of states on a closed loop in a graphical representation, the product of transition rates should be equal in both directions and is also fulfilled in our system. Hence, our system obeys the detailed balance relation $P_i/P_j = W_{ij}/W_{ji}$ for the stationary probabilities.

Based on the above two criteria, it is then obvious that the dual system fulfills detailed balance as well and a stationary duality relation can be derived between the stationary probabilities P_i of the real and $\bar{P}_i$ of the dual system[49],

$$\bar{P}_i = \frac{P_i^{-1}}{\sum_k P_k^{-1}}. \tag{4.55}$$

Here, the sum includes all energy states separately counting degenerate states. We give the alternative derivation of our stationary duality (4.54) based on an adapted form of Eq. (4.55) in App. E. The result (4.54) nicely connects to our earlier result that the stationary state for the actual system $|z)$ and the dual system $|\bar{z})$ are simultaneously legitimate states: conditions (4.51) and (4.52) are equivalent since the factor F drops out in $|\langle A\rangle_z|/[\frac{1}{2}[1+\langle p\rangle_z]] = |\langle A\rangle_{\bar{z}}|/[\frac{1}{2}[1+\langle p\rangle_{\bar{z}}]] \leq 1$. Hence,the duality mapping between stationary states preserves the magnitude of the (1-dimensional) Bloch vector relative to the (1-dimensional) Bloch sphere in the parity $+1$ sector.

Self-duality of stationary observables. Relation (4.54) also highlights the special situation of self-duality of stationary observables drawn in green in Fig. 4.2. By self-duality, we here mean

$$\langle \bar{A}\rangle_{\bar{z}} = -\langle A_{\bar{z}}\rangle = \langle A\rangle_z, \qquad \langle p\rangle_{\bar{z}} = \langle p\rangle_z. \tag{4.56}$$

In this case the dual stationary state $|\bar{z})$ and actual one, $|z)$ [Fig. 4.1], differ, but only by inverting the polarization vector, leaving its component invariant. The definition (4.56) of self-duality is justified, as the duality mapping inverts the energy spectrum, swapping the Andreev states $\overline{|\tau)} = |-\tau)$ and thus inverting the polarization of their occupations. Self-duality is equivalent to $F(\langle A\rangle_z, \langle p\rangle_z) = 1$, which by Eq. (4.54b) corresponds to having parity uniquely fixed by polarization in the stationary actual system and likewise in the dual system:

$$\langle p\rangle_z = \langle A\rangle_z^2, \qquad \langle p\rangle_{\bar{z}} = \langle A\rangle_{\bar{z}}^2. \tag{4.57}$$

One verifies[7] that this condition is equivalent to self-duality of the charge decay rate, $\bar{\gamma}_c \equiv \gamma_p - \gamma_c = \gamma_c$, which is satisfied if and only if

$$\gamma_c = \tfrac{1}{2}\gamma_p, \tag{4.58}$$

or $\gamma_C \equiv \gamma_c - \gamma_p/2 = 0$.

Self-duality and infinite temperature. For $T \to \infty$, self-duality is even satisfied for all values of the remaining parameters, including U. More interestingly, at any finite T for $U = 0$, it always holds as we verify in App. F.1. We find the following general relations:

$$\gamma_c > \tfrac{1}{2}\gamma_p \Leftrightarrow U > 0, \qquad \gamma_c = \tfrac{1}{2}\gamma_p \Leftrightarrow U = 0, \qquad \gamma_c < \tfrac{1}{2}\gamma_p \Leftrightarrow U < 0 \tag{4.59}$$

Thus, zero interaction is equivalent to requiring exact self-duality (4.56) for all values of the remaining parameters. Approximate self-duality $\gamma_c \approx \frac{1}{2}\gamma_p$, however, can be obtained asymptotically, by rendering the interaction ineffective. This can be achieved by making one energy scale dominate, e.g., large bias voltage $|\mu|$, strong pairing $|\alpha|$, large detuning $|\delta|$, or high temperature T, see App. F.2.

Self-duality and negative parity. A system that is self-dual in the above sense ($U = 0$) necessarily has non-negative stationary parity $\langle p\rangle_z \geq 0$ [Eq. (4.57)] for any value of the remaining parameters as seen in Fig. 4.2. Strictly negative parity for some parameters thus requires nonzero magnitude of the interaction, $U \neq 0$. Such a violation of self-duality furthermore corresponds to a nonzero value of the $(+)$ invariant $\gamma_C = \gamma_c - \gamma_p/2$ [Eq. (4.59), cf. (4.49)] with the same sign as the interaction U.

Self-duality and invariance of the stationary state. As mentioned, self-duality (4.56) should not be confused with equality of the actual and dual stationary state, $|\bar{z}) = |z)$. The latter is a stronger condition and occurs when $\langle A\rangle_{\bar{z}} = \langle A\rangle_z$ and $\langle p\rangle_{\bar{z}} = \langle p\rangle_z$. This relation is satisfied only[8] for $\langle A\rangle_z = \langle p\rangle_z = 0$ implying $F = 1$. It is thus a special case of self-duality indicated by a black dot in Fig. 4.2, for which the stationary state is maximally mixed, $|z) = \frac{1}{4}|\mathbb{1})$, i.e., with uniform occupation of Andreev states ($z_\tau = 1/4$) and spin states ($z_1 = 1/2$, including spin-degeneracy). In addition to $\gamma_c = \gamma_p/2$ required by self-duality, invariance of the stationary state requires a vanishing transition-rate asymmetry,

[7] Inserting Eq. (B.19) into Eq. (4.57) gives two solutions: $\gamma_c = \gamma_p/2$ and $|\gamma_s| = \gamma_c$. For the latter case the physical bound $|\gamma_s| \leq \gamma_p - \gamma_c$ [Eq. (4.48)] implies $\gamma_p/2 \geq \gamma_c$. Noting the bounds (4.59) we find that for $U \geq 0$ the lower-bound $\gamma_p/2 \leq \gamma_c$ implies $\gamma_p/2 = \gamma_c$, i.e., the second solution is a special case of the first one, whereas for $U < 0$ the strict upper-bound $\gamma_p/2 > \gamma_c$ rules it out.

[8] $\langle A\rangle_{\bar{z}} = \langle A\rangle_z$ in Eq. (4.54) implies $\langle A\rangle_{\bar{z}} = \langle A\rangle_z = 0$, since $F \geq 0$ and by Eq. (4.54b), $F = [1 - \langle p\rangle_z]/[1 + \langle p\rangle_z]$. Requiring $\langle p\rangle_{\bar{z}} = \langle p\rangle_z$ by Eq. (4.54) gives $[1 + \langle p\rangle_{\bar{z}}]/2 = [1 + \langle p\rangle_z]/2 = [1 - \langle p\rangle_z]/2$, so $\langle p\rangle_z = 0$.

$\gamma_s = 0$ [Eq. (B.19a)]. The latter condition is a relevant one for our parameter space of interest[9]. , and holds trivially in the limit $T \to \infty$ for all parameters. Unlike self-duality, at $U = 0$, the condition $\gamma_s = 0$ does not hold for all remaining parameters.

4.4 | Transient transport

In the previous section we derived the time evolution kernel in the duality-adapted polarization basis and pointed to physical constraints imposed by fermionic duality. Now the state evolution and transport currents can be easily obtained in a rather compact form. We will start with the state evolution in Subsec. 4.4.1. Afterwards, charge-and energy/heat current observables will be given in the polarization basis in Subsecs. 4.4.2-4.4.3. Finally, at the end of each subsection, the implications of self-duality on the transient evolution of the state/observable under consideration will be discussed.

4.4.1 | State evolution

Duality-adapted solution. In Sec. 4.2.1, the time-evolving state was expressed in the kernel eigenbasis (4.13). Using the representation (4.43) of p' in the polarization basis and the constraint (4.53) imposed by its orthogonality to the stationary state, we obtain the final result for the state

$$|\rho(t)) = |z) + e^{-\gamma_c t}(c'|\rho_0)|c) + e^{-\gamma_p t}(p\bar{z}|\rho_0)|p) \tag{4.60}$$

$$= \{\tfrac{1}{4}|\mathbb{1}) + \langle A\rangle_z \tfrac{1}{2}|A) + \langle p\rangle_z \tfrac{1}{4}|p)\} + \tfrac{1}{2}\Big[|A) - \langle A\rangle_{\bar{z}}|p)\Big] e^{-\gamma_c t}\big[\langle A\rangle_{\rho_0} - \langle A\rangle_z\big]$$
$$+ |p) e^{-\gamma_p t}\Big\{\tfrac{1}{4}\big[\langle p\rangle_{\rho_0} - \langle p\rangle_z\big] + \tfrac{1}{2}\langle A\rangle_{\bar{z}}\big[\langle A\rangle_{\rho_0} - \langle A\rangle_z\big]\Big\}. \tag{4.61}$$

This solution applies to any initial state $|\rho_0)$ that is diagonal in the energy basis at final parameters x. The initial state, if diagonal in the initial energy basis as well, can be specified by its expectation values of the polarization $\langle A_0\rangle_{\rho_0}$ and parity $\langle p\rangle_{\rho_0}$. These are subject to the constraint (4.48), $|\langle p\rangle_{\rho_0}| \leq 1$ and $|\langle A_0\rangle_{\rho_0}| \leq \frac{1}{2}[1 + \langle p\rangle_{\rho_0}]$, thus guaranteeing that the state is physical. By A_0, we indicate the dependence of polarization on the initial, in general different parameters x_0, see Sec. 5.1 for a more detailed discussion of the initial state.

In the duality-based solution (4.61), the state-evolution is entirely expressed in terms of stationary expectation values of the appropriate observables p and A, in particular the amplitudes of the transient decay with rates γ_c and γ_p. These amplitudes are expressed

[9] In particular, note that $\gamma_s = 0$ can hold at the often discussed "symmetry point" $\delta = 0$ ($\epsilon = -\frac{1}{2}U$) even when $U \neq 0$.

as the difference between initial and stationary value of A and p, their "initial excess". The entire intermediate state evolution can thus be understood from the initial and stationary values of A and p as well as the polarization of the dual stationary state, which only enters if there is initial polarization excess. This result is thus complementary to a generalized Bloch expansion of the time-evolving quantum state: In such an expansion, the time-dependent state would be expressed in a set of fixed observables with their time-dependent averages in that state as coefficients [Ref. [16]]. Eq. (4.61) is thus more than a rewriting of the expression for $|\rho(t))$ given in Ref. [16], see Eq. (20-25) of that work for the special case of zero transverse Bloch vector ($I_x = I_y = 0$).

As an alternative to evaluating dual stationary observables, one can substitute the stationary duality relation (4.54a) into Eq. (4.61), which enables an expression of the time-dependent state in terms of stationary expectation values of A and p of the real system alone. Thus, apart from the decay rates, the evolution towards the stationary state can be understood in detail by the stationary state itself at the expense of its non-linear dependence on the stationary state (4.54b). This non-linearity can be avoided using the representation in terms of dual stationary observables instead.

Self-duality and transient evolution. The state and transport evolutions simplify considerably when the system obeys self-duality (4.56), i.e., $\gamma_c = \frac{1}{2}\gamma_p$ [Eq. (4.58)]. As discussed in Sec. 4.3.2, self-duality can either hold exactly for all applied voltages for $U = 0$ or asymptotically (e.g., $\mu \to \infty$). We can then generically simplify the stationary state (4.50) by eliminating parity in favour of polarization [Eq. (4.57)]:

$$|z) = \tfrac{1}{4}|\mathbb{1}) + \langle A\rangle_z \tfrac{1}{2}|A) + \langle A\rangle_z^2 \tfrac{1}{4}|p) = \sum_\tau |\tau) \tfrac{1}{4}\left[1 + \tau\langle A\rangle_z\right]^2 + |1) \tfrac{1}{2}\left[1 - \langle A\rangle_z^2\right]. \quad (4.62)$$

If the initial state obeys self-duality as well, (such a condition applies by the above assumptions e.g. to an initial state prepared from a stationary state z_0 of the system at some different gate voltage δ_0 [Sec. 5.1]), the evolving state (4.61) further simplifies. As the initial state then fulfills $\langle p\rangle_{\rho_0} \neq \langle A_0\rangle_{\rho_0}^2$, all decay amplitudes of the state are fixed by the stationary and initial polarization:

$$\begin{aligned}|\rho(t)) =& \tfrac{1}{4}|\mathbb{1}) + \langle A\rangle_z \tfrac{1}{2}|A) + \langle A\rangle_z^2 \tfrac{1}{4}|p) + \tfrac{1}{2}\left[|A) + \langle A\rangle_z|p)\right] e^{-\frac{1}{2}\gamma_p t}\left[\theta\langle A_0\rangle_{z_0} - \langle A\rangle_z\right] \\ &+ |p) e^{-\gamma_p t}\left\{\tfrac{1}{4}\langle A_0\rangle_{z_0}^2 + \tfrac{1}{4}\langle A\rangle_z^2 - \tfrac{1}{2}\theta\langle A\rangle_z\langle A_0\rangle_{z_0}\right\}. \quad (4.63)\end{aligned}$$

Here, we used $\langle A\rangle_{\rho_0} = \theta\langle A_0\rangle_{z_0}$, where $\theta \in [-1, 1]$ captures details of the initialization [Sec: 5.1]. The coefficient of the parity contribution can be verified to be non-negative in this case.

4.4.2 | Charge current

Transient charge current. In our duality-adapted approach, an expression of the charge current in terms of a maximum number of stationary observables and a minimum number of (transient) transport rates can be easily obtained. We find a most compact form of the current supervector by first transforming Eq. (4.18) into the polarization basis and only afterwards to the left kernel eigenbasis,

$$(I_N| = \sum_{\eta\tau} \eta \left[W^{\eta}_{1,\tau}(\tau| + 2W^{\eta}_{\tau,1}(1| \right] \overset{\text{Eq. (4.40)}}{=} \gamma'_c(\mathbb{1}| + \gamma'_s(A| \tag{4.64a}$$

$$\overset{\text{Fig. 4.1}}{=} \left[\gamma'_c + \gamma'_s\langle A\rangle_z\right](z'| + \gamma'_s(c'|. \tag{4.64b}$$

As anticipated, we thus profited from duality not only for the state evolution, but also for a duality-adapted formulation of the transport rates: The current supervector as represented in the duality-adapted polarization basis [Sec: 4.2.5] leads to its expression in terms of duality-invariant (primed) transport rates γ'_c, γ'_s. The prime indicates that they are η-antisymmetric und thus sensitive to the electron transfer direction η.

The charge current follows by taking the scalar product of the state (4.61) with the corresponding left current supervectors [Eqs. (4.64b) and (4.79)] and using bi-orthonormality of the eigen-supervectors:

$$I_N(t) = (I_N|\rho(t)) = (I_N|z) + (I_N|c)e^{-\gamma_c t}(c'|\rho_0) + (I_N|p)e^{-\gamma_p t}(p'|\rho_0) \tag{4.65}$$

$$= (I_N|z) + ae^{-\gamma_c t} \tag{4.66}$$

$$= \left(\gamma'_c + \gamma'_s\langle A\rangle_z\right) + \gamma'_s e^{-\gamma_c t}\left[\langle A\rangle_{\rho_0} - \langle A\rangle_z\right]. \tag{4.67}$$

According to (4.65), each term $y = z, c, p$ contributing to a transport quantity $I_x(t)$ (here I_N) on time-scale γ_y^{-1} depends on two factors $(I_x|y)$ and $(y'|\rho_0)$. The first factor quantifies the ability of quantity x to "probe" the y-part of the state evolution, the second one captures the initial-state dependence of the latter. The charge current (4.67) does not probe the parity decay, $(I_N|p) = 0$, and thus –by duality– depends on the physical parameters only through the stationary state of the actual system, in particular, through the value of the polarization observable $\langle A\rangle_z$.

Stationary charge current. In view of efficiently extracting the behavior of the stationary charge current, we further decompose the (shifted-) duality invariant rates (4.36) into components,

$$\gamma_C = \kappa_C + \frac{\delta}{\delta_A}\kappa'_s, \quad \gamma_c = \kappa_c + \frac{\delta}{\delta_A}\kappa'_s, \quad \gamma'_c = \kappa'_c + \frac{\delta}{\delta_A}\kappa_s, \tag{4.68a}$$

$$\gamma_s = \kappa_s + \frac{\delta}{\delta_A}\kappa'_c, \quad \gamma'_s = \kappa'_s + \frac{\delta}{\delta_A}\kappa_c, \quad \gamma'_S = \kappa'_s + \frac{\delta}{\delta_A}\kappa_C. \tag{4.68b}$$

In the same way as the γ- rates are (shifted-) duality invariants, so are the κ-components, composed of sums of Fermi functions, (anti-) symmetric in η or τ or both, like the corresponding γ-rates. However, the contributions from the two summands in $\Gamma_\pm = \gamma_p(1 \pm \delta/\delta_\mathrm{A})/2$ entering the γ-rates are now split and their explicit δ-dependence is extracted.

The components thus have the advantage that they strictly separate all resonant behaviour of the superconductor (explicit δ dependence relative to $\mu_\mathrm{S} = 0$ through $\Gamma_{\eta\tau}$) from the superconductor's indirect effect via the Andreev levels (implicit δ dependence relative to μ through $f^{-\eta}(E_{\eta,\tau})$). By doing so, the decomposition (4.68) shows that the pairs of duality invariants γ_c, γ_s' and γ_c', γ_s, respectively, which play distinct physical roles, actually similarly behave since they depend on the same components which can mix up and cancel out when simplifying final expressions at the price of losing the physical distinction. This is nicely illustrated for the expression for the stationary charge current $I_N(\infty) = \gamma_c' + \gamma_s'\langle A\rangle_z$ given by the first term in Eq. (4.67):

$$I_N(\infty) = \frac{\gamma_c'\gamma_c - \gamma_s'\gamma_s}{\gamma_c} = \frac{\kappa_c\kappa_c' - \kappa_s\kappa_s'}{\kappa_c + \frac{\delta}{\delta_A}\kappa_s'}\left(1 - \frac{\delta^2}{\delta_A^2}\right). \tag{4.69}$$

We automatically extract a resonant Lorentzian δ-dependence reflecting the non-equilibrium charge transport to the superconductor, while its non-trivial modification by the Andreev states is contained in the pre-factor governed by the components of the invariants.

Self-duality and $I_N(\infty)$. The stationary charge current further simplifies if self-dualtiy is fulfilled: Whenever there is stationary transport, $\alpha \neq 0$, self-duality $\gamma_c = \gamma_p/2$ is equivalent to having a constant component, $\kappa_c = \gamma_p/2$, and a vanishing one, $\kappa_s' = 0$ [Eq. (4.36), (4.68)]. The stationary current (4.69) is then modulated by just one component:

$$I_N(\infty) = \gamma_c' + \gamma_s'\langle A\rangle_z = \kappa_c' \times \left(1 - \frac{\delta^2}{\delta_A^2}\right). \tag{4.70}$$

For the case of a non-interacting quantum dot ($U = 0$), thus obeying exact self-duality, we obtain

$$I_N(\infty) = \gamma_c' + \gamma_s'\langle A\rangle_z = \tfrac{1}{2}\gamma_p\tfrac{1}{2}\sum_{\lambda\eta}\eta f^{-\eta}(\tfrac{1}{2}\lambda\delta_\mathrm{A} - \mu) \times \left(1 - \frac{\delta^2}{\delta_A^2}\right), \tag{4.71}$$

see App. G.2 for the derivation. If self-duality is fulfilled asymptotically, $\mu \gg |\alpha|, U, |\delta|, T, \Gamma$, Eq.(4.70) reads

$$I_N(\infty) = \gamma_c' + \gamma_s'\langle A\rangle_z \overset{|\mu|\to\infty}{=} \tfrac{1}{2}\gamma_p \tanh\left(\frac{\mu}{2T}\right) \times \left(1 - \frac{\delta^2}{\delta_A^2}\right), \tag{4.72}$$

see also App. G.3 for the derivation.

4.4.3 | Energy and heat currents

Differently from the charge current, the energy current into the metal can be derived from the energy loss of the proximized dot, as the Cooper pair condensate does not contribute to the energy of the proximized quantum dot, whereas it does contribute to its charge:

$$I_E(t) = -\partial_t \langle H_\mathrm{D}\rangle(t) = -(H_\mathrm{D}|W|\rho(t))\,. \tag{4.73}$$

In the energy basis representation of $(H_D|$ and $|W\rho)$, we find

$$I_E(t) \overset{(4.76a),\,(3.27)}{=} -\sum_{\tau=\pm}\Big[[E_1-E_\tau]W_{1,\tau}\rho_\tau(t) + [E_\tau - E_1]W_{\tau,1}\rho_1(t)\Big] \tag{4.74}$$

$$\overset{(3.28)}{=} -\sum_{\tau=\pm} E_{-,\tau}\Big[W_{1,\tau}(\tau| - 2W_{\tau,1}(1|\Big]|\rho(t)) = (I_E|\rho(t)). \tag{4.75}$$

Eq. (4.74) gives the well-known representation of I_E in terms of probabilities $\times$ transition rates $\times$ addition energies $E_{\eta,\tau}$. As we will explain in Chap. 5, this is the most convenient representation for any further analysis, if only one amplitude of the state evolution (4.60), the charge amplitude, contributes to the transient energy transport due to the specific choice of the initial state.

In its most general form, however, the energy current probes both the charge-and parity amplitudes of the transient decay (4.60). In this case, the representation in the polarization basis is more convenient [Chap. 5]. We first expand the energy supervector in all three bases,

$$(H_D| = 2E_1(1| + \sum_\tau E_\tau(\tau| \tag{4.76a}$$

$$\overset{(4.40)}{=} \tfrac{1}{2}\delta_\mathrm{A}(A| + \tfrac{1}{4}U(p| + \big[\ldots\big](\mathbb{1}| \tag{4.76b}$$

$$\overset{(3.8)}{=} \tfrac{1}{2}\big(\delta_\mathrm{A} - U\langle A\rangle_{\bar z}\big)(c'| + U(p'| + \big[\ldots\big](z'|. \tag{4.76c}$$

Here, the polarization basis reveals that energy couples to the interaction U via parity. As $(z'|W = 0$, we find

$$(I_E| = \tfrac{1}{2}\big(\delta_\mathrm{A} - U\langle A\rangle_{\bar z}\big)\gamma_c(c'| + U\gamma_p(p'| \tag{4.77}$$

for the energy current supervector. The supervector for the heat current, which measures the energy transported by charge carriers relative to the chemical potential, reads

$$(I_Q| = (I_E| - \mu(I_N| \tag{4.78}$$

$$= -\mu\Big[\gamma_c' + \gamma_s'\langle A\rangle_z\Big](z'| + \Big[\tfrac{1}{2}\big(\delta_\mathrm{A} - U\langle A\rangle_{\bar z}\big)\gamma_c - \mu\gamma_s'\Big](c'| + U\gamma_p(p'|. \tag{4.79}$$

As a key result, we find the energy/heat-currents

$$I_Q(t) = -\mu I_N(t) + a_c e^{-\gamma_c t} + a_p e^{-\gamma_p t} \tag{4.80a}$$

$$= -\mu\{\gamma_c' + \gamma_s'\langle A\rangle_z\} + \left\{\tfrac{1}{2}(\delta_A - U\langle A\rangle_{\bar{z}})\gamma_c - \mu\gamma_s'\right\}e^{-\gamma_c t}\left[\langle A\rangle_{\rho_0} - \langle A\rangle_z\right] + U\gamma_p e^{-\gamma_p t}\left\{\tfrac{1}{4}\left[\langle p\rangle_{\rho_0} - \langle p\rangle_z\right] + \tfrac{1}{2}\langle A\rangle_{\bar{z}}\left[\langle A\rangle_{\rho_0} - \langle A\rangle_z\right]\right\}, \tag{4.80b}$$

where a_c denotes the charge and a_p denotes the parity amplitude. The energy current is given by setting $\mu = 0$. As for the time-evolving state (4.61), we have written the parity amplitude in terms of the initial excess of parity and polarization (4.80b). Another useful form for the later analysis in Chap. 5 is given by the overlap of the actual initial and dual stationary state,

$$a_p = U\gamma_p(\bar{z}p|\rho_0)e^{-\gamma_p t}. \tag{4.81}$$

In contrast to the (transient) charge current, the dual stationary state matters for the transient energy/heat-currents. As discussed in the previous Secs. 4.3.2, 4.4.1, this dependence can ultimately written in merely real stationary observables $\langle A\rangle_z$ and $\langle p_z\rangle$[Eq. (4.54a)], but only at the price of a non-linear dependence.

Self-duality. If self-duality is fulfilled, however, the real polarization is the only remaining observable, while the parity amplitude vanishes:

$$I_Q(t) = -\mu\{\gamma_c' + \gamma_s'\langle A\rangle_z\} + \{\tfrac{1}{2}\delta_A\gamma_c - \mu\gamma_s'\}e^{-\frac{1}{2}\gamma_p t}\left[\theta\langle A_0\rangle_{z_0} - \langle A\rangle_z\right]. \tag{4.82}$$

Note, that in the case of asymptotic self-duality with large μ, $\frac{1}{2}\delta_A\gamma_c$ must also be dropped.

Transport currents in the $\alpha = 0$ limit. As mentioned earlier [Sec. 3.3], our solution of the transport problem is discontinuously connected to the case $\alpha = 0$, as we cannot simply send $\alpha \to 0$ within the range of applicability of the master equation (3.27). However, for $\Gamma \ll |\alpha| \ll T$, temperature fluctuations eradicate every effect of the pairing except for a gate voltage regime around the resonance with the superconductor, $|\delta| \lesssim |\alpha|$, which becomes vanishing small as $\alpha \to 0$. For a more detailed discussion of the transport problem in this limit, referring to simplifications in the duality-invariant formulation, see App. G.1. Furthermore, the behavior of our expressions in the $\alpha = 0$-limit will be discussed in more detail in the next Chap. 5, especially when studying the modifications in heat transport, caused by the presence of the superconductor as compared to the normal conducting case previously studied in Ref. [17].

4.5 | Conclusions and Outlook

In this chaper, we derived the full time-dependent solution (4.61)-(4.80b) of the dynamics of a quantum dot proximized by a superconductor and weakly probed by charge- and heat currents into a normal-metal contact. Here, we demonstrated how the fermionic duality can be fully exploited from the very first step of setting up the time-evolution and the current equations. Starting from the energy basis, the whole transport problem can be covered by a set of six rates, whose functional structure is highly constraint and governed by duality invariance. The construction of these duality-invariant rates is motivated by a transient displacement current into the quantum dot. Unlike ordinary symmetry, the dissipative symmetry fermionic duality aids the construction of a corresponding duality-adapted orthogonal Liouville-space basis, in which the shifted kernel $W + \frac{\gamma_p}{2}\mathcal{I}$ is represented by just three of these rates. The duality-adapted basis is optimal for finding the distinct left and right eigenvectors of the time-evolution kernel W.

For the general case we have shown that the transient approach to the stationary state can most conveniently be understood from four of these duality-invariant rates and from expectation values of two duality-adapted observables in the initial and stationary state of the system, polarization and parity. By mere inspection of transition-rate expressions this was not obvious at all. However, this result directly emerged from a calculation in the duality-adapted basis: The solution is expressed as a function of the stationary expectation values of parity and polarization for the actual system as well as for its dual system with inverted energies. These two stationary values provide the key to an exhaustive analysis of the solution.

The obtained compact expressions capture a variety of effects when interaction and induced pairing compete, warranting a separate analysis, which will be the subject of the next chapter. In this chapter, we instead analytically investigated our all-encompassing solution and also discussed several covered limiting cases ($\alpha = 0$, $U = 0$, or $|\mu| \to \infty$) which may prove useful for comparison with other approaches.

Going beyond the prior work [17] for an ND-system, we here have shown that the duality-based analysis in terms of duality-invariant rates does not only apply to the time-evolving state, but can be extended to the measurable time-dependent transport quantities, when duality-invariant parts of the transport rates are included as well in the analysis. Likewise, extending other prior work [49], we combined duality with the detailed-balance property of this system [77, 78]. We have shown that the stationary values of observables in the actual model in fact determine their values of the dual model by a stationary duality relation [Eq. (4.54)]. This relation is "universal" in the sense of being independent of the values of all physical parameters: temperature T,

coupling Γ, voltage μ, but also the –attractive or repulsive– interaction U and induced superconducting pairing α.

The so-called universal stationary duality relation naturally suggested a notion of self-duality of parity and polarization. We have shown that this relation occurs essentially whenever the interaction is irrelevant, either explicitly zero or made ineffective asymptotically. When the interaction is relevant, however, self-duality is violated but duality remains valid and is intimately linked with interactions within the open system. In particular, we have pointed out that the sign of the interaction U (repulsive/attractive) equals the sign of one of the duality invariants (γ_C), irrespective of the induced superconducting pairing α.

Thus, we have illustrated that fermionic duality is a powerful tool for advancing the quantitative understanding not only of the decay rates / time-scales of electronic open quantum systems, but also of the amplitudes which decide their (ir)relevance depending on the initial state. It is an intriguing open question how to systematically extend our work to even more complicated transport models (with orbital and spin splittings) within the broad class governed by weak-coupling fermionic duality.

So far, we have only used fermionic duality as a tool to simplify the procedure of solution and analysis of a given quantum master equation, previously also derived in Ref. [15] for the infinite-gap limit. As a further step one can express duality already on the level of the derivation of the master equation, in particular, allowing for strong coupling effects to the normal reservoirs: such a derivation in Ref. [17] in fact applies to any parity conserving Hamiltonian which includes pairing terms describing infinite gap superconductors.

A key remaining open question therefore is as to whether a more general duality relation can be found for a finite superconducting gap described by the approaches of Ref. [79] or [74]. The continued interest in (time-)controlled proximized nanoelectronic systems [64, 65, 80–82] provides a strong experimental impetus for such work.

5

Controlling transport currents in an NDS-device

This chapter is devoted to a detailed analysis of the full time dependence of the solution of our transport problem addressing both the decay rates and the amplitudes in dependence of the initial state and the observables of interest. We will study the time-dependent response of the SQD-system to a switch in the gate voltage. Such a response is interesting from the perspective of transport spectroscopy, as especially the heat current reveals information on the interplay of the different types of interaction, effective Coulomb interaction and pairing that are not accessible from the stationary state alone. In particular, the amplitude functions of the dynamics control the non-trivial competition of the various time-scales. These amplitudes decide the actual time scale on which a system responds: a slow decay term may well have a negligible amplitude depending on the gate voltages of the switching procedure and other control parameters. A complete analysis of both the time-scales and the amplitudes of the transient decay will be of central importance for controlling the transport currents in view of possible applications.

We consider two distinct physical preparation procedures and map out the full time-dependence of charge and heat currents based on the analytical solution developed in the previous Chap. 4. Section 5.1 is devoted to introduce the state initialization, performed by a slow and a fast switch in gate voltage. The initialization requires special attention as compared to the voltage switch considered in the prior work [17] for an ND-system, as in a quantum dot proximized with superconductivity, the even parity eigenstates are gate-voltage dependent. This fact actually motivates the complementary switching procedures.

In Sec. 5.2.1, we specify different transport regimes in our four dimensional parameter space and given an overview of the behavior of the relevant quantities which fully

characterize the transport problem [Chap. 4], the four duality invariants and two observables, parity and polarization, evaluated in the stationary state of the real and dual systems.

In Sec. 5.3, we characterize the non-monotonicity of the transient heat and energy-currents by a single parameter. Non-monotonicity is induced in these currents, as there are two competing time scales. The different non-monotonic behavior differ by the number and type of local extrema and the way the currents saturate to their stationary values.

In Sec. 5.4, we analyze the amplitudes of the transient transport observables, charge and heat currents, by detailed spectroscopy predictions. As we will see, it is possible to analyze the corresponding spectroscopy plots in a systematic way by considering the overview of zero-temperature energy thresholds for transport and the associated particle transfers developed in Sec. 3.4. This way, the real and dual stationary states will be efficiently extracted for any value in the four-dimensional parameter space and as explained in the previous Chap. 3, these stationary states crucially determine the transient dynamics of the problem. Instead of searching for interesting features by scanning a four-dimensional parameter space, this analysis will allow us to project on characteristic changes in the observables of interest. In this sense, we will provide a kind of classification of the transport problem. Sec. 5.5 gives the conclusions and an outlook.

5.1 | State initialization

To analyze the time-dependent transport resulting from a physical initialization procedure we discuss in the following how an initial energy mixture, described by a density operator denoted ρ_0, can be prepared by controlling experimental parameters. This issue was left open in Chap. 4, where we assumed any given diagonal ρ_0. Red (blue) color indicates the charge current is directed into (out of) the metal, respectively.

5.1.1 | Gate switch in presence or absence of the superconductor

We focus on the experimentally relevant situation where the initial state is prepared by switching a gate. Therefore we consider possible extensions of the simple scenario analyzed in Ref. [17] where an interacting quantum dot was probed using time-dependent observables in the metal after a sudden change $\epsilon_0 \to \epsilon$. It is assumed that before this switch the dot has already decayed to its stationary mixed state denoted z_0. Then after switching to ϵ the dot decays to its new stationary mixed state denoted by z. Throughout the thesis, we will refer to quantities at the initial value before the switch, namely at ϵ_0

by a 0 subscript compared to the respective quantity at the final value ϵ after the switch. As a result of this simple procedure, in the absence of the superconductor ($\alpha = 0$) the

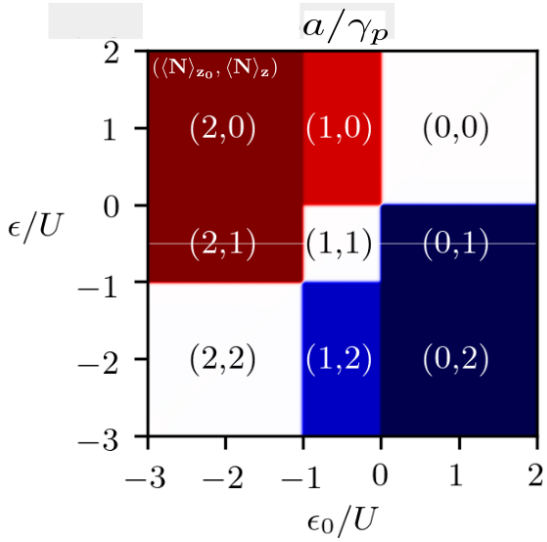

FIGURE 5.1. Gate-switch spectroscopy of a QD without superconductor ($\alpha = 0$), attached to a normal metal (ND-device): Color-coded amplitude of the transient charge current $[(a/\gamma_p)(\epsilon_0, \epsilon)]$, Eq. (4.66)], as a function of initial and final gate-voltages ϵ_0, ϵ before and after the switch, respectively. Dark/light-red (dark/light-blue) color indicates the current is directed into (out of) the metal. Possible integer charge values $(\langle N \rangle_{z_0}, \langle N \rangle_z)$ in the initial and final stationary states z_0 and z before and after the switch, respectively, are indicated in the corresponding regions of the plot. For further explanation see the main text.

predictions for physical quantities for all possible gate voltage switches can be analyzed using a single gate-switch spectroscopy plot shown in Fig. 5.1a for the transient charge current. This is a very convenient way of presenting such time-dependent experiments. Up to thermal smearing nine basic switches are possible since depending on ϵ_0 or ϵ, respectively, the stationary dot state has $\langle N \rangle_{z_0}$ or $\langle N \rangle_z = 0, 1$ or 2 electrons, respectively. A transient charge current ensues when switching between regimes $\langle N \rangle_{z_0} > (<) \langle N \rangle_z$, which is directed into (out of) the metal as indicated by the red (blue) color in Fig. 5.1, resepectively. The charge current is always associated with a heat current (not shown). Interestingly, in the regimes $\langle N \rangle_{z_0} = \langle N \rangle_z$ there can be a heat current without a charge current except along the diagonal strip $|\epsilon_0 - \epsilon| \lesssim T$, where both currents are zero because no switch is taking place on the relevant scale of thermal fluctuations, see Sec. 4.4.3 and Refs. [17, 47].

The extension of this scenario to include the large-gap superconductor is, however, not unique because the Andreev states (3.19) for the gate voltage ϵ after the switch differ

from those at the gate voltage ϵ_0 before the switch [see Eq. (3.19)]. Therefore, in Sec. 5.1.2 and 5.1.3, we will discuss in detail how two experimentally relevant initial states are prepared by gate switching.

Note that depending on the switch scenario, the simple description by occupations alone might become invalid. The odd parity spin states $|\sigma\rangle$ for $N = 1$ are not affected by this, thus we first ignore them in the following argument. If one switches $\epsilon_0 \to \epsilon$ on a timescale comparable or smaller than the inverse induced pairing gap α^{-1} and at the same time aims at a readout at time scales of the order of α^{-1}, coherent superpositions between even-parity states would be relevant for the system state dynamics after a gate switch. In this special case, a state $|\tau_0\rangle$ prepared as the stationary state at gate voltage ϵ_0 before the switch is a superposition –not a mixture– of energy states $|\tau\rangle$ for the new gate voltage ϵ after the switch. Denoting (up to a global phase)

$$|2\rangle = \sum_\tau \tau \sqrt{\tfrac{1}{2}\left[1 + \tau \frac{\delta}{\delta_\mathrm{A}}\right]}\, |\tau\rangle \tag{5.1a}$$

$$|0\rangle = \sum_\tau \sqrt{\tfrac{1}{2}\left[1 - \tau \frac{\delta}{\delta_\mathrm{A}}\right]}\, |\tau\rangle \ , \tag{5.1b}$$

we see that this happens with maximal amplitudes if we start far from resonance ($|\delta_0| \gg \alpha$), meaning that the stationary state before the switch is either $|-_0\rangle = |0\rangle$ or $|-_0\rangle = |2\rangle$, and then rapidly switch the gate voltage to resonance ($|\delta| \ll \alpha$) where the charge states are uniform superpositions $|0,2\rangle = (|+\rangle \pm |-\rangle)/\sqrt{2}$. Such a switch is not described by the equations developed in Sec. 3.4 and previously in Ref. [15], where energy off-diagonal elements are neglected, see Refs. [16, 72].

In the present work, we instead focus on two experimentally relevant scenarios, for which the simpler description developed in this thesis remains applicable. In contrast to the normal case, discussed in Ref. [17] where it was sufficient to assume a fast gate-voltage switch, this requires to specify switching and probing time scales in the metal as follows.

5.1.2 | Slow switch

We start with considering a situation, in which the switching time τ_s of the gate voltage is longer than the timescale α^{-1}, but much shorter than the time scale set by the dissipative tunneling γ_p^{-1}. In a realistic setting [83] with $\gamma_p \sim \mu$eV and $\alpha \sim$meV, this would correspond to switching times of tens of fs. Alternatively, it could be realized by temporarily decoupling the metal $\gamma_p \to 0$ to prevent dissipative effects, lifting the upper limit on the switching time. Gate-voltage switches on time scales much larger than α^{-1}

ensue that the states $|\tau_0\rangle$ will evolve unitarily to $|\tau\rangle$ during the switch:

$$|\tau_0\rangle \to |\tau\rangle = U(\epsilon, \epsilon_0)\,|\tau_0\rangle\ . \tag{5.2}$$

For the above mentioned example (5.1), where the state before the switch is a pure, even-parity state, this implies that one prepares a pure energy state

$$|\tau_0\rangle\langle\tau_0| \to |\tau\rangle\langle\tau| = (|0\rangle - \tau\,|2\rangle)(\langle 0| - \tau\,\langle 2|)/2$$

for $\tau = \pm$ instead of a complete mixture, as will be shown for the fast switch in the following section. Including the odd parity part into our discussion, this slow switch procedure maintains the stationary mixing coefficients but alters the basis vectors

$$\begin{aligned} z_0 &= \sum_{\tau=\pm} z_{0\tau}\,|\tau_0\rangle\langle\tau_0| + z_{01}\tfrac{1}{2}\sum_{\sigma}|\sigma\rangle\langle\sigma| \\ \to\quad \rho_0 &= \sum_{\tau=\pm} z_{0\tau}\,|\tau\rangle\langle\tau| + z_{01}\tfrac{1}{2}\sum_{\sigma}|\sigma\rangle\langle\sigma|\ . \end{aligned} \tag{5.3}$$

Since this scenario generates no off-diagonal elements in the new, final energy basis, we can compute the evolution and transport currents using the equations developed in the previous Chap. 4.

An example of a slow switch is shown in Fig. 5.2 (A): Initially before the switch, the superconductor is assumed to be off-resonant with the proximity effect (black bar) and in the stationary $|2)$-charge state. After switching to a final gate ϵ, where the superconductor is on-resonant with the proximity effect (red bar), the initial state $|\rho_0) = |-)$ is in a superposition of 0- and 2-charges before the onset of the transient decay. The decay to the final $|1)$-stationary state in this resonant gate region can hence in general occur by electron transfers in both directions, from the metal to the dot or vice versa, as indicated by the red arrows.

We finally point out that the slow switch is not well-defined in the $\alpha \to 0$-limit considering the associated time scales ($\tau_s > \alpha^{-1}$). Therefore, results of Ref. [17] can only be reproduced from a fast switch to be introduced in the next Sec. 5.1.3.

5.1.3 | Fast switch

The second situation that we consider is the one where the switch may be much faster than α^{-1}, however, the time-resolved readout is at a much lower time-scale [Fig. 5.2 (B)] (see for example Ref. [64], where time-resolved readout at the μs scale was realized). This corresponds to a time-resolved readout, where features occurring on the time-scale α^{-1} are averaged out.

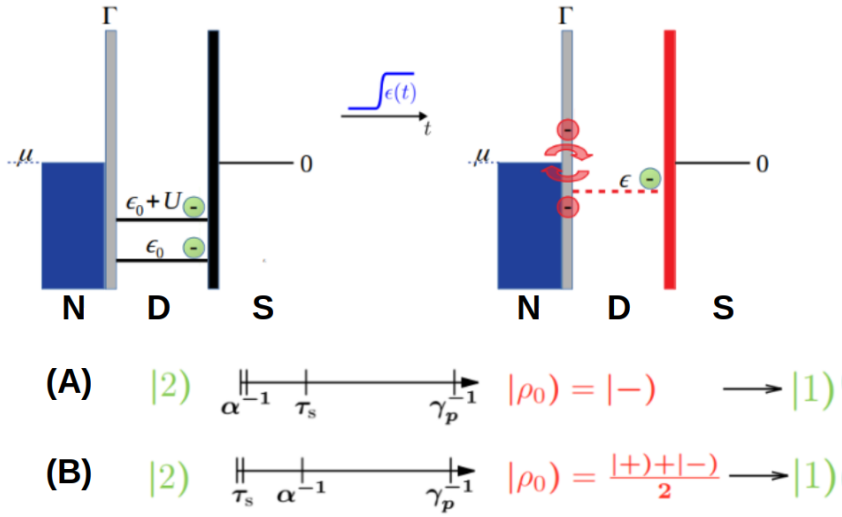

Figure 5.2. Schematics of an exemplary gate switch $\epsilon(t)$ applied to a quantum dot (D) (center) when attached to a normal metal (N, dark blue) at chemical potential μ and proximized with a superconductor (S, right) at potential zero. Black (red) bar indicates D is off (on) resonance with the proximity effect of S, respectively. Green bullets refer to the stationary charge of D before (top, left) and after the switch (top, right) with two types of possible particle transfers to the final state, as indicated by red arrows (top, right). (Bottom) Comparison of the different time scales $\tau_s, \alpha^{-1}, \gamma_p^{-1} \equiv \Gamma^{-1}$ characterizing the two types of switches (A) slow and (B) fast as well as the resulting initial states $|\rho_0)$. For further explanation, see the main text.

If we instantly switch the gate voltage from $\epsilon_0 \to \epsilon$, the initial state is in general a superposition of the proximized energy eigenstates at the new gate voltage ϵ:

$$|\tau_0'\rangle = \sum_\tau |\tau\rangle \langle\tau|\tau_0'\rangle \,. \tag{5.4}$$

Their similarity is quantified by transition probabilities

$$|\langle\tau|\tau_0'\rangle|^2 = \tfrac{1}{2}\big[1 + \tau\tau'\theta\big], \quad \tau,\tau' = \pm\,, \tag{5.5}$$

which can be expressed in terms of the probability-bias parameter $\theta \in [-1,1]$. Inserting Eq. (3.19) gives

$$\theta = \frac{1}{2}\sum_{\tau\tau'} \tau\tau' |\langle\tau|\tau_0'\rangle|^2 = \frac{\delta\delta_0 + \alpha^2}{\delta_\mathrm{A}\delta_{\mathrm{A}0}}. \tag{5.6}$$

When we subsequently let the system relax to the new stationary situation, the state and the currents probing this evolution will decay on a timescale γ_p^{-1} while oscillating on the much shorter timescale α^{-1}, set by the induced pairing gap, since we assume

$\alpha \gg \gamma_p$ [Sec. 3.3]. We now consider current measurements in the metal probe which are time-averaged over these rapid oscillations. In a Bloch vector picture that can be defined by the energy-basis [Eq. (4.50) and (5.10)] this can be understood as ignoring the rapid precession of the transverse Bloch components (off-diagonal elements), which occur during the slow relaxation of the longitudinal Bloch component (diagonal elements).

To describe only this longitudinal decay needed for the time-averaged currents, we can modify the stationary state prepared before the switch by keeping only the part that is energy-diagonal in the energy basis $|\tau\rangle$ after the switch:

$$|\tau_0'\rangle\langle\tau_0'| \to \sum_\tau |\langle\tau|\tau_0'\rangle|^2 \cdot |\tau\rangle\langle\tau| \ . \tag{5.7}$$

This coarse-grained description in time corresponds to an irreversible complete decoherence in the final energy basis. Note that this does not mean that effects of superconducting coherence are lost (which would be decoherence in the charge basis). In the above mentioned example, this procedure implies that if we switch to resonance ($|\delta| \ll \alpha$) coming from afar ($|\delta| \gg \alpha$), we consider the preparation of a completely mixed state: $|\tau_0'\rangle\langle\tau_0'| \to \frac{1}{2}\sum_\tau |\tau\rangle\langle\tau|$ as illustrated in Fig. 5.2 (B). Including the odd parity part into our discussion, the fast switch initialization maps the stationary probabilistic mixture in the $|\tau_0\rangle$ basis before the switch to a mixture in the basis after the switch

$$\begin{aligned} z_0 &= \sum_{\tau'} z_{0\tau'} |\tau_0'\rangle\langle\tau_0'| + z_{01}\tfrac{1}{2}\sum_\sigma |\sigma\rangle\langle\sigma| \\ \to \quad \rho_0 &= \sum_\tau \Big(\sum_{\tau'} |\langle\tau|\tau_0'\rangle|^2 z_{0\tau'} \Big) |\tau\rangle\langle\tau| + z_{01}\tfrac{1}{2}\sum_\sigma |\sigma\rangle\langle\sigma| \ . \end{aligned} \tag{5.8}$$

The evolution of these initial occupations using the equations of Chap. 4 gives the time-averaged transport current after a fast switch $\epsilon_0 \to \epsilon$.

5.1.4 | Generalized description of state initialization

Switches (5.8) and (5.3) are two distinct schemes that generalize time-dependent transport spectroscopy [17] to proximized quantum dot systems. The two switches provide two possible, experimentally relevant limits of physical initializations for which the description of Ref. [15] applies. They have two useful features: Firstly, given fixed α, the initialization is completely characterized by the pair of gate voltages (ϵ_0, ϵ), which allows a complete analysis of the feature-rich dynamics in terms of two-dimensional spectroscopy diagrams like Fig. 5.1b.

Secondly, both switching procedures can be specified completely by giving the function θ. Indeed, formally setting $\theta = 1$ independent of δ, δ_0, we have $|\langle\tau|\tau_0'\rangle|^2 = \delta_{\tau,\tau'}$ and

Eq. (5.8) reduces to Eq. (5.3). Comparing the two cases is interesting since for the fast switch the induced pairing α affects both the final mixed state (z) of the transient dynamics and the initial state ρ_0 [through z_0 by Eq. (5.8)]. This is important, since without the superconductor ($\alpha = 0$) these states are at best mixtures of one even- and one odd-parity state. When we tune to resonance with the superconductor, this creates a "shortcut" in the decay sequence by connecting the two even-parity states. As we will see, this can effectively counteract the time-dependent decay into the metal by the superconducting coherence of the energy states which form the initial energy mixtures.

The full description of the evolution following one of the switching procedures is obtained by inserting for the initial polarization and parity

$$\langle A\rangle_{\rho_0} = \theta\langle A_0\rangle_{z_0}, \quad \langle p\rangle_{\rho_0} = \langle p\rangle_{z_0}\,, \tag{5.9}$$

and choosing $\theta = 1$ for the slow switch and θ given by Eq. (5.6) for the fast switch. As before, $\langle A_0\rangle_{z_0}$ and $\langle p\rangle_{z_0}$ denote the stationary values at gate voltage δ_0 instead of δ, but importantly also the polarization itself is gate-dependent: we have A_0 instead of A. Thus, exploiting the description based on duality, the difference between the fast switch and the slow one can be clearly identified as the simple contraction of the polarization, $|\theta| < 1$, and possibly, its inversion if $\theta/|\theta| = -1$.

Eq. (5.9) is obtained by expanding the initial state as Eq. (4.50). For both switches, the change of the gate voltage $\delta_0 \to \delta$ leads to a change of the basis from

$$|\mathbb{1}), |A_0), |p)\} \to \{|\mathbb{1}), |A), |p)\}\,,$$

where A_0 and A are the different polarization operators at gate voltage δ and δ_0, respectively. This amounts to

$$\begin{aligned} |z_0) &= \tfrac{1}{4}|\mathbb{1}) + \langle A_0\rangle_{z_0}\tfrac{1}{2}|A_0) + \langle p\rangle_{z_0}\tfrac{1}{4}|p) \\ \to |\rho_0) &= \tfrac{1}{4}|\mathbb{1}) + \theta\langle A_0\rangle_{z_0}\tfrac{1}{2}|A) + \langle p\rangle_{z_0}\tfrac{1}{4}|p) \end{aligned} \tag{5.10}$$

for the fast switch (5.8), and yields the result for the slow switch (5.3) when setting $\theta = 1$. Here we have used $\frac{1}{2}(A|A_0) = \sum_{\tau\tau'}\tau\tau'(\tau|\tau_0') = \sum_{\tau\tau'}\tau\tau'|\langle\tau|\tau_0'\rangle|^2 = \theta$.

5.2 | Transport regimes, rates and local observables of interest

Now, where we have introduced the two initialization procedures to be considered in this work, we describe the generic behavior of the transient evolution after the initialization.

We first specify different transport regimes in our 4d-parameter space [Sec. 5.2.1] and afterwards give an overview of the behavior of the four invariants and two observables, which fully characterize the transient evolution (4.61) [Chap. 4]. The overview serves to specify regions in parameter space, where these quantities assume their boundary values as specified in Sec. 4.3.1. Furthermore, we will point out relations between them. The discussion will be kept on a qualitative level in Sec. 5.2.1, while a more detailed analysis of a few specific regions of interest will be subject to Sec. 5.4. In Sec. 5.2.2, we will start with the invariants and discuss the observables afterwards [Sec. 5.2.3].

5.2.1 | Specification of transport regimes

In the following, we consider the interaction U and bias μ as given and use the detuning δ, controlled by a gate voltage, to initialize the state of the proximized dotand consider the effect of the pairing α. Thus, in terms of these controllable parameters, using Eq. (3.28), we see that the condition $E_{\eta,\tau} = \mu$ is met at two concentric semicircles with radii in the $\alpha - \delta$ plane set by the interaction and the transport bias:

$$\alpha_\eta(\delta) \equiv \sqrt{(2\mu - \eta U)^2 - \delta^2}, \quad \eta = \pm\,. \tag{5.11}$$

The relative magnitude of these two possible α_η-values depends on the sign of the bias. We have $\alpha_+ \lesseqgtr \alpha_-$ for $\mu \gtreqless 0$ and $\alpha_+ = \alpha_-$ for $\mu = 0$. By

$$\pm\delta_\eta = \pm\sqrt{(2\mu - \eta U)^2 - \alpha^2}\,, \tag{5.12}$$

we denote the values of detuning at which the resonance condition with the inner [outer] semicircle is met, corresponding to $\eta_{\min}[\eta_{\max}] = +[-]\frac{\mu}{|\mu|}$, respectively. Which resonance conditions are met at α_η depends on the bias relative to the interaction as follows. There are two bias regimes:

(I) *Low bias*, $|\mu| \leq U/2$: Only resonance $E_{\eta,-} = \mu$ for state $\tau = -$ can be achieved when varying δ.

(II) *High bias*, $|\mu| \geq U/2$: Resonances $E_{\eta,\tau} = \mu$ for either state τ can be achieved for $\eta = \tau \operatorname{sign}\mu$, depending on the bias sign.

In each bias regime $|\mu| \gtreqless U/2$, one can distinguish three pairing regimes separated by the semi-circles (5.11) based on $\alpha_{\min} = \min\{\alpha_+(0), \alpha_-(0)\}$ and $\alpha_{\max} = \max\{\alpha_+(0), \alpha_-(0)\}$ and different regimes of detuning δ. This leads to the following specification of transport regimes:

(i) *Low detuning*, $|\delta| \leq \delta_{\min}$: The stationary proximized-dot state is predominantly singly occupied in the low-bias regime, but in the high-bias regime it is a mixture of all states. This regime is only present for weak pairing ($\alpha \leq \alpha_{\min}$) and absent for $|\mu| = U/2$ ($\alpha_{\min} = 0$).

(ii) *Moderate detuning*, $\delta_{\min} \leq |\delta| \leq \delta_{\max}$: The stationary state is dominated either by the singly-occupied state or the $\tau = -$ state, depending on the sign of the detuning δ. The regimes of moderate pairing ($\alpha_{\min} \leq \alpha \leq \alpha_{\max}$)- and detuning are absent for $|\mu| = 0$ ($\alpha_+ = \alpha_-$). The regime of moderate detuning is also absent for strong pairing $\alpha \geq \alpha_{\max}$.

(iii) *Strong detuning*, $\delta_{\max} \leq |\delta|$: The stationary state is dominated by the $\tau = -$ state resulting in a suppressed stationary current in all pairing regimes. Transport is merely determined by the δ-dependent hybridization of the even charges in the Andreev-states for strong pairing ($\alpha_{\max} \leq \alpha$). The regimes of strong detuning and pairing are present for any μ.

For the case of strong interaction U, which is of interest here, these six combinations of bias and detuning (pairing) are experimentally accessible, and expected to show qualitatively distinct behavior, in particular in the low-temperature, weak-coupling regime $U, \alpha \gg T \gg \gamma_p$, see, e.g., Ref. [84], where these regimes are specifically mapped out. Although μ can be arbitrary relative to the induced pairing gap α, the limits $\mu \to \infty$ and $\alpha \to 0$ fail to commute in the sense that $\alpha \to 0$ reduces the width of the ϵ-interval to zero, for which the superconductor is transparent, to zero. However, there is still no quasiparticle transport possible for $\alpha \to 0$, since the model only describes bias voltages μ deeply within the gap of the superconductor strictly discarding its inaccessible quasiparticles [Sec. 3.3].

5.2.2 | Duality-invariants

Thus so far we have reduced the problem of analyzing the complete dynamics to the understanding of just four duality invariants, Eq. (4.36). Now we establish their complete dependence on the physical parameters and exploit this in the remainder of the analysis. The four invariants are plotted in Fig. 5.3 as function of the controllable pairing α and gate voltage ϵ for bias values $\mu = 0, U/2, U, 3U/2$ displaying the distinct physical regimes [Sec. 5.2.1]. We first comment their overall structure, which also applies to later figures.

Clearly all plots are dominated by sharp changes occurring for gate voltages when the conditions for Andreev-state resonances $E_{\eta,\tau} = \mu$ are met. Here and in the following

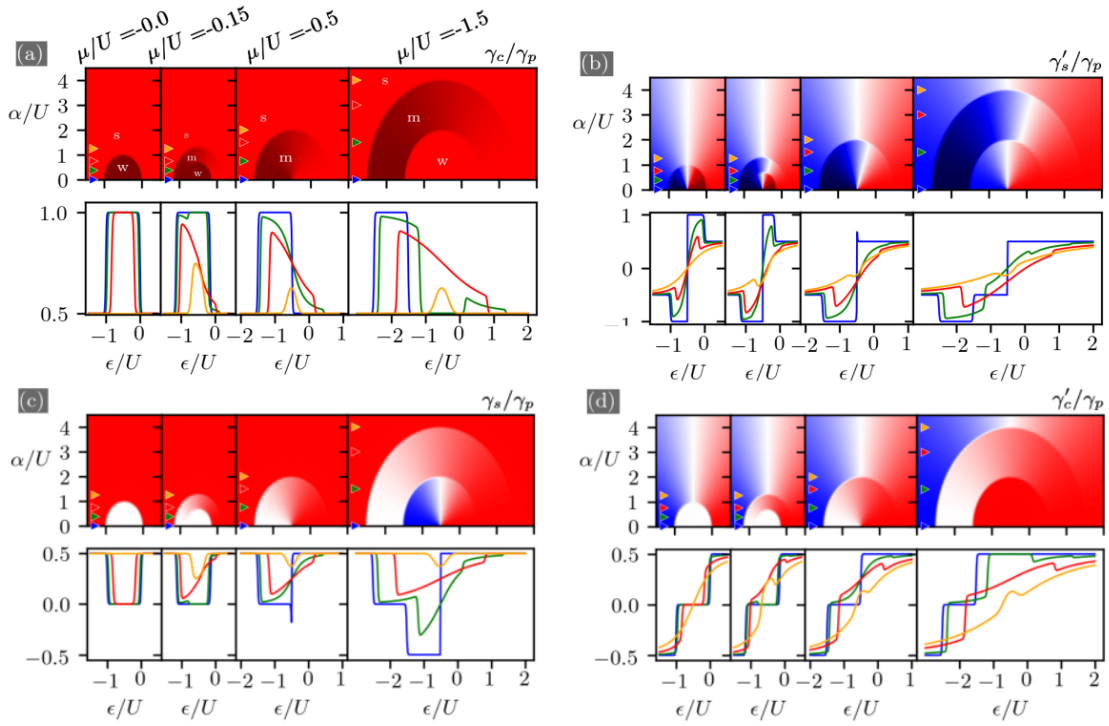

FIGURE 5.3. Duality invariants for $T = 0.02U$ as function of the gate-voltage $\epsilon = \delta - U/2$ and induced pairing α. All color plots use the same color scale, positions of horizontal line cuts are indicated by arrows. The semi-circles centered at $\epsilon = -U/2$ with radii $|2\mu \pm U|$ [Eq. 5.11] separate the regimes of weak (w), moderate (m) and strong (s) pairing as indicated in panel (a). For further explanations see the text.

we chose a sufficiently low temperature $T/U = 0.02$ such that the Andreev features are readily identified by sharp contrast changes in color plots and steps in line cuts. For $|\mu| = 0$ there is only a weak and a strong pairing regime separated by the semi-circle of radius U around the symmetry point $\delta = 0$ [first panel from the left in Fig. 5.3(a)-(d)]. For generic bias $|\mu| < U/2$ and $|\mu| > U/2$ there are always three pairing regimes, which can be distinguished for sufficiently low temperature [second and third panel in Fig. 5.3(a)-(d), respectively]. Typically, as the pairing α is increased, the gate-voltage dependence of all invariants shows qualitative changes at $\alpha = \alpha_{\pm}(0) = 2|U/2 \mp \mu|$, see the line cuts. For example, γ_c in the first panel of Fig. 5.3(a) shows a step-like structure for weak pairing (blue, green, red line cuts), which gets completely suppressed when changing to strong pairing (yellow line cut).

In Fig. 5.3 (a) and (c) [(b) and (d)] there is an overall pattern of the gate-voltage dependence which is (anti-)symmetric in δ, respectively. This is characteristic of the (primed) invariants γ_c and γ_s (γ_c' and γ_s'), which are the ones not involved (being involved) in

transport and is clearly visible at low bias. The antisymmetric pattern explicitly reflects the δ/δ_A dependence introduced by the pair resonance with the superconductor. In addition to these similarities between panels (a) and (c), respectively (b) and (d), duality reveals that in fact the functional dependence of Fig. 5.3 (a) and (b) [(c) and (d)] are more closely related: (γ_c and γ_s') [γ_s and γ_c'] share the same components [Eq. (4.36)].

We now discuss some particular features of the specific invariants. In Fig. 5.3 (a) the shifted-invariant γ_c is the physical rate of charge decay and equals an average of transition rates of the master equation (3.27), $\sum_\tau W_{1,\tau}/2$, i.e., whenever some transition $\tau \to 1$ is enabled, it will show up additively in γ_c. Positivity of the transition rates requires that γ_c is bounded by the parity decay rate γ_p and is positive [Eq. (4.48)]. In addition, it is lower bounded by its $T \to \infty$ limit:

$$\tfrac{1}{2}\gamma_p \leq \gamma_c \leq \gamma_p \,. \tag{5.13}$$

This means that the two decay-time scales γ_c and γ_p are always of the same order of magnitude, thus transient measurements will always probe their interesting interplay discussed later on. In Fig. 5.3(a), we see that γ_c reaches the upper bound in the weak pairing regime, see the plateaus in line cuts. In the intermediate regime visible in the panels on the right hand side, γ_c interpolates between the bounds (5.13) as δ is varied. In the strong pairing regime, the charge decay rate is always suppressed to its lower bound, $\gamma_c \approx \gamma_p/2$.

Fig. 5.3 (b) shows the transport invariant γ_s' connecting polarization decay to currents [Eq. (4.66)]. Overall, the δ dependence is an S-shaped curve inverting its sign around $\delta = 0$ except in the moderate pairing regime, where the zero shifts in the direction of the bias as $\alpha \approx -\mu/|\mu|\delta$. This can be seen by the white area that is shifted in the central circle with respect to the inner and outer ones.

Fig. 5.3 (c) shows the invariant γ_s which is the transition rate asymmetry taking on both negative and positive values to favor transitions to $\tau = +$ over transitions to $\tau = -$. It is thus associated with the polarization of the even-parity energy states (below). Importantly, it is suppressed in the weak pairing, low bias regime [first and second panel] for low detuning.

Fig. 5.3 (d) shows the invariant γ_c' related to charge transport rather than energy transport. Importantly, for weak pairing and low detuning it is suppressed like γ_s for low bias, but for high bias it behaves like γ_c in the weak pairing regime.

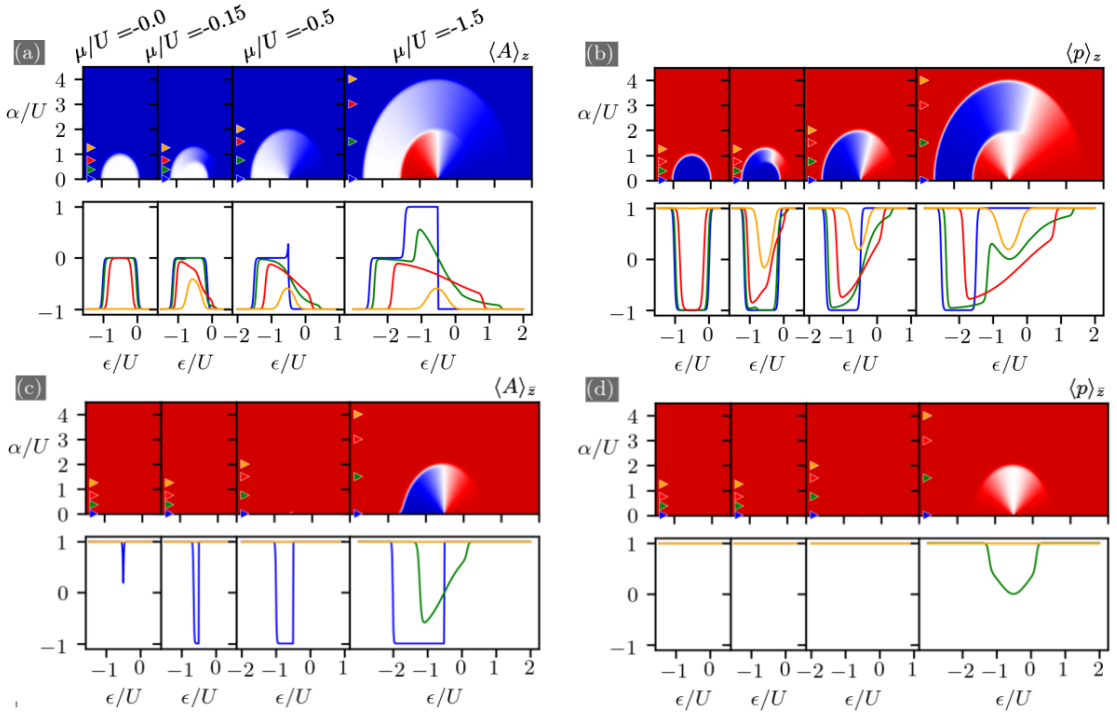

Figure 5.4. Expectation values of polarization A and parity p in the stationary state of the system (z) [(a) and (b)] and the dual system ($\bar{z}$) [(c) and (d)]. Parameters and conventions are the same as in Fig. 5.3.

5.2.3 | Polarization and parity

It is now straightforward to give an overview of the complete parameter dependence of expectation values of the observables p and A. First, the polarization $\langle A\rangle_z = -\gamma_s/\gamma_c$ plotted in Fig 5.4 (a) is non-zero whenever the transition rate-asymmetry γ_s is nonzero, taking the opposite sign, it is amplified in magnitude when the decay rate γ_c is small, see Figs. 5.3 (a) and (c). Next, the boundary values of stationary parity $\langle p\rangle_z = 1-2(\gamma_c^2-\gamma_s^2)/(\gamma_p\gamma_c)$ [Fig. 5.4 (b)] can be extracted from Figs. 5.3 (a) and (c): Having strictly parity $\langle p\rangle_z = 1$, requires $\gamma_c = |\gamma_s|$, i.e., saturating the positivity bound on the transition rate-asymmetry (5.13), see the red and blue areas of Fig. 5.3 (c). Strict parity $\langle p\rangle_z = -1$ instead requires $|\gamma_s| = 0$ [Fig. 5.3 (c)] together with $\gamma_c = \gamma_p$ [Fig. 5.3 (a)] and gives the blue regions of Fig. 5.4 (b).

The dual polarization $\langle A\rangle_{\bar{z}} = \bar{\gamma}_s/\bar{\gamma}_c$ plotted in Fig. 5.4 (c) can be understood in the same way by considering the dual invariants $\bar{\gamma}_s = \gamma_s$ and $\bar{\gamma}_c = \gamma_p - \gamma_c$ [Eqs. (4.35), (4.47)] instead, i.e., inverting the colors in Fig. 5.3 (a). This leads to the result that the dual polarization is almost always $+1$ for the considered bias sign ($\mu \leq 0$), except in the weak pairing, high bias regime at low detuning in Fig 5.4 (c).

The dual parity $\langle p\rangle_{\bar{z}} = 1-2(\bar{\gamma}_c^2-\bar{\gamma}_s^2)/(\bar{\gamma}_p\bar{\gamma}_c)$ plotted in Fig. 5.4 (d) then follows in

the same way as above for the actual system: It is almost always $+1$ except in the weak pairing, high bias regime in Fig. 5.4 (d) at low detuning.

Since the dual stationary values are important for understanding the dynamics of the actual system, it is useful to also have an intuitive explanation by applying duality "microscopically": For the dual system, the interaction $\bar{U} = -U < 0$ is attractive which favors pairwise occupation and thus stationary parity $\langle p \rangle_{\bar{z}} = 1$, see Refs. [48, 85]. The only way to access odd (dual) parity states is to apply a sufficiently large voltage bias, $|\mu| > U/2$, and to tune the gate voltage to the weak pairing regime at low detuning, around the symmetry point $-U/2 < \delta < 0$. as in Fig. 5.4 (d). For the dual polarization one argues similarly recovering the $\langle A \rangle_{\bar{z}} = -1$ area in Fig. 5.4 (c).

5.3 | Non-monotonicity of the heat-and energy currents

As the transient charge current (4.66) is determined by a single amplitude a, there is no competing behavior of different time scales, and it behaves montonically. Therefore, an analysis based on spectroscopy plots is sufficient, which will be given in the next Sec. 5.4. By contrast, the transient energy- and heat-currents feature more intricate dependencies on the initial state and on time, as in general both amplitudes a_c and a_p of the state evolution (4.61) contribute. This derives from the fact that the dot energy H_{D} is a two-particle quantity –in contrast to charge– allowing to probe the full correlated proximized dot state. Hence we give a preliminary analysis, before we analyze the parameter dependence of the heat current in the two switch scenarios in Sec. 5.4.3.

5.3.1 | Initial-state dependence

To highlight the dependence on the initial condition, the transient heat current can be decomposed as

$$\begin{aligned} &I_Q(t) - I_Q(\infty) = \\ &I_{Q,A}(t)\left[\langle A \rangle_{\rho_0} - \langle A \rangle_z\right] + I_{Q,p}(t)\left[\langle p \rangle_{\rho_0} - \langle p \rangle_z\right] \end{aligned} \tag{5.14}$$

into transient heat current contributions flowing in response to an initial "excess" of quantities A and p on the proximized dot relative to their stationary values. The prefac-

tors are given by

$$I_{Q,A}(t) = \left\{\tfrac{1}{2}\Big(\delta_{\mathrm{A}} - U\big(1 - \frac{\gamma_p}{\gamma_c}e^{-(\gamma_p-\gamma_c)t}\big)\langle A\rangle_{\bar{z}}\Big)\gamma_c - \mu\gamma_s'\right\}e^{-\gamma_c t} \tag{5.15}$$

$$I_{Q,p}(t) = U\tfrac{\gamma_p}{4}e^{-\gamma_p t}\,. \tag{5.16}$$

The transient heat current thus probes both the decay of the excess polarization and parity. It is in principle possible to prepare suitable energy-mixtures $|\rho_0)$ for which these responses can be measured separately:

For initial states with $\langle A\rangle_{\rho_0} = \langle A\rangle_z$ the second term in Eq. (5.14) constitutes the full heat current with a response $I_{Q,p}(t)$ that depends only on the interaction U and the bare coupling $\gamma_p = \Gamma$. It is independent of all other parameters, in particular, of the pairing α induced by the superconductor. Again, for the basic physical initialization procedures (5.9) considered here, the condition $\langle A\rangle_{\rho_0} = \theta\langle A_0\rangle_{z_0} = \langle A\rangle_z$ is achievable by tuning parameters. In this case the transient charge current vanishes [Eq. (4.66)] due to the choice of initial condition when $\gamma_s' \neq 0$ [Fig. 5.3 (b)].

By contrast, for initial states with $\langle p\rangle_{\rho_0} = \langle p\rangle_z$ only the first term in Eq. (5.14) contributes, and it depends nontrivially on all parameters. Interestingly, the sign of the interaction contribution to $I_{Q,A}(t)$ is reversed at a time $t_1 \in [\gamma_p^{-1}, \gamma_c^{-1}]$ given by

$$t_1 = \frac{\ln(\gamma_p/\gamma_c)}{\gamma_p - \gamma_c}. \tag{5.17}$$

For example, for strong pairing $\alpha > \alpha_{\max}$ [Eq. (5.11)], the decay rates differ maximally $\gamma_c = \gamma_p/2$ [Eq. (5.13)], while the sign change takes place at $t_1 = \ln(2)\gamma_c^{-1}$.

5.3.2 | Non-monotonicity of the time-dependence

Due to their two-particle nature the transient energy- and heat currents also probe the state of the proximized dot through their double-exponential time-dependence (4.80a) that generically follows after either switch (5.8) or (5.3). Although this proximized dot is expected to have two finite timescales—based on its Liouville-space dimension 3 and 1 constraint by trace preservation—only by means of their amplitudes we can tell that interaction U is required for both scales to be *relevant* ($a_p = 0$ for $U = 0$). This extends the considerations of Ref. [17] without a superconductor ($\alpha = 0$).

The heat current (4.80a) can exhibit non-monotonic decay since the amplitudes a_c and a_p can have opposite sign. In fact, there are two types of such behavior. Firstly, the

transient $I_Q(t) - I_Q(\infty)$ will pass through zero at time

$$t_0 = \frac{\ln(-a_p/a_c)}{\gamma_p - \gamma_c}, \tag{5.18}$$

provided this expression is positive. In this case the fast parity decay has a larger amplitude than the slow charge decay with opposite sign, $0 \leq -a_c/a_p \leq 1$. It will therefore initially push the transient through zero, i.e., the heat current intersects its stationary asymptote once, $I_Q(t_0) = I_Q(\infty)$, before decaying to it from the opposite side.

Secondly, the presence of a zero implies that there is a local extremum—either a maximum or a minimum—at later time. However, having a zero is not a necessary condition: a local extremum can occur at a time

$$t_2 = \frac{\ln[-(\gamma_p a_p)/(\gamma_c a_c)]}{\gamma_p - \gamma_c} = t_0 + t_1 \tag{5.19}$$

whenever $0 \leq (-\gamma_c a_c)/(\gamma_p a_p) \leq 1$. In this case the initial rate of change of the parity decay term dominates that of the opposing charge decay,

$$|(d/dt)a_p e^{-\gamma_p t}|_{t=0}| > |(d/dt)a_c e^{-\gamma_c t}|_{t=0}|,$$

without necessarily inducing a zero. Although the time t_0 is negative when there is no zero [Eq. (5.18)] it can still be compensated by t_1, the positive time (5.17) at which the interaction contribution to $I_{Q,A}(t)$ reverses its sign [Eq. (5.16)].

We stress that the scales t_0, t_1 and t_2 characterizing the transient heat current profile in time are not the two decay time scales of the state evolution (γ_c, γ_p), but functions of these for (t_1) and of their amplitudes for (t_0, t_2). They emerge only due to interaction.

A simple quantifier of the profile of the transient heat current is provided by its extremal value at t_2 relative to its initial value:

$$\frac{I_Q(t_2) - I_Q(\infty)}{I_Q(0) - I_Q(\infty)} = R\left(\frac{\gamma_c}{\gamma_p}, \frac{a_c}{a_p}\right), \tag{5.20a}$$

which depends only on ratios of decay rates, $x = \gamma_c/\gamma_p$, and amplitudes, $y = a_c/a_p$, through the function ($y \leq 0$)

$$R(x,y) = (-yx)^{\frac{x}{1-x}} \frac{y}{y+1}(1-x). \tag{5.20b}$$

The possible values are plotted in Fig. 5.5 as function of the two ratios. Its sign indicates the type of non-monotonicity and its magnitude quantifies its degree. For $y \leq -1/x$ and $y \geq 0$ (not shown) there is no extremum. We thus see that the initial value $I_Q(0) - I_Q(\infty) = a_c + a_p$ does not characterize the visibility of the transient

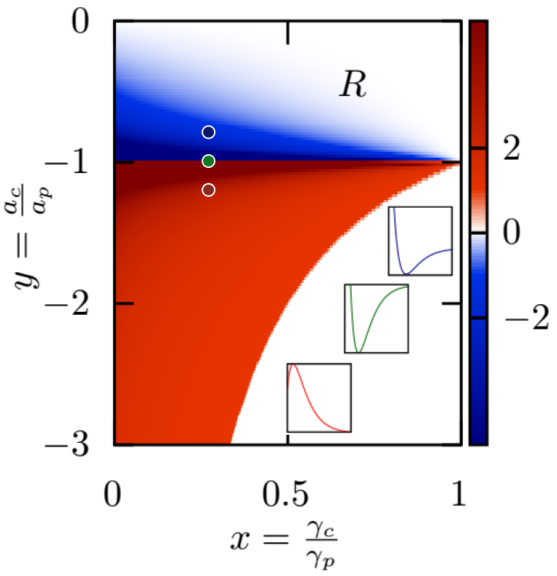

Figure 5.5. Possible values of the non-monotonicity quantifier R [Eq. (5.20)] as function of the possible values of the ratio of decay rates and of amplitudes. The insets show examples for non-monotonic profiles of the transient heat current as function of time for decay with a zero (blue, $-1 \leq y < 0$), for decay without a zero (red $-1/x \leq y < -1$) and an intermediate case (green, $y = -1$). In the latter case the transient heat current is both initially and finally zero.

heat current, quantifying the maximum amplitude of the time-dependent evolution. Instead, one needs the extremal value relative to the initial value, given by R. Note that for the special case of complete initial cancellation $a_c = -a_p$ the value $|R|$ diverges, see Fig. 5.5, inset with green curve. In this case it is insightful to use the extremal value of the transient relative to a_p to characterize the visibility:

$$[I_Q(t_2) - I_Q(\infty)]/a_p = x^{1/(1-x)}(1 - 1/x)\,. \tag{5.21}$$

The expression depends only on $x = \gamma_c/\gamma_p$ and quantifies the degree of nonmonotonicity.

5.4 | Amplitudes of transient transport observables - from the perspective of 2d spectroscopy

In Secs. 5.2.2- 5.2.3, we gave an overview of the behavior of the six quantities, four invariants and two observables, characterizing the transport problem in the different transport regimes [Sec. 5.2.1]. We now proceed with analyzing a few parameter regions of interest

in more detail. In this section, the analysis of transient transport will be complementary to the one given in Secs. 5.2.2- 5.2.3, as based on a microscopic understanding of the processes involved in the transient decay, it will be oriented along the entire current (amplitudes) and less explicitly related to the four duality invariants.

5.4.1 | Strategy in extracting real and dual stationary states

Still exploiting fermionic duality, we will use that to a large extent the current amplitudes as transient quantities can be expressed in terms of averages of observables, evaluated in the real and dual stationary states. In view of systematically exploiting the four-dimensional parameter space with respect to characteristic changes in the observables of interest and thereby specifying different transport regimes, we therefore aim at understanding the real and dual stationary states as a function of $(\epsilon, \alpha, U, \mu)$ in a first step, hence very differently from Secs. 5.2.2- 5.2.3. This can be achieved once the few relevant state transitions, which contribute to the master equation, as well as their associated particle transfers between the metal and the dot can be efficiently extracted for any given values of the four parameters.

In extracting the stationary state for a given point in parameter space, we proceed in the following way: From Fig. 3.4, we determine which of the four energy thresholds (black curves) are passed ($\mu - E_{\eta,\tau} \gtrless 0$) for given values of $(\epsilon, \alpha, U, \mu)$. From Table 3.1, the corresponding real and dual state transitions can then be extracted together with the associated particle transfers from the metal to the dot, as indicated by the arrows $\underset{h}{\overset{e}{\rightleftarrows}}$, $\underset{e}{\overset{h}{\rightleftarrows}}$ in the first row of columns 4 and 5. As can be concluded from the coupling rates $\Gamma_\pm$ (blue curves) in Fig. 3.4, the total number of eight processes listed in Table 3.1 is reduced by half, when the superconductor is off-resonant with the proximity effect ($|\delta| >> \alpha$) and one of the coupling rates vanishes. This agrees with the fact that a specific directed state transition ($\tau \leftarrow 1, 1 \leftarrow \tau$) can only be realized by a single associated charge transfer (e or h) between the metal and the dot, when there is no hybridization of the even-parity charge states due to the absence of the superconductor. In contrast, near the particle-hole symmetry point ($|\delta| << \alpha$), the hybridization is at maximum, and all eight processes listed in Table 3.1 contribute with equal coupling strengths ($\Gamma_\pm = \frac{\gamma_p}{2}$), if the corresponding energy thresholds indicated in the first column are passed. This agrees with the fact that a specific directed state transition ($\tau \leftarrow 1, 1 \leftarrow \tau$) can in principle be realized by both charges, an e or a h being transferred from the metal to the dot, due to the hybridization of the superconductor, compare e.g. row 2 and 5 of column 4.

Applying this strategy, we provide a detailed analysis of the amplitudes of transient

charge and heat decay in this Sec. 5.4, comparing the two opposite switch scenarios introduced in 5.1. We start with the transient charge current amplitude [Sec. 5.4.2] to provide a detailed overview of the charge transfers involved in the transient decay, before we combine this understanding with the duality-motivated expressions for the heat current amplitudes. The heat current amplitudes will be discussed in 5.4.3.

5.4.2 | Charge current amplitude at zero chemical potential

We discuss first a fast switch and next a slow one.

5.4.2.1 | Fast switch

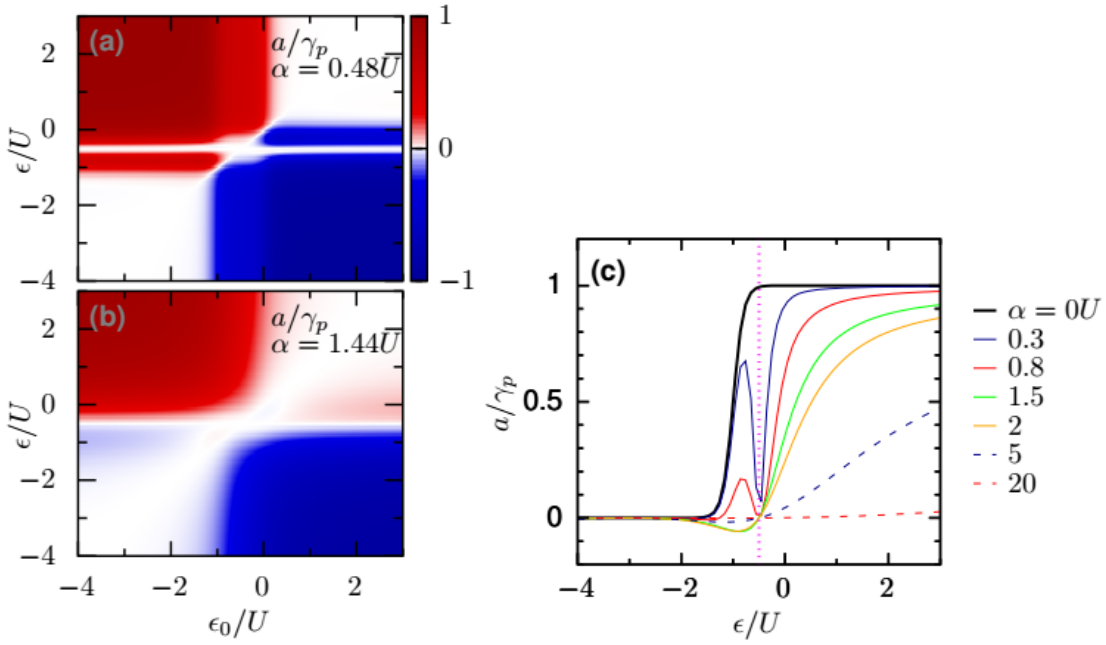

Figure 5.6. Charge amplitudes a after a fast switch at zero chemical potential and temperature $T = 0.1U$: (a) for weak pairing $\alpha = 0.48U$, (b) for strong pairing $\alpha = 1.44U$, (c) for different pairing strengths α at initial gate voltage $\epsilon_0 = -3U$.

Limit of zero α. Before analyzing our results for the charge current, we briefly describe as reference the case where the superconductor is absent ($\alpha = 0$) and the initial state is prepared by a sudden switch. In this limit, previously discussed in Ref. [17], the currents are purely transient, such that the charge current reads $I_N = ae^{-\gamma_c t}$.

In Fig. 5.6 (a), the behavior of the amplitude a for this limit of $\alpha = 0$, is represented by the red and blue off-diagonal blocks, neglecting the white horizontal line, which is due

to the superconductor. For $\alpha = 0$, Eq. (4.66) reduces to (charge decay rate) $\times$ (excess dot charge), $a = \gamma_c(N_0 - N_z)$. As a function of the level position before the switch, ϵ_0, the amplitude follows the initial stationary occupation $N_0 = trN_{\rm D}z(\epsilon_0)$, changing stepwise at $\epsilon_0 = 0$ and $-U$ as was explained in Fig. 5.1 (a). However, both γ_c and $N_z = trN_{\rm D}z(\epsilon)$ change as a function of the final level position ϵ, resulting in only a single symmetric step from zero to $a = \pm 2\Gamma$ with ϵ_0-dependent position, $\epsilon = 0$ for $\epsilon_0 \geq 0$ and $\epsilon = -U$ for $\epsilon_0 \leq -U$, respectively. An additional step that one might expect at $\epsilon = -U$ is absent since although $N_0 - N_z$ decreases from 2 to 1 with increasing ϵ, this is compensated by the simultaneous increase of the γ_c factor from Γ to 2Γ.

Limit of nonzero α. We now discuss the impact of the superconducting coupling on the decay amplitude a of the charge current $I_N = ae^{-\gamma_c t}$ into the metal when the dot is coupled to a superconductor at zero bias $\mu = 0$. The amplitude a is plotted in Fig. 5.6(a)-(b) as a function of the initial, ϵ_0, and final level position, ϵ, for different superconducting coupling strengths α.

Limit of weak pairing $\alpha \ll U$. For the weak pairing $\alpha \ll U$ in Fig. 5.6(a) the superconductor only modifies the above described known behavior by introducing a *pronounced dip at the symmetry point $\epsilon = -U/2$ of the final gate voltage* independently of ϵ_0. As seen in the line plots of Fig. 5.6 (c), this dip broadens with increasing pairing α. The current gets completely suppressed at the symmetry point because the transitions between Andreev states occur both by the transfer of electrons and holes at equal transport rates $\Gamma_+ = \Gamma_-$.

For example, consider the switch $\epsilon_0 = -3\,U \to \epsilon = -U/2$ [blue cut in Fig. 5.6(c)]. Here, the dot is in the double occupied state $|2)$ before the switch, such that right after the switch the initial state of the decay is $|\rho_0) = \big[|+) + |-)\big]/2$, see the discussion of Eq. (5.8). Since $\alpha \ll U$ is small, the final state is single occupied, $|z(\epsilon)) \approx |1)$. The decay $\big[|+) + |-)\big]/2 \to |1)$ occurs both by tunneling of an electron *and* of a hole into the metal contact with equal probabilities. Their contributions to the charge currents cancel out leading to the full suppression at the symmetry point. Electrons and holes tunnel with approximately the same probability in the vicinity of the point. This area increases with α as explained in Fig. 5.6(b,c). Thus the dip broadens.

In contrast to the final gate voltage at the symmetry point, we note that for $\mu = 0$ the superconductor introduces *no modification at the symmetry point $\epsilon_0 = -U/2$ of the initial gate voltage*, i.e., along a vertical line in Fig. 5.6(a,b). For $\alpha \ll U$, the reason for this behavior is that the state is single occupied, $|z(\epsilon_0)) \approx |1)$, before the switch and thus

also right afterwards [Eq. (5.8)].

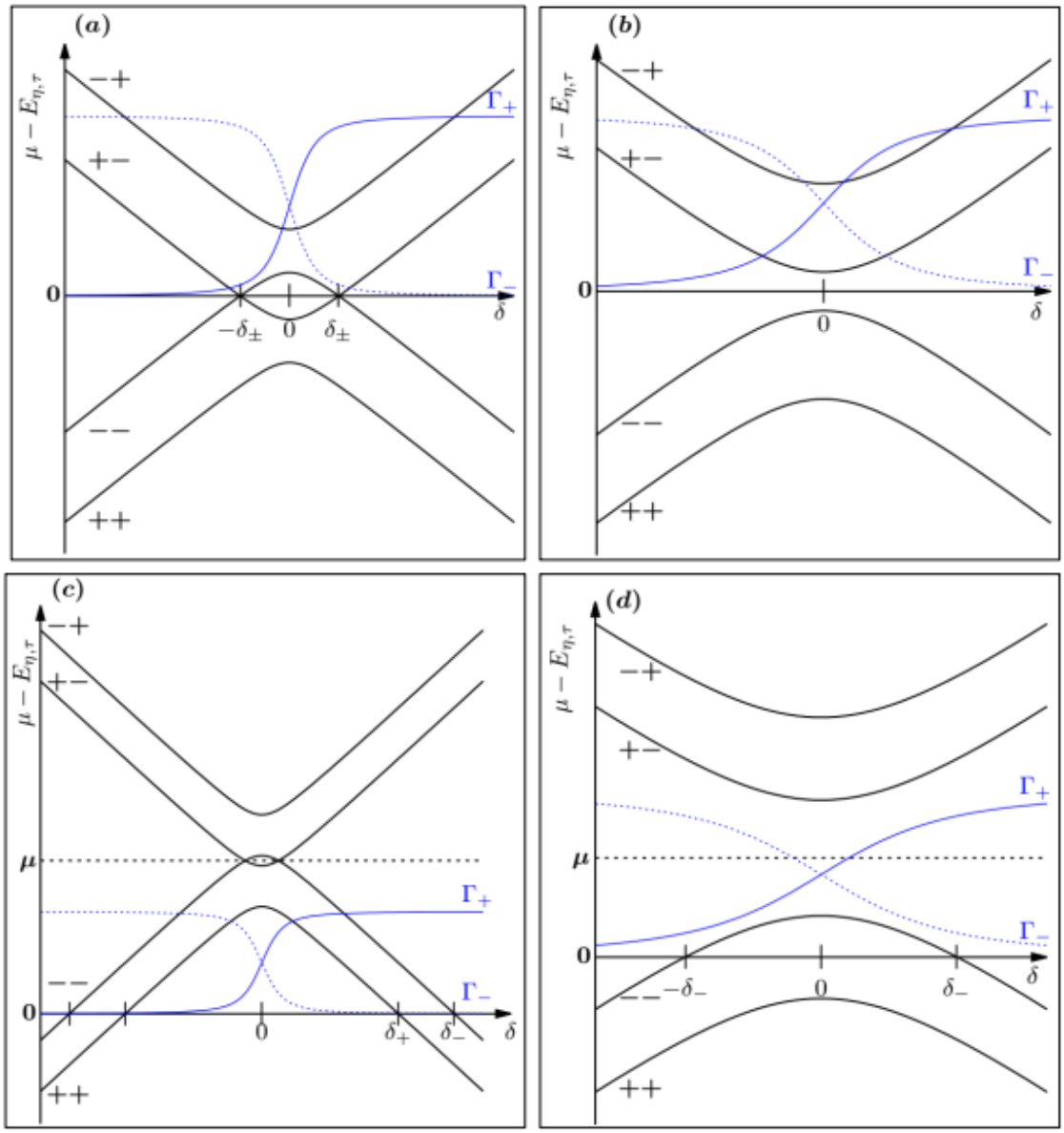

Figure 5.7. Schematic overview of zero temperature energy thresholds $\mu - E_{\eta,\tau}$ (Table 3.1) for the cases of (a) $\mu = 0$ and weak pairing α, (b) strong α, (c) $\mu > 0$ and weak α and (d) moderate α. $\delta_\pm$ specifies the region of detuning, as introduced in Sec. 5.2.1.

Limit of strong pairing $\alpha \geq U$. For strong superconducting coupling $\alpha \gtrsim U$, the state is initially $|-_0)$, an equally-weighted superposition of $0-$2-charge states, which

after the switch to an off-resonant region is represented by $|-_0) = \big[|+) + |-)\big]/2$. After the switch one of its components $\pm$ decays to the opposite off-resonant stationary component, either via an e- or an h-sequence, see table 3.1 in 3.4 and panel (b) of Fig. 5.7. Therefore the current is neither suppressed along the vertical line for strong pairing $\alpha \gtrsim U$.

In general, going to strong pairing $\alpha \gtrsim U$, the overall behavior of the amplitude completely changes as illustrated in Fig. 5.6 (b)-(c). The dip at the symmetry point $\epsilon = -U/2$ turns into a sign change of a, i.e., the transient charge current is *reversed* on one side. The step of a to values $a = \pm\gamma_p$ is now non-symmetric and effectively located at the symmetry point $\epsilon = -U/2$ with a tail broadening with increasing α. As can be seen in Fig. 5.6 (c), the magnitude of the reverse current initially grows with increasing α, reaching a maximum which is then suppressed.

This change of behavior starting when $\alpha \sim U$ can be understood as follows. For ϵ at the symmetry point, the final state to which the system decays is $|z(\epsilon)) \approx |-)$ instead of $|1)$ as for weak pairing. Thus for strong pairing $\alpha \gtrsim U$ we have a decay $\big[|+) + |-)\big]/2 \to |-)$ at the symmetry point, coming from the pure off-resonant charge state 2 for $\epsilon_0 = -3U$. At the symmetry point, particle- and hole contributions to the decay are equally weighted and cancel to zero net current, see Fig. 5.7(b) and Table 3.1 in 3.4.

For $\epsilon < -\frac{U}{2}$, due to hybridization with the superconductor the $+$ -contribution in the initial mixture contains a charge contribution 0 opposite to the stationary 2-charge in this region. This causes a reversed transient current, see Fig. 5.6(b)-(c). Technically, this sign change arises in (4.66) due to the factor $\Gamma_+ - \Gamma_-$ in a, since for strong pairing the sign of $(A|\rho_0) - (A|z)$ is independent of ϵ.

5.4.2.2 | Slow switch

We now discuss the results for the transient charge current after a slow switch, as introduced in 5.1.2. Differently from the fast gate switch, the slow switch is performed on a timescale larger than α^{-1} but much shorter than Γ^{-1}. The stationary state before the switch therefore evolves unitarily to the initial state after the switch, following the gate-dependent hybridization of even parity charge states due to the presence of the superconductor. In contrast to the fast switch, part of the initial dot charge is therefore already exchanged with the superconductor, before the onset of the transient decay. We now discuss this behavior in more detail by comparing the slow switches indicated in Fig. 5.8(a)-(b) with the corresponding fast ones in Fig. 5.6(a)-(b) discussed in the previous Sec.5.4.2.1.

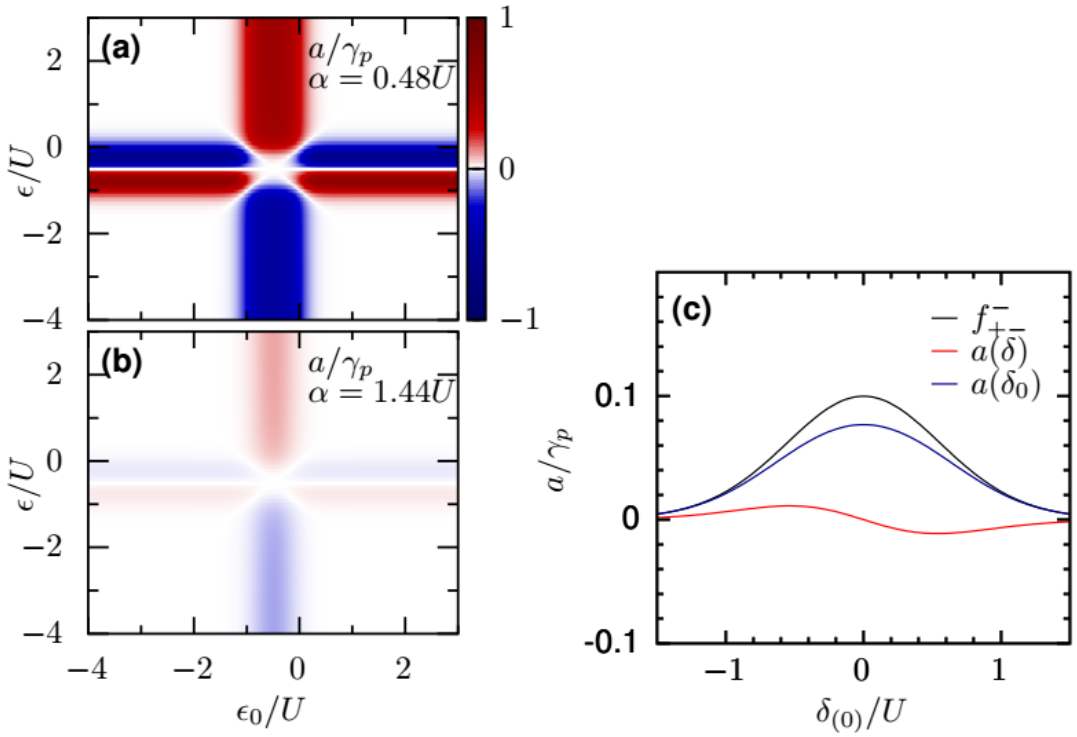

Figure 5.8. Charge amplitudes a after a slow switch at zero chemical potential and temperature $T = 0.1U$ (a) for weak pairing $\alpha = 0.48U$ and (b) for strong pairing $\alpha = 1.44U$. (c) For the final (initial) far off-resonant state $|-) = |0)$ ($|-_0)$), a horizontal (vertical) linecut $a(\delta_{(0)})$ is given, respectively.

Limit of weak coupling α. In the limit of weak coupling $\alpha < U$, the gate parameter region of the pure stationary $|1)$- state is confined by $\delta_{(0)} = \pm\sqrt{U^2 - \alpha^2}$, corresponding to the colored cross in Fig. 5.8(a). Outside this region, the system is always in the stationary $|-)$-state, see Fig. 3.4 and Table 3.1. The stationary $|+)$- state can be only excited at non-zero bias. Otherwise it is not excited during the switching procedure due to the unitary evolution. As a result, here we do not find any transient charge decay in the off-diagonal blocks of Fig. 5.8(a), as the stationary state at the initial gate parameter $|-_0)$ evolves unitarily into the corresponding one at the final gate parameter $|-)$.

Note that the gate-dependent hybridization of $0-2$-charges due to the presence of the superconductor becomes visible in the current sign change around the symmetry point $\epsilon = -\frac{U}{2}$ of the final gate. Next, let us argue why there is the sign change. Depending on the weight $\Gamma_+(\Gamma_-)$ of $0(2)$ charges in the initial $|-)$-state after the switch, the transient decay towards the $|1)$-final stationary state occurs preferably via $e(h)$- transfers to the dot, when $\Gamma_+ > (<)\Gamma_-$, corresponding to the blue (red) regions in Fig. 5.8(a),

respectively. For comparison, see also the blue lines in panel (a) of Fig. 5.7 and rows 2 and 3 of Table 3.1. In the vertical part of the cross in Fig. 5.8(a)-(b), however, there is no such sign change of the current, as the initial state $|1)$ decays to pure off-resonant charge states, either $|-) = |0)$ (or $|2)$), corresponding to $\epsilon > (<) - \frac{U}{2}$, respectively.

Limit of strong pairing α. In this limit of α, we observe that transport is merely temperature induced. Let us first discuss the vertical part of the colored cross, see Fig. 5.8(b). Differently from the case of weak pairing, we expect the system to always be in the stationary $|-)$-state, independently of the chosen initial and final gate parameters, based on the zero temperature energy thresholds established in Table 3.1, see also the corresponding panel (b) of Fig. 5.7 for this regime of α. As the initial state evolves unitarily into the final stationary state *during* the slow switch, there should then be no transient charge flow on average based on that expectation. However, the average charge current is nonzero as shown in Fig. 5.8(b), but considerably reduced in strength compared to the $\alpha = 0.48U$ case (Fig. 5.8(a)). It is therefore a mere temperature effect, as we explain in the following.

For the pairing strength $\alpha = 1.44U$, the zero-temperature thresholds for transient decay into or from the 1-state and therefore the condition for a nonzero current amplitude, can be effectively passed by excitations of the Fermi sea around the symmetry point, as $-E_{\eta,\tau} \sim 2k_BT$ holds there, with $2k_BT$ the broadening of the Fermi function. In more detail, the relevant temperature-smeared quantity for the vertical part of the cross in Fig. 5.8(b) is the initial $|1)$-stationary occupation, given by

$$\rho_1 = \frac{f^-_{+-}}{1.5 f^-_{+-} + 0.5}.$$

It follows the shape of the addition energies $E_{\eta,\tau}$ for the corresponding $- \to 1$-transfers, the contributing excitations thereby moving δ-symmetrically into the tail of the Fermi-functions. Therefore, the $|1)$-stationary occupation has a maximum at the symmetry point, decreasing δ-symmetrically to zero (see Fig. 5.8(c)). The transient charge amplitude is then given by $\rho_1 \frac{\gamma_p}{2}$, as the decay occurs off-resonant at the constant ϵ-independent transport rate $\frac{\gamma_p}{2}$, all corresponding energy thresholds being 1.

Let us now discuss the horizontal part of the cross, see Fig. 5.8(b). Differently from the vertical part of the cross, the temperature broadening does not enter the initial $|-)$-occupation, which is off-resonant 1 (either the 0 or the 2-charge state), but the Fermi functions of the transient transport rates enter instead. The charge amplitude is

determined by the $- \rightarrow$ 1-transfers given in the 2nd and 3rd row of Table 3.1 . Both transfers are realized by excitations in the Fermi function f^{-}_{+-}, as the corresponding zero-temperature energy thresholds cannot be fulfilled. The total amplitude is then given by the transport rate

$$a = f^{-}_{+-}(\Gamma_{-} - \Gamma_{+}),$$

see Fig 5.8(c). Differently from the vertical part of the cross, the horizontal part is therefore completely suppressed at the symmetry point, as the $\Gamma_{\pm}$ compensate there. Their difference increases with increasing δ, the excitations moving into the tail of f^{-}_{+-}. These opposite tendencies in the transport rate result in a total reduction of the temperature-induced horizontal charge amplitude as compared to the vertical one, see Fig. 5.8 (c).

In summary of the analysis of the charge current, we provided a detailed understanding of the changes in the current direction. We explained the difference between slow and fast switches as a function of the pairing strength. In particular, we understood that for strong pairing after an adiabatic switch, transport is merely temperature induced.

5.4.3 | Heat current amplitudes

Having discussed the transient charge current amplitudes at zero chemical potential for both switch-scenarios, we will now discuss the amplitudes of the heat current. The heat current is the more relevant spectroscopic tool for Coulomb interaction. In 5.4.3.1, we discuss the amplitudes similarly to the charge amplitudes, at zero chemical potential for the pairing strengths $\alpha = 0.48U$ and $\alpha = 1.44U$. Afterwards, the charge amplitude a_c and the parity amplitude a_p will be further analyzed at nonzero chemical potential in 5.4.3.2. There we will restrict the analysis only to the fast switch scenario, as both scenarios result in less diverse behavior, when there are more excitations in the system. We choose the fast scenario, as the signature of attractive Coulomb interaction in the dual system (previoulsly discussed in Ref. [17]) is specific to this scenario. Finally, we discuss a region of a negative heat current after an adiabatic switch, which is related to the spin-degeneracy of the 1-charge state.

5.4.3.1 | Zero chemical potential

Fast switch: both amplitudes relevant. After a fast switch at zero chemical potential, there are gate parameter regions for which the $|+)$-state is initially populated after the switch, and transient two-particle transport takes place to the final $|-)$-stationary state, see the discussion of the charge amplitude a in 5.4.2.1 . Therefore, not only a_c, but also

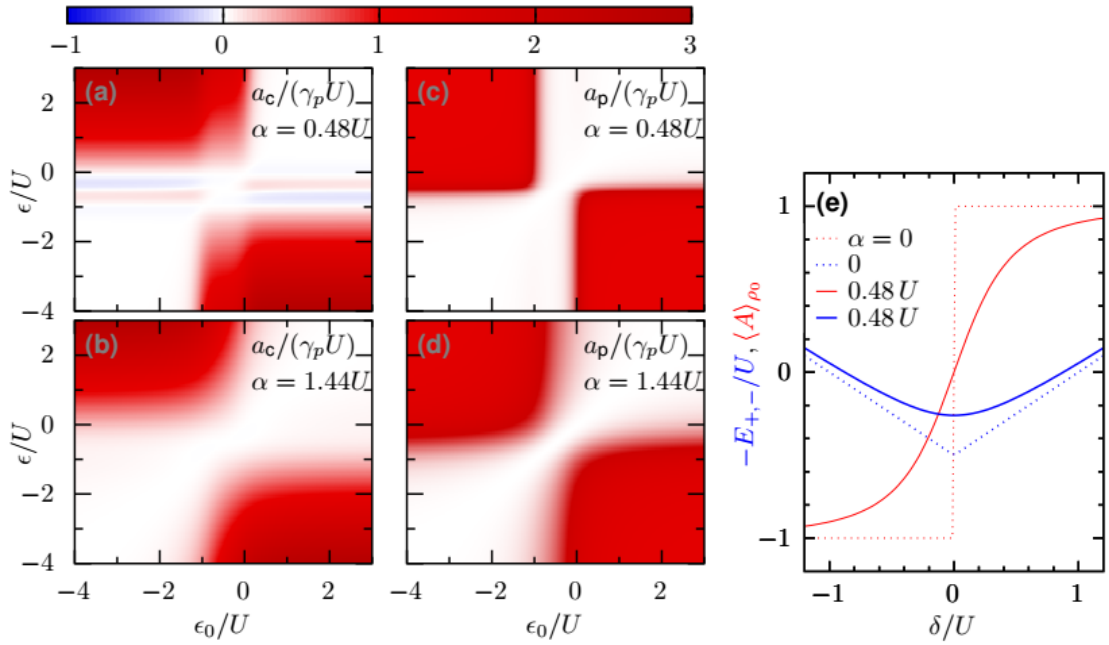

Figure 5.9. Heat current amplitudes after a fast switch at zero chemical potential and temperature $T = 0.1U$: (a) charge amplitude a_c for weak pairing $\alpha = 0.48U$ and (b) a_c for strong pairing $\alpha = 1.44U$; (c) parity amplitude a_p for weak pairing $\alpha = 0.48U$ and (d) for strong pairing $\alpha = 1.44U$. (e) Heat current amplitude a_c decomposed into its factors, $-E_{+,-}$ (blue) and $\langle A \rangle_{\rho_0}$ (red) for the case of weak pairing, $\alpha = 0.48U$ (solid) and the normal conducting case $\alpha = 0$ (dashed). The initial state is off-resonant, $|\rho_0) = |2)$.

the second heat current amplitude a_p plays a role, which accounts for the interaction energy U, a many-particle property. In the following, it is therefore essential to discuss the splitting of the total initial heat current into its two transient amplitudes by analyzing their explicit expressions, which are motivated by duality, see Eq. (4.80b). Here the microscopic physical picture related to the total heat current (transferred addition energies x transport rates) is no longer sufficient to understand the transient decay on different time scales.

Off-resonant region. In the following, we will analyze different regions of the spectroscopy plots in the limit of weak pairing. We start as reference with the region that is off-resonant with the proximity effect. We thereby reproduce results from [17] in the polarization basis that is specific to our setup with a superconductor.
The charge amplitude for $\alpha = 0.48U$ is given in Fig. 5.9(a), (see also the corresponding charge amplitude of the charge current in Fig. 5.6 (a)). We first describe the gate-parameter regions off-resonant with the proximity effect, where two-particle decay takes

place ($\delta_0 < \delta_\pm$, $\delta > \delta_\pm$ or vice versa): They have been previously discussed in [17] in the dot-charge basis in the limit of $\alpha = 0$:

$$a_c = \left[\epsilon + \frac{U}{2}[2 - \langle N_D\rangle_{\bar{z}}]\right] \gamma_c \left[\langle N_D\rangle_{\rho_0} - \langle N_D\rangle_z\right]. \tag{5.22}$$

As expected, our expression for a_c in the Andreev-polarization basis reproduces Eq.(5.22) from [17] in the off-resonant region: Note that the dual system is always in the final $|+)-$stationary state at zero chemical potential, independently of the initial and final gate parameters, see panel (a) of Fig. 5.7 and column 4 of Table (3.1). Therefore, $\langle A\rangle_{\bar{z}} = 1$. Furthermore, $\gamma_{s'} = \gamma_c$ in the charge amplitude a, see Eq.(4.66). Therefore the prefactor in Eq.(4.80b)

$$\frac{1}{2}[\delta_A - U] = \epsilon + \frac{U}{2}[2 - \langle N_D\rangle_{\bar{z}}]$$

can be interpreted as an average energy transported per particle in the same manner as in Ref. [17], while a_p accounts for the interaction energy:

$$a_p = \gamma_p U(\bar{z}P|\rho_0) = (+|+) = \gamma_p U.$$

On-resonant region. We now focus on the gate parameter region, approximately corresponding to the $|1)-$stationary occupation at the initial or final gate parameter, $|\delta_0| \leq \delta_\pm$ or $|\delta| \leq \delta_\pm$, respectively. For simplicity, we restrict the discussion to the left lower quarter of the spectroscopy plots, $\epsilon_0, \epsilon < 0$, the upper right one following from symmetry. We first note that a_c is not symmetric under exchange of initial and final gate parameters: The *horizontal stripe* of the lower left block in a_c is determined by oscillations, see Fig. 5.9 (a), while in the *vertical stripe*, a_c does not change sign. The latter is due to the fact that the initial pure $|1)-$stationary state before the switch does not change during the switch. Afterwards, it decays into the final $|-)$-stationary state via a single electron transfer to the dot. Therefore, a_c merely depends on the final gate parameter ϵ in this region, while a_p as a many-particle property vanishes.

Differently, in the *horizontal stripe*, the initially off-resonant $|2)$-state before the switch, is after the switch transformed into a mixture of Andreev-states $|\rho_0)$, its weights being determined by ϵ. Especially, $|2) \to |\rho_0) = \frac{|+)+|-)}{2}$ at the symmetry point. Therefore, a_c depends crucially on the final gate ϵ via the polarization of the initial state $\langle A\rangle_{\rho_0}$,

$$a_c = \frac{1}{2}[\delta_A - U]\gamma_c\langle A\rangle_{\rho_0} = -E_{+-}\gamma_c\frac{\delta}{\delta_A}. \tag{5.23}$$

Here we used $\langle A\rangle_{\bar{z}} = 1$ and $\langle A\rangle_z \approx 0$ in the final $|1)$-stationary region corresponding to the horizontal stripe and $\gamma_c \approx \gamma_p$ for weak α.

For later comparison let us now explain the origin of Coulomb oscillations in the same

final $|1)$-stationary region at zero superconducting pairing, before we discuss Eq. (5.23) in more detail.

Coulomb oscillations for zero superconducting pairing. In the $\alpha = 0-$limit, a_c increases linearly with δ up to $\frac{U}{2}\gamma_p$ at $\delta = 0$, where it changes sign to $-\frac{U}{2}\gamma_p$. When considering a_c in the charge basis according to Eq. (5.22), it was possible to relate the cusp at $\delta = 0$ to a corresponding step-like change of the dual stationary state from $|0)$ to $|2)$ (note that $(A|\rho_0 = 2) = (N|\bar{z}) - 1$ for $\alpha = 0$). At $\delta = 0$, two charges are simultaneously transferred when varying between *stationary* (rather than transient) states, instead of sequentially traversing the $0, 1, 2$-stationary charge states in the dual system.

This fact can be related to the Coulomb interaction being attractive in the dual system: The dual electrostatic threshold for the $0-2$ transition (short: Coulomb threshold) is given by $\epsilon - \mu = -\frac{U}{2}$, coinciding with the symmetry point at $\mu = 0$, while the corresponding threshold for the $0-1$ transition is shifted to higher gates in the dual system. Therefore, the oscillations of a_c in the final $|1)$-stationary region are a signature of attractive Coulomb interaction in the dual system, see Ref.[17].

Now we explain the changes with respect to the normal conducting reference that are caused by superconducting pairing.

Coulomb oscillations for weak superconducting pairing. The final dual stationary state $|\bar{z}) = |+)$ is in a coherent equally weighted superposition of 0- and 2-charge states at the symmetry point, independently of the strength of α, as long as α fulfills the limits specified in Sec. 3.3 ($\alpha > T$). Varying δ, the charge superposition interpolates between the pure 0- and 2 dual final stationary charge states, which are off-resonant with the proximity effect.

In the same manner, the polarization $\langle A\rangle_{\rho_0} = \frac{\delta}{\sqrt{\delta^2+\delta_A^2}}$ of the initial state $|\rho_0) = |-_0) = |2)$ after the switch, interpolates smoothly between the polarizations -1 and 1 of the $\alpha = 0$-case, when varying δ between the off-resonant regions, see Eq. (5.23) and Fig. 5.6(e) . Especially, it is zero at the symmetry point, when $\rho_0 = |-_0) = \frac{|+)+|-)}{2}$, and the width of the resonant region increases with α. Therefore, the oscillations in a_c get suppressed with nonzero α and hence the signature of the attractive Coulomb interaction in the dual system. We note that the light-blue shaded region in a_c near $\delta = \delta_\pm$ is a consequence of the nonzero temperature, which will be discussed in more detail in 5.4.2.2 and 5.4.3.2. There it shows up in the same manner for the adiabatic switch.

Coulomb oscillations for strong pairing: Further increasing α to the strong pairing regime, the real final stationary state is, apart from thermal smearing, populated in the $|-)-$state, see Fig. 5.9 (b) for $\alpha = 1.44U$. Consequently, the $\langle A\rangle_{\rho_0}$ factor in Eq. (5.23) is shifted by 1,

as $\langle A\rangle_z = -1$ in Eq. (4.80b). Therefore $a_c \geq 0$ and the Coulomb signature is completely suppressed in this pairing regime. Next we go back to the weak pairing regime and discuss the parity amplitude.

Parity amplitude a_p. Differently from a_c, a_p is zero for weak pairing in the *vertical stripe* ($|\delta_0| < \delta_\pm$), see Fig. 5.9(c), as in this region, only single particles are transferred in transient transport between the initial $|1)$-state after the switch and the final off-resonant $|-)$-stationary state.

In the region of the final $|1)$-stationary state (*horizontal stripe*), a_p is determined by the $+$-component of the initial off-resonant $|-_0) = |2)-$stationary state before the switch,

$$a_p = \gamma_p U \frac{1}{2}(1 + \frac{\delta}{\delta_A}).$$

In the final $|1)$-stationary region, a_p therefore interpolates smoothly between 0 in the lower ($\delta < 0$) off-resonant block and 1 in the upper ($\delta < 0$) off-resonant block. At the symmetry point $a_p = \gamma_p \frac{U}{2}$. Therefore, in the same manner as a_c, the step like increase of a_p at $\delta = 0$ from 0 to $\gamma_p U$ in the $\alpha = 0$-limit, (which is a direct consequence of the change between $|0)$-and $|2)$-stationary charge states), gets smeared due to the hybridization of the 0 and 2 charge states in the presence of the superconductor. The region of hybridization and therefore the smearing of the step in a_p further increases with α, see Fig. 5.9(d) for $\alpha = 1.44U$.

Strong pairing and the similarity of a_c and a_p. Finally, we discuss the similarity of a_c and a_p for strong pairing, see Fig.5.9 (b),(d), by giving their explicit forms in this limit of α. First, we note that the real stationary state $|z) = |-)$ for any gate parameters. Furthermore, $\langle A\rangle_{\bar{z}} = 1$ and $\gamma_c \approx \frac{\gamma_p}{2}$. Therefore a_c reads

$$a_c = -E_{+-}\frac{\gamma_p}{2}[\langle A\rangle_{\rho_0} + 1],$$

its δ- and α-dependence entering via δ_A and A_{ρ_0}. For a_p, we use the form given in Eq.(4.81) and note that $\Delta p = 0$, as the final and initial stationary states are always in the even parity sector for any gate parameters. Therefore,

$$a_p = U\frac{\gamma_p}{2}[\langle A\rangle_{\rho_0} + 1]$$

is invariant under the exchange of initial and final gate parameters. So a_c and a_p merely differ in their energy prefactor in the limit of strong α: a_p accounts for U, while $E_{+-} = E_- - \epsilon$ can be considered as the addition energy from the 1 to the $-$ state, which is realized via transfer of a single particle (or hole).

Slow switch: At zero chemical potential, the charge amplitude a_c of the heat current after a slow switch takes a particularly convenient form. As the parity amplitude vanishes, a_c equals the total initial heat current and the duality-motivated expression in Eq.(4.80b) can hence be directly related to a microscopic understanding in terms of transferred particles and associated addition energies $E_{\eta,\tau}$. In this section, we therefore restrict the discussion to a_c in the microscopic picture in analogy to the charge amplitude discussed in 5.4.2.2, for weak (strong) pairing, $\alpha < (>)U$, respectively.

The transient heat current amplitude is determined by the initial state after the switch, by the state transitions possible for the chosen initial and final gate parameters, as well as by the associated transferred addition energy. For an overview of the relevant states, we refer to the discussion of the corresponding charge amplitude in 5.4.2.2, for $\alpha = 0.48U$ and $\alpha = 1.44U$. In contrast to the charge current, the heat current does not depend on the type of transferred charge (particle or hole) during a specific process at zero chemical potential. It takes the following simple form, which applies in general to the adiabatic switch, for weak and strong pairing

$$a_c = -(H_D|W\rho_0) \tag{5.24}$$

$$= -\rho_{0,-}\sum_\eta W^\eta_{1,-}E_{-,-} - \rho_{0,1}\sum_\eta W^\eta_{-,1}E_{+,-}. \tag{5.25}$$

Here, $E_{-,-} = \epsilon - E_-$ and $E_{+,-} = E_- - \epsilon$ denote the addition energies associated with the $- \to 1$ and $1 \to -$ state transitions, respectively, $\eta = \pm$ denotes the type of particle transferred between the metal and the dot.

Limit of weak coupling. For weak coupling, $\alpha = 0.48U$, the vertical part of the cross in Fig 5.10(a) is therefore determined by $-E_{+,-}(\epsilon)$, increasing with increasing distance δ from the symmetry point. Similarly, a line cut through the horizontal part of the cross, is determined by $-E_{-,-}$, see also Fig. 5.7, panel (a). It is therefore reduced in strength compared to the vertical part, as the transient transport takes place near the symmetry point in the horizontal case and far off resonant in the vertical case. Note, that the two sign changes in the horizontal part of a_c are directly related to the corresponding ones in $-E_{-,-}$, while the type of transferred charge remains the same, compare a_c with the charge amplitude a in Fig. 5.8 (a).

The sign changes in a_c are the consequence of a nonzero temperature, which provides excitations of the Fermi sea in gate parameter regions $|\delta| > \delta_\pm$. In this region, transient transport into the $|1)$-state is forbidden according to the zero-temperature energy thresholds in Table 3.1 . The effect can be related to an entropy increase due to the degeneracy of the final $|1)$- state and will be discussed in more detail in 5.4.3.2.

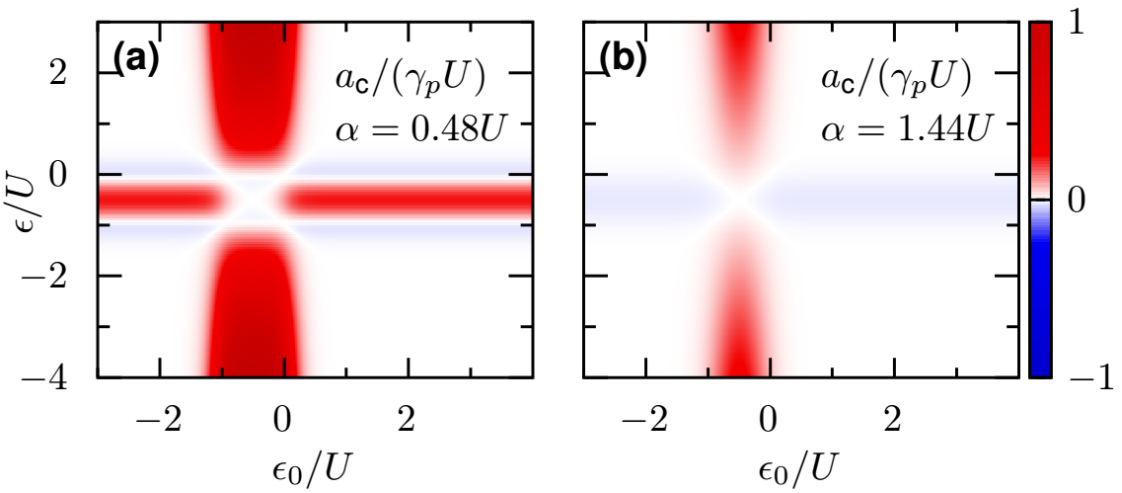

Figure 5.10. Heat current amplitudes after a slow switch at zero chemical potential and temperature $T = 0.1U$: (a) charge amplitude a_c for weak pairing $\alpha = 0.48U$ and (b) a_c for strong pairing $\alpha = 1.44U$. The parity amplitude a_p is zero (not shown).

Limit of strong coupling. For strong coupling, $\alpha = 1.44U$, all charge transfers are enabled by thermal energy, see the discussion of the corresponding charge amplitude in Fig. 5.8(b). The red part of the horizontal region in Fig. 5.10 (a) vanishes with increasing α, as $-E_{-,-}$ is shifted below zero, see panel (b) of Fig. 5.7 . Note that contrary to the previously discussed case of weak pairing, for strong pairing it is the transferred charge, which changes sign with ϵ, while the addition energy remains positive, compare a_c in Fig. 5.10 (b) with the charge amplitude in Fig. 5.8 (b). In the vertical part of the cross in Fig. 5.10 (a), the sign of a_c remains constant with increasing α, as $-E_{+,-}$ does not change sign far off-resonance.

Zero parity amplitude. Finally, we justify the zero parity amplitude after a slow switch at zero chemical potential, thereby referring to its duality motivated form given in Eq. (4.81). After an adiabatic switch, the dual stationary state $\bar{z}$ is independently of the initial and final gates, always in the $|+\rangle$ state for any pairing strength α. This can be concluded from the panels (a)-(b) in Fig. 5.7 and the corresponding allowed dual transitions in column 4 of Table 3.1. In the real system, however, only the $|1\rangle$- and $|-\rangle$-states are populated, as during the switching procedure the $|-\rangle$-state at the initial gate parameter transforms unitarily into the $|-\rangle$-state at the final one, thereby leaving the $|+\rangle$-state unpopulated. Therefore, a_p is zero according to Eq. (4.81). This illustrates the fact that $a_p \propto U$ accounts for the interaction energy, a many-particle property. After the adiabatic switch, the final stationary state is reached via single particle transfer between the metal and the dot. Therefore, no interaction energy is transported and a_p vanishes.

In summary, we have discussed a_c and a_p at zero chemical potential. In this case, the Coulomb threshold, $\epsilon - \mu = -\frac{U}{2}$, which is visible in the heat current amplitudes after the fast switch, coincides with the symmetry point, $\epsilon = -\frac{U}{2}$, where the effect of the superconductor is dominant. We found that the signatures of dual attractive Coulomb interaction in a_c and a_p get suppressed at sufficiently large superconducting pairing. In the following, we split these two interaction effects in parameter space by applying a suitable chemical potential. The effect of the dual attractive Coulomb interaction is then unaltered compared to the purely normal conducting system of a metal and a quantum dot [17], as it occurs in the off-resonant region of the parameter space. Therefore, in the following, we restrict the discussion to the gate parameter regions, where the superconductor is resonant with the proximity effect.

5.4.3.2 | Nonzero chemical potential-for a fast switch

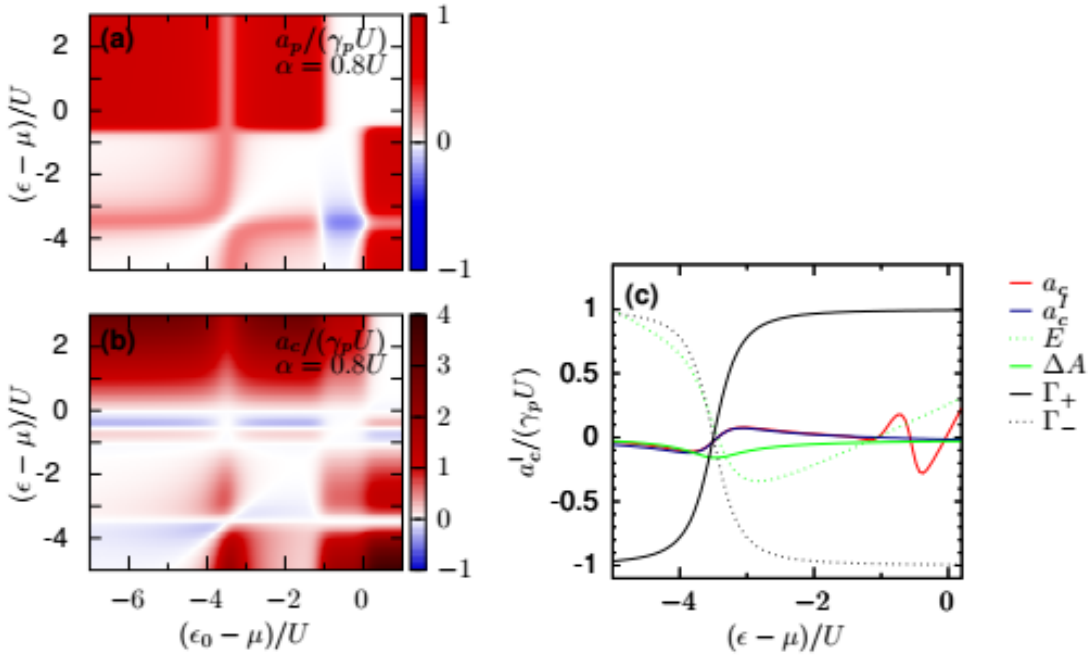

Figure 5.11. Charge amplitudes of the heat current (a) a_c and (b) a_p after a fast switch at the chemical potential $\mu = 3.0\,U$ and temperature $T = 0.1U$. The pairing is weak, $\alpha = 0.8U$. (c) Approximation of the S-shape of a_c (red) near the final symmetry point $\epsilon = -\frac{U}{2}$ by the result a_c^{I} (blue) from an effective master equation. The energy factor E (dashed green) and polarization factor ΔA (solid green) that contribute to a_c^{I} are given separately, as well as the tunneling rates $\Gamma_\pm$ (black), the latter offset for clarity.

Stationary limit. In the high bias regime, $|\mu| \geq \frac{U}{2}$, all energy basis states $+, -, 1$ can be populated in the stationary limit when varying the gate, if the pairing α is chosen to be weak, $\alpha < \alpha_{sign(\mu)}(\delta = 0)$, see panel (c) of Fig. 5.7. Especially, at the symmetry point, the system is in a mixture of all states, $\frac{1}{4}[|+) + |-)] + \frac{1}{2}|1)$, which is also identical to the dual stationary state at this point.

Charge amplitude: choice of chemical potential to preserve Coulomb oscillations. The Coulomb-oscillations are specific to the region of moderate detuning (short the II-region), $\delta_+ < \delta < \delta_-$, see panel (c), Fig. 5.7, where the real stationary state is the $|1)$-state and the dual stationary state changes from 0 to 2, (here $+$ to $-$) with increasing δ. Note that in this region a_c in Eq. (4.80b) can be written as

$$a_c^{\mathrm{II}} \approx \begin{cases} -\gamma_p[\mu - E_{++}] & \text{if} \langle A \rangle_{\bar{z}} = -1, \\ -\gamma_p[\mu - E_{--}] & \text{if} \langle A \rangle_{\bar{z}} = 1. \end{cases} \tag{5.26}$$

Here we used $\langle A \rangle_z = 1$, $\langle A \rangle_{\rho_0} = 1$ and off-resonant transport rates, $\gamma_{s'}^{II} \approx \gamma_c \approx \gamma_p$ as $\Gamma_+ \approx 1$. In order to maintain the Coulomb oscillations in a_c, $A_{\bar{z}}$ has to change sign at the final gate parameter $\epsilon_{\mathrm{Coul}} = \mu + \frac{U}{2}$, the center of the II-region, compare Eq.(5.26) for a_c^{II} with the addition energies in panel (c), Fig.(5.7). This is the case if the final dual stationary state $|\bar{z})$ of the II-region is separated well enough from the proximity effect of the superconductor, which is dominant near the symmetry point. In order to achieve this, μ has to be chosen large enough and simultaneously α small enough, such that $\Gamma_+ \approx 1$ in the II-region. Otherwise, the dual final stationary state tends to be the $|+)$-state instead of the $|-)$-state for the whole II-region of moderate pairing. For an explanation, see the transport chain $-, 1, +$ associated with the Γ_--rate, in rows 1 and 2 of Table 3.1. Only in the I-region of weak pairing, $\delta < \delta_+$, the stationary state is $|-)$ according to the zero temperature thresholds in Table 3.1. Therefore, the characteristic change in $\langle A \rangle_{\bar{z}}$ from -1 to $+1$ is shifted to δ_+ instead of δ_{Coul}. This leads to a suppression of the first peak in a_c and hence the Coulomb oscillations, see the relevant addition energies E_{++} and E_{--} in panel (c) of Fig. 5.7. To maintain both peaks in a_c, we therefore choose $\mu = 3.0U$ and $\alpha = 0.8U$, see Fig. 5.11 and the temperature $T = 0.1U$ high enough to stabilize the $|-)$-occupation in the II-region of moderate pairing. This way we see the impact of pairing and attractive Coulomb interaction in the dual system independently.

Resonant transport. Having separated the impact of attractive dual Coulomb interaction from the symmetry point (PHS) in parameter space, we now restrict the discussion to the modifications in a_c introduced by the superconductor, along the horizontal line $\epsilon \approx \epsilon_{\mathrm{PHS}}$ and the vertical one, $\epsilon_0 \approx \epsilon_{\mathrm{PHS}}$.

S-shape for $\epsilon \approx \epsilon_{PHS}$. For ϵ_0 far off-resonant, here $\epsilon_0 \ll \epsilon_{\rm PHS}$, a_c is approximately zero at the symmetry point, $\epsilon = \epsilon_{\rm PHS}$, as $\langle A\rangle_{\rho_0} \approx 0$ and $\langle A\rangle_z \approx 0$ there, and as well in the off-resonant regions near the symmetry point. In the region between these off-resonant regions, that is the I-region of weak pairing, it is nonzero and changes shape following an S-shape (see the line cut in Fig. 5.11(c)). The scale on which a_c changes sign is determined by α, as we will show below. It is hence larger than the scale of the Coulomb oscillations, which is determined by temperature, as $\alpha > T$, in the limits of our model of Sec. 3.3.

More concretely, let us derive an effective master equation for the resonant region $\delta \approx \delta_{\rm PHS}$, $|\delta_0| \gg \delta_{\rm PHS}$ based on the zero-temperature thresholds in Table 3.1, as $\mu - E_{\eta,\tau} \gg 0$ for all η, τ in the high-bias regime. As a result, we find

$$\langle A\rangle_z = \frac{\delta}{\delta_A},\ \gamma_s' = \frac{\gamma_p}{2}\frac{\delta}{\delta_A}, \tag{5.27}$$

$$\langle A\rangle_{\bar z} = -\frac{\delta}{\delta_A},\ \gamma_c = \frac{\gamma_p}{2}, \tag{5.28}$$

see App. H and

$$a_c^{\rm I} = \left[\left[\tfrac{\delta_A}{2} - \tfrac{U}{2}\langle A\rangle_{\bar z}\right]\gamma_c - \mu\gamma_s'\right]\left(\langle A\rangle_{\rho_0} - \langle A\rangle_z\right) \tag{5.29}$$

$$= \tfrac{\gamma_p}{2}\left[\tfrac{\delta_A}{2} + \tfrac{\delta}{\delta_A}[\tfrac{U}{2} - \mu]\right]\left(\langle A\rangle_{\rho_0} - \tfrac{\delta}{\delta_A}\right). \tag{5.30}$$

Here, $|\rho_0)$ corresponds to the initial off-resonant $|-_0)$ state before the switch, as we consider $\epsilon_0 \ll \epsilon_{\rm PHS}$. The polarization difference can therefore be approximated by

$$\langle A\rangle_{\rho_0} - \langle A_z\rangle = -\left(\frac{\delta}{\delta_A}(1 + \frac{\delta_0}{\delta_{A_0}}) + \frac{\alpha^2}{\delta_{A_0}\delta_A}\right) \approx -\frac{\alpha^2}{\delta_{A_0}\delta_A}, \tag{5.31}$$

leading to the total charge amplitude of the heat current in the final resonant region (Fig. 5.11 (c))

$$a_c^{\rm I} = -\frac{\gamma_p}{2}\left[\frac{\delta_A}{2} + \frac{\delta}{\delta_A}\left[\frac{U}{2} - \mu\right]\right]\frac{\alpha^2}{\delta_{A_0}\delta_A}. \tag{5.32}$$

Note that the S-shape of $a_c^{\rm I}$ is caused by simultaneous sign changes in $\langle A\rangle_{\bar z}$ and γ_s' at the symmetry point. At the PHS, $a_c^{\rm I} = -\frac{\alpha^2\gamma_p}{4\delta_{A_0}}$. $a_c^{\rm I}$ has a max/min at $\delta = \pm\alpha$, respectively, determining the scale of the oscillations.

Peak/dip for $\epsilon_0 \approx \epsilon_{PHS}$. When the superconductor is resonant with the proximity effect before the switch, $\epsilon_0 \approx \epsilon_{\rm PHS}$, and off-resonant after the switch, $\epsilon \gg (\ll)\epsilon_{\rm PHS}$, its effect results in a suppression (enhancement) of a_c at the symmetry point, respectively, see Fig. 5.11 (b). When ϵ is fixed and so the energy prefactor in Eq.(5.30), the variation of a_c is determined by the polarization difference $\Delta A := [\langle A\rangle_{\rho_0} - \langle A\rangle_z] = [\langle A\rangle_{\rho_0} + 1]$ as a

function of ϵ_0. For any fixed value of $\epsilon \ll 0$, there is a peak in a_c, see Fig. 5.11, which can be explained as follows: For ϵ_0 near the PHS, but off-resonant with the proximity effect, $|\rho_0) = |-)$ and $\Delta A = 0$. In comparison, for $\epsilon_0 = \epsilon_{\text{PHS}}$, $|\rho_0) = \frac{1}{4}[|+) + |-)] + \frac{1}{2}|1)$ and $\Delta A = 1$, leading to an enhancement. Differently, for any fixed value of $\epsilon \gg 0$, $|\rho_0) = |+)$ near the PHS and $\Delta A = 2$, while $\Delta A = 1$ for $\epsilon_0 = \epsilon_{\text{PHS}}$, resulting in a dip.

Parity amplitude. From now on, we will turn to the parity amplitude. Similarly to the charge amplitude, the superconductor modifies the parity amplitude with respect to the normal conducting case along the vertical and horizontal lines, $\delta_{(0)} = 0$, see Fig. 5.11 (a).

Horizontal line, $\delta = 0$. We evaluate a_p according to Eq.(4.81), as given by the overlap of the final dual stationary state and the initial one. At $\delta = 0$,

$$(P\bar{z}| = \frac{1}{4}[(+| + (-|] - \frac{1}{2}(1|,$$

while $|\rho_0) = \frac{1}{2}[|+) + |-)]$ or $|1)$ when off-resonant, ($\delta_0 \neq 0$), corresponding to $(\bar{z}P|\rho_0) = \frac{1}{4}$ (red region) or $-\frac{1}{4}$ (blue region), respectively. On resonance ($\delta_0 = 0$), $|\rho_0) = \frac{1}{4}[|+) + |-)] + \frac{1}{2}|1)$ and hence $(\bar{z}P|\rho_0) = 0$. The negative overlap in the initial $|1)$-stationary region is a consequence of all energy states being populated in the dual stationary state at the symmetry point, and hence a property of the two-terminal setup. We note that the region of the initial $|1)$-stationary occupation is a region of pure transient parity decay, as $\Delta A = 0$ in this region, see Eq.(4.80b).
Vertical line, $\delta_0 = 0$. If the final gate parameter is off-resonant with the proximity effect, $|\rho_0) = \frac{1}{4}[|+) + |-)] + \frac{1}{2}|1)$. Furthermore, $(\bar{z}P| = (+|$ (or $(-|$) off-resonant. Therefore, as $(\bar{z}P|\rho_0) = \frac{1}{4}$ when ϵ off-resonant, a_p is suppressed by a factor of $\frac{1}{4}$ in the $\delta \gg 0$ off-resonant region and increases up to a finite value of $a_p = \frac{\gamma_p U}{4}$ for $\delta \ll 0$, where it is otherwise zero, when varying the initial gate. At the symmetry point, $\epsilon = \epsilon_{\text{PHS}}$, $(\bar{z}P|\rho_0) = 0$, see Fig. 5.11(b).

In summary, the suppression or enhancement of a_p at the symmetry point along $\delta_0 = 0$ ($\delta = 0$) is therefore a consequence of the $|1)$-state being occupied in the stationary limit in the real (dual) system, respectively.

Some remarks are in order with respect to strong pairing and the stationary current, though we do not discuss them in more detail.

Strong pairing.: So far, we discussed the heat current amplitudes for weak pairing α in the high-bias regime $\mu > \frac{U}{2}$. We finally note that sweeping α to a stronger pairing

regime, more energy-basis states get depopulated in the stationary limit and transient transport resembles the one of the low bias regime. The previously discussed structure of peaks and dips in a_c and a_p of Fig. 5.11 (a)-(b) disappears, as the $|1)$-state is no longer populated at the symmetry point, when increasing α to the strong pairing regime.

Stationary current $\mu I_N(\infty)$. At nonzero chemical potential, there is the possibility for a

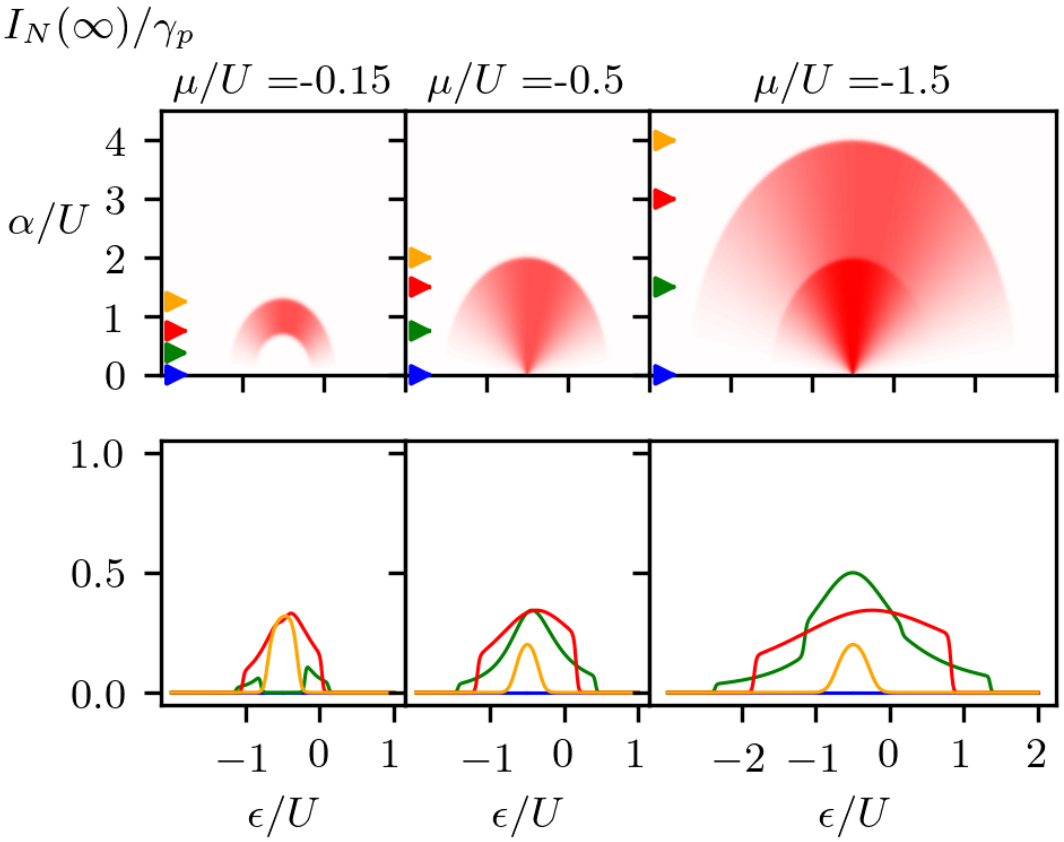

Figure 5.12. Stationary charge current $I_N(\infty)$ with horizontal line cuts indicated by the corresponding arrows. Parameters and conventions are the same as in Fig. 5.3.

nonzero stationary current, when the final stationary state is in a mixture of at least two energy eigenstates. For strong pairing, a stationary current is hence absent in all bias regimes [Fig. 5.12], see also Fig. 5.7 (b) and Table 3.1, whereas it is present for moderate pairing and detuning [Figs. 5.12 (a), green line and 5.7 (d)]. In the high bias regime, it is also present for weak pairing, along the symmetry point $\delta = \delta_{\mathrm{PHS}}$, when all energy states are occupied [Fig. 5.7 (c)].

Depending on the direction of the bias, electrons or holes are transferred from the metal to the dot via the transport chain $|\pm) \rightarrow |1) \rightarrow |\pm)$ (see Fig. 5.12). In the

intermediate pairing regime, the stationary mixture of the resonant region is composed of the $|-)$- and $|1)$-stationary states. The strength of the current decreases at the symmetry point for intermediate pairing, as the larger occupied $|1)$-state ($z_1 = \frac{2}{3}$) contributes to the current at half the rate of the less occupied $|-)$-state. This is a consequence of spin degeneracy. Furthermore, the δ-region of nonzero stationary current broadens with α, as the resonant region broadens, compare green and red lines in Fig. 5.12, right panel. Further increasing α within the moderate pairing regime, the current peak reduces again in width, as the region of moderate detuning reduces (see the red circle and yellow curves in Fig. 5.12).

The overall δ-dependence of $I_N(\infty)$ (4.69) is a Lorentzian peak of width $\alpha/2$, which has been discussed in prior work [71, 79, 86, 87]. In our compact analytical expression, the prefactor contains merely the components κ of the duality invariants. Hence it reproduces the bias asymmetry and nontrivial modifications due to the Andreev states, which is reflected in the step-like behavior of the green and red lines in Fig. 5.12, when changing to another regime of detuning, where different Andreev states are involved in the transport.

5.4.3.3 | Slow switch: spin degeneracy and entropy

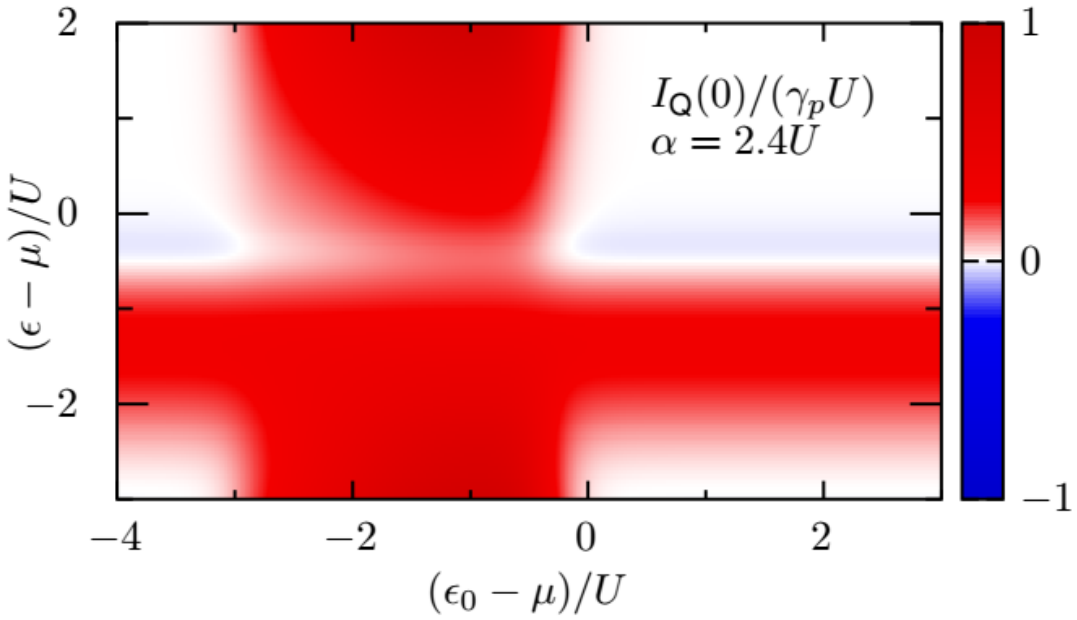

Figure 5.13. Initial total heat current after a slow switch at the chemical potential $\mu = 1.2U$ and temperature $T = 0.1U$. The pairing is $\alpha = 2.4U$.

Finally, we discuss how the spin-degeneracy of the $|1)$-state is related to the entropy change of the quantum dot according to the Maxwell-relation, when changing into the $|1)$-stationary state. We apply the discussion of Ref. [88] to our example of the initial heat current after an adiabatic switch in the high bias regime $\mu = 1.2U$, for intermediate pairing $\alpha = 2.4U$, see Fig. 5.13.

Negative heat current. As can be seen in Fig. 5.13, there is a small amount of heat current flowing out of the metal (blue shaded region) for $\delta \approx 0$ [$\epsilon \approx -U/2$] at the boundary between the $|1)$- and $|-)$-stationary occupations, while it otherwise flows into the metal. For clarity of the discussion, we fix $\delta_0 \ll 0$, off-resonance, such that the initial stationary $|-_0)$-state evolves into $|-)$ during the adiabatic switch. Subsequently, in the left horizontal part of the cross, $|\delta| < \delta_-$, $|-)$ decays into the $|1)$-state, as the final stationary state is in a mixture of the $|-)$-and the $|1)$-state in this interval of δ, see also panel (d) of Fig. 5.7. According to Table 3.1, row 3, the relevant process, which contributes to the heat current, is therefore given by

$$I_Q = -(H_D - \mu N|W\rho) \tag{5.33}$$

$$= -[p_- W^-_{1,-}[E_{-,-} - \mu]]. \tag{5.34}$$

The quantity $E_{-,-} = \epsilon - E_-$ is the addition energy for the $- \to 1$-transition. As can be seen from panel (d), Fig. 5.7, $\mu - E_{-,-} > 0$ for $|\delta| < \delta_-$, hence the heat current is positive. At nonzero temperature, however, the addition energy for the $0 \to 1$-transition can be carried away from the reservoir by excitations above the chemical potential of the reservoir, $E_{-,-} - \mu > 0$. Therefore, $I_Q < 0$, when the zero-temperature threshold is passed, see also the discussion in section 5.4.3.1 . Now, we relate the transport at this threshold to the entropy change of the quantum dot, when *changing between stationary (not transient) states by varying* δ.

Determining the entropy change from a change in the chemical potential. Following the argumentation in [88], the quantity $[E_{--} - \mu]$ can be related to the entropy by starting from the Maxwell relation:

$$\left(\frac{\partial \mu_N}{\partial T}\right)_{p,N} = -\left(\frac{\partial S}{\partial N}\right)_{p,T}. \tag{5.35}$$

Here, $\partial\mu_N/\partial T$ denotes the change in the chemical potential of the quantum dot and $\partial S/\partial N$ the entropy change of the metal. The quantity μ_N equals the addition energy needed to transfer the Nth electron to the dot, which is in our setting $\mu_1 = \epsilon - E_- = E_{-,-}$. Its temperature dependence is determined by the temperature-dependent gate voltage

$\epsilon(T)$, for which the transition between the stationary $|1)$-state and the stationary $|-)$-state occurs, i.e., for which $z_- = z_1 = \frac{1}{2}$. At $T = 0$, the transition occurs at the chemical potential of the metal, $\mu_1^{(T_0=0)} = E_{--}(\epsilon_{T_0}) = \mu$, which coincides with the final gate voltage ϵ_{T_0}, at which the transient heat current $I_Q(t = 0)$ changes sign, see Eq. (5.34). In evaluating the shift in chemical potential with temperature,

$$\frac{\Delta\mu}{\Delta T} = \frac{\mu_1^{(T_1)} - \mu_1^{(T_0)}}{T_1 - T_0} = \frac{\mu_1^{(T_1)} - \mu}{T_1},$$

the addition energy $\mu_1^{(T_1)} = E_{--}(\epsilon_{T_1})$ and corresponding gate voltage ϵ_{T_1} remain to be further specified by the master equation in the stationary limit: At the final gate parameter ϵ_{T_1}, a transition between stationary states $1, -$ corresponds to probabilities $z_- = z_1 = \frac{1}{2}$. With the two contributing processes in the third row of Table 3.1, it follows:

$$d_1 \frac{\Gamma_+}{2} f\left(\frac{E_{-,-}(\epsilon_{T_1}) - \mu}{T_1}\right) z_- = d_- \frac{\Gamma_+}{2}\left[1 - f\left(\frac{E_{-,-}(\epsilon_{T_1}) - \mu}{T_1}\right)\right] z_1. \tag{5.36}$$

Note that the $- \to 1$-transition is realized by the transfer of an electron to the dot and vice versa via a hole. The tunnel rates into the dot (metal) are determined by $\frac{\Gamma_+}{2}$ and the degeneracy of the final state, which is $d_1 = 2$ for the $|1)$-state and $d_- = 0$ for the final $|-)$-state. Finally, according to Eq. (5.36), we identify

$$\frac{\mu_1^{(T_1)} - \mu}{T_1} = \frac{E_{--} - \mu}{T_1} = \ln d_1 - \ln d_- = \Delta S_{N-1\to N}, \tag{5.37}$$

with $\Delta S_{N-1\to N}$ the change in von Neumann-entropy with the particle number. This means: If we derive the entropy change as the change of the chemical potential with temperature according to the Maxwell relation (familiar from macroscopic quantities), the result takes the form of the von Neumann-entropy in terms of the microscopic spin degress of freedom of the quantum dot. Here, the entropy change occurs upon a change between the stationary states.

A further step would be to analyze the possibility of entropic shifts in the resonant parameter dependence of the transient transport, such as the temperature-induced shift of the step in the parity amplitude, when it is plotted against the gate voltage. We postpone such a discussion to future work.

5.5 | Conclusions and Outlook

In a normal conductor-dot-superconductor system we have considered transient charge and heat currents from an arbitrarily prepared initial state. By means of the dissipative

symmetry that is fermionic duality, we expressed transient transport observables of charge and heat in terms of stationary expectation values.

It should be noticed that two different time scales are involved in the transient dynamics, set by the charge decay rate and the parity decay rate. The parity decay rate is not affected by the superconductor and a mere interface property. Without the superconductor, the charge decay rate approaches its maximum value (equal to the parity rate) in the gate region of the single-occupied (and hence repulsive) dot. In the presence of the superconductor, the charge decay rate decreases below the parity rate in this region and therefore the two amplitudes of the transient heat decay are distinguishable.

We identified three types of non-monotonic heat currents, where the non-monotonicity was characterized by a single parameter R. They differed in the type and number of local extrema and the way they saturated to their stationary values. As initial states, we studied in particular two complementary gate switch scenarios, a slow and a fast switch. At zero chemical potential both scenarios show clear differences in the transport properties. In the fast switch, both the charge and parity amplitudes of the heat current are non-vanishing, they reflect single and multiple particle properties, respectively.

In the fast switch we identified the superconductor and the repulsive Coulomb interaction as opposing each other. The typical features of (dual attractive) Coulomb interaction in the charge and parity amplitudes of the heat current get washed out by the superconducting pairing α at zero chemical potential, when the effect of both type of interactions cannot be separated in parameter space.

In the slow switch the parity amplitude vanishes at zero chemical potential, as only two out of three stationary states are populated. In the charge amplitude of the heat current, there is no "off-diagonal" current, that means, switching the gate voltage between the regions, where the dot is empty or doubly occupied in the stationary limit, does not cause any current. The reason is that charge has already been exchanged with the superconductor during the initialization of the state. For non-zero chemical potential the transport resulting from both switch scenarios is more similar, since all states of the quantum dot can be populated.

As we have shown, it is possible to analyze the corresponding spectroscopy plots in a systematic way by considering the zero-temperature energy thresholds for transport and the associated particle transfers. Instead of searching for interesting features by scanning a four-dimensional parameter space, this analysis allows us to project on characteristic changes in the observables of interest. In particular we can predict the direction of currents, from the metal to the dot or vice versa. Thus, we have achieved a detailed microscopic understanding of particle transfer processes involved in the heat and charge current, and more generally, the time evolution of the density matrix for the

dot-superconductor system.

In general these results allow to control heat currents in superconducting nano-devices when NDS are used as building blocks. In future work it is of interest to study the thermoelectric response of such a device, characterized by its thermoelectric response coefficients. In particular it will be of interest to explore how the previously studied results for an NDN-system [18] change in the presence of the superconductor.

6

NDS device with a negative-U quantum dot

So far we have analyzed an NDS-system with a quantum dot with repulsive Coulomb interaction between the electrons on the quantum dot. Recall that the repulsive Coulomb interaction on the QD is related to the charging energy of adding an electron to the QD by $U = 2E_C$. Next we are interested in the case of effectively attractive Coulomb interaction between the electrons on the QD. Such quantum dots with attractive interaction between the electrons can actually be realized [11–14]. We give two realizations with different mechanisms behind the tuning of the interaction.

In the first one the tuning mechanism is well understood and similar to the repulsive case above, it can be understood based on the electrostatic energy balance of the device: The two electrons which effectively are exposed to an attractive interaction are each assigned to a dot of a quantum double dot which is the system. The attractive interaction is then realized by capacitive coupling to an auxiliary polarizer double QD [14, 89]. The interaction is attractive in the sense that the addition energy to add a second electron to the second system dot is lowered as compared to the one for adding the first electron to the first dot, as the first one has to excite the state of the polarizer quantum dot system to obtain the ground state configuration of the device. If this energy is chosen to be larger than the Coulomb repulsion energy to be paid by the second electron, one obtains effective attractive interaction between the electrons on the system dots.

The second example refers to a realization of a quantum dot in an oxide hetero structure at the interface of $LaAlO_3/SrTiO_3$ [11], in which the underlying mechanism for the attractive interaction of the electrons on the dot (local pairing) is not known. The second example is more interesting from the perspective of fundamental physics. Such a quantum dot which can be realized at the interface between $LaAlO_3$ and $SrTiO_3$ can be modeled by a negative U-Anderson model as confirmed by the measured transport

spectroscopy when the QD is attached to normal leads in the geometry [11]. The negative U-Anderson model plays an important role in explaining local preformed pairing of electrons without a global superconducting phase, which is important for unconventional high-T_c superconductors and in contrast to the Cooper pairs in conventional BCS-superconductors which form simultaneously with the superconducting phase transition. The attractive properties of this NDN-device is reflected in the measurable transport spectroscopy. For example, a pronounced difference to repulsive quantum dots is visible in the excitation spectrum and the appearance of an energy gap at low bias voltage.

In our project we assume that one can experimentally realize an NDS device (rather than NDN), but also with attractive effective Coulomb interaction on the QD, that is, a negative sign is assumed in the Anderson model of Eq. (3.14). Note that in our NDS-device we have additional electron-pairing induced on the QD by the BCS-superconductor attached. Therefore it is interesting to study the interplay of these types of pairing mechanisms.

We further note that for the understanding of the transport characteristics of an NDN-device it was necessary to include next-to-leading order perturbation theory in the tunnel coupling between the quantum dot and the leads [11]. As an example the temperature dependence of the low-bias conductance in the weak-tunneling regime was explained by a combination of second-order pair tunneling and thermally excited sequential tunneling. Hence the temperature dependence was different from conventional (repulsive) QDs with transport being dominated by sequential tunneling only in the corresponding regime. Nevertheless we restrict in the following to a treatment of the dynamics of our device to leading order in the tunnel coupling to identify the effect of the leading order.

6.1 | Master equation and transport regimes

6.1.1 | Overview of transport regimes

First we note that the eigenstates (3.19) remain valid for the case of negative U in the Anderson model. In the sequential tunneling regime possible state transitions occur between even and odd parity states of the hybridized QD. All thresholds and associated processes of Table 3.1 remain valid with the Coulomb interaction $U \to -U$ in the addition energies $E_{\kappa,\kappa'}$, and tunneling rates $\Gamma_\pm$, see Table 6.1. However, in the panels of Fig. 5.7, the labels change as displayed in Fig. 6.1. In the following we restrict to analyze a few adiabatic switching scenarios based on Table 6.1 and Fig. 6.1 to compare them with

$\kappa\kappa'$	threshold	coupling rate	real transition $\overset{e}{\underset{h}{\rightleftarrows}}$	dual transition $\overset{h}{\underset{e}{\rightleftarrows}}$
$-+$	$\mu - E_{-+} \gtrless 0$	Γ_-	$+ \rightleftarrows 1$	$1 \rightleftarrows +$
$+-$	$\mu - E_{+-} \gtrless 0$	Γ_-	$1 \rightleftarrows -$	$- \rightleftarrows 1$
$--$	$\mu - E_{--} \gtrless 0$	Γ_+	$- \rightleftarrows 1$	$1 \rightleftarrows -$
$++$	$\mu - E_{++} \gtrless 0$	Γ_+	$1 \rightleftarrows +$	$+ \rightleftarrows 1$

Table 6.1. Overview of all possible real and dual transitions between $+, -, 1$-states of the hybridized quantum dot. They are constrained by corresponding energy thresholds at zero temperature and have coupling rates $\Gamma_\pm$ (see Fig. 6.1). $\rightleftarrows$ corresponds to $\gtrless$ in column 2 and refers to an $\overset{e}{h}$ ($\overset{h}{e}$)-transfer from the metal to the dot in the real (dual) system, respectively. Note that this table is identical to Table 3.1 of Chap 3 and displayed here again for completeness.

the corresponding figures for the repulsive quantum dot. It should be mentioned that the state evolution and the transport currents of the new attractive system are given by Eqs. (4.60) and (4.67), (4.80b) with a simple inversion of the sign of U.

6.1.2 | Accounting for finite temperature

Before we discuss slow switches we want to draw the attention to a subtle point in deriving the gate-dependent stationary states based on zero temperature energy thresholds as indicated in Table 6.1. The subtlety is specific to the real system of the negative-U case and the dual system of the repulsive case. Concretely we refer to the transition between the two even-parity states $+$ and $-$ as a function of detuning δ. Such a region is given for values $-\delta_+ < \delta < -\delta_-$ in panel (c) of Fig. 6.1, i.e., the high-bias regime for weak pairing α.

In the following we term the interval $-\delta_+ < \delta < -\delta_-$ region A. Let us assume in the following that the pairing α is weak enough such that $\Gamma_- \approx 0$ in region A and hence its impact can be neglected. Based on the zero-temperature thresholds we would conclude that transitions are directed out of the 1-state from the odd to the even parity sector, i.e., $1 \to -$ and $1 \to +$ at equal rates $\Gamma_+/2$. However, this does not allow to conclude

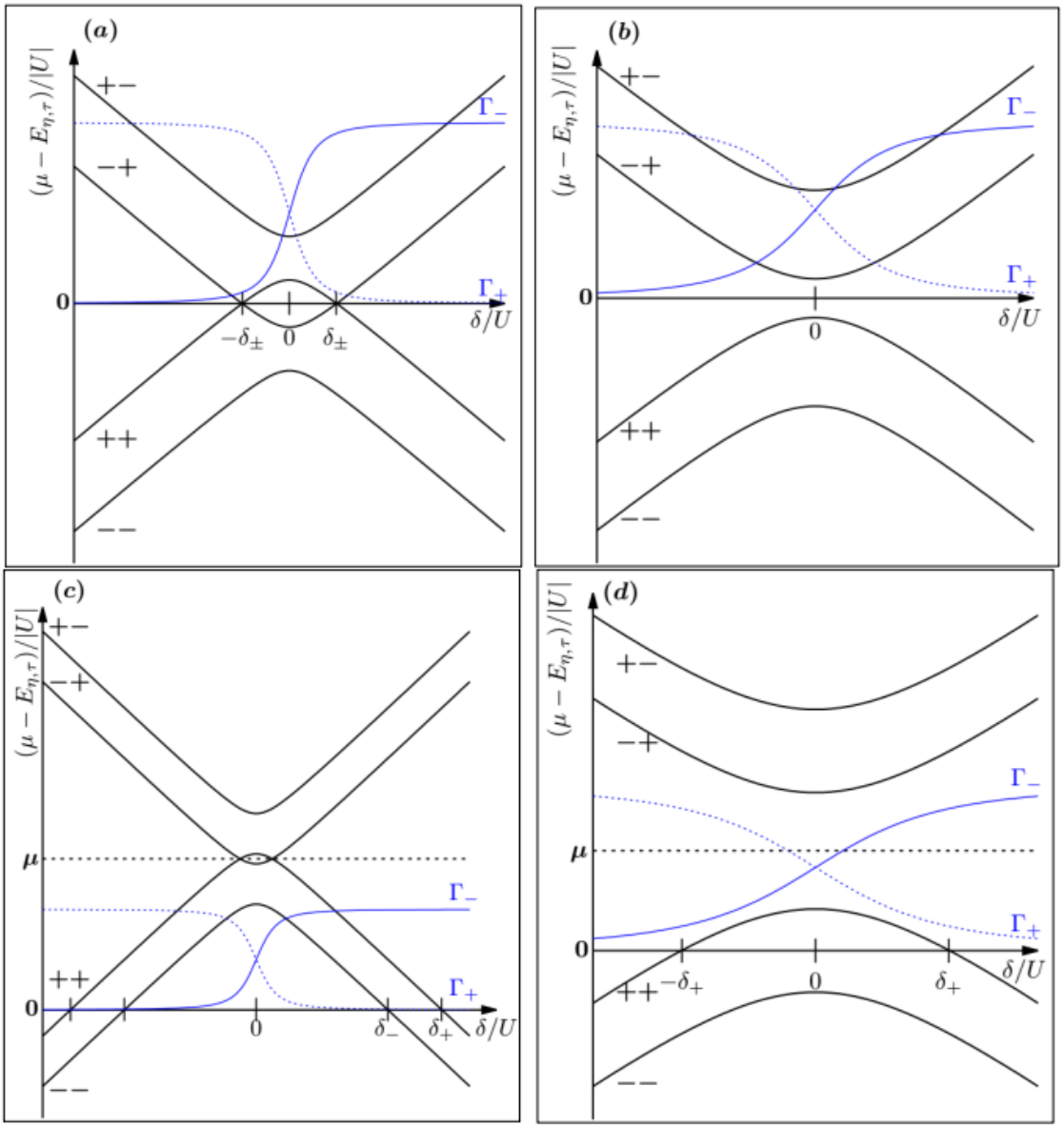

Figure 6.1. Schematic overview of zero temperature energy thresholds $\mu - E_{\eta,\tau}$ (Table 6.1) for the cases of (a) $\mu = 0$ and weak pairing α, (b) strong α, (c) $\mu > 0$ and weak α and (d) moderate α. $\delta_\pm$ specifies the region of detuning, as introduced in Sec. 5.2.1. Note the modification of labels compared to Fig. 5.7 for the positive-U case.

the occupations of the even-parity state sector in the stationary state. Their precise functional dependence of detuning is governed by temperature and pairing. Instead we can account for finite temperature by deriving an approximate master equation based

on the relevant processes as given in the rows 3 and 4 of Table 6.1, column 4:

$$0 = \frac{d\rho_+}{dt} = \rho_1 \frac{\Gamma_+}{2} f(E_{+,+} - \mu) - \rho_+ \Gamma_+ f(\mu - E_{+,+}) \tag{6.1}$$

$$0 = \frac{d\rho_-}{dt} = \rho_1 \frac{\Gamma_+}{2} f(\mu - E_{-,-}) - \rho_- \Gamma_+ f(E_{-,-} - \mu), \tag{6.2}$$

with $f(x) = \frac{1}{exp(x/T)+1}$ the Fermi function. This leads to the ratio of stationary occupations

$$\frac{\rho_+}{\rho_-} = \frac{f(E_{+,+} - \mu)}{1 - f(E_{+,+} - \mu)} \frac{1 - f(\mu - E_{-,-})}{f(\mu - E_{-,-})}. \tag{6.3}$$

Finally we are able to extract the detuning value

$$\delta_{1/2} = -\sqrt{(T \ln(2) + 2\mu)^2 - \alpha^2}, \tag{6.4}$$

for which the ratio $\frac{\rho_+}{\rho_-} = 1/2$ and hence the transition between the states $+$ and $-$ occurs. Note that in Eq. (6.4) α enters via the addition energies, and not due to the hybridization as we assumed $\Gamma_- \approx 0$. Furthermore, the $\ln 2$-factor does not enter due to the spin-degeneracy of the 1-state, as this cancels out in the ratio $\frac{\rho_+}{\rho_-}$, cf. with the master equation (6.2). Instead, it is relevant to the requirement that $\rho_+/\rho_- = \frac{1}{2}$. Therefore, here the spin-degeneracy does not play an analogous role as in the previous discussion on the entropy of Sec. 5.4.3.3, where the transition between stationary states from the even and odd parity sector was discussed.

In the A-region the temperature induced $+-$ transition is associated with a steplike change in the parity amplitude after a fast switch and could therefore serve for analyzing the precise temperature dependent variation of the detuning value, at which the step occurs. However, in the following we will not further pursue with the discussion of fast switches and continue with the discussion of slow switches instead.

6.2 | Charge amplitudes after a slow switch

In Sec. 5.4.2.2 we discussed the transient charge current after a slow switch for positive U when no bias was applied to the normal metal. The non-zero transient current there was due to an occupation of the odd-parity 1-state and the even parity ground state. Here, according to panel (a) of Fig. 6.1 and Table 6.1 the odd-parity state cannot be occupied at zero chemical potential. Hence we have to apply a non-zero bias to see transient charge currents.

Fig. 6.2 displays the transient charge current at chemical potential $\mu = 1.2U$ and temperature $T = 0.1|U|$ for two pairing strengths: $\alpha = 0.48|U|$ and $\alpha = 1.44|U|$.

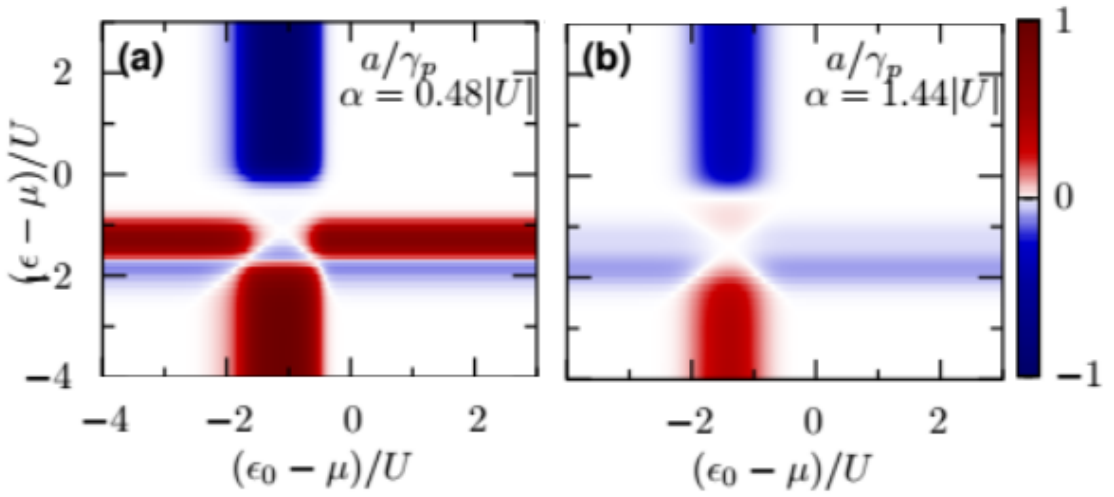

Figure 6.2. Charge amplitudes a after a slow switch at chemical potential $\mu = 1.2U$ and temperature $T = 0.1|U|$ (a) for weak pairing $\alpha = 0.48|U|$ and (b) for strong pairing $\alpha = 1.44|U|$.

Similarly to the repulsive case, there is no current in the off-diagonal blocks, as the $-$ state at the initial gate parameter unitarily evolves into the $-$ state at the final gate parameter. Hence it equals the final stationary state. For understanding of the colored cross we use panel (c) of Fig. 6.1, but with $\mu < 0$ for which the black curves are shifted accordingly. Let us now consider a line cut (not displayed) through the lower vertical part of the cross. The final stationary state is the $-$-state and charge transport can only be induced when starting from the $+$ or the 1-state. The $+$ and the 1-sate are only occupied in the region around the PHS, see panel (c) of Fig. 6.1. As all energy thresholds are negative in this region, transport is enabled by electron transfers into the metal, explaining the red color of the cross.

Let us next turn to a line cut through the horizontal part of the cross for $\epsilon_0 - \mu = -3U$. At this initial gate value, transport starts from the $-$ state evaluated at the final gate parameter and hence is determined by $- \to 1$-transitions, which are again associated with electron transfers to the metal, i.e. we expect $a > 0$ around the final symmetry point ϵ_{PHS}. However, $a < 0$ for $\epsilon < \epsilon_{\mathrm{PHS}}$. The reason is that $z_- > z_1$ and $I_N(t = 0) < I_N(t \to \infty)$ in the corresponding gate interval, i.e. the transient charge current is initially smaller than in the stationary limit. Hence, the amplitude is negative, such that the stationary value

is approached from below, as can be verified from the master equation:

$$0 = \frac{d\rho_1}{dt} = -\frac{\Gamma_+}{2}\rho_1 + \Gamma_-\rho_-, \quad \rho_1 = \frac{2\Gamma_-}{\Gamma_+}\rho_-$$
$$0 = \frac{d\rho_-}{dt} = \frac{\Gamma_+}{2}\rho_1 - \Gamma_-\rho_-, \quad \rho_- = \frac{\Gamma_+}{2\Gamma_-}\rho_1$$
$$I_N(t=0) = \frac{\Gamma_+}{2}\rho_1^0 + \Gamma_-\rho_-^0 = \Gamma_-, \quad I_N(t\to\infty) = 2\Gamma_- z_- \,.$$

Going over to stronger pairing, $\alpha = 1.44|U|$, panel (d) of Fig.6.1 shifted to $\mu < 0$ can be used for a discussion based on a similar reasoning. Here, we just point out that the transient amplitude is negative in the whole horizontal part of the cross, while the total initial charge current is positive.

6.3 | Heat current amplitudes after a slow switch

6.3.1 | Charge amplitude a_c

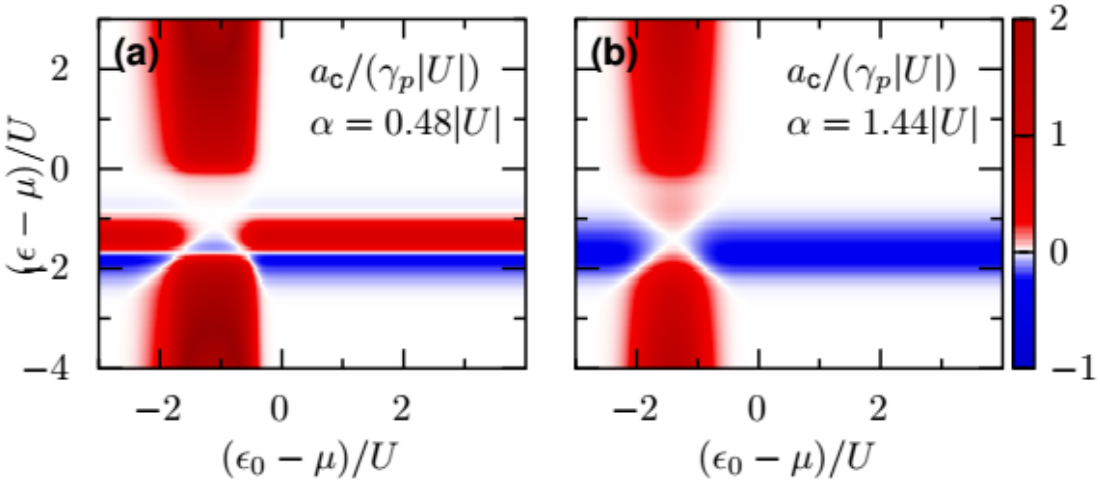

Figure 6.3. Charge amplitudes a_c of the heat current after a slow switch at chemical potential $\mu = 1.2U$ and temperature $T = 0.1|U|$ (a) for weak pairing $\alpha = 0.48|U|$ and (b) for strong pairing $\alpha = 1.44|U|$.

The charge amplitude of the heat current,

$$a_c = \left[\tfrac{1}{2}(\sqrt{\delta^2+\alpha^2} + \langle A\rangle_{\bar{z}})\gamma_c - \mu\gamma_s'\right](\langle A\rangle_{\rho_0} - \langle A\rangle_z) \tag{6.5}$$

is displayed in Fig. 6.3. For the case of weak pairing, $\alpha = 0.48|U|$, the sign of the horizontal part of the cross follows closely the one of the transient charge amplitude a

displayed in Fig. 6.2. The reason is that the energy prefactor $\delta_A + \langle A \rangle_{\bar{z}} \approx 0$ in that region and a_c is dominated by the contribution of a. Differently, in the upper vertical part of the cross, $a_c > 0$ while $a < 0$. Here, the dual polarization at the final gate parameter $\delta \gg 0$ is $+1$ and $\delta_A \gg 0$ with a positive polarization difference $\Delta A \equiv \langle A \rangle_{\rho_0} - \langle A \rangle_z > 0$. Hence, according to Eq. 6.5, $a_c > 0$. The same reasoning applies to the vertical part of a_c for stronger pairing $\alpha = 1.44|U|$ [Fig. 6.3 (b)]. The horizontal part, $a_c < 0$, is dominated by the energy prefactor and the sign of ΔA instead.

6.3.2 | Parity amplitude a_p

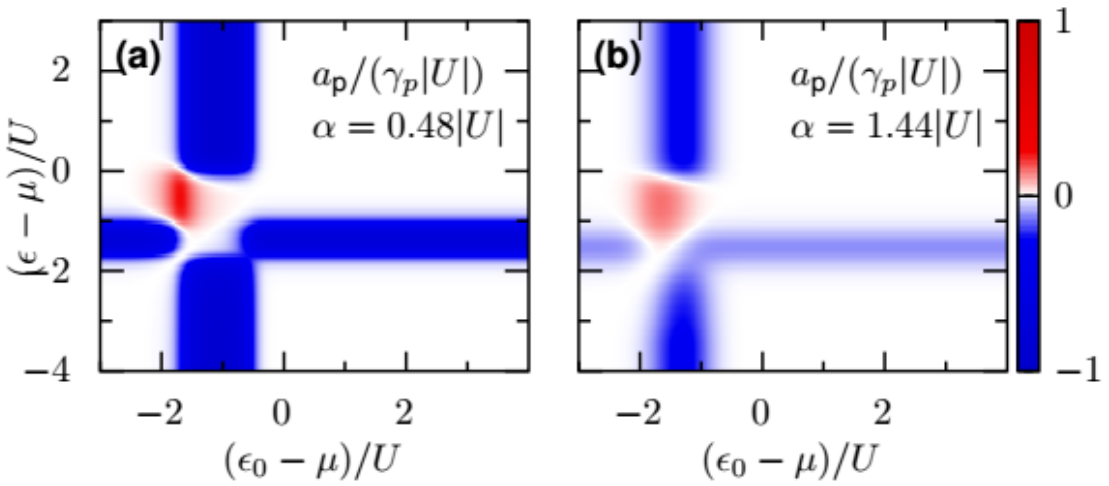

Figure 6.4. Parity amplitudes a_p of the heat current after a slow switch at chemical potential $\mu = 1.2U$ and temperature $T = 0.1|U|$ (a) for weak pairing $\alpha = 0.48|U|$ and (b) for strong pairing $\alpha = 1.44|U|$.

The parity amplitude of the heat current

$$a_p = \gamma_p U(P\bar{z}|\rho_0) = -\gamma_p|U|\left[\bar{z}_-\rho_{0,+} + \bar{z}_+\rho_{0,-} - \bar{z}_1\rho_{0,1}/2\right] \tag{6.6}$$

is displayed in Fig. 6.4. Let us first consider the blue horizontal stripes for $|\delta_0| \gg 0$. Here, $\rho_{0,-} = 1$, such that $a_p = -\bar{z}_+\gamma_p|U|$, which is reduced in strength for strong pairing $\alpha = 1.44|U|$, as the dual $-$ state occupation, $\bar{z}_+$, is as well reduced (see Table 6.1, panel (d)). The negative sign of the vertical stripe can be similarly explained for $|\delta| \gg 0$: The final dual stationary state is $+$, such that $a_p = -\gamma_p|U|\rho_{0,+} < 0$.

A positive amplitude (red region) is assumed when the overlap in real and dual occupations in the odd parity sector $\frac{\bar{z}_1\rho_{0,1}}{2}$ exceeds the overlap in the even sector. This is the case for initial gate values near the PHS, as $\rho_{0,1}$ here assumes its maximum value in

the real attractive system and for final values $\epsilon > \epsilon_{\mathrm{PHS}}$, as 1 is assumed here in the dual repulsive system.

Let us finally compare a_p of the attractive system with the corresponding amplitude of the repulsive system (not displayed). Going from attractive to repulsive interaction, the sign of U is inverted in the real and dual system. A certain stationary state assumed at an initial gate voltage in the real attractive system therefore corresponds to the dual stationary state at the same gate voltage in the repulsive system. Therefore, a_p of the negative-U system transforms into the corresponding positive-U amplitude by exchange of $\epsilon_0 \leftrightarrow \epsilon$ and an additional sign change of $U \to -U$ in a_p. After a fast switch, on the other hand, their mutual relation is more involved, as the occupations of the initial stationary state change w.r.t the basis at the final gate parameter and the simple form (6.6) of a_p does not apply.

6.4 | Stationary current

Let us finally discuss the stationary charge current displayed in Fig. 6.5. For a non-vanishing stationary charge current in the negative-U system, the stationary 1 state has to be occupied in the high-bias, weak pairing regime, see Fig. 6.5 and panel (c) of Fig. 6.1. In this case, all energy thresholds of table 6.1 are negative, and I_{N} can be derived from the master equation as follows:

$$\frac{dz_1}{dt} = z_+\Gamma_+ + z_-\Gamma_- - z_1\left(\tfrac{\Gamma_+}{2} + \tfrac{\Gamma_-}{2}\right) = 0\,, \tag{6.7}$$

$$I_{\mathrm{N}}(t \to \infty) = z_+\Gamma_+ + z_-\Gamma_- + z_1\gamma_p = 2z_1\gamma_p\,. \tag{6.8}$$

Hence, $I_{\mathrm{N}} \propto z_1$. Let us now discuss, why there is no analogous regime of $I_{\mathrm{N}} \neq 0$ for moderate pairing and low bias, as displayed by the ring-shaped structure of Fig. 5.12 (a) of the repulsive case: To this end, we assume a small negative bias is applied to panel (a) of Fig. 6.1 and Fig. 5.7 of the repulsive case. In the region of moderate detuning, transitions $1 \leftrightarrow -$ are enabled in both directions in the repulsive case and hence result in a non-vanishing charge current, as we conclude according to table 6.1. However, in the attractive case, probability always flows from $1 \to -$ such that there is no stationary 1-occupation and $I_{\mathrm{N}}(t \to \infty) = 0$. This explains the absence of an analogous form of Fig. 5.12 (a) for the negative-U case.

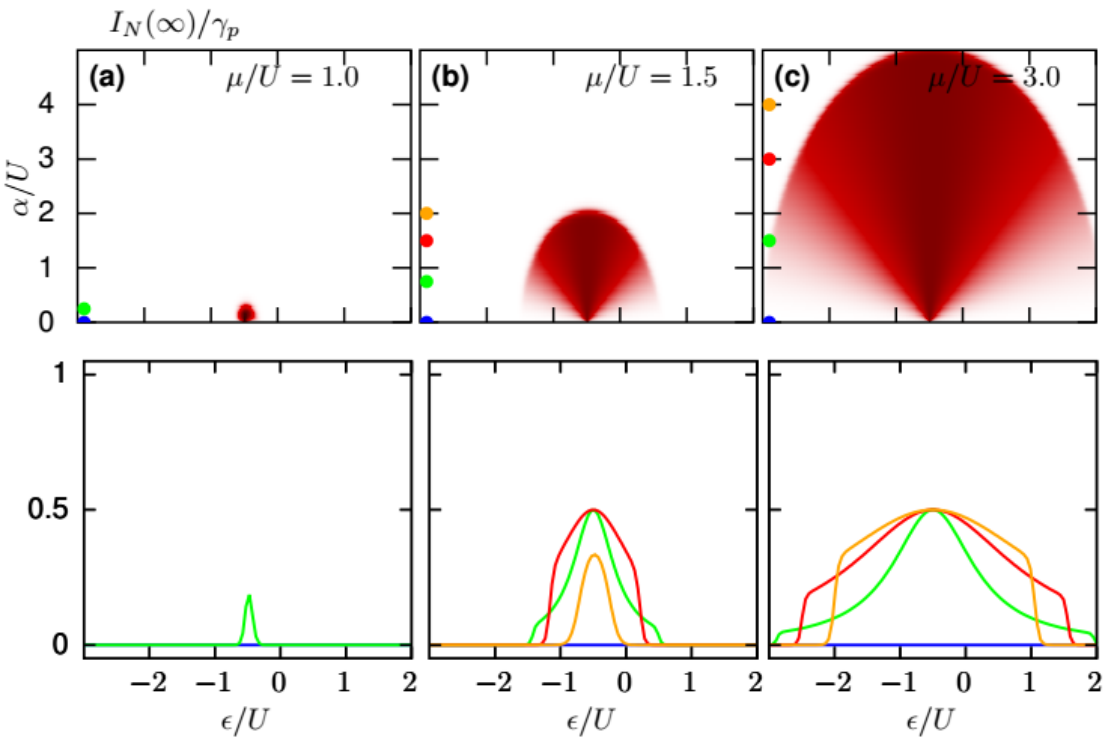

Figure 6.5. Stationary charge current $I_N(\infty)$ for different values of the chemical potential and $T = 0.02|U|$. The upper plots show the current as function of the gate-voltage $\epsilon = \delta - U/2$ and induced pairing α, while the corresponding bullets indicate the position of horizontal line cuts shown in the lower plots.

6.5 | Outlook

Immediate follow-up work would consist of the following steps. (i) I would analyze the impact of a finite temperature on transient quantities such as the parity amplitude and search for the possibility to explain them in terms of the already analyzed temperature induced shift of the gate dependent transition between the even parity stationary states as discussed in Sec. 6.1.2. (ii) Further I would study parameter regions of non-monotonic behavior in heat currents for the repulsive as well as the attractive case for comparison. (iii) So far the impact of designed attractive pairing on the quantum dot was manifest in our analysis as a reduced odd occupation in the real system as compared to the repulsive case. For further analysis it is of interest to study how this designed pairing mechanism combines with the pairing induced on the quantum dot by the BCS superconductor by further exploring the range of parameters α and U. (iv) As a next step fast switches should be discussed. For the repulsive case we had identified superconducting pairing and repulsive effective Coulomb interaction as opponents in the charge-and parity am-

plitudes of the heat current. Thus it will be of interest how the behavior changes for attractive U. Note that for the slow switch a simple relationship was found between the negative- and the positive-U case. For fast switches one cannot expect such as simple relationship.
Further extensions would account for contributions to the transport from higher orders in the tunnel coupling.

7

Conclusions

As to the first topic of this thesis, two-dimensional van der Waals magnets are currently quite topical. Among other reasons, they are tunable and hence allow to analyze the competition between different type of interactions in a broad range of parameter regimes, theoretically and experimentally. We considered materials with the metal cations arranged on a hexagonal lattice such as BrI_3. Our bilayers were ferromagnets with (anti-) ferromagnetic interlayer exchange coupling and perpendicular anisotropy.

Based on analytical expressions for the magnon band structure, derived by us in earlier work, we better understood the interplay between FM intra- and AFM interlayer coupling by two arguments, referring to different properties of the magnon band dispersion, the fundamental gap and the finite wave-vector magnon dispersion. The first argument made use of an effective modelling and suggested that an increased ferromagnetic intralayer coupling stabilizes AFM order in a similar manner as an appropriate stacking of the two bilayers does. The second argument confirmed this result. It was based on the energy cost associated with adding an additional magnon to the system.

Moreover, we traced back the degeneracy of the magnon dispersion as well as the vanishing Berry curvature of each band n to an underlying PT-symmetry of the momentum space Hamiltonian. The spin-resolved Berry curvature associated with each of the two modes within a band have opposite signs and therefore add up to zero band curvature. This way we could exclude a magnon (thermal) Hall effect, while a spin-Nernst effect associated with the difference in the spin-resolved curvatures of each band was only excluded to linear order in the temperature gradient as a result of their point-symmetry.

Although the results for our bilayer were negative in the sense that its topological properties are trivial, the analyses offered insights in how to modify the model to have a chance of creating a nonvanishing (spin-resolved) Berry curvature and interesting topological effects. We pointed to a number of natural extensions of the first topic, exploiting

e.g. the analogy between the description of electrons as Bloch waves and magnons as spin waves. One would explore the option of weak localization of magnons on hexagonal lattices such as in CrI3. Since we had to deal with quantum transport phenomena in the main part of this thesis, it would be natural to pursue the propagation of magnons in 2D van-der Waals heterostructures. The goal would be to predict transmission coefficients associated with possible tunneling processes through barriers.

As to the second topic of this thesis, we considered a special case of a superconductor-quantum dot hybrid devices (NDS). In general, superconductor quantum dot hybrid devices have a wide range of applications, e.g. in view of contributing to qubit designs in cQED geometries or as building blocks of quantum thermal machines. An important task in such devices is to control charge and heat currents and a fundamental operation is a gate switch.

We specifically studied the transient dynamics of an NDS-device after a switch in gate voltage had been applied to the QD. We considered the superconductor in the large gap limit and the limit of weak coupling between the dot and the metal, while the strength of Coulomb interaction was not restricted. Like this, dissipative quasi particle transport was only possible between the metal and the dot. Furthermore, the superconducting pairing induced on the proximized dot was assumed to be large w.r.t the tunnel coupling strength between the dot and the normal metal. In this limit, coherences did not have to be explicitly accounted for when aiming at a time-averaged description of the Born-Markov dynamics. Hence, it was possible to derive the time evolution kernel based on Fermi's Golden Rule and the electrostatics of the device. This derivation including general background on open system dynamics and superconductor QD hybrids were provided in Chap. 3.

As the studies of the system were restricted to the case of a large gap, our model fitted into the class of models tractable by the recently developed fermionic duality relation, a dissipative generalized hermiticity of the time evolution kernel. In applying the fermionic duality, we aimed in this thesis at its optimal exploitation, starting from the level of setting up the time-evolution and the transport equations in terms of duality-invariant rates. These rates have been motivated by a splitting of the total charge current into the metal. Aiming at a compact description of the transient transport in terms of mostly stationary observables and a minimum number of transient invariant rates, the (shifted) kernel was expressed in the so-called duality-adapted polarization basis. This basis directly provided these later required observables (polarization and parity), and the (shifted) kernel assumed a lower triangular form, being fully represented by just three of the invariant rates. Such an expression of the kernel can hence be considered as

a useful intermediate step between its derivation in the original more physical eigenbasis and its fully diagonalized form, in which the transient time-evolution as dictated by the two time scales and amplitudes becomes accessible. If the transient decay is dictated by just one amplitude, though, the energy basis remains the most convenient choice in analyzing the transient (energy) current.

In Chap. 4, we furthermore discussed constraints imposed by the duality on the transient transport. As we have shown, the stationary values of observables in the actual model in fact determine their values of the dual model by a stationary duality relation, independent of the values of all physical parameters: temperature, tunnel coupling, gate voltage, but also the effective - attractive or repulsive - Coulomb interaction U as well as the induced superconducting pairing. A related notion of parity and polarization is fulfilled whenever the interaction is irrelevant, either explicitly zero or made ineffective asymptotically. Otherwise, self-duality is violated but duality remains valid and is intimately linked with interactions within the open system. In particular, we have pointed out that the sign of the interaction U (repulsive/attractive) equals the sign of the shifted charge decay rate, irrespective of the induced superconducting pairing.

The duality-adapted formulation of the time-evolution developed in Chap. 4 provided the key to its exhaustive analysis given in the subsequent chapter. In Chap. 5, we studied the transient dynamics after two complementary examples of initial state preparation, by a fast and a slow switch in gate voltage, where fast (slow) refers to the switching time being smaller (larger) than the time scale set by the inverse superconducting pairing strength. A major difference in the switching scenarios refers to the fact that during the slow switch, the QD already exchanges charge with the superconductor before the onset of the transient dynamics. Consequently, the charge amplitude of the heat current vanishes when switching between gate regions of empty or double occupation. Furthermore, the parity amplitude of the heat current vanishes at zero chemical potential, as there are only two out of three stationary states populated.

After the fast switch, in contrast, both time scales contribute in general to the heat current, also at zero chemical potential. The superconductor and the repulsive Coulomb interaction could be identified as opposing each other. At zero chemical potential, the typical features of (dual attractive) Coulomb interaction in the charge and parity amplitudes of the heat current get washed out by the superconducting pairing when the effect of both type of interactions cannot be separated in parameter space.

As we have shown, it is possible to analyze the corresponding spectroscopy plots in a systematic way by considering the zero-temperature energy thresholds for transport with their associated particle transfers and resulting stationary states in the real and dual system. Instead of searching for interesting features by scanning the four-dimensional

parameter space, this analysis allowed us to project on characteristic changes in the observables of interest and hence to control the heat current in an NDS-device. Finally, we identified three types of non-monotonicity in the transient heat current characterized by a single parameter R. They differed in the type and number of local extrema and the way they saturated to their stationary values.

In Chap. 6, we considered the case of effective attractive Coulomb interaction on the quantum dot. Here, some limitations of the analysis by an approach based on zero temperature energy thresholds showed up in the real system, which were previously in the positive-U case present in the dual system. These limitations refer to the inability of extracting stationary state occupations for a specific interval of the detuning strength. However, we presented an analytical way of completing the analysis. So far, we considered the stationary charge transport and transient transport amplitudes only of the slow switch. Main differences between the repulsive and attractive-U system could be traced back to a reduced occupation of the 1-stationary state. Furthermore, we established a simple relation between the parity amplitudes of the repulsive and attractive U-systems for the slow switch. As extensions, one should study the fast switch-scenario, as the differences between attractive and repulsive interaction seem to be more involved. Contributions to the transport from higher orders in the tunnel coupling should be included in future work.

So far, we have only used fermionic duality as a tool to simplify the procedure of solution and analysis of a given master equation in the infinite-gap limit. A key remaining open question therefore is as to whether a more general duality relation can be found for a finite superconducting gap described by the approaches of Ref. [79] or [74]. Such an extension would be interesting in view of studying the dynamics of superconductor-QD hybrid devices with two superconductors, as introduced in Chap. 3.

A

Derivation of the dual master equation

The dual stationary state $|\bar{z}) \equiv I|z)$, with $I : x \to -x, x = \epsilon, U, \alpha, \mu$ the parameter inversion, as introduced in Eq. (4.3) of the main text, can formally be obtained from a dual master equation for a dual state $I|\rho(t))$:

$$\frac{d}{dt} I|\rho(t)) = I\frac{d}{dt}|\rho(t)) = I[W|\rho(t))] = \overline{W} I|\rho(t)) \tag{A.1}$$

In the following, we show that alternatively to directly applying the parameter inversion, the dual kernel $\overline{W}$ can be efficiently derived based on zero temperature thresholds and Fermi's Golden Rule. We proceed in analogy to the derivation of the real kernel W presented in Sec. 3.4 of the main text.

Analogously to the real system, a state transition $i \to f$ in the dual system is induced by a particle transfer η from the metal to the SQD, when the addition energy can be paid by the metal kept at chemical potential μ:

$$-\eta\bar{\mu} \geq \gamma[\bar{E}_f - \bar{E}_i] = \gamma[\bar{E}_\tau - \bar{\epsilon}] \overset{(4.4)}{=} \gamma[-E_{\bar{\tau}} - (-\epsilon)] \tag{A.2}$$

$$\overset{(3.18),(3.28)}{=} E_{\bar{\gamma},\bar{\tau}} \overset{(3.28)}{=} -E_{\gamma,\bar{\tau}} \overset{(4.5)}{=} \bar{E}_{\gamma,\tau}. \tag{A.3}$$

Here, similarly to the real system, $\gamma = \pm$ indicates that the dual state transitions from $1 \rightleftarrows \bar{\tau}$, respectively. The threshold (A.3) corresponds to the Fermi function

$$f^{-\eta}(\bar{E}_{\bar{\eta}\gamma,\tau} - \bar{\mu}) = f^{-\eta}(-E_{\bar{\eta}\gamma}, \bar{\tau} + \mu)\,,$$

at finite temperature, which can be equivalently obtained from the Fermi function (3.30) for the corresponding transition $1 \rightleftarrows \tau$ in the real system by applying the parameter transformation (4.3). Finally, the effective tunnel coupling rates are given by the overlap

of the initial dual state after annihilation (creation) of an electron with the final state

$$\begin{aligned}\Gamma_{\eta\gamma,\bar{\tau}} &= \Gamma |\left\langle \bar{f} \right| \hat{d}^{(\dagger)} \left| \bar{i} \right\rangle|^2 \\ &= \frac{\gamma_p}{2}[1 + \eta\bar{\gamma}\bar{\tau}\frac{\delta}{\delta_{\mathrm{A}}}]\,.\end{aligned}$$

An overview of all dual state transitions and associated particle transfers are given in column 5 of Table 3.1 together with their energy thresholds (A.3).

B

Diagonalization of the kernel

B.1 | Energy basis

In the following, we give some details of the kernel diagonalization sketched in Sec. 4.2.1 and explicitly the energy representation of some relevant super(co-) verctors.

The polarization vector $(A| = |+) - -$ introduced in Eq.(4.10) is chosen to fulfill $(A|\mathbb{1}) = (A|p) = 0$ and can be guessed easily, when $|\mathbb{1})$ and $|p)$ are given in the energy basis,

$$|\mathbb{1}) = |+) + |-) + 2|1)\,, \tag{B.1}$$

$$|p) = |+) + |-) - 2|1)\,. \tag{B.2}$$

Having guessed A and therefore the ansatz (4.10) for $(c'|$, we now determine the general form of the corresponding REV $|c)$ by the cross-relation (4.7):

$$c_3\overline{(c'|\mathcal{P}}^{\dagger} = |c) = c_3\Big[-\bar{c}_1|A) + \bar{c}_2|p)\Big]. \tag{B.3}$$

Next, we determine the factors c_i from the orthonormality of the kernel eigenbasis. From the orthogonality $(c'|z) = 0$, we obtain

$$c_1(A|z) + c_2(\mathbb{1}|z) = 0 \Leftrightarrow c_2 = -c_1\langle A\rangle_z \tag{B.4}$$

and from $(p'|c) = 0$, we obtain

$$-\bar{c}_1(p\bar{z}|A) + \bar{c}_2(p\bar{z}|p) = 0 \Leftrightarrow \bar{c}_2 = \bar{c}_1\langle A\rangle_{\bar{z}}\,, \tag{B.5}$$

as $(p\bar{z}|A) = (\bar{z}|A) = (A|\bar{z})$ and $(p\bar{z}|p) = (\bar{z}|p^2) = (\bar{z}|\mathbb{1}) = 1$ due to the normalization of the dual stationary state $\bar{z}$.

Using relation (B.4) in (4.10) and (B.5) in (B.3), the ortho*normality* of the kernel basis implies

$$1 = (c'|c) = -\bar{c}_3\bar{c}_1 c_1 (A|A) = -2c_3\bar{c}_1 c_1, \tag{B.6}$$

where we used $(\mathbb{1}|p) = 0$. We choose $c_1 = 1$ and $c_3 = -\frac{1}{2}$ to obtain Eq. (4.12) of the main text. Note that the additional normalization factor c_3 necessary in (B.6) has been introduced in the REV $|c)$ instead of the LEV $(c'|$, as the latter is the relevant quantity used to express the charge current operator, which should have no additional prefactors.

Finally, we determine the third eigenvalue $-\gamma_c$ of W explicitly in the energy basis, by solving for $(c'|W = -\gamma_c(c'|$, using the energy representations (3.26, 4.11, B.2) of W, A and p, respectively:

$$-\gamma_c = -\frac{1}{2}\sum_{\eta,\tau} W^{\eta}_{1,\tau} \tag{B.7}$$

Furthermore, we need the representation of the stationary state in the energy basis, which is obtained from solving $W|z) = 0$. In the energy basis, the real and dual stationary states read

$$|z) = \frac{1}{\left[\sum_\tau W_{1,\tau}\right]}\left[W_{1,-}\left(1 - \frac{W_{1,+}}{\gamma_p}\right)|+) + W_{1,+}\left(1 - \frac{W_{1,-}}{\gamma_p}\right)|-) + 2\frac{W_{1,+}W_{1,-}}{\gamma_p}|1)\right], \tag{B.8}$$

$$|\bar{z}) = \frac{1}{\left[\sum_\tau W_{\bar{\tau},1}\right]}\left[W_{+,1}\left(1 - 2\frac{W_{-,1}}{\gamma_p}\right)|-) + W_{-,1}\left(1 - 2\frac{W_{+,1}}{\gamma_p}\right)|+) + 4\frac{W_{-,1}W_{+,1}}{\gamma_p}|1)\right]. \tag{B.9}$$

For completeness, we give the energy basis representation of the L-and R charge EVs as well:

$$|c) = \frac{1}{\left[2\gamma_p - \sum_\tau W_{1,\tau}\right]}\left[\left(\gamma_p - W_{1,+}\right)|+) - \left(\gamma_p - W_{1,-}\right)|-) - \left(W_{1,-} - W_{1,+}\right)|1)\right], \tag{B.10}$$

$$(c'| = \frac{1}{2\left[\gamma_p - \sum_\tau W_{\tau,1}\right]}\left[\left(\gamma_p - 2W_{-,1}\right)(-| - \left(\gamma_p - 2W_{+,1}\right)(+| + 2\left(W_{+,1} - W_{-,1}\right)(1|\right]. \tag{B.11}$$

B.2 | Polarization basis

In the following, we determine the left and right eigenvectors of the (shifted) kernel in the polarization basis. We use the bi-orthogonality of the basis vectors and their

normalization

$$\tfrac{1}{4}(\mathbb{1}|\mathbb{1}) = \tfrac{1}{4}(p|p) = \tfrac{1}{2}(A|A) = 1, \tag{B.12}$$

which leads to the following completeness relation in the diagonal subspace:

$$\mathcal{I} = \tfrac{1}{4}|\mathbb{1})(\mathbb{1}| + \tfrac{1}{2}|A)(A| + \tfrac{1}{4}|p)(p|\,. \tag{B.13}$$

As pointed out in Sec. 4.2.5, the basis vectors are cross-related by duality according to

$$\overline{\mathcal{P}|\mathbb{1})}^{\dagger} = (p|, \quad \overline{\mathcal{P}|A)}^{\dagger} = -(A|, \quad \overline{\mathcal{P}|p)}^{\dagger} = (\mathbb{1}| \tag{B.14a}$$

$$\overline{(\mathbb{1}|\mathcal{P}}^{\dagger} = |p), \quad \overline{(A|\mathcal{P}}^{\dagger} = -|A), \quad \overline{(p|\mathcal{P}}^{\dagger} = |\mathbb{1}). \tag{B.14b}$$

Starting from the spectral decomposition (4.41) of the shifted kernel in the $\mathbb{1}, A, p$-basis, its diagonal form (4.42) can be easily obtained: (i) The eigenvalues can be read off from the diagonal of Eq. (4.41) giving $\pm\frac{1}{2}\gamma_p$ and $-\gamma_C$ along with the normalization (B.13). (ii) The first left basis vector $(\mathbb{1}|$ and the last right basis vector $|p)$ are eigenvectors for different eigenvalues. The two remaining left (right) eigenvectors are then found by standard forward (backward) recursion for lower-triangular matrices:

$$(z'| = (\mathbb{1}|, \tag{B.15a}$$

$$(c'| = (A| + \frac{\gamma_s}{\frac{1}{2}\gamma_p + \gamma_C}(\mathbb{1}|, \tag{B.15b}$$

$$(p'| = \tfrac{1}{4}(p| + \frac{\gamma_s}{\frac{1}{2}\gamma_p - \gamma_C}\tfrac{1}{2}(A| + \Big(\frac{\gamma_C}{\gamma_p} + \frac{\gamma_s}{\gamma_p}\frac{\gamma_s}{\frac{1}{2}\gamma_p - \gamma_C}\Big)\tfrac{1}{2}(\mathbb{1}|, \tag{B.15c}$$

$$|z) = \tfrac{1}{4}|\mathbb{1}) - \frac{\gamma_s}{\frac{1}{2}\gamma_p + \gamma_C}\tfrac{1}{2}|A) - \Big(\frac{\gamma_C}{\gamma_p} - \frac{\gamma_s}{\gamma_p}\frac{\gamma_s}{\frac{1}{2}\gamma_p + \gamma_C}\Big)\tfrac{1}{2}|p), \tag{B.15d}$$

$$|c) = \tfrac{1}{2}\Big[|A) - \frac{\gamma_s}{\frac{1}{2}\gamma_p - \gamma_C}|p)\Big], \tag{B.15e}$$

$$|p) = |(-\mathbb{1})^N). \tag{B.15f}$$

This compact result reveals that the coefficients of the different eigenvectors in fact have a very similar functional form (B.15). Notably, the eigenvectors are specified by the eigenvalues, namely the duality invariants $\pm\frac{1}{2}\gamma_p$ and γ_C, and a single additional parameter, the duality invariant γ_s. (iii) Due to their recursive construction, the normalization of the eigenvectors is automatically fixed by that of the basis vectors:

$$(z'|z) = \tfrac{1}{4}(\mathbb{1}|\mathbb{1}) = 1, \qquad (c'|c) = \tfrac{1}{2}(A|A) = 1, \qquad (p'|p) = \tfrac{1}{4}(p|p) = 1. \tag{B.16}$$

(iv) Finally, the cross-relation of eigenvectors (4.7) dictated by duality is manifest,

$$\overline{\mathcal{P}|z)}^{\dagger} = (p'|, \qquad \overline{\mathcal{P}|c)}^{\dagger} = -\tfrac{1}{2}(c'|, \qquad \overline{\mathcal{P}|p)}^{\dagger} = (z'|, \tag{B.17a}$$

$$\overline{(z'|\mathcal{P}}^\dagger = |p), \qquad \overline{(c'|\mathcal{P}}^\dagger = -2|c), \qquad \overline{(p'|\mathcal{P}}^\dagger = |z), \tag{B.17b}$$

by merely noting the cross-relation of the duality-adapted basis vectors [Eq. (B.14)] and the duality invariance of the scalar coefficients [Eq. (4.35)]. This mapping preserves the bi-orthogonality of the left and right eigenvectors. It also shows how the spectral form (4.42) of $W + \frac{1}{2}\gamma_p \mathcal{I}$ ensures duality $(-)$ invariance: The mapping cross relates the first and last spectral projectors and it relates the middle spectral projector to itself[1]. Together with the $(+)$ invariance of the eigenvalue $\pm\frac{1}{2}\gamma_p$ and the $(-)$ invariance of the eigenvalue γ_C this implies that Eq. (4.42) simply inverts its sign as it should by Eq. (4.2). Note in particular that this inversion is not simply achieved by inverting the signs of all eigenvalues.

Finally, we give the representation of the expectation values of parity and polarization in the real and dual stationary states in terms of the invariant variables γ, using the explicit representation (B.15) of the stationary state:

$$\langle A\rangle_z = -\frac{\gamma_s}{\frac{1}{2}\gamma_p + \gamma_C}, \quad \langle p\rangle_z = -\frac{2\gamma_C}{\gamma_p} + \frac{2\gamma_s^2}{\gamma_p(\frac{1}{2}\gamma_p + \gamma_C)}, \tag{B.18a}$$

$$\langle A\rangle_{\bar z} = \frac{\gamma_s}{\frac{1}{2}\gamma_p - \gamma_C}, \quad \langle p\rangle_{\bar z} = \frac{2\gamma_C}{\gamma_p} + \frac{2\gamma_s^2}{\gamma_p(\frac{1}{2}\gamma_p - \gamma_C)}. \tag{B.18b}$$

In terms of the (shifted) invariants $\gamma_p, \gamma_c, \gamma_s$, they read

$$\langle A\rangle_z = -\frac{\gamma_s}{\gamma_c}, \qquad \langle p\rangle_z = 1 - 2\frac{\gamma_c^2 - \gamma_s^2}{\gamma_p\gamma_c}, \tag{B.19a}$$

$$\langle A\rangle_{\bar z} = \frac{\gamma_s}{\gamma_p - \gamma_c}, \quad \langle p\rangle_{\bar z} = 1 - 2\frac{(\gamma_p - \gamma_c)^2 - \gamma_s^2}{\gamma_p(\gamma_p - \gamma_c)}. \tag{B.19b}$$

.

[1] The left and right eigenvectors to middle eigenvalue $-\gamma_C$ cannot be normalized to eliminate the factors $-1/2$ resp. -2 without undesirable effects. The $-$ sign *can* be eliminated at the expense of normalization factors which are either complex (making c, c' non-self adjoint) or discontinuous in δ, both unnecessary complications. The factor $1/2$ *can* be eliminated by normalization $1/\sqrt{2}$ but our choice ensures that $(c'|$ occurs without pre-factors in the charge current operators (which later on cancel in expectation values).

C

Charge current contributions

In the following, we give the full derivation of the total charge current (4.17) and its constituents (4.31-4.32) of the main text. Furthermore, we determine the transient charge amplitudes of these constituents and their stationary part.

First, we note that the extended labeling n of the number of Cooper pairs in the (Andreev) states introduced in Eq.(4.24-4.25) of the main text corresponds to the effective Hamiltonian

$$H_{\mathrm{D}}^{+\mathrm{S}} = \epsilon N_{\mathrm{D}} \otimes \mathbb{1}_{\mathrm{S}} + U N_{\uparrow} N_{\downarrow} \otimes \mathbb{1}_{\mathrm{S}} - \tfrac{1}{2}\alpha \sum_{n} d_{\uparrow}^{\dagger} d_{\downarrow}^{\dagger} \left|n\right\rangle \left\langle n+1\right| + \mathrm{h.c} \tag{C.1}$$

of the SQD, with the complete dot-charge operator

$$|N_{\mathrm{D}}) = 2|2) + 2|1) \tag{C.2}$$

and the completeness relation

$$|\mathbb{1}_{\mathrm{S}}) = \sum_{n} |n\rangle \langle n| = \sum_{n} |n) \,. \tag{C.3}$$

The total charge current I_N can be determined by applying the total charge operator $(N|\bullet$, see Eq. (4.29), to the master equation (4.28) and using the orthogonality of the extended basis,

$$(\tau, n|\tau', n') = \delta_{\tau,\tau'}\delta_{n,n'} \,, \tau^{(\prime)} = \pm \,, \tag{C.4}$$

$$(1, n|\kappa, n') = \delta_{1,\kappa}\delta_{n,n'} \,, \kappa = \pm, 1 \,. \tag{C.5}$$

The orthogonality relations have to be explicitly verified by inserting the definitions of the extended (Andreev) states (4.24-4.25).

The dot-charge contribution to the total charge current

$$I_{N_{\mathrm{D}}} = -(N_{\mathrm{D}} \otimes \mathbb{1}_{\mathrm{S}} | W^{+\mathrm{S}} \rho^{+\mathrm{S}}) \tag{C.6}$$

can be derived from the master equation (4.28) using the relations

$$(N_D \otimes \mathbb{1}_S|\tau, n) = \frac{2}{\gamma_p}\Gamma_\tau, \tau = \pm$$
$$(N_D \otimes \mathbb{1}_S|1, n) = 1.$$

We explicitly determine

$$\begin{aligned}
(N_D \otimes \mathbb{1}_S|\tau, n) &= (\mathbb{1}_S| \otimes (N_D|\tau, n) \\
&= (\mathbb{1}_S| \otimes \Big[2(2| + 2(1|\Big] \frac{1}{\gamma_p}\Big[\Gamma_{\bar\tau}|0) \otimes |n+1) + \Gamma_\tau|2) \otimes |n) + \tau|0,2)...\Big] \\
&= (\mathbb{1}_S| \otimes \frac{2}{\gamma_p}\Gamma_\tau(2|2)|n) \\
&= \frac{2}{\gamma_p}\Gamma_\tau \sum_{n'}\langle n'|n\rangle\delta_{n,n'} \\
&= \frac{2}{\gamma_p}\Gamma_\tau .
\end{aligned}$$

According to Eq.(4.28), I_{N_D} is then given by

$$\begin{aligned}
I_{N_D} &= -\sum_{n,\tau\in\pm}\frac{2}{\gamma_p}\Gamma_\tau(p_{1n}[W^e_{\tau 1} + W^h_{\tau 1}] - p_{\tau n}[W^h_{1\tau} + W^e_{1\tau}]) \\
&\quad -\sum_{n,\tau\in\pm}(p_{\tau n}[W^h_{1\tau} + W^e_{1\tau}] - p_{1n}[W^e_{\tau 1} + W^h_{\tau 1}]) \\
&= -\sum_{\tau\in\pm}(1 - \frac{2}{\gamma_p}\Gamma_\tau)\Big[p_\tau[W^h_{1\tau} + W^e_{1\tau}] + p_1[W^e_{\tau 1} + W^h_{\tau 1}]\Big] \\
&= -\sum_{n,\tau\in\pm}(-\tau\frac{\delta}{\delta_A})\Big[p_\tau[W^h_{1\tau} + W^e_{1\tau}] - p_1[W^e_{\tau 1} + W^h_{\tau 1}]\Big].
\end{aligned}$$

Similarly, using the relations

$$(2N_{cp} \otimes \mathbb{1}_D|\tau, n) = 2n + \frac{2}{\gamma_p}\Gamma_{\bar\tau}, \tau = \pm$$
$$(2N_{cp} \otimes \mathbb{1}_D|1, n) = 2n\,,$$

we obtain the Cooper pair contribution

$$\begin{aligned}
I_{N_{cp}} &= -\sum_{n,\tau\in\pm} p_{1,n}\Big[\Big(2n + \frac{2}{\gamma_p}\Gamma_{\bar\tau}\Big)W^e_{\tau 1} + \Big(2(n-1) + \frac{2}{\gamma_p}\Gamma_{\bar\tau}\Big)W^h_{\tau 1}\Big] \\
&\quad + \sum_{n,\tau\in\pm} p_{\tau,n}\Big(2n + \frac{2}{\gamma_p}\Gamma_{\bar\tau}\Big)\Big[W^h_{1\tau} + W^e_{1\tau}\Big] \\
&\quad - \sum_{n,\tau\in\pm} p_{\tau,n}[2nW^h_{1\tau} + 2(n+1)W^e_{1\tau}] + \sum_{n,\tau\in\pm} p_{1,n}2n\Big[W^e_{\tau 1} + W^h_{\tau 1}\Big]
\end{aligned}$$

$$= -\frac{2}{\gamma_p}\sum_{n,\tau\in\pm} p_{\tau,n}[\Gamma_\tau W^e_{1\tau} - \Gamma_{\bar\tau} W^h_{1\tau}] - \frac{2}{\gamma_p}\sum_{n,\tau\in\pm} p_{1n}[\Gamma_{\bar\tau} W^e_{\tau,1} - \Gamma_\tau W^h_{\tau 1}]$$
$$= -\frac{2}{\gamma_p}\sum_{\tau\in\pm} p_{\tau}[\Gamma_\tau W^e_{1\tau} - \Gamma_{\bar\tau} W^h_{1\tau}] - \frac{2}{\gamma_p}\sum_{\tau\in\pm} p_{1}[\Gamma_{\bar\tau} W^e_{\tau,1} - \Gamma_\tau W^h_{\tau 1}]\,. \tag{C.7}$$

Having derived the components $C^{N_x}_\kappa$ of the contribution x to the total charge current in the energy basis, see Eq.(4.18) for the definition of the $C^{N_x}_\kappa$, their transient and stationary parts are according to Eq. (4.21) given by

$$e^{-\gamma_c t}\Big[\langle A\rangle_{\rho_0} - \langle A\rangle_z\Big]\sum_{\kappa=\pm,1} C^{\mathrm{x}}_\kappa c_\kappa\,,$$
$$\sum_{\kappa=\pm,1} C^{\mathrm{x}}_\kappa z_\tau\,,$$

respectively. Inserting the components of the charge mode (B.10) and the stationary state (B.8) in the energy basis, one obtains the stationary and transient parts listed in table C.1 by polynomial division. They can be derived more efficiently in the polarization basis introduced in Sec. 4.2.5 of the main text.

x	$I^{\mathrm{x},c} \equiv \sum_{\kappa=\pm,1} C^{\mathrm{x}}_\kappa c_\kappa$	$I^{\mathrm{x},z} \equiv \sum_{\kappa=\pm,1} C^{\mathrm{x}}_\kappa z_\tau$
N	$\frac{1}{2}\sum_{\eta,\tau}\eta\tau W^\eta_{1,\tau}$	$\langle A\rangle_z \frac{1}{2}\sum_{\eta,\tau}\eta\tau W^\eta_{1,\tau} + \frac{1}{2}\sum_{\eta,\tau}\eta W^\eta_{1,\tau}$
N_{D}	$\frac{\delta}{\delta_{\mathrm{A}}}\frac{1}{2}\sum_{\eta,\tau} W^\eta_{1,\tau}$	0
N_{cp}	$= I^{N,c} - I^{N_{\mathrm{D}},c}$	$= I^{N,c}$

Table C.1. Overview of transient (middle column) and stationary (right column) parts of the different current contributions x.

D

Relations between real and dual transport rates

Fermionic duality is based on the behaviour of the fermionic reservoir distribution function $f^\eta(\omega) = (e^{\eta\omega}+1)^{-1} = f^{-\eta}(-\omega)$ under inversion of the energy: $f^\eta(\omega) = 1 - f^\eta(-\omega)$. It implies the following relations between actual and dual transport rates $W_{i,j}, \bar{W}_{i,j}$:

$$W^\eta_{1,\tau} = \Gamma_{\eta\tau} - \bar{W}^\eta_{1,\bar{\tau}}, \qquad 2W^\eta_{\tau,1} = \Gamma_{\bar{\eta}\tau} - 2\bar{W}^\eta_{\bar{\tau},1}, \qquad W^\eta_{1,\tau} = 2\bar{W}^{\bar{\eta}}_{\bar{\tau},1}. \tag{D.1}$$

In the last relation, inverting the direction of the transition from $\tau \to 1$ to $1 \to \tau$ inverts both the state ($\bar{\tau} = -\tau$) and the direction of electron transfer ($\bar{\eta} = -\eta$)[1]. These relations allow to eliminate kernel rates in one direction in favour of those for the opposite direction by a sum rule, which is obtained by combining the second and third relation of (D.1):

$$2W^\eta_{\tau,1} + W^{\bar{\eta}}_{1,\tau} = \Gamma_{\bar{\eta}\tau}, \qquad 2W_{\tau,1} + W_{1,\tau} = \gamma_p. \tag{D.2}$$

Here, the second expression results from summing over η. In the main text, we can thus focus on parametrizing the rates for one direction, say $\tau \to 1$.

[1] Note that the ansatz (4.34) of the main text for rewriting the kernel rates $W_{1,\tau}$ in terms of the duality-invariant rates γ by decomposing it into η, τ-(anti-) symmetric contributions, is therefore also motivated by the last relation of (D.1), independently of our original motivation given in the main text.

E

Stationary duality and Kolmogorov detailed balance

Here we present two derivations of the stationary duality relation (4.54).

Direct derivation: Using Eqs. (B.18) we first express the parity -1 probability $\frac{1}{2}[1-\langle p\rangle_z]$ in terms of $\langle A\rangle_z$ and $\langle A\rangle_{\bar z}$ by eliminating $(\frac{1}{2}\gamma_p+\gamma_C)/\gamma_p=[1-\langle A\rangle_z/\langle A\rangle_{\bar z}]^{-1}$ and then express the remainder in $\langle A\rangle_z$. One then similarly expresses the parity $+1$ probability:

$$\tfrac{1}{2}[1-\langle p\rangle_z]=\frac{1-\langle A\rangle_z^2}{1-\langle A\rangle_z/\langle A\rangle_{\bar z}},\qquad \tfrac{1}{2}[1+\langle p\rangle_z]=\frac{1-\langle A\rangle_z\langle A\rangle_{\bar z}}{1-\langle A\rangle_{\bar z}/\langle A\rangle_z} \tag{E.1}$$

$$\tfrac{1}{2}[1-\langle p\rangle_{\bar z}]=\frac{1-\langle A\rangle_{\bar z}^2}{1-\langle A\rangle_{\bar z}/\langle A\rangle_z},\qquad \tfrac{1}{2}[1+\langle p\rangle_{\bar z}]=\frac{1-\langle A\rangle_z\langle A\rangle_{\bar z}}{1-\langle A\rangle_z/\langle A\rangle_{\bar z}}. \tag{E.2}$$

The second row is obtained in a similar way and corresponds to formally replacing $z\to\bar z$ in the first row. From the first (second) relation in the first (second) row one then finds the dual polarization (parity) in terms of the actual polarization and parity as given by Eq.(4.54a).

Derivation based on detailed balance: In the following, we derive Eq. (4.54) of the main text alternatively, starting from the energy basis. The derivation is based on the "universal" fermionic duality relation (4.55) previously found in Ref. [49] for normal conducting systems. The underlying assumptions of this relation apply to our system of interest, see Sec.4.3.2 of the main text for a discussion. In our notation, these relations connect the energy-basis probabilities [Eq. (3.24)] of $|z)=\sum_\tau z_\tau|\tau)+z_1|1)$ and $|\bar z)=\sum_\tau \bar z_\tau|\bar\tau)+\bar z_1|1)$ of which we eliminate z_1 and $\bar z_1$ by normalization. Accounting for the degeneracy of the $N=1$ spin states, Eq. (4.55) gives for the Andreev states $\tau=\pm$

$$\bar z_\tau=\frac{(z_{-\tau})^{-1}}{\sum_\tau z_\tau^{-1}+2(z_1/2)^{-1}}=\frac{z_1}{z_1\sum_\tau z_\tau+4z_+z_-}\,z_\tau=Fz_\tau, \tag{E.3}$$

with rescaling factor (4.54b)

$$F = \frac{z_1}{z_1 \sum_\tau z_\tau + 4 z_+ z_-} = \frac{\frac{1}{2}\big[1 - \langle p \rangle_z\big]}{\frac{1}{2}\big[1 + \langle p \rangle_z\big] - \langle A \rangle_z^2}. \tag{E.4}$$

Changing to duality-adapted variables $z_\tau = \frac{1}{4}\big[1 + \langle p \rangle_z\big] + \tau \frac{1}{2} \langle A \rangle_z$ and $z_1 = \frac{1}{2}\big[1 - \langle p \rangle_z\big]$, we obtain relation (4.54a)

$$\langle \bar{A} \rangle_{\bar{z}} \equiv \sum_\tau \tau \bar{z}_\tau = F \sum_\tau \tau z_\tau = F \langle A \rangle_z, \tag{E.5}$$

$$\tfrac{1}{2}\big[1 + \langle p \rangle_{\bar{z}}\big] \equiv \sum_\tau \bar{z}_\tau \quad = F \sum_\tau z_\tau \quad = F \tfrac{1}{2}\big[1 + \langle p \rangle_z\big]. \tag{E.6}$$

F

Condition for self-duality

Here we consider the self-duality condition $\gamma_c = \frac{1}{2}\gamma_p$ for the charge decay rate, which is according to Eqs. (4.46), (3.32) of the main text, given by

$$\gamma_c = \tfrac{1}{2}\sum_{\eta\tau} W^{\eta}_{1,\tau} = \tfrac{1}{2}\gamma_p \sum_{\lambda} \tfrac{1}{2}\Big(1+\lambda\frac{\delta}{\delta_{\rm A}}\Big)\sum_{\eta} f^{-\eta}\Big(\tfrac{1}{2}(\lambda\delta_{\rm A}+\eta U)-\mu\Big)\,. \tag{F.1}$$

F.1 | Exact self-duality and its breakdown due to interaction

The strict lower / upper bounds (4.59), $\gamma_c \gtrless \frac{1}{2}\gamma_p$ for $U \gtrless 0$ at finite temperature T follow using $f(x) = [e^{x/T}+1]^{-1} = \frac{1}{2}\big[1+(1-e^{x/T})/(1+e^{x/T})\big]$ and $f^{\eta}(x) = f(\eta x)$:

$$\sum_{\eta} f^{-\eta}(x+\eta y) = 1 + \frac{1-e^{-2y/T}}{(e^{-(x+y)/T}+1)(e^{(x-y)/T}+1)} \gtrless 1. \tag{F.2}$$

With $x = \lambda\delta_{\rm A} - \mu$ and $y = U/2$, Eq. (F.1) gives $\gamma_c \gtrless \frac{1}{2}\gamma_p \sum_{\lambda}\frac{1}{2}(1+\lambda\frac{\delta}{\delta_{\rm A}}) = \frac{1}{2}\gamma_p$ for $U \gtrless 0$. For $T < \infty$, the condition for self-duality (4.56), $\gamma_c = \gamma_p/2$ [Eq. (4.58)], holds for all values of parameters other than U, if and only if $U = 0$, since Eq. (F.2) is an equality if and only if $y = 0$. For $T \to \infty$ the equality is satisfied trivially for all parameter values.

F.2 | Asymptotic self-duality

It is possible to achieve self-duality asymptotically, i.e., by making one energy scale dominate all others (excluding Γ which cancels out $\gamma_c = \gamma_p/2$). All that is needed is to eliminate the dependence on η in the argument of the Fermi distribution in Eq. (F.1).

This is always possible by choosing a high temperature $T \gg |U|, |\alpha|, |\delta|$

$$\gamma_c \approx \tfrac{1}{2}\gamma_p \sum_\lambda \tfrac{1}{2}\Big(1 + \lambda \frac{\delta}{\delta_\mathrm{A}}\Big) \sum_\eta f^{-\eta}(0) = \tfrac{1}{2}\gamma_p. \tag{F.3}$$

If the temperature is not dominant, to achieve self-duality, the η dependence should be made ineffective, which is tied to the interaction U in Eq. (F.1) in the transition energy $E_{\eta,\eta\lambda} = \frac{1}{2}(\lambda\delta_\mathrm{A} + \eta U) - \mu$. For large bias voltage $|\mu| \gg |\delta|, |\alpha|, U$ such that $|\mu| \gg |E_{\eta,\eta\lambda}|$, this works:

$$\gamma_c \approx \tfrac{1}{2}\gamma_p \sum_\lambda \tfrac{1}{2}\Big(1 + \lambda \frac{\delta}{\delta_\mathrm{A}}\Big) \sum_\eta f^{-\eta}(-\mu) = \tfrac{1}{2}\gamma_p. \tag{F.4}$$

Similarly, for large pairing $|\alpha| \gg |\delta|$ relative to detuning, we recover the $U \to 0$ limit:

$$\gamma_c \approx \tfrac{1}{2}\gamma_p \sum_\lambda \tfrac{1}{2}\Big(1 + \lambda \frac{\delta}{\alpha}\Big) \sum_\eta f^{-\eta}(\lambda\tfrac{1}{2}|\alpha| - \mu) = \tfrac{1}{2}\gamma_p. \tag{F.5}$$

For large detuning $|\delta| \gg |\alpha|, U$ one recovers

$$\gamma_c \approx \tfrac{1}{2}\gamma_p \sum_\lambda \tfrac{1}{2}\Big(1 + \lambda \frac{\delta}{|\delta|}\Big) \sum_\eta f^{-\eta}(\lambda\tfrac{1}{2}|\delta| - \mu) = \tfrac{1}{2}\gamma_p. \tag{F.6}$$

G

Transport expressions in different limiting cases

G.1 | Interacting dot without pairing

In the following, we summarize our results for the state evolution and transport equations in the limit $\alpha \to 0$. First, we point out that the labeling of the eigenstates [Eq. (3.19)] becomes a discontinuous choice of labeling the obvious even parity charge eigenstates at $\alpha, \delta = 0$:

$$|\tau\rangle\langle\tau| \overset{\alpha\to 0}{=} |0\rangle\langle 0| \text{ for } \tau = -\frac{\delta}{|\delta|} \quad \textit{and} \quad |\tau\rangle\langle\tau| \overset{\alpha\to 0}{=} |2\rangle\langle 2| \text{ for } \tau = +\frac{\delta}{|\delta|}. \tag{G.1}$$

Similarly, the invariants γ_s, γ_s' associated with an asymmetry with respect to energy eigenstates [τ branches, see Eq. (4.36a)-(4.36b)] are discontinuous and are related by the δ-sign to continuous invariants γ_c, γ_c' which are ignorant of this asymmetry:

$$\gamma_s \overset{\alpha\to 0}{=} \frac{\delta}{|\delta|}\gamma_c', \qquad \gamma_s' \overset{\alpha\to 0}{=} \frac{\delta}{|\delta|}\gamma_c. \tag{G.2}$$

As mentioned in the main text [Eq. (4.16)], the parameter-dependent polarization observable [cf. Eq. (B.14)] is discontinuous in δ but in a simple way,

$$A = \sum_\tau \tau\,|\tau\rangle\langle\tau| \overset{\alpha\to 0}{=} \frac{\delta}{|\delta|}(N - \mathbb{1}). \tag{G.3}$$

Inserting Eq. (G.2) and Eq. (G.3) into the observables (B.18) we recover the continuous expressions of Ref. [17] but in the more compact form of duality invariants,

$$\langle N - \mathbb{1}\rangle_z \overset{\alpha\to 0}{=} -\frac{\gamma_c'}{\gamma_c}, \qquad \langle p\rangle_z \overset{\alpha\to 0}{=} 1 - 2\frac{\gamma_c^2 - \gamma_c'^2}{\gamma_p\gamma_c}, \tag{G.4a}$$

$$\langle N-\mathbb{1}\rangle_{\bar{z}} \overset{\alpha\to 0}{=} \frac{\gamma_c'}{\gamma_p-\gamma_c}, \quad \langle p\rangle_{\bar{z}} \overset{\alpha\to 0}{=} 1-2\frac{(\gamma_p-\gamma_c)^2-\gamma_c'^2}{\gamma_p(\gamma_p-\gamma_c)}. \tag{G.4b}$$

Thus, for $\alpha \to 0$ our appropriate duality-adapted observables essentially reduce to the parity p and the charge polarization $N-\mathbb{1}$ and our four duality invariants simplify to just two invariants γ_c (state) and γ_c' (transport) both continuous in gate voltage δ. This result shows that also in Ref. [17], it is possible to eliminate all dual stationary observables in favour of the actual ones. Indeed, the stationary duality relation (4.54) also holds with the substitution $A \to N-\mathbb{1}$ (the δ-signs cancel) and shows the consistency of the actual and dual positivity constraints $|\langle N-\mathbb{1}\rangle_z| \leq \frac{1}{2}[1+\langle p\rangle_z]$ and $|\langle N-\mathbb{1}\rangle_{\bar{z}}| \leq \frac{1}{2}[1+\langle p\rangle_{\bar{z}}]$.

We recover the state evolution Eqs. (S3-S5) of Ref. [17] for $\alpha \to 0$ in (4.61):

$$\begin{aligned}|\rho(t)) \overset{\alpha\to 0}{=}& \Big[\tfrac{1}{4}|\mathbb{1}) + \langle N-\mathbb{1}\rangle_z \tfrac{1}{2}|N-\mathbb{1}) + \langle p\rangle_z \tfrac{1}{4}|p)\Big] \\ &+ \tfrac{1}{2}\Big[|N-\mathbb{1}) - \langle N-\mathbb{1}\rangle_{\bar{z}}|p)\Big] e^{-\gamma_c t}\big[\langle N\rangle_{\rho_0} - \langle N\rangle_z\big] \\ &+ |p) e^{-\gamma_p t}\Big\{\tfrac{1}{4}\big[\langle p\rangle_{\rho_0} - \langle p\rangle_z\big] + \tfrac{1}{2}\langle N-\mathbb{1}\rangle_{\bar{z}}\big[\langle N\rangle_{\rho_0} - \langle N\rangle_z\big]\Big\}. \end{aligned} \tag{G.5}$$

Likewise, for the currents (4.67)-(4.80b) we recover Eq. (S8) of Ref. [17] with continuous factors:

$$I_N(t) \overset{\alpha\to 0}{=} \gamma_c e^{-\gamma_c t}\big[\langle N\rangle_{\rho_0} - \langle N\rangle_z\big] \tag{G.6}$$

$$\begin{aligned} I_Q(t) \overset{\alpha\to 0}{=}& \big[\tfrac{1}{2}\big(\delta - U\langle N-\mathbb{1}\rangle_{\bar{z}}\big) - \mu\big]\gamma_c e^{-\gamma_c t}\big[\langle N\rangle_{\rho_0} - \langle N\rangle_z\big] \\ &+ U\gamma_p e^{-\gamma_p t}\Big\{\tfrac{1}{4}\big[\langle p\rangle_{\rho_0} - \langle p\rangle_z\big] + \tfrac{1}{2}\langle N-\mathbb{1}\rangle_{\bar{z}}\big[\langle N\rangle_{\rho_0} - \langle N\rangle_z\big]\Big\}. \end{aligned} \tag{G.7}$$

These expressions have been successfully applied to the analysis of both repulsive ($U > 0$) [17] and attractive ($U < 0$) quantum dots [48] in prior works to which we refer for concrete worked-out examples and discussion of experimental protocols. Compared to the result of Ref. [17] the last term in Eqs. (G.5) and (G.7) has been simplified using Eq. (4.53) and (4.61). This makes explicit that without initial excess charge ($\langle N\rangle_{\rho_0} = \langle N\rangle_z$) the heat current exhibits strictly single-exponential γ_p decay, whereas without initial excess parity ($\langle p\rangle_{\rho_0} = \langle p\rangle_z$) one still has double exponential heat decay.

A final point to note is that the distinct behaviour $\langle N\rangle_z$ and $\langle p\rangle_z$ is due to the interaction: only when additionally sending $U \to 0$ do we have $\gamma_c \to \frac{1}{2}\gamma_p$ since $E_{\eta,\eta} = \epsilon$ independent of η. By Eq. (4.58) the system is then self-dual such that the parity is completely fixed by the charge-polarization

$$-\langle N-\mathbb{1}\rangle_{\bar{z}} \overset{\alpha,U\to 0}{=} \langle N-\mathbb{1}\rangle_z, \quad \langle p\rangle_z \overset{U,\alpha\to 0}{=} \langle N-\mathbb{1}\rangle_z^2, \quad \langle p\rangle_{\bar{z}} \overset{U,\alpha\to 0}{=} \langle N-\mathbb{1}\rangle_{\bar{z}}^2. \tag{G.8}$$

The other nonzero invariant simplifies to an antisymmetric step function, $\gamma_c' \to \frac{1}{2}\gamma_p\big[1-2f(\epsilon-\mu)\big]$ which determines the charge-polarization [Eq. (G.4a)]:

$$\langle N-\mathbb{1}\rangle_z \overset{\alpha,U\to 0}{=} 2f(\epsilon-\mu)-1. \tag{G.9}$$

G.2 | Proximized dot without interaction

For a non-interacting dot ($U = 0$) proximized by a superconductor ($\alpha \neq 0$), see Ref. [90], fermionic duality also remains a dissipative symmetry, but its implications in this case have not been considered. Since in this case γ_c has one vanishing component [Eq. (4.68)], $\kappa_s' \to 0$, and the other is constant, $\kappa_c \to \gamma_p/2$, the invariants again simplify:

$$\gamma_c \overset{U\to 0}{=} \tfrac{1}{2}\gamma_p, \qquad \gamma_s' \overset{U\to 0}{=} \tfrac{1}{2}\gamma_p \frac{\delta}{\delta_\mathrm{A}}. \tag{G.10}$$

Thus exact self-duality is fulfilled by Eq. (4.58), and the corresponding discussion in Sec. 4.4.1 applies. The reason is that $E_{\eta,\tau} \to \frac{1}{2}\eta\tau\delta_\mathrm{A}$ depends only on the product $\eta\tau \equiv \lambda = \pm$ unlike the interacting case [Eq. (3.28)]. For the two remaining invariants $\gamma_c' = \kappa_c' + \frac{\delta}{\delta_\mathrm{A}}\kappa_s$ and $\gamma_s = \kappa_s + \frac{\delta}{\delta_\mathrm{A}}\kappa_c'$, the components read

$$\kappa_s \overset{U\to 0}{=} \tfrac{1}{2}\gamma_p \sum_{\lambda\eta} \tfrac{1}{2}\lambda\eta f^{-\eta}(\tfrac{1}{2}\lambda\delta_\mathrm{A} - \mu), \quad \kappa_c' \overset{U\to 0}{=} \tfrac{1}{2}\gamma_p \sum_{\lambda\eta} \tfrac{1}{2}\eta f^{-\eta}(\tfrac{1}{2}\lambda\delta_\mathrm{A} - \mu). \tag{G.11}$$

Importantly, for $U = 0$ the self-duality (G.10) holds for all values of the remaining parameters δ, μ, T, Γ, and in particular, the pairing α, such that we have according to Eq. (B.19)

$$\langle A\rangle_z \overset{U\to 0}{=} \langle \bar{A}\rangle_{\bar{z}}, \quad \langle p\rangle_z \overset{U\to 0}{=} \langle p\rangle_{\bar{z}}, \quad \langle p\rangle_z \overset{U\to 0}{=} \langle A\rangle_z^2, \quad \langle p\rangle_{\bar{z}} \overset{U\to 0}{=} \langle A\rangle_{\bar{z}}^2. \tag{G.12}$$

Applying all simplifications [(4.62)-(4.63), (4.70), (4.82)], we obtain for the stationary polarization

$$\langle A\rangle_z \overset{U\to 0}{=} -2\frac{\gamma_s}{\gamma_p} = -\sum_\lambda \tfrac{1}{2}\Big(\lambda + \frac{\delta}{\delta_\mathrm{A}}\Big)\sum_\eta \eta f^{-\eta}(\tfrac{1}{2}\lambda\delta_\mathrm{A} - \mu), \tag{G.13}$$

and for the non-interacting stationary current (4.71):

$$I_\mathrm{N}(\infty) = \gamma_c' + \gamma_s'\langle A\rangle_z = \tfrac{1}{2}\gamma_p \tfrac{1}{2}\sum_{\lambda\eta} \eta f^{-\eta}(\tfrac{1}{2}\lambda\delta_\mathrm{A} - \mu) \times \Big(1 - \frac{\delta^2}{\delta_A^2}\Big). \tag{G.14}$$

G.3 | Proximized dot at high bias

Finally, for an interacting and proximized dot at high bias, $\mu \gg U, |\alpha|, |\delta|, T, \Gamma$ (for simplicity denoted as "$|\mu| \to \infty$") we have asymptotic self-duality as mentioned in Sec. 4.4.1. In this case $|\mu| \gg |E_{\eta,\tau}|$ such that all dependence on the Andreev energies (and thus on η and τ) drops out in the components (4.68). Therefore the two components $\kappa_s, \kappa_s' \to 0$ vanish, one is constant $\kappa_c \to \gamma_p/2$ and one simplifies to

$\kappa_c' \to \frac{1}{2}\gamma_p \sum_\eta \eta f^{-\eta}(-\mu) = \frac{1}{2}\gamma_p \tanh[\mu/(2T)]$. Once more the invariants have a simple property

$$\gamma_s \overset{|\mu|\to\infty}{=} \frac{\delta}{\delta_\mathrm{A}}\gamma_c', \qquad \gamma_s' \overset{|\mu|\to\infty}{=} \frac{\delta}{\delta_\mathrm{A}}\gamma_c, \tag{G.15}$$

which is very similar to the $\alpha \to 0$ case (G.2) except for the fact that the "sign function" $\delta/|\delta|$ in Eq. (G.10) gets "broadened" by α in δ/δ_A. Note that this gate-voltage dependence of the pre-factor, originating from the state-dependence of the effective rate $\Gamma_{\eta\tau}$ [Eq. (3.31)], is not wiped out by the high bias which by our assumptions has to remain below the (infinite) gap of the superconductor, see Sec. 3.3. The remaining invariants read

$$\gamma_c \overset{|\mu|\to\infty}{=} \tfrac{1}{2}\gamma_p, \qquad \gamma_c' \overset{|\mu|\to\infty}{=} \tfrac{1}{2}\gamma_p \tanh\left(\frac{\mu}{2T}\right), \tag{G.16}$$

such that by Eq. (4.58) we again have self-duality (4.56):

$$\langle A\rangle_z \overset{|\mu|\to\infty}{=} \langle \bar{A}\rangle_{\bar{z}}, \qquad \langle p\rangle_z \overset{|\mu|\to\infty}{=} \langle p\rangle_{\bar{z}} \quad \langle p\rangle_z \overset{|\mu|\to\infty}{=} \langle A\rangle_z^2, \quad \langle p\rangle_{\bar{z}} \overset{|\mu|\to\infty}{=} \langle A\rangle_{\bar{z}}^2. \tag{G.17}$$

and the simplifications [(4.62)-(4.63), (4.70), (4.82)] apply. Now the stationary polarization consists of factors independently controlled by the applied voltages:

$$\langle A\rangle_z \overset{|\mu|\to\infty}{=} -\frac{\delta}{\delta_\mathrm{A}} \tanh\left(\frac{\mu}{2T}\right). \tag{G.18}$$

Likewise, in the stationary current (4.69) the pre-factor κ_c' depends only on the bias μ:

$$I_N(\infty) = \gamma_c' + \gamma_s' \langle A\rangle_z \overset{|\mu|\to\infty}{=} \tfrac{1}{2}\gamma_p \tanh\left(\frac{\mu}{2T}\right) \times \left(1 - \frac{\delta^2}{\delta_A^2}\right). \tag{G.19}$$

H

Derivation of an effective master equation for the resonant region

We derive an effective master equation for the resonant region $\delta \approx \delta_{\mathrm{PHS}}$ in the regime of high bias and weak pairing. Based on Table 3.1 and panel (c) of Fig. 5.7, we note that all Fermi functions can be replaced by the zero-temperature thresholds $\mu - E_{\eta,\tau} \gg 0$ in this regime. This considerably simplifies the master equation:

$$\frac{d\rho_1}{dt} = -\frac{1}{2}(\sum_{\tau}\Gamma_{\tau})\rho_1 + \sum_{\tau}\Gamma_{\bar{\tau}}\rho_{\tau} \tag{H.1}$$

$$\frac{d\rho_{\tau}}{dt} = -\Gamma_{\bar{\tau}}\rho_{\tau} + \frac{\Gamma_{\tau}}{2}\rho_1 \,. \tag{H.2}$$

From the stationary state, we extract the real and dual polarizations as given in Eqs. (5.27-5.28) of the main text. In the same manner, the transport rates

$$\gamma_c = \frac{1}{2}\sum_{\eta,\tau} W^{\eta}_{1,\tau}, \tag{H.3}$$

$$\gamma_s' = \frac{1}{2}\sum_{\eta,\tau} \eta\tau\, W^{\eta}_{1,\tau} \tag{H.4}$$

simplify by replacing the $W^{\eta}_{1,\tau}$ with the corresponding $\Gamma_{\pm}$-rates. They can be extracted from the $\tau \to 1$ transitions for particle η according to Table 3.1,

$$\gamma_c = \frac{\Gamma_+ + \Gamma_-}{2}, \tag{H.5}$$

$$\gamma_s' = \frac{\Gamma_+ - \Gamma_-}{2}, \tag{H.6}$$

or equivalently as given in Eqs. (5.27-5.28).

References

[1] L. C. Ortmanns, G. E. W. Bauer, and Y. M. Blanter, "Magnon dispersion in bilayers of two-dimensional ferromagnets", Phys. Rev. B **103**, 155430 (2021).

[2] L. C. Ortmanns, M. R. Wegewijs, and J. Splettstoesser, "Solution of master equations by fermionic-duality: Time-dependent charge and heat currents through an interacting quantum dot proximized by a superconductor", SciPost Phys. **14**, 095 (2023).

[3] L. C. Ortmanns, J. Splettstoesser, and M. R. Wegewijs, "Transient transport spectroscopy of an interacting quantum dot proximized by a superconductor: Charge- and heat-currents after a switch", arXiv, 10.48550/arXiv.2304.14893 (2023).

[4] K. S. Burch, D. Mandrus, and J.-G. Park, "Magnetism in two-dimensional van der Waals materials", Nature **563**, 47–52 (2018).

[5] L. C. Ortmanns, *Magnons in bilayers of van der Waals materials, third project of the master thesis* (2019).

[6] B. Sothmann and M. Büttiker, "Magnon-driven quantum-dot heat engine", Europhys. Lett. **99**, 27001 (2012).

[7] J. König, J. Martinek, J. Barnaś, and G. Schön, "Quantum Dots Attached to Ferromagnetic Leads: Exchange Field, Spin Precession, and Kondo Effect", in *CFN Lectures on Functional Nanostructures Vol. 1* (Springer, Berlin, Germany, Dec. 2004), pp. 145–164.

[8] S. M. Tabatabaei, D. Sánchez, A. L. Yeyati, and R. Sánchez, "Andreev-Coulomb Drag in Coupled Quantum Dots", Phys. Rev. Lett. **125**, 247701 (2020).

[9] F. Giazotto, T. T. Heikkilä, A. Luukanen, A. M. Savin, and J. P. Pekola, "Opportunities for mesoscopics in thermometry and refrigeration: Physics and applications", Rev. Mod. Phys. **78**, 217–274 (2006).

[10] J. P. Pekola and B. Karimi, "Colloquium: Quantum heat transport in condensed matter systems", Rev. Mod. Phys. **93**, 041001 (2021).

[11] G. E. D. K. Prawiroatmodjo, M. Leijnse, F. Trier, Y. Chen, D. V. Christensen, M. von Soosten, N. Pryds, and T. S. Jespersen, "Transport and excitations in a negative-U quantum dot at the LaAlO3/SrTiO3 interface", Nat. Commun. **8**, 1–7 (2017).

[12] G. Cheng, M. Tomczyk, S. Lu, J. P. Veazey, M. Huang, P. Irvin, S. Ryu, H. Lee, C.-B. Eom, C. S. Hellberg, and J. Levy, "Electron pairing without superconductivity", Nature **521**, 196–199 (2015).

[13] G. Cheng, M. Tomczyk, A. B. Tacla, H. Lee, S. Lu, J. P. Veazey, M. Huang, P. Irvin, S. Ryu, C.-B. Eom, A. Daley, D. Pekker, and J. Levy, "Tunable Electron-Electron Interactions in $LaAlO_3/SrTiO_3$ Nanostructures", Phys. Rev. X **6**, 041042 (2016).

[14] A. Hamo, A. Benyamini, I. Shapir, I. Khivrich, J. Waissman, K. Kaasbjerg, Y. Oreg, F. von Oppen, and S. Ilani, "Electron attraction mediated by Coulomb repulsion", Nature **535**, 395–400 (2016).

[15] B. Sothmann, D. Futterer, M. Governale, and J. König, "Probing the exchange field of a quantum-dot spin valve by a superconducting lead", Phys. Rev. B **82**, 094514 (2010).

[16] M. Kamp and B. Sothmann, "Higgs-like pair amplitude dynamics in superconductor–quantum-dot hybrids", Phys. Rev. B **103**, 045414 (2021).

[17] J. Schulenborg, R. B. Saptsov, F. Haupt, J. Splettstoesser, and M. R. Wegewijs, "Fermion-parity duality and energy relaxation in interacting open systems", Phys. Rev. B **93**, 081411 (2016).

[18] J. Schulenborg, A. Di Marco, J. Vanherck, M. R. Wegewijs, and J. Splettstoesser, "Thermoelectrics of Interacting Nanosystems—Exploiting Superselection Instead of Time-Reversal Symmetry", Entropy **19**, 668 (2017).

[19] M. A. McGuire, "Crystal and Magnetic Structures in Layered, Transition Metal Dihalides and Trihalides", Crystals **7**, 121 (2017).

[20] N. Sivadas, S. Okamoto, X. Xu, C. J. Fennie, and D. Xiao, "Stacking-Dependent Magnetism in Bilayer CrI3", Nano Lett. **18**, 7658–7664 (2018).

[21] L. Chen, J.-H. Chung, B. Gao, T. Chen, M. B. Stone, A. I. Kolesnikov, Q. Huang, and P. Dai, "Topological Spin Excitations in Honeycomb Ferromagnet CrI_3", Phys. Rev. X **8**, 041028 (2018).

[22] M. Gibertini, M. Koperski, A. F. Morpurgo, and K. S. Novoselov, "Magnetic 2D materials and heterostructures", Nat. Nanotechnol. **14**, 408–419 (2019).

[23] A. Prabhakar and D. D. Stancil, *Spin Waves* (Springer US).

[24] T. Holstein and H. Primakoff, "Field Dependence of the Intrinsic Domain Magnetization of a Ferromagnet", Phys. Rev. **58**, 1098–1113 (1940).

[25] E. McCann and V. I. Fal'ko, "Landau-Level Degeneracy and Quantum Hall Effect in a Graphite Bilayer", Phys. Rev. Lett. **96**, 086805 (2006).

[26] W. Nolting and A. Ramakanth, *Quantum Theory of Magnetism* (Springer, Berlin, Germany).

[27] H. Kondo and Y. Akagi, "Nonlinear magnon spin Nernst effect in antiferromagnets and strain-tunable pure spin current", Phys. Rev. Res. **4**, 013186 (2022).

[28] S. A. Owerre, "Magnon Hall effect in AB-stacked bilayer honeycomb quantum magnets", Phys. Rev. B **94**, 094405 (2016).

[29] *Thermal Hall Effect of Magnons*, [Online; accessed 26. Mar. 2023], Mar. 2023.

[30] B. M. Victor, "Quantal phase factors accompanying adiabatic changes", Proc. R. Soc. Lond. A. **392**, 45–57 (1984).

[31] R. Matsumoto and S. Murakami, "Theoretical Prediction of a Rotating Magnon Wave Packet in Ferromagnets", Phys. Rev. Lett. **106**, 197202 (2011).

[32] R. Matsumoto and S. Murakami, "Rotational motion of magnons and the thermal Hall effect", Phys. Rev. B **84**, 184406 (2011).

[33] H. Katsura, N. Nagaosa, and P. A. Lee, "Theory of the Thermal Hall Effect in Quantum Magnets", Phys. Rev. Lett. **104**, 066403 (2010).

[34] Y. Onose, T. Ideue, H. Katsura, Y. Shiomi, N. Nagaosa, and Y. Tokura, "Observation of the Magnon Hall Effect", Science **329**, 297–299 (2010).

[35] H. Kondo, Y. Akagi, and H. Katsura, "Non-Hermiticity and topological invariants of magnon Bogoliubov–de Gennes systems", Prog. Theor. Exp. Phys. **2020**, 12A104 (2020).

[36] S. A. Owerre, "A first theoretical realization of honeycomb topological magnon insulator", J. Phys.: Condens. Matter **28**, 386001 (2016).

[37] L. Chen, J.-H. Chung, B. Gao, T. Chen, M. B. Stone, A. I. Kolesnikov, Q. Huang, and P. Dai, "Topological Spin Excitations in Honeycomb Ferromagnet CrI_3", Phys. Rev. X **8**, 041028 (2018).

[38] T. Moriya, "Anisotropic Superexchange Interaction and Weak Ferromagnetism", Phys. Rev. **120**, 91–98 (1960).

[39] H. Schoeller and G. Schön, "Mesoscopic quantum transport: Resonant tunneling in the presence of a strong Coulomb interaction", Phys. Rev. B **50**, 18436–18452 (1994).

[40] J. König, J. Schmid, H. Schoeller, and G. Schön, "Resonant tunneling through ultrasmall quantum dots: Zero-bias anomalies, magnetic-field dependence, and boson-assisted transport", Phys. Rev. B **54**, 16820–16837 (1996).

[41] R. B. Saptsov and M. R. Wegewijs, "Fermionic superoperators for zero-temperature nonlinear transport: Real-time perturbation theory and renormalization group for Anderson quantum dots", Phys. Rev. B **86**, 235432 (2012).

[42] R. B. Saptsov and M. R. Wegewijs, "Time-dependent quantum transport: Causal superfermions, exact fermion-parity protected decay modes, and Pauli exclusion principle for mixed quantum states", Phys. Rev. B **90**, 045407 (2014).

[43] V. Bruch, K. Nestmann, J. Schulenborg, and M. Wegewijs, "Fermionic duality: General symmetry of open systems with strong dissipation and memory", SciPost Phys. **11**, 053 (2021).

[44] G. C. Wick, A. S. Wightman, and E. P. Wigner, "The Intrinsic Parity of Elementary Particles", Phys. Rev. **88**, 101–105 (1952).

[45] Y. Aharonov and L. Susskind, "Charge Superselection Rule", Phys. Rev. **155**, 1428–1431 (1967).

[46] L. D. Contreras-Pulido, J. Splettstoesser, M. Governale, J. König, and M. Büttiker, "Time scales in the dynamics of an interacting quantum dot", Phys. Rev. B **85**, 075301 (2012).

[47] J. Vanherck, J. Schulenborg, R. B. Saptsov, J. Splettstoesser, and M. R. Wegewijs, "Relaxation of quantum dots in a magnetic field at finite bias – Charge, spin, and heat currents", Phys. Status Solidi B **254**, 1600614 (2017).

[48] J. Schulenborg, M. R. Wegewijs, and J. Splettstoesser, "Thermovoltage in quantum dots with attractive interaction", Appl. Phys. Lett. **116**, 243103 (2020).

[49] J. Schulenborg, J. Splettstoesser, and M. R. Wegewijs, "Duality for open fermion systems: Energy-dependent weak coupling and quantum master equations", Phys. Rev. B **98**, 235405 (2018).

[50] T. Prosen, "Pt-symmetric quantum liouvillean dynamics", Phys. Rev. Lett. **109**, 090404 (2012).

[51] G. E. Blonder, M. Tinkham, and T. M. Klapwijk, "Transition from metallic to tunneling regimes in superconducting microconstrictions: Excess current, charge imbalance, and supercurrent conversion", Phys. Rev. B **25**, 4515–4532 (1982).

[52] Y. V. Nazarov and Y. M. Blanter, *Quantum Transport: Introduction to Nanoscience* (Cambridge University Press, Cambridge, England, UK, May 2009).

[53] C. Karrasch, S. Andergassen, and V. Meden, "Supercurrent through a multilevel quantum dot close to singlet-triplet degeneracy", Phys. Rev. B **84**, 134512 (2011).

[54] T. Meng, S. Florens, and P. Simon, "Self-consistent description of Andreev bound states in Josephson quantum dot devices", Phys. Rev. B **79**, 224521 (2009).

[55] J. Bardeen, L. N. Cooper, and J. R. Schrieffer, "Theory of Superconductivity", Phys. Rev. **108**, 1175–1204 (1957).

[56] J. Bardeen, L. N. Cooper, and J. R. Schrieffer, "Microscopic Theory of Superconductivity", Phys. Rev. **106**, 162–164 (1957).

[57] J. Koch, T. M. Yu, J. Gambetta, A. A. Houck, D. I. Schuster, J. Majer, A. Blais, M. H. Devoret, S. M. Girvin, and R. J. Schoelkopf, "Charge-insensitive qubit design derived from the Cooper pair box", Phys. Rev. A **76**, 042319 (2007).

[58] V. Bouchiat, D. Vion, P. Joyez, D. Esteve, and M. H. Devoret, "Quantum coherence with a single Cooper pair", Phys. Scr. **1998**, 165 (1998).

[59] A. Wallraff, D. I. Schuster, A. Blais, L. Frunzio, and R. J. Schoelkopf, "Strong coupling of a single photon to a superconducting qubit using circuit quantum electrodynamics", Nature **431**, 162–7 (2004).

[60] C. Padurariu and Y. V. Nazarov, "Theoretical proposal for superconducting spin qubits", Phys. Rev. B **81**, 144519 (2010).

[61] S. Reynaud, E. Giacobino, and J. Zinn-Justin, *Fluctuations Quantiques / Quantum Fluctuations: Les Houches Session LXIII, June 27 - July 28, 1995.* (1997).

[62] R. Hanson, B. Witkamp, L. M. K. Vandersypen, L. H. W. van Beveren, J. M. Elzerman, and L. P. Kouwenhoven, "Zeeman Energy and Spin Relaxation in a One-Electron Quantum Dot", Phys. Rev. Lett. **91**, 196802 (2003).

[63] F. H. L. Koppens, K. C. Nowack, and L. M. K. Vandersypen, "Spin Echo of a Single Electron Spin in a Quantum Dot", Phys. Rev. Lett. **100**, 236802 (2008).

[64] M. Hays, V. Fatemi, D. Bouman, J. Cerrillo, S. Diamond, K. Serniak, T. Connolly, P. Krogstrup, J. Nygård, A. L. Yeyati, A. Geresdi, and M. H. Devoret, "Coherent manipulation of an Andreev spin qubit", Science **373**, 430–433 (2021).

[65] J. Cerrillo, M. Hays, V. Fatemi, and A. L. Yeyati, "Spin coherent manipulation in Josephson weak links", Phys. Rev. Res. **3**, L022012 (2021).

[66] S. De Franceschi, L. Kouwenhoven, C. Schönenberger, and W. Wernsdorfer, "Hybrid superconductor–quantum dot devices", Nat. Nanotechnol. **5**, 703–711 (2010).

[67] J. M. Thijssen and H. S. J. Van der Zant, "Charge transport and single-electron effects in nanoscale systems", Phys. Status Solidi B **245**, 1455–1470 (2008).

[68] V. D. J. A., N. Y. V., B. E. P., S. De Franceschi, and K. L. P., "Supercurrent reversal in quantum dots.", Nature **442**, 667–670 (2006).

[69] J.-P. Cleuziou, W. Wernsdorfer, V. Bouchiat, T. Ondarçuhu, and M. Monthioux, "Carbon nanotube superconducting quantum interference device", Nat. Nanotechnol. **1**, 53–59 (2006).

[70] A. Martin-Rodero and A. L. Yeyati, "Josephson and Andreev transport through quantum dots", Phys. Rep., 10.1080/00018732.2011.624266 (2011).

[71] M. Governale, M. G. Pala, and J. König, "Real-time diagrammatic approach to transport through interacting quantum dots with normal and superconducting leads", Phys. Rev. B **77**, 134513 (2008).

[72] M. Kamp and B. Sothmann, "Phase-dependent heat and charge transport through superconductor–quantum dot hybrids", Phys. Rev. B **99**, 045428 (2019).

[73] M. Heckschen and B. Sothmann, "Pair-amplitude dynamics in strongly coupled superconductor–quantum dot hybrids", Phys. Rev. B **105**, 045420 (2022).

[74] J. Siegl, J. Picó-Cortés, and M. Grifoni, "A particle conserving approach to AC-DC driven interacting quantum dots with superconducting leads", arXiv, 10.48550/arXiv.2205.13936 (2022).

[75] A. V. Rozhkov and D. P. Arovas, "Interacting-impurity Josephson junction: Variational wave functions and slave-boson mean-field theory", Phys. Rev. B **62**, 6687–6691 (2000).

[76] J. Schulenborg, "Dynamics of open fermionic nano-systems – a fundamental symmetry and its application to electron transport in interacting quantum dots", PhD thesis (Chalmers University of Technology, Sweden, 2018).

[77] A. Kolmogoroff, "Zur Theorie der Markoffschen Ketten", Math. Ann. **112**, 155–160 (1936).

[78] R. Serfozo, *Basics of Applied Stochastic Processes* (Springer, Berlin, Germany, 2009).

[79] M. G. Pala, M. Governale, and J. König, "Nonequilibrium Josephson and Andreev current through interacting quantum dots", New J. Phys. **9**, 278 (2007).

[80] L. Tosi, C. Metzger, M. F. Goffman, C. Urbina, H. Pothier, S. Park, A. L. Yeyati, J. Nygård, and P. Krogstrup, "Spin-Orbit Splitting of Andreev States Revealed by Microwave Spectroscopy", Phys. Rev. X **9**, 011010 (2019).

[81] C. Jünger, A. Baumgartner, R. Delagrange, D. Chevallier, S. Lehmann, M. Nilsson, K. A. Dick, C. Thelander, and C. Schönenberger, "Spectroscopy of the superconducting proximity effect in nanowires using integrated quantum dots", Commun. Phys. **2**, 1–8 (2019).

[82] D. Bouman, R. J. J. van Gulik, G. Steffensen, D. Pataki, P. Boross, P. Krogstrup, J. Nygård, J. Paaske, A. Pályi, and A. Geresdi, "Triplet-blockaded Josephson supercurrent in double quantum dots", Phys. Rev. B **102**, 220505 (2020).

[83] A. Jellinggaard, K. Grove-Rasmussen, M. H. Madsen, and J. Nygård, "Tuning Yu-Shiba-Rusinov states in a quantum dot", Phys. Rev. B **94**, 064520 (2016).

[84] E. J. H. Lee, X. Jiang, M. Houzet, R. Aguado, C. M. Lieber, and S. De Franceschi, "Spin-resolved Andreev levels and parity crossings in hybrid superconductor–semiconductor nanostructures", Nat. Nanotechnol. **9**, 79–84 (2014).

[85] F. D. M. Haldane, "Hartree-Fock study of the Anderson model coupled to a boson field; mixed valence states", Phys. Rev. B **15**, 281–289 (1977).

[86] B. Sothmann and J. König, "Transport through quantum-dot spin valves containing magnetic impurities", Phys. Rev. B **82**, 245319 (2010).

[87] S. Droste, J. Splettstoesser, and M. Governale, "Finite-frequency noise in a quantum dot with normal and superconducting leads", Phys. Rev. B **91**, 125401 (2015).

[88] N. Hartman, C. Olsen, S. Lüscher, M. Samani, S. Fallahi, G. C. Gardner, M. Manfra, and J. Folk, "Direct entropy measurement in a mesoscopic quantum system", Nat. Phys. **14**, 1083–1086 (2018).

[89] B. A. Placke, T. Pluecker, J. Splettstoesser, and M. R. Wegewijs, "Attractive and driven interactions in quantum dots: Mechanisms for geometric pumping", Phys. Rev. B **98**, 085307 (2018).

[90] C. W. J. Beenakker, "Quantum transport in semiconductor-superconductor microjunctions", Phys. Rev. B **46**, 12841–12844(R) (1992).